Microstructure and Microtexture Developments in Grain Oriented Electrical Steels

Swansea University
Prifysgol Abertawe

Ali Nadoum

Supervisor: Dr. Soran Birosca

Materials Research Centre

Swansea University

A dissertation submitted in fulfilment of the requirements for

the Degree of Doctor of Philosophy,

Swansea University

Acknowledgements

I would like to show my deepest gratitude to my academic supervisor, Dr. Soran Birosca for offering me the opportunity to further pursue my interest in the academic and scientific research, his guidance, support and his friendship. His advice and corrections through the progress of this research and push made my publications see the light.

I would like to thank AIM (Advanced Imaging of Materials) for the training and Cogent power for supplying materials necessary for this project. Special thanks to Dr. Fiona Robinson from Cogent Orb for her support and advice throughout this project. I am also grateful to my friends and colleagues, especially, Diween Hawezy for his help in coding and Liu Gang for lab support.

I am indebted to my wife, Zainab, and her love over the years and here support, without her being there for me, I wouldn't be able to reach my goal. I would also like to thank my family for their support, kindness and encouragements.

Finally, I am thankful to Swansea University and their friendly staff, including lab technicians and PhD students, for their help and the exchange of knowledge.

Abstract

The first Si-Fe electrical steel was produced in 1905, and the grain-oriented steel was discovered in 1930 after Goss demonstrated how optimal combinations of heat treatment and cold rolling could produce a texture giving Si-Fe strip good magnetic properties when magnetised along its rolling direction. This technology has reduced the power loss in transformers greatly and remains the basis of the manufacturing process today. Since then, many postulations reported on the mechanism on abnormal grain growth (AGG) which is the key for Si-Fe superior magnetic properties. However, none have provided a concrete understanding of this phenomenon. Identifying and classifying the driving force behind Goss abnormal grain growth is of industrial and academic importance to further optimise the manufacturing process and reduce losses.

In the current investigation, the deviation from easy magnetisation direction <001> was studied to find a correlation between crystallographic orientation and magnetic domain structure. Both deviation angles α: the angle between <001> and in-plane rolling direction (RD), and β: the angle between <001> and out-plane rolling direction were calculated using electron backscatter diffraction (EBSD) raw data. Further, EBSD combined with forescatter detector (FSD) is used to reveal the magnetic domain configuration within individual oriented grains. The magnetic domain patterns were directly imaged and correlated to the crystal orientation and α and β deviation angles. It was demonstrated that the size of the deviated orientation grains from ideal (110) <001> Goss orientation is a critical microtexture parameter for the optimisation of magnetic property. It is concluded that the magnetic domain patterns and α and β angle of deviations are strongly correlated to the magnetic losses in GOES (grain oriented electrical steel).

Furthermore, the effect of grain boundaries, grain size, heating rate and dislocation density on Goss abnormal grain growth was investigated using EBSD. It was found that in the early stages of secondary recrystallisation random grains grow and abnormal growth of Goss achieved in low heating rate. The advantage of Goss abnormal grain growth in secondary recrystallisation is lost while annealing at a high heating rate, and random orientation can grow abnormally. Also, statistical analysis of grain boundaries, including CSL (coincident site lattice), shows no distinct behaviour and high angle grain boundaries and CSL are not exclusive to Goss oriented grains. In addition, GND (geometrically necessary dislocation) and Taylor Factor showed to be randomly distributed around Goss grains, and the hypothesis of Goss grains grow by consuming high GND and Taylor Factor grains cannot be the reason for Goss abnormal grain growth. Neutron diffraction experiment was conducted at Rutherford Appleton Laboratory, ISIS facility at Oxford, UK using GEM beamline. It was demonstrated that Si atom positions in the solid solution disorder α-Fe cubic unit cell that cause lattice distortions and BCC symmetry reduction is the most influential factor in early stages of Goss AGG than what was previously thought to be dislocation related stored energy, grain boundary characteristics and grain size/orientation advantages.

Finally, heat flux, heat flow direction, and strain effect on Goss abnormal grain growth investigated. It was found that heat flow direction greatly impacts the rate of abnormal grain

growth of Goss. Also, strain areas can disrupt Goss AGG and promotes randomly oriented grains to grow abnormally.

Declaration

This work has not previously been accepted in substance for any degree and is not being concurrently submitted in candidature for any degree.

Signed.....AliNadoum[redacted] (candidate)

Date .....14/12/2020.....

STATEMENT 1

This thesis is the result of my own investigations, except where otherwise stated. Other sources are acknowledged by footnotes giving explicit references. A bibliography is appended after each chapter.

Signed.....AliNadoum[redacted] (candidate)

Date.....14/12/2020.....

STATEMENT 2

I hereby give consent for my thesis, if accepted, to be available for photocopying and for interlibrary loan, and for the title and summary to be made available to outside organisations.

Signed.....AliNadoum[redacted] (candidate)

Date.....14/12/2020.....

Publications

[1] Birosca, S., Nadoum, A., Hawezy, D., Robinson, F., & Kockelmann, W. (2020). Mechanistic approach of Goss abnormal grain growth in electrical steel: Theory and argument. *Acta Materialia*, *185*, 370-381. (Chapter 5-7)

A summary of co-authors:

Ali Nadoum: Conducting the experiment, data collection and analysis, paper writing.

S. Birosca: Guiding through the project, correcting and editing the text.

D. Hawezy: Writing of Matlab code.

F. Robinson: supplying the materials necessary for the entire project.

W.Kockelmann: Neutron beamline scientist at ISIS facility at Oxford, UK.

[2] Nadoum, A., Robinson, F., & Birosca, S. (2020). On the correlation between magnetic domain and crystallographic grain orientation in grain oriented electrical steels. *Journal of Magnetism and Magnetic Materials*, *494*, 165772. (Chapter 4)

A summary of co-authors:

Ali Nadoum: Conducting the experiment, data collection and analysis, paper writing.

S. Birosca: Guiding through the project, correcting and editing the text.

F. Robinson: supplying the materials necessary for the entire project.

Contents

Nomenclature

AGG	Abnormal grain growth
BCC	Body centre cubic
CGO	Conventional grain oriented silicon steel
CSL	Coincident site lattice
EBSD	Electron Backscatter Diffraction
EM	Electromagnetic
EMF	Electromotive force
FSD	Forescatter detector
GND	Geometrically necessary dislocation
GOES	Grain oriented electrical steel
Hi-B	high permeability grain oriented silicon steel
HR-EBSD	High Resolution Electron Backscatter Diffraction
HR-SEM	High Resolution Scanning Electron Microscopy
IPF	Inverse pole figure
ND	Normal direction
ODF	The Orientation Distribution Function
RD	Rolling direction
SEM	Scanning Electron Microscopy
TD	Transverse direction
RT	Room temperature

Chapter 1: Introduction

Grain oriented electrical steel (GOES), also called Grain Oriented Silicon Steel, is widely used as the core of electric transformers due to its low power losses and good magnetic property. The manufacturing of grain oriented silicon steel is costly and requires careful control of thermomechanical processing in order to generate the desired microstructure and texture for a specific GOES application. In general, GOES production starts from conventional steelmaking, then follows continuous casting, slab reheating at 1400°C, hot rolling to 2mm thickness where the final GOES product inherits its crystallographic texture. A hot band is then annealed at a temperature ranging between 925°C to 1050°C for a very short period before cold rolling. Two-stage cold rolling is followed with intermediate annealing for conventional silicon steels, whereas a single stage of cold rolling is used for high-permeability silicon steels. Following cold rolling, decarburisation, i.e., primary annealing, is performed at 830°C in a wet hydrogen atmosphere after a cold reduction to the final thickness. The last stage of the process is a secondary recrystallisation annealing at 1200°C in a dry protective atmosphere where the desirable Goss (110) <001> grains grow and consume other oriented grains. The sharp Goss texture develops owing to abnormal Goss grain growth during the last annealing process. In general, the microstructure characteristics, grain size, and GOES sheet thickness affect the magnetic performance and magnetic losses. Furthermore, it was reported that a sharp Goss texture achieved during secondary annealing, also known as abnormal grains growth, has a great impact on the reduction of magnetic losses. To achieving further improvement in

magnetic performance and reduction of magnetic losses, a fundamentally understand the mechanism of Goss abnormal grain growth is required.

This project is a collaboration with Cogent Power in Newport, UK, in which commercial grain oriented electrical steel of different grades and chemical compositions were supplied. The aim of this study is to establish a fundamental understanding of the mechanism by which Goss oriented grains grow abnormally. Also, the effect of the microstructure, grain size, grain boundaries, stored energy and heating rate on microstructure evolution during secondary recrystallisation were investigated. In this study, the material characterisations were carried out using High Resolution Scanning Electron Microscopy (HR-SEM), High Resolution Electron Backscatter Diffraction (HR-EBSD) and Neutron diffraction facility. In addition, statistical and quantitative analysis of grain boundary distribution, grains size, texture component volume fraction and Geometrically Necessary Dislocation (GND) were performed to achieve further understanding of Goss abnormal grain growth phenomenon. In the current investigation, Type II magnetic contrast method was applied to visualise the magnetic domain structure of commercial GOES samples. The magnetic domain patterns were successfully captured using Scanning Electron Microscopy (SEM) equipped with a Forescatter Detector (FSD), revealing the correlation between deviation angles and magnetic domain configurations.

The main aim and objective of this research are to investigate the effect of crystallographic characteristics and annealing parameters on Goss texture evolution in 3% Si-Fe grain oriented electrical steel (GOES) / grain oriented silicon steel during secondary annealing. The expected objectives to be achieved in this research were as follow:

- Static magnetic domain imaging in GOES via forscatter imaging technique.
- The effect of ideal orientation and the deviation angles from rolling direction (RD) on magnetic domain pattern configuration.
- The effect of Goss grains deviation from the ideal Goss orientation on magnetic losses and magnetic permeability.
- The effect of grain size on magnetic losses.
- The effect of heating rate on Goss abnormal grain growth.
- The effect of heat flow direction (heat flux) on Goss abnormal grain growth.
- The impact of grain boundaries, CSL, grain size and stored energy on abnormal grain growth.
- Reviewing the available postulations and theories on Goss abnormal grain growth and validating their main concepts.
- Establishing a new theory for abnormal grain growth mechanism in GOES sheet during the secondary annealing process.

Based on the objectives mentioned above, the main chapters in this thesis are arranged as below: In literature review (Chapter 2), the general information about magnetisation, magnetic materials and magnetic losses are covered. Also, an introduction to grain oriented silicon steel manufacturing process and types of grain oriented silicon steel are presented. Following this, a detailed manufacturing process and the effect of each processing line on the development of grain oriented silicon steel are reported. In experimental procedures (Chapter 3), in addition to alloy chemistry, sample preparation and the annealing conditions, the observation techniques and the basic principle of EBSD and neutron diffraction are reported.

In Chapter 4, the effect of deviation angles in-plane α, and out-of-plane β, as well as grain boundaries on magnetic structure, were investigated. Furthermore, the grain size, grain oriented silicon steel sheet thickness and the deviation angles correlation with magnetic losses and magnetic permeability were thoroughly studied. In Chapter 5, the role of grain size, grain boundaries (including CSL) and stored energy on Goss abnormal grain growth was investigated. Statistical and quantitative analysis carried out on grain size, grain boundaries and CSL in the early stages of secondary recrystallisation were demonstrated. In Addition, the average GND and Taylor Factor were extracted from EBSD raw data, and the impact on Goss abnormal grain growth is reported.

In Chapter 6, the effect of heating rate and precipitation on Goss abnormal grain growth was studied using in-situ neutron diffraction tests that were carried out at ISIS facility at Oxford, UK using GEM beamline. The impact of the heating rate on d-spacing and lattice expansion is studied extensively. Additionally, the neutron diffraction peaks, profile and evolution in an in-situ beamline elucidated. Finally, the correlation between heating rate, abnormal grain growth and lattice distortion at high temperature was considered. In Chapter 7, the heating rate and the heat flux (heal flow direction) by means of SEM equipped with EBSD were further investigated. The impact of heating rate on texture evolution and abnormal grain growth as well as the heat flow direction on directional growth and growth rate is reported. Moreover, the effect of strain on abnormal grain growth and heat flow in secondary recrystallisation was

studied. Chapter 8 covers the conclusions from the general discussion and general findings during this study, and suggestions for future work are listed in Chapter 9.

Chapter 2: Literature Review

2.1 Introduction

The works of Michael Faraday made a significant contribution to the principles of electrical power generation. It was Michael Faraday who exposed the basic functioning of alternators in the backdrop of producing electrical power. Beyond any doubt, it was an astonishing discovery that made a breakthrough in the field of electric power generation. The reason is, electricity entirely changed the way of life, and the latest technological advancements are also connected with electrical power generation in one form or the other.

Electromagnetic induction is the concept which is also associated with Michael Faraday. Electromagnetic (EM) induction is referred to as the combination of magnetism and electricity when electricity is applied to a conducting material. It produces a magnetic field in the response [1]. The latest technological advancements are also tagged with the discovery of EM induction. Based on EM, when electrically conductive materials are moved inside a magnetic field, an electric current is generated inside the conductors. This current is referred to as the induced current [1].

When it comes to explaining the operation of a transformer, it contains the arrangement of 2 electrically isolated coils where an electromotive force (EMF) is induced in one coil due to the time-dependent (alternating) flux in the other coil. Hence, the device which is called a transformer is nothing less than an electrical device which is made by the arrangement of two magnetically attached coils [2]. A simple transformer can be seen in Figure 2-1. The induced EMF is proportional to the number of turns of the coils. It is worth mentioning here that if the secondary coil has more number of turns as compared to the primary coil, the secondary coil will contain higher voltage in response. In this scenario, a set-up transformer is formed [2].

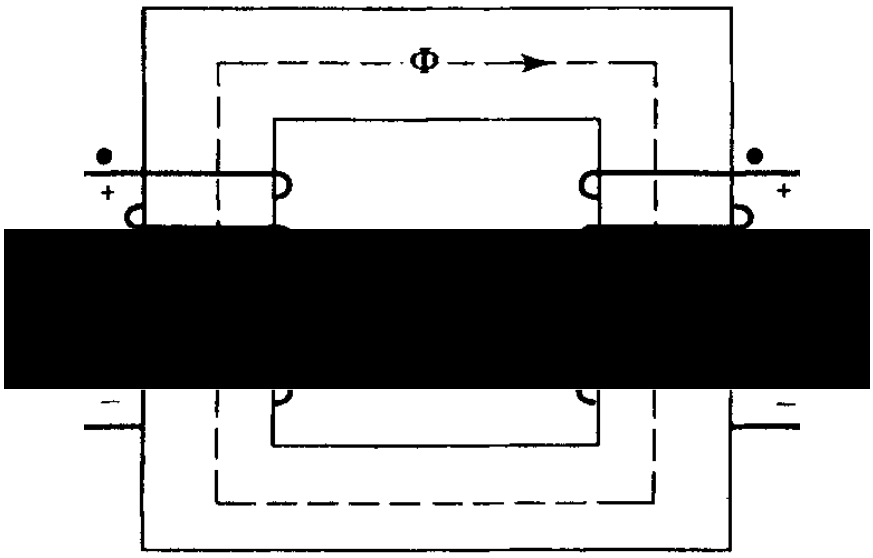

Figure 2-1 An idealized transformer [3].

Normally a set-up transformer functions to connect a low-voltage generating station to the high-voltage transmission line. In this setting, a generator is attached to the primary side of

transformer whilst the secondary side is attached to the transformer. On the flip side, the transformer with lower voltage windings on the secondary side is called a step-down transformer such as a welding transformer. In a welding transformer, the secondary side is designed accordingly to generate a comparatively high load current [3].

The transformer core is likely to undergo magnetic losses, that is why the core is constructed using thin laminations of highly permeable ferromagnetic material, i.e. silicon steel sheets, which reduces the magnetic losses. Furthermore, grain oriented silicon steel is manufactured in the lamination thickness of 0.17-0.35 mm. In general, silicon steel is preferred because it is tagged with low magnetic losses and good magnetic permeability. The two main types of transformers are Shell type and Core type transformers [1]. The following Figure 2-2 shows a Shell type transformer:

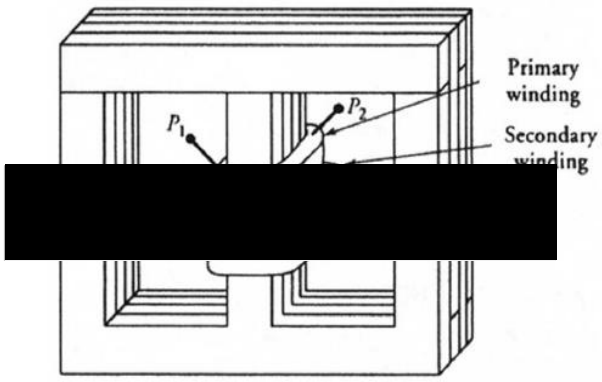

Figure 2-2 Shell Type Transformer [3].

The Shell-type transformer is constructed in the way that over the same leg of the agentic core, the two windings are coiled. However, the Core-type transformer is made in the way in which

the windings are split evenly and coiled on both legs of the rectangular core. The following Figure 2-3 shows the Core-type transformer.

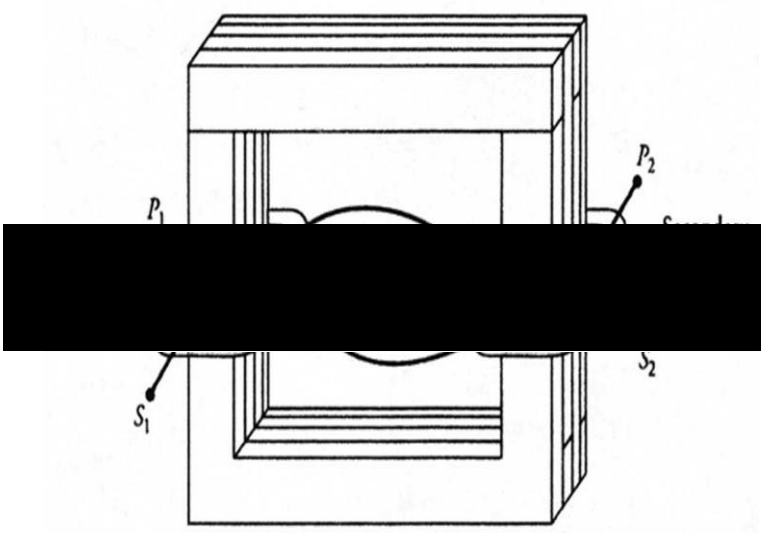

Figure 2-3 Core Type Transformer [3].

It is the coupling of the magnetic field between the windings, which forms the basis of efficient energy transfer from primary to the secondary windings inside a transformer. Ideally, the magnet core would transfer all the magnet lines of force produced around the primary winding to the secondary winding. Still because some lines of force flow out to the surrounding, the magnet loss occurs in response. The undesirable eddy currents also result in power losses that is why the cores are constructed with laminated iron to reduce the eddy currents. The efficiency of a transformer will be improved if its capacity is increased. A typical distribution transformer's efficiency is between 98% to 99% [4], [5].

The transformer losses are generally expressed as no-load-loss, half-load loss, full-load loss, and a few others because these losses tend to fluctuate with the load [6]. At all load levels, the eddy current losses and hysteresis remain constant, and they tend to dominate noticeably in the absence of load. On the other hand, when the load increases, the variable winding joule losses increases considerably. It is to be noted here that there can be substantial no-load-loss even in an idle transformer interrupting an electrical supply. The transformers need to be designed with larger cores coupled with high quality silicon steel to make them energy efficient. They are hence made using high quality silicon steel for the core, and the thicker wire is likely to increase the initial cost of the transformer. The construction choice is dependent upon the trade difference between the operating cost and the initial cost [6].

2.2 Magnetisation: Fundamentals and Theories

2.2.1 Ferromagnetism

Ferromagnetic materials have a magnetism moment which is aligned parallel or antiparallel due to a strong electron interaction [7]. These materials are commonly found in the shape of steel and iron. It is to be noted that a ferromagnet that is hard to magnetise initially, but once it is magnetised, the magnetization is permanent and is known as hard magnetic materials. On the other hand, it is relatively easier to magnetise the soft magnetic materials, but once the field causing the induction is removed, they lose their magnetism.

Furthermore, the electrons in ferromagnetic materials, spin spontaneously; thus, they align themselves and produce a powerful directional magnetic field in the response. Because of this attribute, the iron is considered as a very powerful magnet since its capable of inducing spontaneously coupled electrical spins. The magnetic moment of individual atoms of a material determines its magnetism which occurs due to the momentum of electrons when they spin in an orbital motion [8]. Magnetic strength is lowered the larger the number of this paired spins. In other words, materials would have stronger magnetic properties if they have fewer paired spins. Generally, the electron spins are the cause of magnetism in the magnetic materials [8-10].

The groundbreaking discovery in electromagnetism was that electric currents could produce magnetic fields, and when the alternating magnetic fields are attached with a conductor, it results in producing electric effects in response. In the case of a crystal lattice of iron, the electrons spin spontaneously and perfectly aligned which provides a magnetic field that is overall directionally coordinated. This is because iron has a set of spontaneously coupled electron spins, which provides a powerful magnet in return [10].

2.2.2 Magnetic Domains

Ferromagnetic materials hold magnetised domains wherein every individual magnetisation of a domain is oriented in a different way with regards to its neighbours magnetisation. When

there is no external field, these materials can be subdivided into many small magnetic regions [11]. Every domain is magnetised spontaneously to the saturation value, but there is a random distribution of magnetisation directions of many domains that the material exhibits no net magnetisation. The magnetisation process is the transformation of a multi-domain state into one wherein the applied external field and the magnetised single domain have the same directions as exhibited in Figure 2-4.

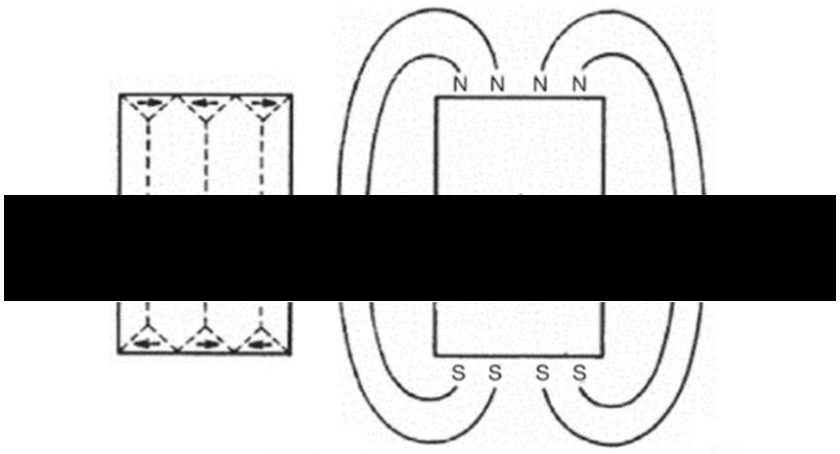

Figure 2-4 Magnetisation of multiple domains. Adopted from [11].

Because there is a powerful exchange interaction between neighbouring atoms due to unpaired electron spins aligned parallel to each other, these domains come into existence [7]. The ferromagnetic material is demagnetised material if the sum of the magnetisation of all of its magnetic domains equals to zero. On the other hand, the ferromagnetic material is magnetized when subjected to an external magnetic field.

2.2.3 Domain walls

Domain walls are a transitional region where the magnetic moment of each domain is separated [11]. If this transition is sudden, the energy which is the results of magnetic exchange between domains is excessive for the equilibrium of the domain structure as shown in Figure 2-5a, whereas a relatively wide magnetic domain wall, smooth transition magnetic domain, results in lower exchange energy [8],[11], as shown in Figure 2-5b. In addition, the magnetic domain walls can be classified as 90° or 180°, as shown in Figure 2-6, these walls separating each magnetic domain that is magnetised in one of the easy magnetization directions [11].

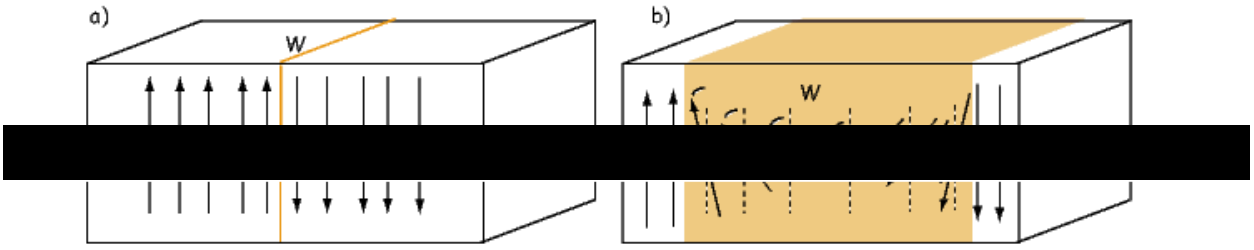

Figure 2-5 Different magnetic domains wall where (a)is Abrupt domain wall (a), and (b) is a smooth domain wall [12].

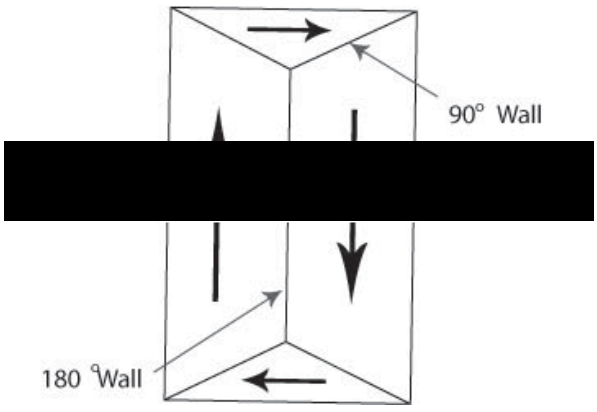

Figure 2-6 180° and 90° magnetic domain wall classification [11].

The two-fundamental magnetisation processes are referred to as domain rotation and domain wall motion [12]. Inside a domain wall, the magnetisation rotates 180 degrees in two ways. Bloch wall is magnetic domain wall that magnetisation rotates out of the plane from one magnetic domain to another. On the other hand, when the magnetisation rotates inside a plane, it is referred to as a Neel wall. Bloch walls can be noticed in thicker films, in the order of microns, but not in thin films, because the out-of-plane component of the magnetisation creates magnetic poles on the surface of the film that in turn, creates a demagnetisation field, which is relative to the film thickness. The demagnetisation field is inversely proportional to the film thickness. A powerful magnetisation field forces the magnetisation to reside in the direction of the film plane. Hence, only Neel walls form when the thickness of the ferromagnetic film equals to 100nm or thinner [12]. Figure 2-7 shows the Bloch and Neel walls.

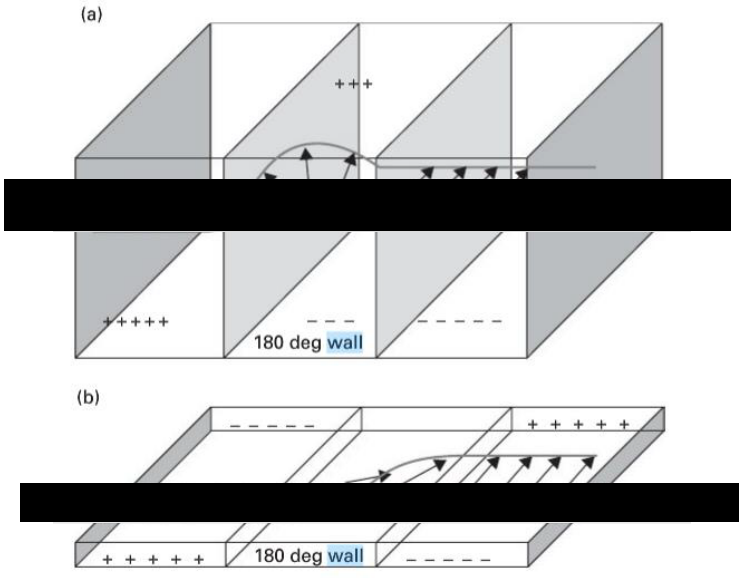

Figure 2-7 Two types of magnetic domain walls, (a) Bloch wall in thick film and (b) Neel wall in a thin film [12].

2.2.4 Magnetocrystalline Anisotropy

Magnetic anisotropy is a term which can be simply defined as magnetic energy or properties and the dependency on the direction of spontaneous magnetisation. It is defined as the external magnetisation required to reach saturation in any direction other than the easy magnetisation direction. In the case of a single iron crystal, the easy magnetisation direction is <100> while the medium and the hard directions are <110> and <111>, respectively. In medium and hard directions, a higher external magnetic field is needed in order to reach saturation, contrary to <100> direction [13]. It is to be noted here that the magnetocrystalline anisotropy energy will be found at the wall boundaries between domains in the demagnetised state.

A grain oriented silicon steel atoms form a cubic unit cell, knowns as body centred cube (BCC). With strong Goss texture {110} <001>, resulting in an easy magnetization in the rolling direction (RD) and minimising magnetocrystalline anisotropy energy [14]. The following Figure 2-8 exhibits the directions.

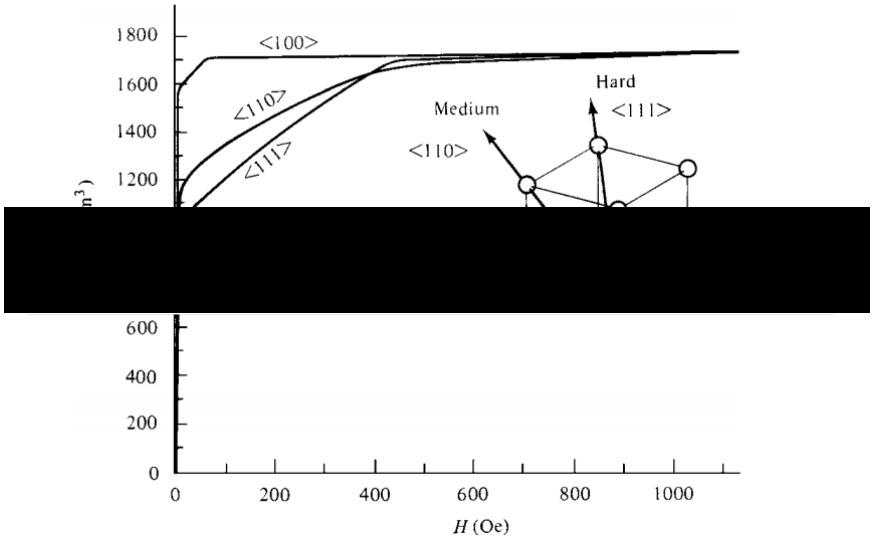

Figure 2-8 Magnetisation along with three directions of a BCC single iron crystal [11].

2.2.5 Magnetostatic Energy

If a ferromagnetic material is magnetised, magnetostatic energy is defined as total energy in the ferromagnetic material external magnetic field. Hence, a field within the sample is formed, which is referred to as the demagnetising field. Furthermore, the exchange energy is increased in the case of neighbouring domains with antiparallel magnetisations, whereas magnetostatic energy is decreased [13]. The magnetisation field, as well as the magnetostatic energy, will be reduced if the material is subdivided into two oppositely magnetised domains [15]. The magnetostatic energy will be further decreased as the domains continue the indefinite subdivisions. This would minimize the magnetostatic energy, which is also reflected in Figure 2-9 [11].

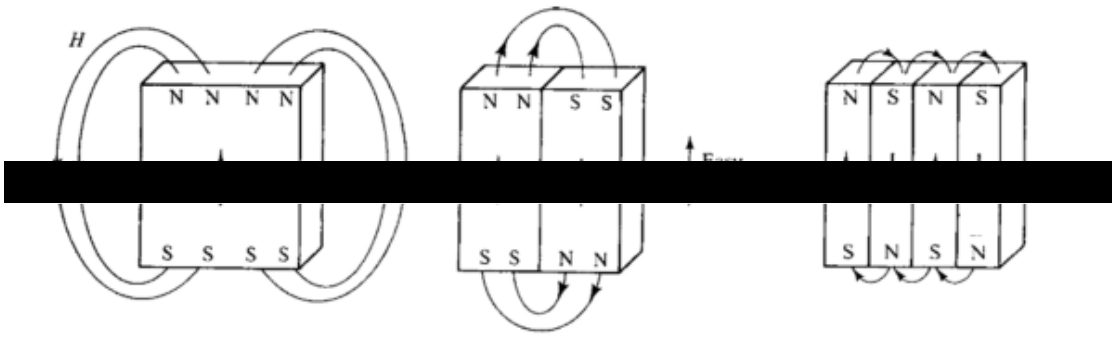

Figure 2-9 Magnetostatic energy reduction by the division of magnetic domains. Adopted from [11].

2.2.6 Magnetostriction

When magnetising the core material, the dimension change by a few parts for every million, and this change in dimension is referred to as magnetostriction [15]. Also, there is a limit for this magnetostriction process since it also reaches a saturation limit, and this effect differs with crystallographic direction as well. In practical applications, the effect of magnetostriction varies substantially and depends on different factors such as the surface effects, impurities, and on crystal orientation since they are associated with the stresses and formed in the base material [16]. Furthermore, magnetostriction can affect other magnetic properties such as magnetic losses (the size and shape of hysteresis) and magnetic permeability [11].

2.2.7 Magnetic Domain Wall Energy

A domain wall is considered as the transition region separating magnetic domains of which spontaneous magnetisation has varying directions. The magnetic domain wall energy is referred to as the stored energy inside the domain wall because of the separation of the neighbouring domains. The domain wall energy can be calculated by the summation of the exchange and anisotropy energies [11]. Hence, when the adjacent moments are aligned antiparallel, the wall would contain large energy exchange. Furthermore, the domain wall expands and becomes as wide as possible, as the exchange energy increases. On the other hand, the opposite effect is triggered by the anisotropy energy, where the domain wall width is decreased [11].

2.2.8 Magnetisation Process

The demagnetise state, which is also called as no magnetisation state, the domains experience spontaneous magnetisations in opposite directions wherein the total magnetisation of an individual crystal equal to zero. The magnetisation of a ferromagnetic material occurs when it is subjected to an external magnetic field, causing 90° and 180° magnetic domain wall motion and by rotating till the total force on the domain wall becomes zero [11].

When the application of the magnetic field is small, the material is free to return to its initial demagnetisation state without any hysteresis after its withdrawal from the field. On the other

hand, if the application of the magnetic field is large, it has the tendency to make the domain walls movements irreversible, and because of the new positions of the domain walls, the material becomes partially magnetised. [11], [16].

The structural factors such as strains, grain size, grain orientation, and impurities affect the process of magnetisation. Apart from this, it is also desirable or might be essential to consider some external factors also such as stresses, radiation, temperature, smoothness, and thickness of laminations which also put an impact on magnetisation [16].

2.2.9 Transformer Losses

The losses in a typical electrical transformer, include the core losses as well as the copper losses [4], [5]. The copper losses dissipated as heat and they occur in the machine's windings of the coil. The core losses can be multiple, which depends upon the eddy current and anomalous loss, hysteresis, and the material used in the construction of the core. The stray flux usually results in stray field losses, which is related to the conductors used for windings and the mechanical structure of the machine [1].

2.2.10 Magnetic Hysteresis

The hysteresis loop is generally called by the name B-H curve, where H is the magnetic field, while B shows the magnetic flux density [17]. Figure 2-10 represents many cycles of magnetisation and demagnetisation, which results in producing the hysteresis loop. The curve moves from the demagnetised at point 0 to the point of saturation 1, by applying an external magnetic field. As there is an increase in the magnetic flux density B from zero to saturation, it also increases the magnetising field H. When the magnetic field H decreases, the path would differ from the initial magnetisation curve because the domain walls would undergo a permanent change. As the magnetic field H value decreased to zero, the magnetic flux density B reduces to point 2, which is called the residual flux or Retentivity, which remains in the material. Then, the magnetic flux density B reduces and reaches to the point of coercivity 3, where the magnetic flux density B becomes zero because the magnetic field is applied in the opposite direction. The reverse magnetic field H, which is needed to change the magnetic flux density B of magnetic material from a positive value to zero, is called Coercivity. The curve is likely to move to the point of negative saturation 4 if magnetic field H is continuously applied in the opposite direction [9],[18],[19]. In case if the magnetic field H direction is changed back to a positive, the magnetisation curve will not return to its starting point, it will cross the points 5 and 6, which are those points opposite in direction to the Coercivity and Retentivity respectively but equal in magnitude [9],[18],[19].

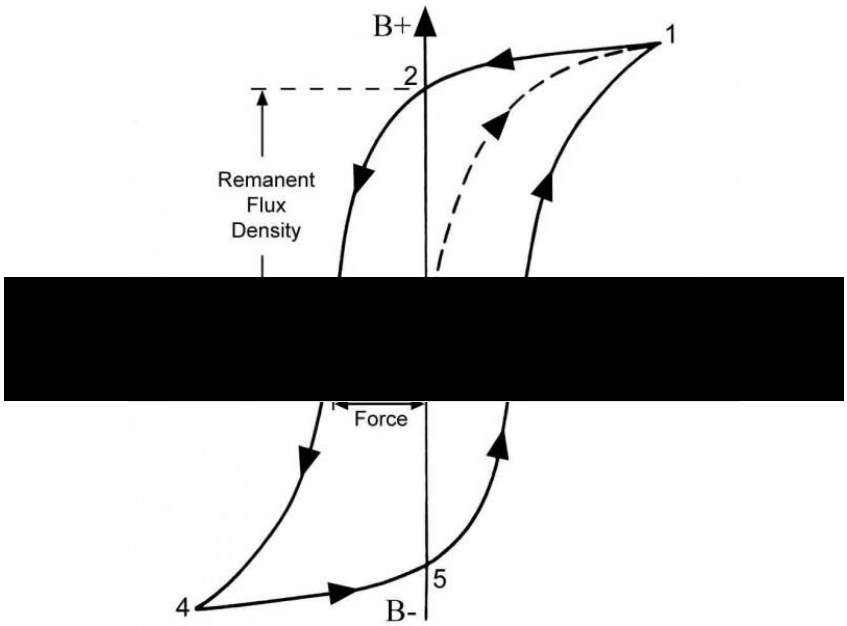

Figure 2-10 Hysteresis Loop (B-H Curve) showing the magnetisation process where the maximum magnetic flux is at point 1, the magnetic flux retained by the sample is at point 2 with no external magnetic field, magnetising in the opposite direction to point 3 where the sample has no magnetic flux, fully magnetised in the opposite direction at point 4 and magnetising field applied in the opposite direction reaching point 5 and 6 which is the opposite to 2 and 3 without passing to the point of origin [20].

As an alternating current would continuously magnetise the material, the magnetisation path would follow the H-B loop. There are wider hysteresis loops in case of hard magnetic materials such as permanent magnets because of the energy that they store. On the other hand, there are narrower hysteresis loops with soft magnetic materials [19].

2.2.11 Eddy Current

When a magnetic material is subjected to a time varying and fluctuating magnetic field, it changes the magnetisation of the material in response, and this, in turn, begins the occurrence

of flux. The changing magnetic field also induces an electromagnetic force inside the material, which is a closed path inside the material. It is worth mentioning here that inside the magnetic material around the magnetic field, there are many similar closed paths. The current has the property that the magnetic flux which produces the current, the current encloses that magnetic flux [21]. The following Figure 2-11 shows a few paths of the induced currents alongside the effects of alternating flux density in a solid magnetic material.

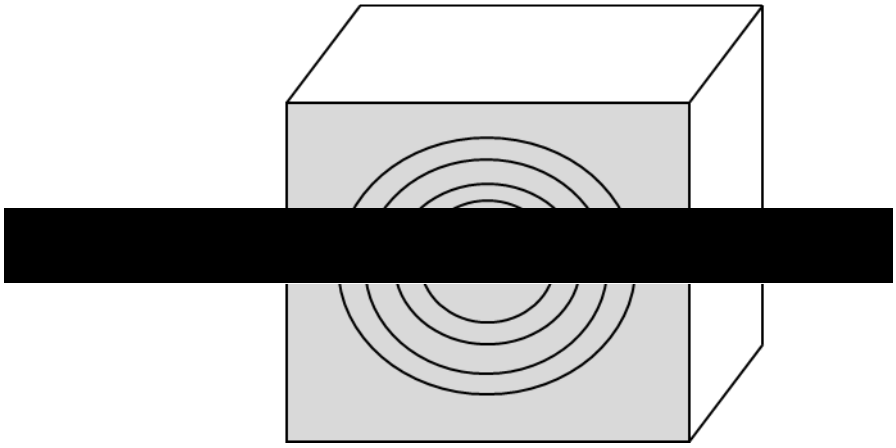

Figure 2-11 Eddy Current in solid core. Adopted from [3].

As the flux in the magnetic field increases, the induced EMF also increases in the circular paths, this gives rise to an increase in the eddy currents present in that path as well. As a result, due to the energy resisting the path, heat is produced, which causes a loss of power in return. The total power loss by the material because of the eddy currents equals to the summation of the power losses in every loop inside the material, and this loss is referred to as eddy current loss [3].

Eddy currents have another characteristic that they establish their flux which is opposite to the original magnetic flux. Hence, the eddy currents also affect the magnetic core because they produce a demagnetisation effect on the core. This increased demagnetisation triggers the requirement for more magnetomotive force (magnetisation force) in a bid to produce an equal amount of flux inside the core [3].

To minimize eddy currents, it is good practice to make the core highly resistive in the direction where the eddy currents have a higher tendency to flow, by arranging thin pieces of the magnetic core material in a stack, coated with varnish or shellac. Also, it makes the core highly resistive in the direction where the eddy currents tend to flow. The laminations are electrically insulated from one another because of the coating, which forces the eddy currents to follow narrow, long paths inside every lamination. Figure 2-12 illustrates this process. During this process, the net eddy currents inside the magnetic material are reduced, especially at the core [22].

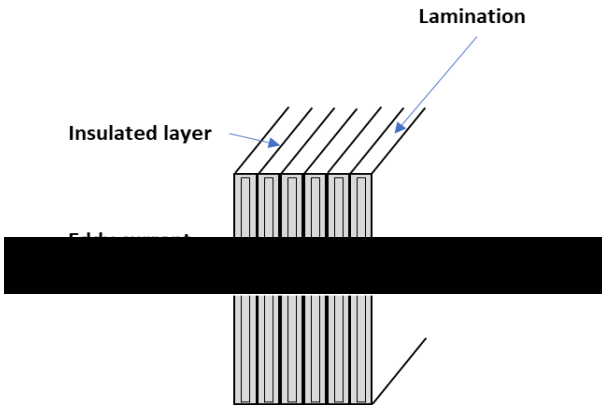

Figure 2-12 Eddy Current in the laminated core. Adopted from [3].

2.2.12 Anomalous Losses

The magnetisation of ferromagnetic materials often results in excessive losses due to complicated domain structures. In modern grain oriented silicon steel, the anomalous loss holds the responsibility of around 50% of the total loss. Hence, it is essential to define the causes and triggers of this loss. Early experiments revealed that such losses occur because of grain size and nucleation of the domains, domain wall pinning, and domain wall spacing which changes with the thickness of laminations, [9],[23],[24]. Figure 2-13 displays the total power loss per cycle of magnetisation, P/f, and f is the cycle frequency. It is to be noted that with the increase of magnetisation frequency, the magnetic losses also increase, excluding hysteresis where it remains constant. It should be noted that the structure of several domain walls also contributes to reducing the anomalous losses as it reduces the distance the domain wall moves during the process of magnetisation.

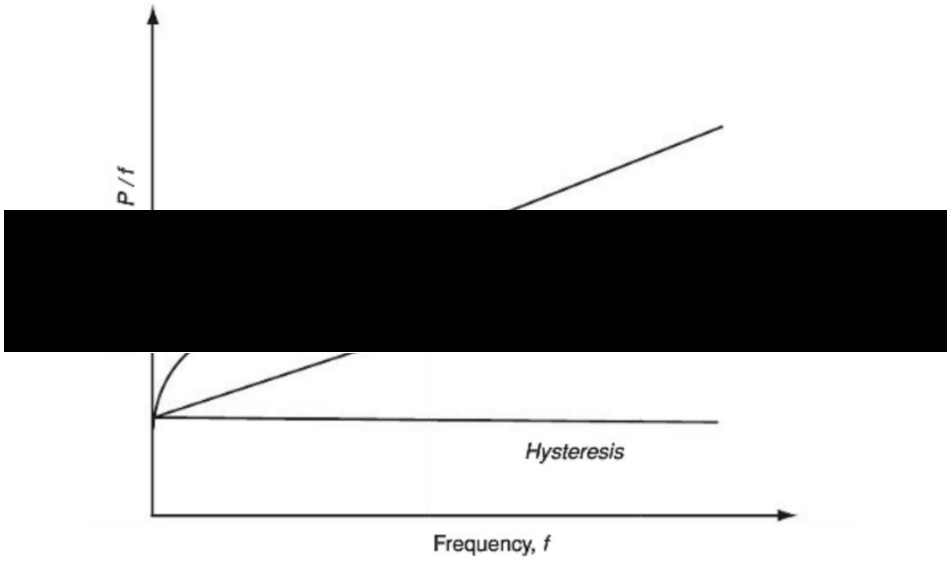

Figure 2-13 transformer core magnetic losses as shown hysteresis, Eddy current and anomalous losses [9].

2.3 Gain Oriented Silicon Steel

There has been a global trend to consume energy efficiently to preserve the natural environment and pollution reduction. Hence, there is a great need for achieving the reduction of electrical consumption nowadays [25]. In transformers, soft magnetic material is used in the shape of grain oriented silicon steel. Because the global trend in protecting the environment on the planet in every possible way, noise reduction and energy saving are needed for transformers, which gives rise to a great demand for low magnetostriction material and low core loss alike [25].

Hadfield had observed the reducing effect of iron loss by adding silicon to iron in 1900. After that, the magnetic anisotropy of iron was discovered by Honda and Kaya. The manufacturing process for grain oriented silicon steel through the process of applying magnetic anisotropy and controlling the texture of crystalline was invented by Goss in 1934 [25, 26]. Further reduction is gained by developing magnetic domain refining techniques, constructing thinner gauge material, and by improving crystalline orientation, that is, {110} <001> alignment [26].

Sharp Goss texture which is {110} <001> preferred crystal orientation, begins to develop during the secondary recrystallisation at the end of the manufacturing process when abnormal Goss grain growth occurs [27]. Though it usually undergoes several complicated steps during its manufacturing, including secondary recrystallisation [28]. The core loss reduction in silicon

steel alongside the important technological inventions and scientific findings are outlined in Figure 2-14 [26].

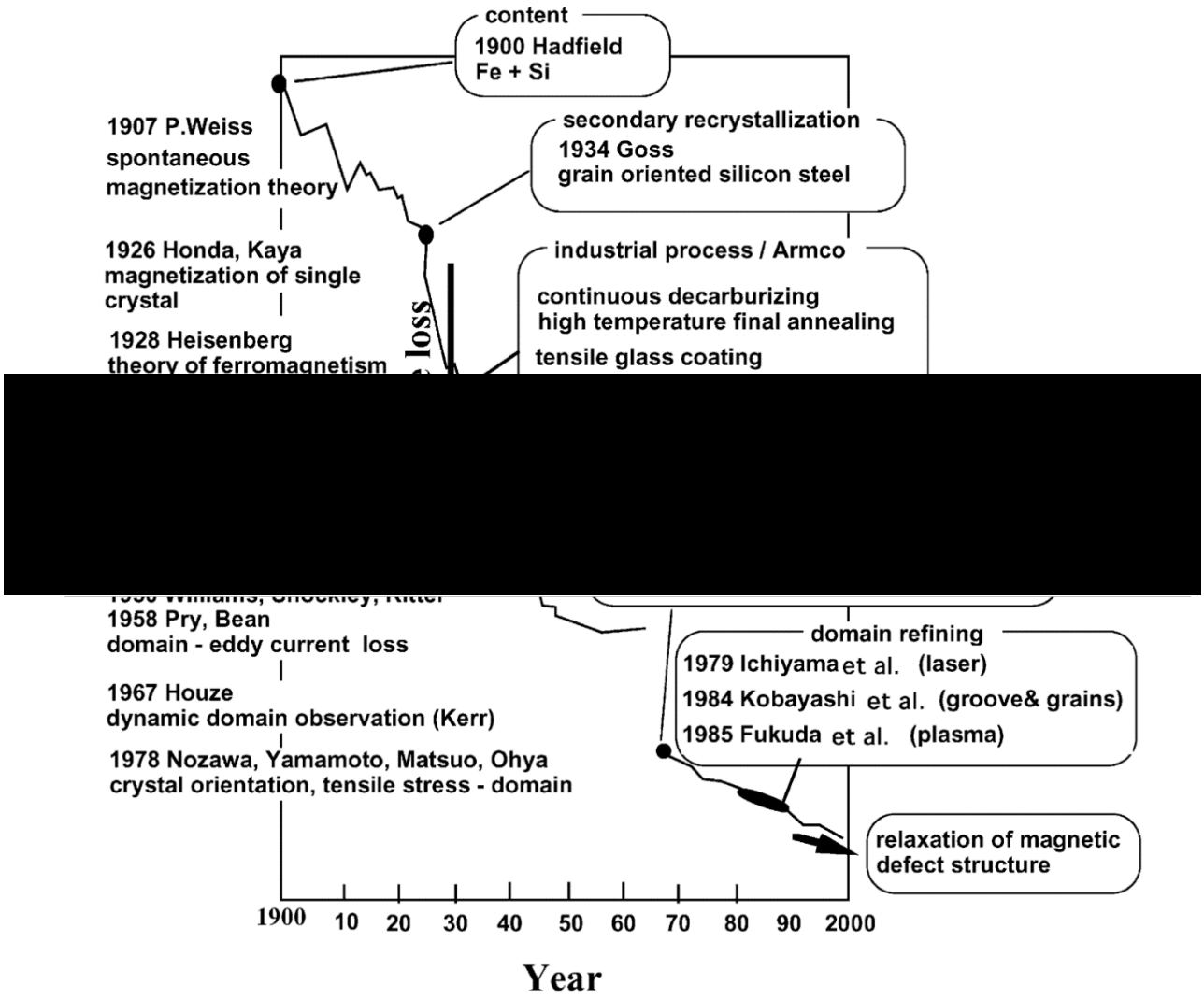

Figure 2-14 Core Loss reduction historical development of grain oriented steel [26].

It is obvious from Figure 2-14 that the core loss has been dramatically improved by the improvement of grain oriented silicon steel manufacturing process. The Nippon Steel Corporation (NSC) made progress in core loss reduction, as shown in Figure 2-15. The loss

reduction achieved by refining magnetic domain, production of thinner-gauge material and improvement of {110} <001> alignment [15].

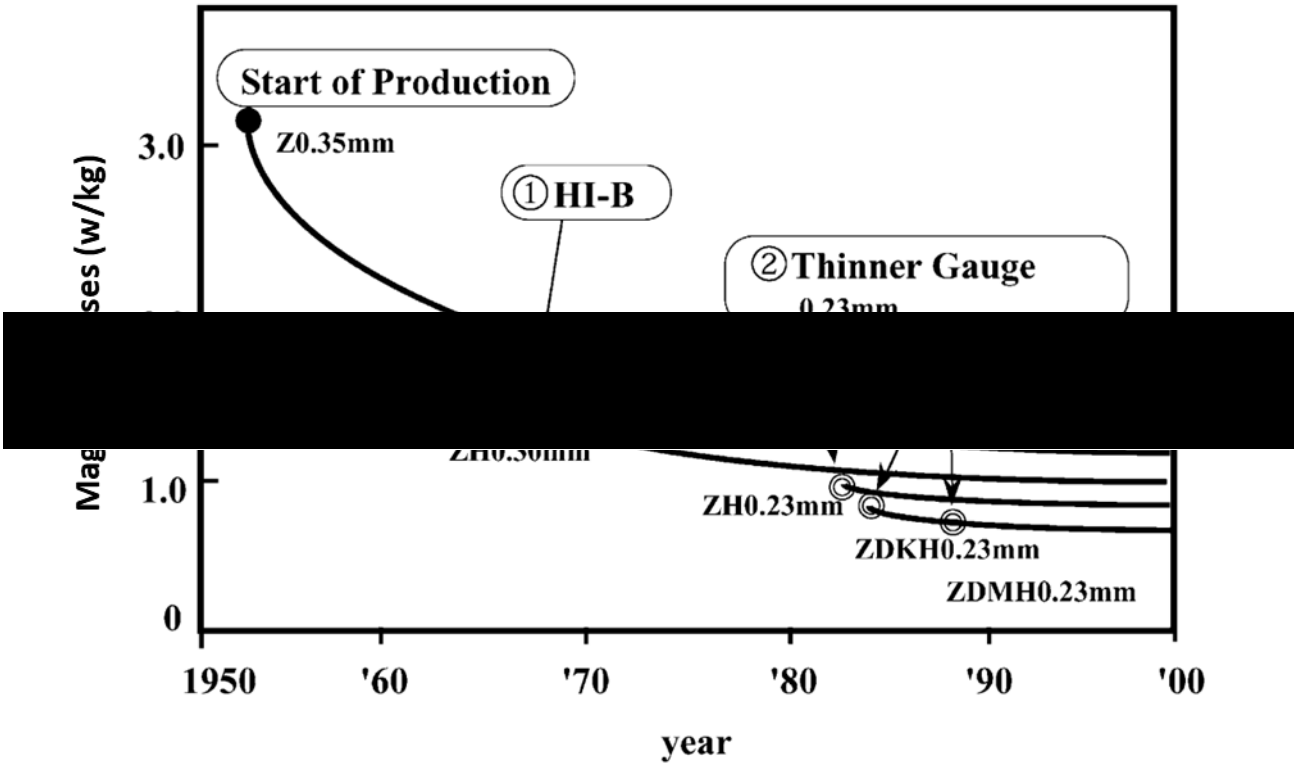

Figure 2-15 Nippon Steel Corporation improvements of core loss reduction in grain oriented [15]

2.3.1 Grain Oriented Silicon Steel Processing

The grain oriented Fe–3% Si steel is used as cores in electrical transformers because of their good magnetic properties. It is characterised by very large grain size and a sharp {011} <100> texture. It is to be noted here that the magnetic properties of grain oriented steel is correlated to the texture sharpness. For conventional grain oriented silicon steel (CGO) and high

permeability grain oriented silicon steel (Hi-B) respectively, the misorientations are 7° and 3° of the <100> axis from the rolling direction are usually accepted [29].

2.3.2. Conventional Grain Oriented Steel

CGO silicon steel has a cube on edge orientation and uses selenium, sulfur, or manganese as a grain growth inhibitor. Different steps involved in the processing of conventional grain oriented silicon sheet and silicon steel strip such as the preparation of a melt of silicon steel and then casting in the shape of strand cast slabs or ingots. The CGO preferable composition is outlined in the following Table 2-1 [30].

Table 2-1 CGO Composition wt% [30].

C	Mn	S and Se	Si
0.02-0.04%	0.04-0.08%	0.015-0.025%	3-3.5%

At 1400° C the steel cast slabs are reheated, this step of heating is crucial because, in addition to preparing the metal for hot rolling, it also used for dissolving the present inhibitor. Hence, after the hot rolling process, the inhibitor precipitate distributed uniformly in small size [31]. Then it is hot rolled to a desired thickness of 2mm after which the hot mill scale is removed.

The hot band is annealed at 925 to 1050 °C before the first stage cold rolling, where the thickness is reduced to minimum 40% to final thickness whilst the intermediate anneal would be somewhere between 850° to 950 °C [30].

Then the grain oriented silicon steel is cold rolled again to its final thickness of about 0.25 to 0.35mm. After the second cold roll, the sheets are annealed at 830 °C in a combination of wet N_2 and H_2 in decarburization stage. After this, the magnesium oxide is used to coat the decarbonised with an annealing separator and a traditional final box anneal performed at 1200°C [30].

2.3.3 High Permeability Grain Oriented Steel

The improvement in core loss is perceived yearly, which has been possible due to the development of domain refining techniques, by increasing the silicon content, and by producing a thinner sheet [25]. Figure 2-16 reveals the process of making high permeability grain oriented silicon steel in Cogent Orb, Newport-UK [32], [33]. Compared to CGO, the steel is reheated at a lower temperature (somewhere between 1200-1250°C), after that the steel was hot rolled in the direct sheet plan in the Netherlands and supplied to Orb accordingly. The hot rolled coil composition can be seen in Table 2-2, whilst the effects of elements used can be seen in Figure 2-17b [32], [33].

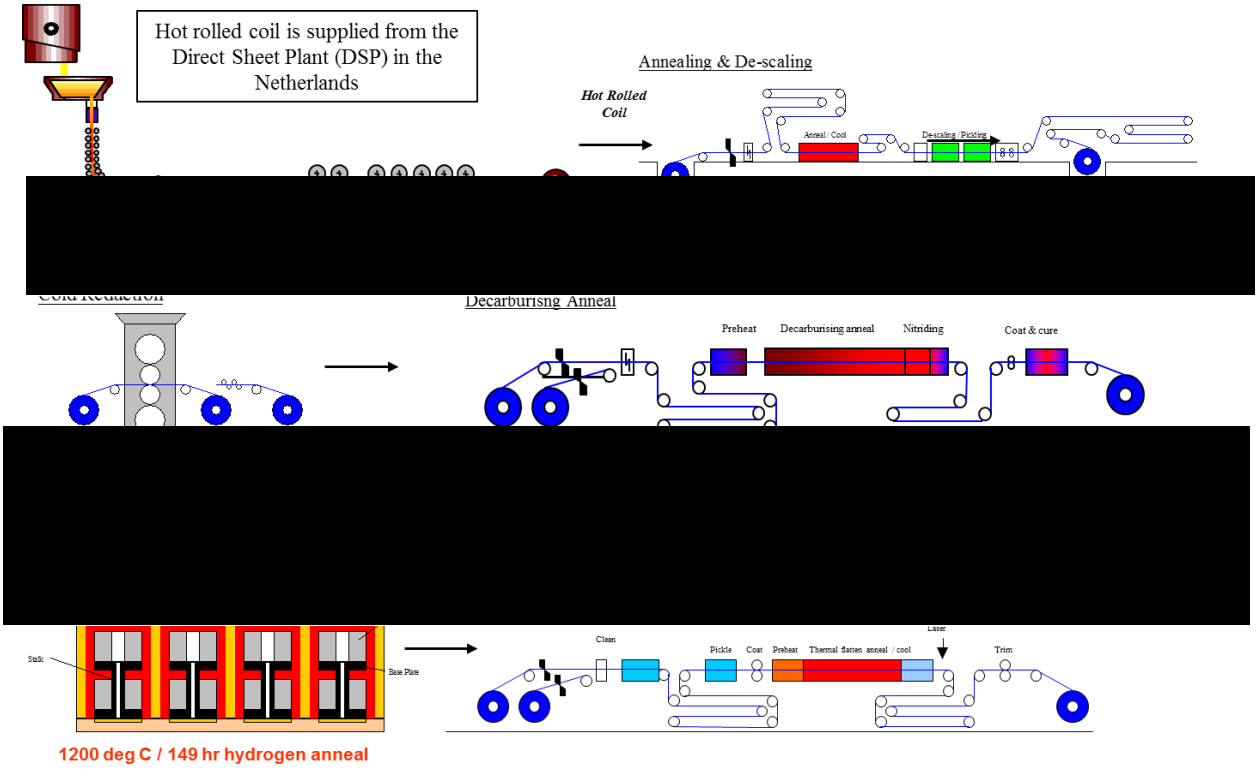

Figure 2-16 Cogent Orb manufacturing process of grain oriented steel.[33],[32].

In a bid to prevent snaps in the later stages, the edge cracks of the hot rolled coil are removed during the side trimming [32]. Then the coil is transferred to annealing and pickle lines where the coil annealed at 1100°C. This stage aims to secure carbon in the solution, makes sure that the inhibitor particles are the correct size, and it also increases the dispersion of precipitates. Then coil is quenched in a consistent, controlled rate after the process of annealing. Surface oxides and scales are removed by subjecting the coils to shot blast and pickled to make the surface ready for cold rolling [32], [33]. Figure 2-17 shows the annealing profile [32], [33].

Table 2-2 Hot rolled coil composition (a), and elements effect (b) supplied by Cogent Orb [33].

	Range	Aim
C	0.050 - 0.060	0.055
Si	3.00 - 3.20	3.10
Mn	0.18 -0.022	0.20
P	0.015 max	0.010
S	0.005 - 0.009	0.007
sol-Al	0.030 - 0.036	0.033
N	0.006 - 0.008	0.007
Cu	0.09 - 0.11	0.10
Sn	0.080 - 0.10	0.090
Ti	0.0030 max	

a

Carbon	A strong austenite (solid solution of carbon and iron) stabilizer, which promotes grain refinement
Silicon	Key element. Promotes low power losses.
Manganese	Austenite stabilizer. Also combines with S and Cu to form precipitates
Phosphorous	Beneficial effect on the microstructure development by improving its homogeneity
Sulphur	This element will combine with Mn/Cu to form the inherent inhibitors
Soluble Aluminium	Al will combine with N to form AlN (Provide the inhibition)
Nitrogen	N – This element will combine with Si/Al to form inherent inhibitors Austenite stabilizer
Copper	Cu – Contributes to the acquired precipitation during nitriding
Tin	Sn – Promotes grain growth inhibition
Titanium	Ti - Unavoidable impurity element. High affinity for N, it tends to form highly stable TiN

b

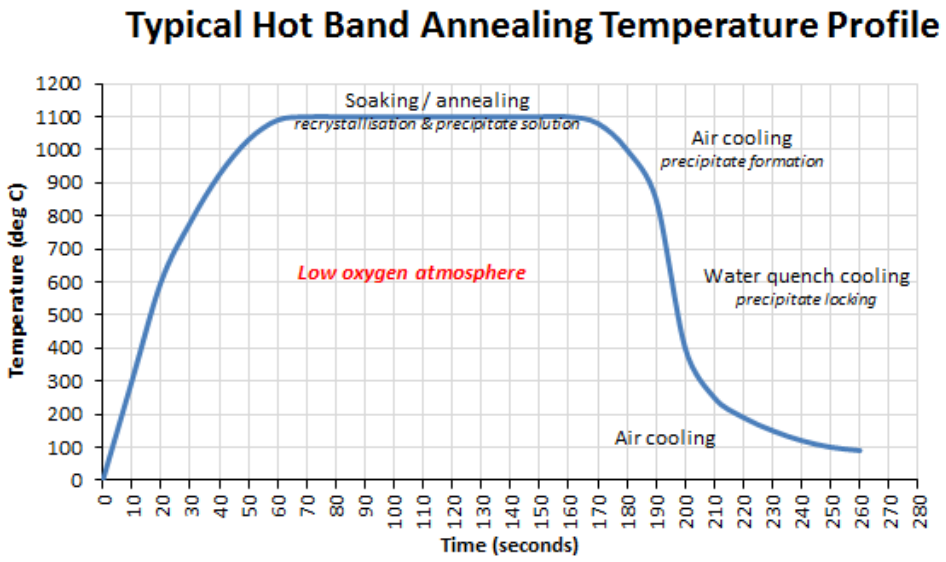

Figure 2-17 Annealing profile of hot rolled coil [33].

Following the hot band annealing, the steel thickness is reduced from 2.3mm to 0.23mm in 5 passes by cold rolling the coil in a reversing mill. As a result, the magnetic losses are reduced because of the thinner gauges which in turn improves the magnetic properties and also increases the stored energy of the structure of cold rolled steel [32], [33].

In the next stage, a fayalite layer is created, and the carbon content is reduced at a temperature of 850°C, this stage is referred to as decarburising and nitriding. In the decarburisation stage, the inhibitors are formed by nitrogen adsorption, and grains are recovered after the deformation of cold rolling [32], [33]. Figure 2-18 exhibits the profile of decarburising annealing temperature [33].

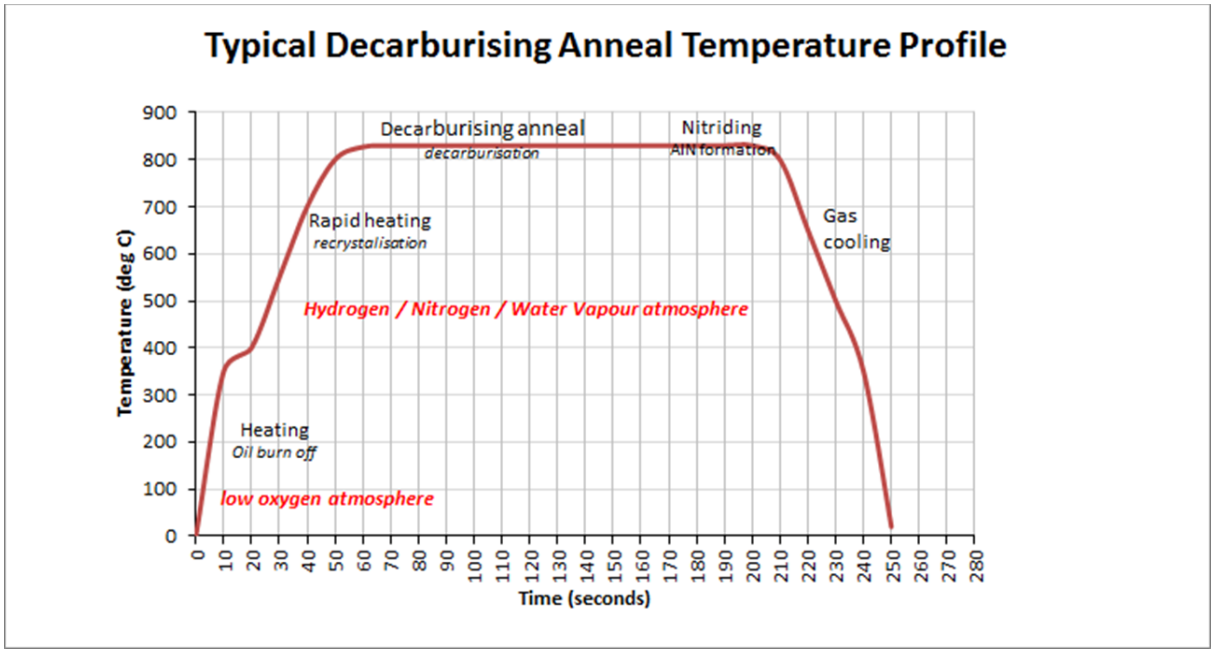

Figure 2-18 Cogent Orb Decarburization annealing Temperature profile [36].

During the process of decarburisation, the interaction of precipitates with the gain boundary occurs and prevent growth until they are exposed to a high temperature annealing process. In the Cogent Orb manufacturing process of grain oriented silicon steel, there are two types of inhibitors which are utilized. These inhibitors are characterized as inherent and acquired. The inherent inhibitor comprises of Mn sulphide (50nm<) and/or Cu sulphideb (~40nm) which has low pinning effect on grain boundary migration, and it is formed before the decarburisation step. While the acquired inhibitor, on the other hand, creates the AlN after nitriding with the injection of Ammonia. The desired magnetic properties are obtained by removing the carbon while oxygen is adsorbed to make an occurrence of the oxide layer to create the glass layer in the following step. In the end, at high temperature annealing, the coil is coated with MgO in to create a glass film [33].

In the process of high temperature annealing, the Goss grains grow and consume all the other grains after the decarburisation. During this process, the coils are subjected to heating up to 1200°C. A reaction takes place between the oxide layer formed in the decarburisation line and MgO, which in turn creates an insulating glass film, also the impurities removed in high temperature annealing [33].

The stresses are taken out to improve magnetic properties in the Thermal Flattening which is regarded as the last line of production. Also, the strips are laser scribed to reduce magnetic domain size which further decreases magnetic losses, and an extra layer insulation coating is also applied to improve the magnetic losses [33].

2.4 Texture Evolution during GOES Processing

There are a few fundamental factors which improve the magnetic properties such as controlling the microstructure of grain oriented silicon steel and the crystallographic orientation as well as the chemical composition. The silicon steel can be manufactured with favourable texture component if it is subjected to controlled conditions of the manufacturing process. The production is an extremely complex process and requires cautious multi-steps processing to obtain the desired steel with favourable magnetic properties, which, during the secondary recrystallisation sharp Goss texture is formed [34].

2.4.1 Hot Rolling

Goss texture originates as a result of shear deformation due to the high friction between the strip surfaces and the rolls during the hot rolling stage, [35]. It is worth mentioning that the thick slabs undergo a continuous hot rolling process with a total reduction of more than 95% during the grain oriented silicon process. A higher amount of {110} <001> component is produced by rolling at a lower temperature, but at the same time, it also limits the progress of {110} <001> grain coarsening [36]. During the process of secondary recrystallisation, the development of sharp Goss orientation can be traced, which has its origin in the process of hot rolling [37].

2.4.2 Hot Band Annealing

As a condition of heat treatment, the process of annealing is essential for both texture control and the inhibitor alike [36]. The annealing of the hot rolled grain oriented silicon steel homogenises the microstructure and coarsening of the AIN and MnS precipitates. Hence, only a weak barrier is provided by the precipitates to the primary and secondary recrystallisation, which leads to a strong grain growth that is Goss-oriented during secondary recrystallisation annealing process. The grain orientations can be noticeably affected in case there has been a longer annealing time after the process of hot rolling [34].

2.4.3 Cold Rolling

As described earlier that the hot rolling stage is the state wherein the Goss component originates, and the Goss orientation progresses near to the surface of the sheet because of the high friction which leads to shear deformation. It was reported that the high angle grain boundaries encircle most of the existing Goss oriented crystal volume, which happens after the highest deformation degree, which is 89% [37].

There are two strong equivalents {111} <112> texture components which characterized after 89% cold rolling reduction in thickness which is also favourable for the sharper Goss texture

and the abnormal growth of {110} <100> grains during the process of secondary recrystallisation. In addition, most of the remaining {110} <100> crystals are surrounded with high angle grain boundaries, which is considered as the misorientation between two neighbouring grains, i.e. the misorientation between {111} <112> orientation and the Goss is 35° [37].

2.4.4 Decarburisation

It is possible to decarburise the steel when it is rolled to thin final thicknesses less than 0.5 mm. This can be done by exposing the steel to a decarburising atmosphere during the time when the strip moves through the strand annealing furnace. Exposing it to wet hydrogen at ~800-850℃ for 60 or 120 seconds is effective enough to achieve the effective decarburisation in return. In fact, carbon dioxide, carbon monoxide, and hydrocarbons are produced upon the diffusion of carbon to the surface and its reaction with the furnace atmosphere gas [10], [38]. In order to form a primary recrystallisation structure, the cold rolled sheet is annealed, also to decarburise it to less than 0.003% carbon in a wet atmosphere [36], [39]. Inner oxidation caused by the decarburisation process which mainly consists of silica (SiO_2) or fayalite (Fe_2SiO_4), iron oxide (FeO) can also be formed if oxygen is too high. Afterwards, magnesia (MgO) slurry coat is applied to the steel before it is annealed at high temperature. The secondary recrystallisation starts in high temperature annealing, and continuous oxidation at the surface takes place because of the reaction among magnesia, silica and fayalite. The continuous oxidation is mainly composed of forsterite (Mg_2SiO_4) [39],[15].

2.4.5 Grain Growth Inhibitors

In high permeability grain oriented silicon steel, there are two different inhibitor methods, which were referred to as the inherent methods and the acquired methods [40],[31]. The manufacturing of high permeability grain oriented silicon steel involves AlN as the main inhibitor [41]. To obtain the sharp {110} <100> secondary recrystallisation texture it becomes imperative that the primary recrystallisation texture which develops at cold rolling of around 87% is secured and the AlN inhibitor which has the quality to keep up its strength even on high temperatures annealing. The first is the inherent methods revolves around adding the inhibitor elements to the melted steel as it was done generally during the process of slab heating, they can be brought into solution and precipitate during the processes of hot rolling and hot strip annealing. The second method is acquired methods, revolves around the formation of inhibitors in decarburisation process and voiding the formation of inhibitor prior processes. Furthermore, by utilizing both methods, direct hot rolling and thin slab casting are the most advanced processes in commercial realisation [31].

2.4.6 Secondary Recrystallisation

By controlling the density, size, and the amount of inhibitors, the microstructure formed during the primary recrystallisation can be controlled. Secondary recrystallisation can be obtained through the achievement of a small primary recrystallisation grain, and the inhibition of normal

grain growth. In addition, the type of nucleation sites has a major impact on the orientation of recrystallised grains, as the orientation depends on their nucleation sites type [36], [41]. Furthermore, the secondary recrystallisation grains (Goss oriented grains) have an advantage over other oriented grains, where a few Goss grains grow abnormally by consuming neighbouring grains. As mentioned earlier, sharp Goss texture can be achieved by pinning the growth of primary annealed grains, where Goss grains overcome the pinning effect of precipitates (grain growth inhibitors) on the grain boundaries, resulting Goss abnormal grain growth. In order to understand the secondary recrystallisation mechanism, many other theories have been proposed as reported in [28]. The theories on Goss abnormal grain growth are detailed and discussed in Chapter 5.

2.5 Summary

In summary, grain oriented (GO) silicon steel is manufactured in lamination with high silicon content to reduce the eddy current. Also, the complicated manufacturing process aims to produce sharp Goss texture through controlling the annealing conditions and precipitation. The achieved abnormal Goss grain contribute in further reducing the magnetic losses by decreasing the magnetisation force needed to reach magnetic saturation in the rolling direction (easy magnetisation direction). Furthermore, the understanding of magnetic domains and domain wall can help in further optimising the magnetisation and demagnetisation process and improve magnetic performance.

References

[1] D. R. Patrick and S. W. Fardo, “Electrical Distribution Systems (2nd Edition).” Fairmont Press, Inc., 2009.

[2] P. Day, *The Philosopher’s Tree: A Selection of Michael Faraday’s Writings*. Philadelphia: CRC Press, 1999.

[3] B. S. Guru and H. R. Hiziroglu, “Electric Machinery and Transformers,” *Oxford university press*. Oxford University Press, p. 741, 2001.

[4] H. De Keulenaer, D. Chapman, S. Fassbinder, and M. McDermott, “The scope for energy saving in the EU through the use of energy-efficient electricity distribution transformers,” in *16th International Conference and Exhibition on Electricity Distribution (CIRED 2001)*, 2001, pp. v4-27-v4-27.

[5] T. Kubo, H. Sachs, and S. Nadel, “Opportunities for New Appliance and Equipment Efficiency Standards: Energy and Economic Savings beyond Current Standards Programs,” Washington, D.C, 2001.

[6] P. Tamizharasi, R. Anuradha, and A. Ayshwarya, “Analysis of Distribution Transformer Losses in Feeder Circuit,” *Int. J. Innov. Res. Adv. Eng.*, vol. 1, no. 1, pp. 1–6, 2014.

[7] D. Jiles, *Introduction to magnetism and magnetic materials*. CRC Press, 2015.

[8] A. Aharoni, *Introduction to the Theory of Ferromagnetism*, vol. 109. Clarendon Press, 2000.

[9] J. M. D. Coey, *Magnetism and magnetic materials*. Cambridge University Press, 2010.

[10] P. Beckley, *Electrical steels for rotating machines*, no. 37. IET, 2002.

[11] B. D. Cullity and C. D. Graham, *Introduction to magnetic materials*. John Wiley & Sons, 2011.

[12] D. D. Tang and Y.-J. Lee, *Magnetic memory: fundamentals and technology*. Cambridge University Press, 2010.

[13] J. Shilling and G. Houze, "Magnetic properties and domain structure in grain-oriented 3% Si-Fe," *IEEE Trans. Magn.*, vol. 10, no. 2, pp. 195–223, 1974.

[14] J. Shilling, "Domain structures in 3% Si-Fe single crystals with orientation near," *IEEE Trans. Magn.*, vol. 9, no. 3, pp. 351–356, 1973.

[15] Y. Ushigami, M. Mizokami, M. Fujikura, T. Kubota, H. Fujii, and K. Murakami, "Recent development of low-loss grain-oriented silicon steel," *J. Magn. Magn. Mater.*, vol. 254–255, pp. 307–314, 2003.

[16] M. Littmann, "Iron and silicon-iron alloys," *IEEE Trans. Magn.*, vol. 7, no. 1, pp. 48–60, 1971.

[17] J. Lucas, P. Lucas, T. Le Mercier, A. Rollat, and W. G. Davenport, *Rare earths: science, technology, production and use*. Elsevier, 2014.

[18] J. G. Webster and H. Eren, *Measurement, instrumentation, and sensors handbook:*

electromagnetic, optical, radiation, chemical, and biomedical measurement. CRC Press, 2014.

[19] Y. Song, *High density data storage: Principle, Technology, and Materials*. World Scientific, 2009.

[20] "Part 5: Magnetic Materials | ITACA." [Online]. Available: http://www.itacanet.org/basic-electrical-engineering/part-5-magnetic-materials/. [Accessed: 14-May-2017].

[21] D. Ribbenfjärd, "Electromagnetic transformer modelling including the ferromagnetic core," KTH, 2010.

[22] C. R. Bayliss, C. Bayliss, and B. J. Hardy, *Transmission and distribution electrical engineering*. Elsevier, 2012.

[23] K. Overshott, "The use of domain observations in understanding and improving the magnetic properties of transformer steels," *IEEE Trans. Magn.*, vol. 12, no. 6, pp. 840–845, 1976.

[24] G. Bertotti, *Hysteresis in magnetism: for physicists, materials scientists, and engineers*. Academic Press, 1998.

[25] N. Takahashi, Y. Suga, and H. Kobayashi, "Recent developments in grain-oriented silicon-steel," *J. Magn. Magn. Mater.*, vol. 160, pp. 98–101, 1996.

[26] T. Kubota, M. Fujikura, and Y. Ushigami, "Recent progress and future trend on grain-oriented silicon steel," *J. Magn. Magn. Mater.*, vol. 215, pp. 69–73, 2000.

[27] D. Dorner, S. Zaefferer, L. Lahn, and D. Raabe, “Overview of Microstructure and Microtexture Development in Grain-oriented Silicon Steel,” *J. Magn. Magn. Mater.*, vol. 304, no. 2, pp. 183–186, 2006.

[28] Z. Xia, Y. Kang, and Q. Wang, “Developments in the production of grain-oriented electrical steel,” *J. Magn. Magn. Mater.*, vol. 320, no. 23, pp. 3229–3233, 2008.

[29] M. Frommert, C. Zobrist, L. Lahn, A. Böttcher, D. Raabe, and S. Zaefferer, “Texture measurement of grain-oriented electrical steels after secondary recrystallization,” *J. Magn. Magn. Mater.*, vol. 320, no. 20, pp. 657–660, 2008.

[30] M. F. Littmann, “Process for producing grain-oriented silicon steel.” Google Patents, 1984.

[31] H. T. Liu *et al.*, “Evolution of microstructure, texture and inhibitor along the processing route for grain-oriented electrical steels using strip casting,” *Mater. Charact.*, vol. 106, pp. 273–282, 2015.

[32] M. Cichuta, “Trends and developments in grain oriented steels,” Internal presentation of Cogent Power Ltd., 2009

[33] D. Richards, “Product & Technology TATA STEEL Presentation.” Internal presentation of Cogent Power Ltd., 2013.

[34] S. M. Shin, S. Birosca, S. K. Chang, and B. C. De Cooman, “Texture evolution in grain-oriented electrical steel during hot band annealing and cold rolling,” *J. Microsc.*, vol. 230, no. 3, pp. 414–423, 2008.

[35] H. Y. Song *et al.*, “Effect of hot rolling reduction on microstructure, texture and ductility of strip-cast grain-oriented silicon steel with different solidification structures,” *Mater. Sci. Eng. A*, vol. 605, pp. 260–269, 2014.

[36] M. Matsuo, “Review Texture Control in the Production of Grain Oriented Silicon Steels Grain Oriented Silicon Steels Texture Control for Improved Magnetic Properties,” *ISII Int.*, vol. 29, no. lO, pp. 809–827, 1989.

[37] D. Dorner, L. Lahn, and S. Zaefferer, “Survival of Goss Grains during Cold Rolling of a Silicon Steel Single Crystal,” *Mater. Sci. Forum*, vol. 495–497, pp. 1061–1066, 2005.

[38] D. Poultney and D. Snell, “Evaluation of oxide layers formed during the decarburisation of grain-oriented electrical steel using a Fourier transform infrared (FTIR) technique,” *J. Magn. Magn. Mater.*, vol. 320, no. 20, pp. 645–648, 2008.

[39] C. C. Silveira, M. A. Da Cunha, and V. T. L. Buono, “The influence of internal oxidation during decarburization of a grain oriented silicon steel on the morphology of the glass film formed at high temperature annealing,” *J. Magn. Magn. Mater.*, vol. 358–359, pp. 65–69, 2014.

[40] T. Kumano, T. Haratani, and Y. Ushigami, “The Relationship between Primary and Secondary Recrystallization Texture of Grain Oriented Silicon Steel,” vol. 42, no. 4, pp. 440–449, 2002.

[41] S. Suzuki, Y. Ushigami, H. Homma, S. Takebayashi, and T. Kubota, “Influence of Metallurgical Factors on Secondary Recrystallization of Silicon Steel,” *Mater. Trans.*, vol. 42, no. 6, pp. 994–1006, 2001.

[42] A. Morawiec, “On abnormal growth of Goss grains in grain-oriented silicon steel,” *Scr. Mater.*, vol. 64, no. 5, pp. 466–469, 2011.

[43] R. D. Doherty *et al.*, “Current issues in recrystallization: a review,” *Mater. Sci. Eng. A*, vol. 238, no. 2, pp. 219–274, 1997.

[44] Y. Hayakawa and J. A. Szpunar, “A new model of Goss texture development during secondary recrystallization of electrical steel,” *Acta Mater.*, vol. 45, no. 11, pp. 4713–4720, 1997.

[45] O. Engler and V. Randle, *Introduction to texture analysis: macrotexture, microtexture, and orientation mapping*. CRC Press, 2009.

Chapter 3: Experimental Procedures

This project focuses on secondary recrystallisation and Goss abnormal grain growth of 3% Fe-Si, Electrical Steel / Silicon Steel, with different grades and compositions. As mentioned in Chapter 1, the aim of this project is to have a better understanding on Goss abnormal grain growth and the effect of the microstructure, and heating (annealing) conditions on secondary recrystallisation texture and texture evolution, hence optimising the final product magnetic property. The project involved a set of experiments that can be divided into two groups. The first group is the magnetic domain imaging using FSD (forescatter detector) and the correlation between deviation angle from RD (rolling direction) and magnetic structure and losses. The second set of experiments mainly focus on Goss abnormal grain growth and the effect of microstructure (including grain size, grain boundaries and stored energy) and heating conditions (including heating rate and heating direction) on the secondary recrystallisation texture development. The heat treatment and material preparation, as well as materials used in this project, are explained and detailed in this chapter.

3.1 Materials Used

In the current project, different grades of commercial 3% - 3.2% Fe-Si grain oriented silicon steel (GOES) sheets were supplied by Cogent Orb in Newport-UK. Specimens through each processing stage were provided, including; hot rolled, cold rolled, primary annealed and

secondary annealed samples. The chemical composition of the final stage (secondary recrystallised) of the seven different grain oriented silicon steel used in Chapter 4 shown in Table 3.1.

Table 3.1 Chemical compositions in wt.% of fully processed commercial (Goss)s used.

Sample	Si	C	N	Mn	P	Al	Cu	Ni	Cr	Sn	Pb
A	3.32	0.0017	0.0011	0.089	0.025	<0.005	0.006	<0.005	0.12	0.052	0.002
B	3.11	0.0026	<0.001	0.058	0.001	<0.005	0.12	0.062	0.028	0.013	<0.001
C	3.33	0.0022	-	0.069	0.009	-	0.098	0.005	0.024	0.01	0.004
D	3.19	0.0025	<0.001	0.067	0.009	<0.005	0.063	0.031	0.052	0.11	0.003
E	3.19	0.0018	<0.001	0.065	0.009	<0.005	0.073	0.036	0.064	0.12	0.003
F	2.84	0.0016	<0.001	0.049	0.011	<0.005	0.15	0.057	0.26	0.018	0.003
G	3.23	0.0038	<0.001	0.059	0.003	<0.005	0.16	0.078	0.046	0.014	<0.001

The Chemical composition of the final stage grain oriented silicon steel samples are similar and have a slight variation in Si content. Also, sample C is a conventional (CGO) grade of grain oriented silicon steel where AlN (grain growth inhibitor) is absent.

The chemical composition of primary annealed samples used in Chapters 5-7 shown in Table 3-2.

Table 3.2 Chemical composition in wt.% of primary annealed samples used in Chapters 5-7.

C	Mn	P	S	Si	Cu	Sn	Cr	Ni	Mo	B	Ti	V	Ca
0.057	0.198	0.01	0.007	3.066	0.104	0.088	0.016	0.018	0.002	0.0002	0.003	0.005	0.00018

Sample	Al	N (Ladle)	N (nitriding)
AA	0.038	0.0073	0.02 (200 ppm)
BB	0.038	0.0073	0.0235 (235 ppm)
CC	0.038	0.0073	0.0235 (235 ppm)
DD	0.032	0.0076	0.02 (200 ppm)

3.2 Material Preparation

3.2.1 Metallography and Electron Microscopy Sample Preparation

The samples were cut using ATM Brilliant 220 cut-off machine with HNF type with superfine grains cutting disk specified for ferrous metals. To minimise the deformation and dislocation at the edge of the sample caused by the cutting process, automatic feeding was used with a feed speed of 0.005 mm/s and cutting disk rotation speed of 1500 rpm. Following the cutting process, ATA Opal 410 was used to hot mount the samples with 4 min heating at 180℃ and 4

min cooldown and mounting press set at level 5 (375 bars). Then, the specimens were ground using an EcoMet 300 Pro auto grinding polishing machine. The samples were ground for 1 minute on each 800, 1200 and 2000 grit papers. A complementary rotation was used during grinding with a base and head rotations of 150 rpm and 50 rpm, respectively, using a force of 15 N. This was followed by polishing for 2 minutes using, 6 µm and 3 µm water-based diamond suspensions. A counter rotation was used during polishing with a base and head rotations of 250 rpm and 50 rpm, respectively, using 15 N force. The final polishing was carried out using a 0.04 µm colloidal silica suspension, a counter rotation with a base and head rotation of 80 rpm and 50 rpm using 10 N force.

3.2.2 FSD Magnetic Domain Imaging Sample Preparation

For magnetic domain imaging, in addition, to sample preparation in Section 3.2.1, the samples were further polished for 6 hours using a VibroMet vibration polishing machine using 0.04 µm colloidal silica suspension. After VibroMet polishing, the specimens were polished by means of a Hitachi IM-4000 ion beam milling machine. The ion beam milling was conducted following the procedures in [1], and the polishing steps shown in Table 3-3.

Table 3-3 Ion Beam Miller polishing steps using Hitachi IM-400.

Voltage (KeV)	Angle of Incidence (°)	Time (min)
6	10	30
4	10	60
2	8	120

It is worth mentioning that the main purpose of using an ion beam was to remove the surface defects created by previous grinding and polishing steps. However, as ion beam milling can also cause some surface damage, thus, further vibrating polishing was carried out using 0.04 μm colloidal silica for 4 extra hours to remove the surface topography created by the ion beam.

3.3 Heat Treatment

Various annealing trials were conducted for different investigation purposes, including interrupted annealing and in-situ annealing. Carbolite furnace was used to study Goss abnormal grain growth behaviour at different annealing temperatures and time at Swansea University laboratories. Sample characterisation was carried out after cold rolling and commercial decarburisation annealing (primary annealing), laboratory annealing at various temperatures and times using different heating rates.

In Chapter 5, the samples were annealed interruptedly for 10sec at 1030℃ and 8min at 1070℃ with a heating rate of 0.1℃. Additional experiments were carried out to study the effect of grain boundaries on Goss abnormal grain growth; where the samples were annealed for 20mins at 1000℃ and 1100℃ from room temperature with a heating rate of 0.1℃. Also, the GND and Taylor Factor were studied in an interrupted annealed test at 850℃ for 3min, 4min and 5min. In Chapter 6, the samples were annealed from room temperature to 1200℃ with a heating rate of 10℃/min and 50℃/min in an in-situ neutron diffraction facility. In Chapter 7, the samples annealed at 1100℃ for 20mins, 60mins and 180mins with a heating rate of 0.1℃/min from RT. Additional samples were annealed in a preheated furnace from 1000℃ to 1100℃ with a dwell time of 60mins, and a heating rate of 0.1℃/sec and maximum furnace heating rate of 0.6℃/sec. Finally, samples of grain oriented silicon steel were annealed for 8mins at 1070℃ and 1080℃, and 10sec at 1100℃. All the samples were annealed in different direction including RD, TD and random direction. The sample positions in the furnace are shown in Figure 3-1. The sample sides are exposed from both sides as shown in Figure 3-1a, and Figure 3-1b and Figure 3-1c show one side of the sample insulated using a thermal insulator (Vermiculite treated silica cloth and Fiberfrax).

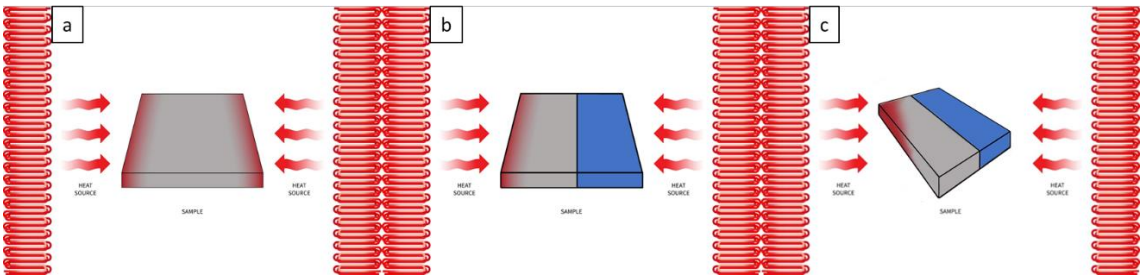

Figure 3-1 The heat flux travelling path (a) both sides of the samples are exposed, (b) one side of the sample is exposed and (c) one side is exposed, and the sample is rotated at a random angle.

3.4 Material Characterisation Tools and Analytical Methods

Various nano/microanalytical tools were used in this study, including Scanning Electron Microscope (SEM), Electron Backscatter Diffraction (EBSD) and neutron diffraction. For the microstructure investigation and characterisation, a JEOL 7800F Field Emission Gun Scanning Electron Microscopy (FEG SEM) equipped with an HKL EBSD and Oxford Energy Dispersive Spectroscopy (EDS) systems.

The EBSD row data were then analysed using ATEX [2], HKL Channel 5 software and MATLAB-MTEX (MTEX is a free Matlab toolbox for analysing crystallographic textures by means of EBSD data [3,4]. In-situ annealing was conducted using neutron diffraction facility at GEM (general materials diffractometer) beamline, ISIS neutron facility at Harwell, UK, which is suitable for structure and texture analysis. The obtained data at different annealing temperatures were then analysed to generate Orientations Distribution Functions (ODF)s and calculate the precipitate volume fractions, lattice expansion and *d*-spacing from variations from the peak shifting measurements. MATLAB-MTEX and MAUD software packages were used for peak fitting, peak position determination and lattice/*d*-spacing expansion calculations. MAUD (Material Analysis Using Diffraction) based on the Rietveld RITA/RISTA method, was developed by L. Lutterotti, H.-R. Wenk, S. Matthies and others [5].

3.4.1 Electron Backscatter Diffraction (EBSD)

Electron backscatter diffraction (EBSD) is an SEM technique that can provide quantitative crystallographic information, including grain size, grain orientation, internal misorientation and grain boundary characteristics. A high polished flat surface that is tilted 70° is required to study a sample. The goal of tilting the sample is to reduce the path of backscattered electrons by lattice planes. Thus the number of the backscattered electron is much greater than a flat surface; as in SEM; where the path of backscattered electrons is large enough to be absorbed and diffracted electron are not sufficient to produce diffraction patterns. Furthermore, the diffraction pattern (electron backscattering patterns) of the tilted sample is captured by a phosphor screen coupled with a TV camera; also called charge couple device (CCD); and SEM is used as the source of electrons [6][7]. Furthermore, the forescatter detector (FSD) which consists of six diodes attached around, which produces image contrast was used. A schematic of the tilted sample for EBSD shown in Figure 3-2.

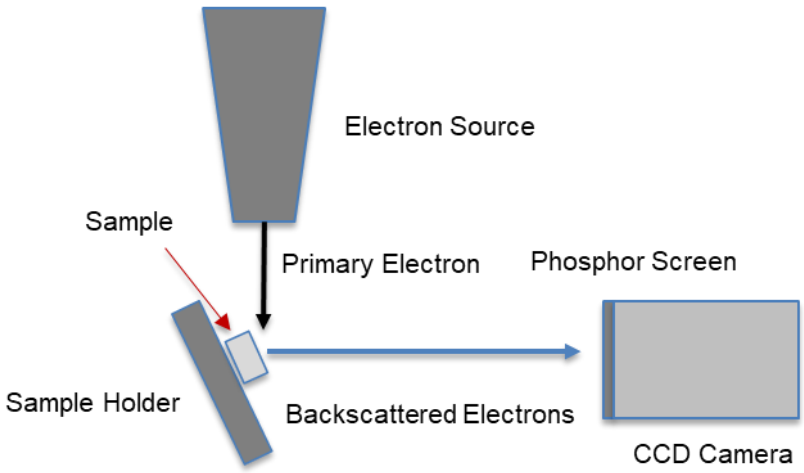

Figure 3-2 A schematic diagram of titled specimen for EBSD showing main SEM components.

The orientation of the patterns identified (indexed) using a computation technique known as Hough transformation. The Hough transform is mainly used to identify the diffraction pattern where the images from the EBSD CCD camera is converted into peaks in Hough space. Then line integral is taken from each peak at a certain angle and intersection, where each of these bands (lines) is a lattice plane. As these bands representing a lattice plane, the orientation of the investigated lattice can be determined using computer software [6].

To achieve a diffraction pattern, the conditions of diffraction must be in according to Bragg's Law, see equation 3-1. Where λ is beam wavelength, d is interplanar spacing (d-spacing), θ_B is Bragg's angle and n is an integer of diffraction orders of reflection and most cases only first order diffraction is considered hence n=1. The relationship between the incident beam of radiation and lattice planes shown in Figure 3-3 [6].

$$n\lambda = 2d\ sin\theta_B \quad (3\text{-}1)$$

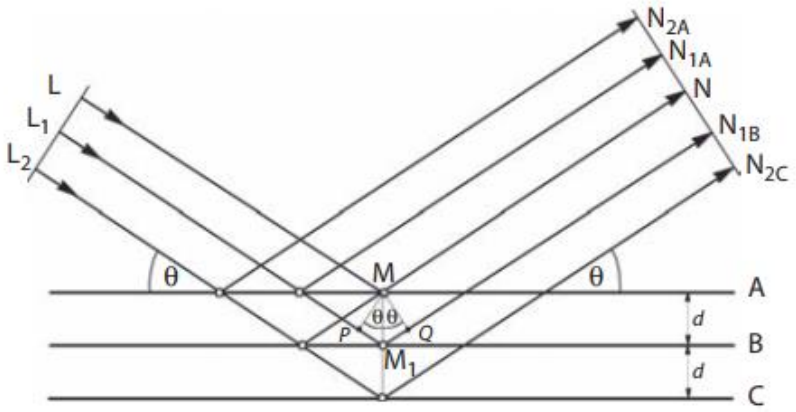

Figure 3-3 Diffraction from lattice planes, indicating the geometry that leads to the derivation of Bragg's Law [6].

Lattice atomic layer A, B and C are shown in Figure 3-3, The incident rays coming from L, L1 and L2 direction to the atomic Plane M, M1 and M2 at an angle of θ, also known as θ_B. At plane A, a percentage of radiation is reflected at angle 2θ while the rest will travel through the lattice planes and diffracted (reflected) at different layers in the direction of MN. The additional reflected beam can be achieved in the same direction (MN) if the reflected waves are in-phase in the direction of N ($N_{2A} - N_{2C}$). Bragg's Law is essential to all diffraction techniques where different lattice parameters can be known through diffraction angles θ_B.

3.4.2 Neutron Diffraction

One of the tools to study macrostructure is neutron diffraction, where the average microstructure/texture information can be obtained. The advantages of neutron diffraction can be seen in the analysis of irregular shapes and large specimen due to its superior penetration depth. Also, the speed at which results can be obtained dynamic and texture evolution can be studied. Other advantages include the minimum sample preparation required, and even low symmetry crystals can be studied. Neutron diffraction analysis and texture analysis is carried out in a research reactor where high speed neutrons are supplied by nuclear fission. Then the neutrons are slowed down by a moderator where the desired wavelength of 0.05-0.3nm is achieved. A pulsed neutron source; as in ISIS facility; where the time of flight (TOF) measurement can be carried out has many advantages over other macrostructure tools. Some of the advantages include a larger sample which can be analysed with minimum correction.

Also because of low absorbing, in-situ investigation can be carried out during sample straining, cooling and heating [6].

The TOF techniques require a fixed neutron position where the time of neutron pulse, collision and detections recorded. In addition, the wavelength of the neutron can be determined by recording the neutron flight path from a fixed position and distance by Broglie wavelength equation 3-2, and Bragg equation 3-1 [6]. Where λ is the wavelength, h is Plank's constant, m is neutron mass, v is neutron speed, t and L are the time of flight and the path length, respectively.

$$\lambda = \frac{h}{mv} = \frac{ht}{mL} \quad (3\text{-}2)$$

The neutron data obtained in the current study were from General Materials diffractometer (GEM) beamline. GEM can cover a wide range of scattering angles from 1.2° to 171.4° and has a very large area. This produces high resolution data and considered the highest resolution diffractometer of its type [8]. A schematic layout of the GEM detector array shown in Figure 3-4 [8].

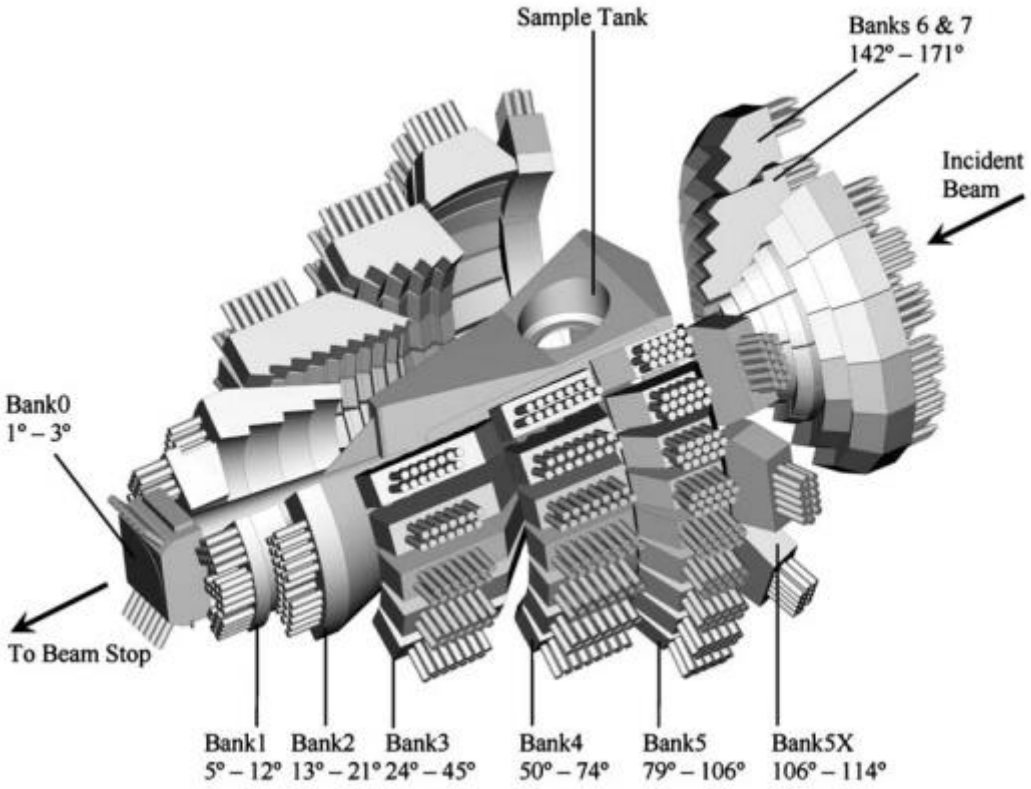

Figure 3-4 A schematic layout of GEM detector bank.

References

[1] M. Gallaugher, N. Brodusch, R. Gauvin, R.R. Chromik, Magnetic domain structure and crystallographic orientation of electrical steels revealed by a forescatter detector and electron backscatter diffraction, Ultramicroscopy. 142 (2014) 40–49. doi:10.1016/j.ultramic.2014.03.013.

[2] B. Beausir, J.J. Fundenberger, Analysis tools for electron and X-ray diffraction, ATEX-Software, Univ. Lorraine-Metz. (2017).

[3] F. Bachmann, R. Hielscher, P.E. Jupp, W. Pantleon, H. Schaeben, E. Wegert, Inferential statistics of electron backscatter diffraction data from within individual crystalline grains, J. Appl. Crystallogr. 43 (2010) 1338–1355. doi:10.1107/S002188981003027X.

[4] R. Hielscher, H. Schaeben, A novel pole figure inversion method: Specification of the MTEX algorithm, J. Appl. Crystallogr. 41 (2008) 1024–1037. doi:10.1107/S0021889808030112.

[5] L. Lutterotti, S. Matthies, H.R. Wenk, A.S. Schultz, J.W. Richardson, Combined texture and structure analysis of deformed limestone from time-of-flight neutron diffraction spectra, J. Appl. Phys. 81 (1997) 594–600. doi:10.1063/1.364220.

[6] O. Engler, V. Randle, Introduction to texture analysis: macrotexture, microtexture, and orientation mapping, CRC press, 2009.

[7] T. Maitland, S. Sitzman, Electron backscatter diffraction (EBSD) technique and

materials characterization examples, Springer Berlin, 2007.

[8] A.C. Hannon, Results on disordered materials from the GEneral Materials diffractometer, GEM, at ISIS, Nucl. Instruments Methods Phys. Res. Sect. A Accel. Spectrometers, Detect. Assoc. Equip. 551 (2005) 88–107.

Chapter 4: On the Magnetic Domain Correlation with Crystallographic Grain Orientation in Grain Oriented Electrical Steel

4.1 Introduction

The direct observation of the magnetic domain alteration allows for a better understanding of the core loss and magnetic permeability correlation with the alloy microstructure [1]. The magnetic domains, in general, are regions in a magnetic material that are uniformly magnetised or have a magnetic polarity [2]. It is generally believed that magnetic loss, iron loss, eddy current and hysteresis loss are significantly affected by microstructural characteristics, including microtexture and grain size [3]. In addition, it is well established that an abnormal grain growth phenomenon during final high-temperature annealing at the end of the GOES manufacturing process leads to a large grain with desired crystal orientation, i.e., {110} <001> Goss texture [4], see Figure 4-1a. The generation of a strong Goss texture during secondary recrystallisation process contributes greatly to the reduction of the power core loss in grain oriented silicon steel when it is subjected to a magnetic field in the rolling direction [5],[6],[7]. This is critical as the magnetic domain pattern in highly oriented grain oriented silicon steel is aligned with the rolling direction (RD). It is demonstrated via dynamic observation that the microstructural defects and inclusions can greatly affect the domain wall movement, which

results in high magnetic losses[8],[9]. Dynamic observation is the observation of magnetic domain movement during magnetisation and demagnetisation.

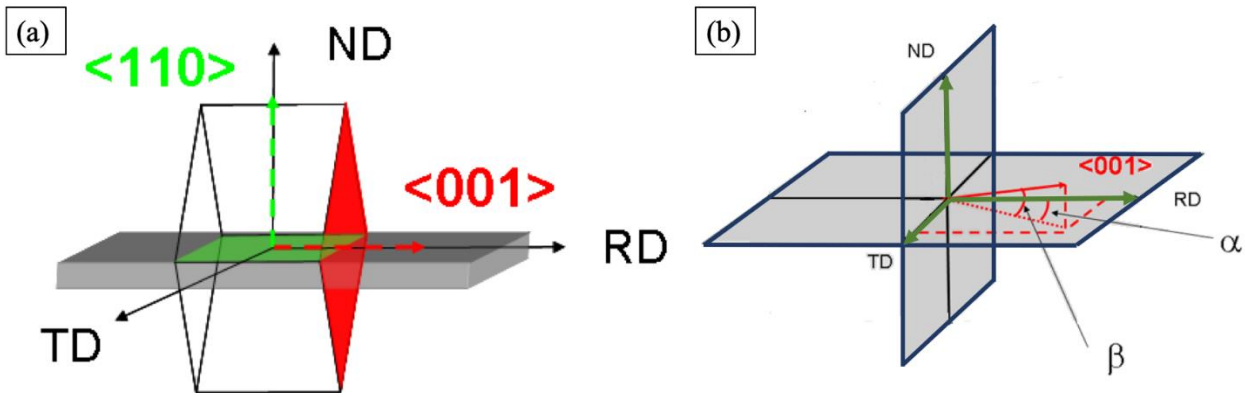

Figure 4-1 Schematics showing ideal Goss orientation (a) and definitions of a and b angles: α is the angle between <001 > and in-plan RD and β is the angle between <001> and out-plan RD (b).

As stated earlier, the magnetic properties are highly dependent on grain orientation and are affected by the deviation of <001> crystal axis from RD. There are two main deviation angles that should be considered for easy magnetisation direction, which are: α: the angle between <001> and in-plane rolling direction, and β: the angle between <001> and out-plane rolling direction, see Figure 4-1b. These two angles are critical for magnetic property optimisation. For instance, If a Goss grain has large α and β angles, the surface domain closure appears to have 90° magnetic domain wall, which causes a magnetic flux deviation and sub-domain formation and hence minimising magnetostatic energy [10]. It is widely reported in the literature, that the inclination of β angle out of the <001> sample axis (RD) is directly proportional to the surface closure domains, i.e., the domain surface closure increases with increasing inclination β angles [1],[11]. Therefore, if the <001> axis's angle of inclination has

a minimum value, it will create a condition of a number of surface closure domains to be zero, thus presenting only a simple 180° wall structure [1],[11],[12]. Practically, in order to reduce the surface closure domain and Eddy current losses [13], and hence total power loses in GOES, the sheet thickness is reduced [2],[10],[14]. It should be noted here that magnetic flux is referred to the total magnetic field passing through the steel sheet surface during the magnetisation process. Moreover, the magnetostatic energy is referred to the total magnetic charges generated by magnetic field polariton that leads to the magnetisation of ferromagnets [8].

4.1.1 Magnetic Domain Imaging

The imaging the domain structure can lead to a better understanding of microstructure feature correlations with magnetic property optimisation. The magnetic domain imaging has a long history, and many techniques have been employed to observe their structure, sub-structure, movement and mobility during the magnetisation process. Magnetic domains can be imaged using various techniques and different types of domain viewers used in industry and academia. Conventionally, magnetic powder or magnetic fluids are used with optical microscopy to reveal the magnetic domain patterns and flux direction on the surface [15]. An additional advantage of using magnetic fluids is that the stray field can also be detected. The disadvantage of this observation method is that the domain patterns and configuration cannot be directly observed in the materials with low stray field or a high magnetic permeability [2]. The magneto-optical or Kerr effect is another technique for domain imaging using standard optical microscopy,

which can cover large sample area imaging [16], [17]. In general, the magneto-optical effect is based on the rotation of the polarised light with resolution limited by optical microscopy. Using this method, the magnetic domains can be observed as narrow as 10 microns in width [21]. With the use of periodic photographing in magneto-optical microscopy, the domain wall motion can also be observed, which is so called, dynamic observation. The limitation of dynamic observation in magneto-optical microscopy even with high-speed photography tools is the low resolution images of domain patterns is achieved [2]. A higher resolution is possible with the use of high-power laser scanning microscopy, as reported in [18]. A more sophisticated method is using Transmission Electron Microscopy (TEM) for magnetic domain imaging [19], [20]. In TEM, a relatively low voltage of 100 - 200 keV as well as a high voltage of 1000 keV can be used for such an observation [24]. This allows high-resolution imaging on a nanometre scale and provides high sensitivity for small magnetic patterns alterations. However, the TEM method is limited to a very small observation area and for a thin magnetic material only [21].

Scanning Electron Microscopy (SEM) can assist in providing a better resolution than optical microscopy method for magnetic domain imaging and cover a relatively larger area than the TEM method. In SEM condition, the low-energy secondary electrons which are sensitive to the stray field on a magnetised sample surface are deflected, and with the help of detectors that are also very sensitive to electron direction changes, the magnetic domain information can be obtained. It is believed that high energy backscattered electrons emitted during electron striking in SEM condition are largely affected by the magnetisation of the sample [2],[22]. In general, there are two types of magnetic contrast that can be obtained using SEM method. The Type I

magnetic contrast can be achieved via secondary electrons to observe the stray field contrast where the sample is oriented perpendicular to the electron beam using 10 KeV or less acceleration voltage during SEM scan. From a large number of these secondary electrons, some are deflected from the sample surface and collected by a highly sensitive detector in the SEM chamber [2]. Type I magnetic contrast is mainly used for hard magnetic materials, whereas Type II magnetic contrast is used for soft magnetic materials, i.e., GOES, that have small stray fields. In Type II contrast, the backscattered electrons are deflected in the forward direction from a tilted sample surface by the local magnetic charge either toward or away from the surface. This creates a difference in contrast for different magnetisation directions in the sample [2],[22]. It is reported that in order to obtain a maximum magnetic contrast, a tilt of 40^{o} is considered to be optimum [2]. However, in the current study, in order to perform the domain imaging and EBSD simultaneously, a 70^{o}-tilt is applied, which provided good magnetic contrast.

By comparing high voltage STEM with low voltage SEM method for domain imaging, it was demonstrated that a high-voltage instrument of 200 keV observation reduces the structural and topography contrasts relative to magnetic signals which assist in providing a clear image with an enhanced magnetic contrast [23]. Whereas, the conventional SEM which uses much lower energy, i.e., 30 keV, has a lower resolution. However, in the current study, careful sample preparation is used in order to obtain higher magnetic contrast. It is reasonable to assume that SEM magnetic imaging contrast is relatively limited, and post-imaging editing is needed to enhance such a contrast. A technical method of obtaining a high resolution SEM magnetic domain imaging for up to 250 to 300 nm using FSD is reported in [22]. In their study, they

used SEM equipped with EBSD detector to image magnetic domains. To summarise FSD method for domain imaging from the available literature and to our best understanding, the following can be acknowledged. It is established that high energy backscattered electrons, ejected from sample surface during SEM scan, can be affected by the local magnetisation in the sample. Therefore, tilting the sample is needed in order to enhance the backscattered electrons deflection by the local domain magnetic charge of the sample. In such a case a large number of electrons are then deflected away from the surface, and some are collected by the FSD detectors inside the SEM chamber that are usually positioned on the EBSD phosphor screen's corners. Here the magnetic imaging contrast difference can be observed as different magnetisation polarity.

In the present experiment, magnetic domain structure and pattern in grain oriented silicon steel are imaged and correlated to the deviation angles α and β; in-plain and out-plan deviation angel from <RD>, respectively. The domain imaging was obtained using Type II contrast via utilising SEM equipped with EBSD and FSD detectors. Moreover, grain boundary characteristic and its effects on the magnetic domain transfer and configuration was investigated, especially during magnetic domains encountering and overpassing between differently oriented grains. Furthermore, the magnetic performance of the different type of GOES was assessed, and magnetic losses, as well as permeability, were measured and correlated to the GOES microstructure, microtexture and <100> deviation angles from RD. Finally, an advanced statistical tool was used for better results visualisation and comparison purposes. The magnetic losses, and permeability B800 (T), of the GOES sheets, were measured at the Cogent Orb Electrical Steel and shown in Table 4-1.

Table 4-1 Magnetic performance of the commercial GOES sheets, showing magnetic losses

Sample	Magnetic losses (W/kg)	B800 (T)	Thickness (mm)
A	0.82	1.94	0.23
B	1.17	1.85	0.27
C	1.11	1.86	0.23
D	0.88	1.92	0.23
E	0.92	1.93	0.27
F	1.4	1.83	0.35
G	1.09	1.84	0.23

4.1.2 FSD Domain Imaging

As discussed in the Introduction, Section 4.1, the magnetic domain observation of Type II magnetic contrast can be obtained through using an electron microscope in two different conditions. First is using high acceleration voltage, i.e., 200 keV to provides high contrast magnetic domain [23]. The second condition can be achieved by using low voltage, i.e., 20 keV, using careful sample preparation in order to reduce surface topography. In this condition, the image enhancement techniques should be used to increase the image contrast, as reported in [22]. In the current study, a low voltage condition was applied to visualise the domain patterns and configurations. Here the magnetic domains were observed using FSD (forescatter detectors) for GOES soft magnetic material. It should be emphasised here that the magnetic contrast was very weak using standard FSD method in the current study, thus a relatively high 30kV acceleration voltage was used. Moreover, in order to increase the backscattering coefficient (the fraction of electrons emerging from the surface), the sample was tilted to 70°.

Figure 4-2 shows certain examples of domain imaging using forescatter detectors under 30 KeV low-voltage SEM conditions. The working distance in the range of 13 - 17mm was used, depending on the obtained magnetic contrast. Figure 4-2 shows successful imaging examples of magnetic domain pattern and domain transfer between serrated wavy low-angle grain boundary (Figure 4-2a), high topology non-flat low-angle grain boundary (Figure 4-2b), domain across small isolated island grain within large recrystallised grain (Figure 4-2c), magnetic domains at triple junction between three different oriented grains with low angle

boundaries (Figure 4-2d). It is evident from Figure 4-2 that this domain imaging methodology is an effective way of studying domain patterns and configuration as well as its transfer, even without applying external magnetic force. This is vital in order to observe the original domain structure before the magnetisation process. For instance, Figure 4-2a shows the domain pattern divergence across the serrated low-angle grain boundary and small precipitates within the grain (see highlighted dashed square). It should be emphasised here, that due to the sample thickness, different grain orientations and sample preparation, the surface of the sample was not even, i.e., not flat, in most of the cases here. This resulted in slightly different surface depth portfolios from different regions, or oriented grains on the surface which caused 3D effects and shadowing during domain imaging as clearly can be seen in Figure 4-2. Figure 4-2b shows the domain fragmentation during its transfer to a different oriented grain through a low angle grain boundary. It should be noted here that ion beam milling may affect the upper grain shown in Figure 4-2b. As reported in [22], excessive use of the ion beam miller can create amorphized surface lattice. Figure 4-2c shows a lancet narrowly spaced and parallel domain pattern crossing a small island grain without significant diversion. Figure 4-2d shows a narrow-branched pattern and lancet domain in the top two grains, as well as a very widely spaced domain patterns in the bottom grain which has a different orientation and they are separated by a low grain boundary. As indicated by a small red dashed square on Figure 4-2d, the branched domain patterns could transfer between the two top grains without significant diversion.

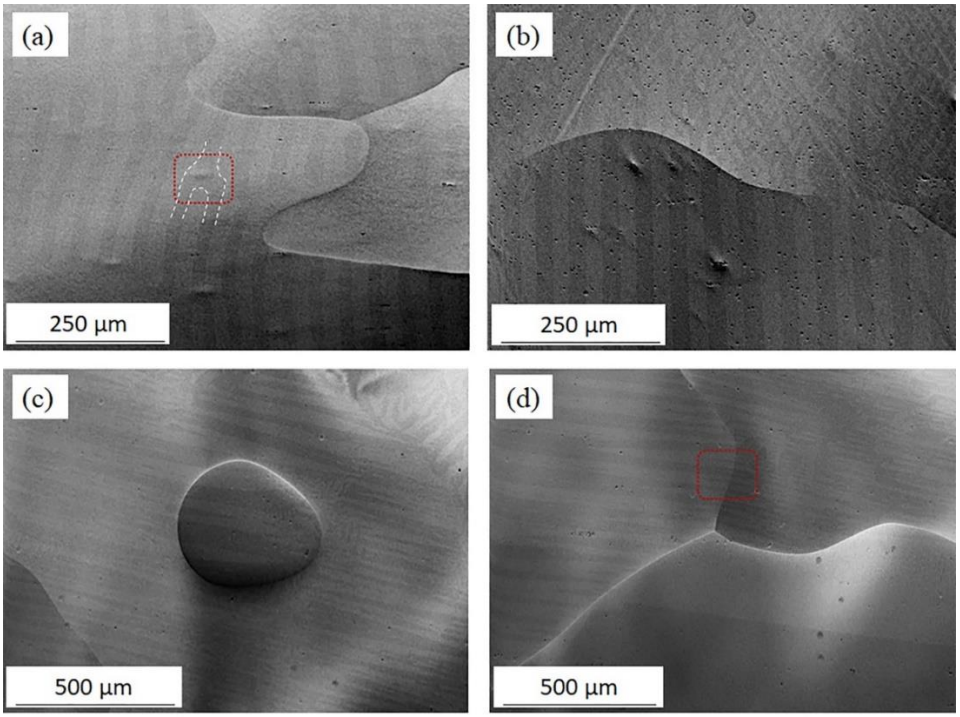

Figure 4-2 Magnetic domain imaging using FSD, (a) Magnetic domain transfer through a serrated low angle grain boundary and precipitates, showing strip branching indicated by dashed white lines, (b) Ion beam milling effects on domain fragmentation depending on grain orientation, (c) Magnetic domain transfer through a small island grain, (d) Lancet domains configuration in the top grains and large slab magnetic domain configuration in the bottom grain.

4.1.3 α and β Deviation Angles Determination

In order to study the magnetic properties such as permeability and magnetic losses of GOES, there are two main deviation angles between crystal direction and sample geometry which should be considered. This is critical as the magnetic properties in each grain are directly related to its crystallographic alignment with the GOES sample coordinate system. Furthermore, magnetic losses and permeability in GOES are anisotropic physical properties and can be significantly affected by their alignments with the sample coordinate system. As shown in Figure 4-1, in the current study, these two angles, namely α and β, are defined as: α is the angle

between <001> crystal direction and the in-plane rolling direction (RD) of the GOES sheet, and β is the angle between <001> crystal direction and out-plane rolling plane (RD). The α and β deviation angles for each individual grain were calculated using EBSD raw data. From EBSD data, the three Euler angles of individual grain (i.e., crystal coordinate system) and sample geometry (i.e., sample coordinate system) can be obtained in order to calculate the exact values of α and β angles. First, the EBSD Euler angles were transformed into the orientation matrix using Equation 1 [24]:

$$g(\varphi_1 \Phi \varphi_2) = \begin{pmatrix} g11 & g12 & g13 \\ g21 & g22 & g23 \\ g31 & g32 & g33 \end{pmatrix} \text{ …….. Eq. (4-1)}$$

The orientation matrix entries are shown as:

$$g(\varphi_1 \Phi \varphi_2) =$$

$$\begin{pmatrix} cos\varphi_1 cos\varphi_2 - sin\varphi_1 sin\varphi_2 cos\Phi & sin\varphi_1 cos\varphi_2 + cos\varphi_1 sin\varphi_2 cos\Phi & sin\varphi_2 sin\Phi \\ -cos\varphi_1 sin\varphi_2 - sin\varphi_1 cos\varphi_2 cos\Phi & -sin\varphi_1 sin\varphi_2 - cos\varphi_1 cos\varphi_2 cos\Phi & cos\varphi_2 sin\Phi \\ sin\varphi_1 sin\Phi & -cos\varphi_1 sin\Phi & cos\Phi \end{pmatrix} \ldots$$

Eq. (4-2)

This orientation matrix assists in the calculation of the deviation angles in relation to the specimen coordinate system (X, Y, Z). Here, the crystal direction is denoted as [xyz], where

[xyz] corresponds to any direction of interest. Since the crystal direction in the coordinate system $M_{crystal}$ equals $gM_{speciment}$, where $M_{speciment}$ is the specimen direction in the coordinate system [25],[26]. For any crystal direction in [xyz], it can be written as the transpose $g^t M_{crystal} = M_{speciment}$ in the specimen frame, as shown in Equation 3, [26].

$$M_{XYZ} = \begin{pmatrix} g11\,x & g21\,y & g31\,z \\ g12\,x & g22\,y & g23\,z \\ g13\,x & g23\,y & g33\,z \end{pmatrix} \text{…….. Eq. (4-3)}$$

The α and β deviation angles were then calculated following Equations 4 and 5 [26]. Here, only RD direction is considered which is <100>, thus $<x'y'z'>$ represent all <100> direction. The angles were calculated for all <100> symmetrical directions and denoted as $<x'y'z'>$.

$$\beta_{x'y'z'} = cos^{-1}\left(\frac{g_{11}x'+g_{21}y'+g_{31}z'}{\sqrt{(g_{11}x'+g_{21}y'+g_{31}z')^2+(g_{13}x'+g_{23}y'+g_{33}z')^2}}\right) \text{……. Eq. (4-4)}$$

$$\alpha_{x'y'z'} = cos^{-1}\left(\frac{g_{11}x'+g_{21}y'+g_{31}z'}{\sqrt{(g_{11}x'+g_{21}y'+g_{31}z')^2+(g_{12}x'+g_{22}y'+g_{32}z')^2}}\right) \text{…….. Eq. (4-5)}$$

The angle $\beta_{x'y'z'}$ is the angle between <001> crystal direction and out-plane rolling plane and $\alpha_{x'y'z'}$ is the angle between <001> crystal direction and the in-plane rolling direction (RD) of the GOES sheet and both angles are calculated for each of the six directions [26].

4.2 Results and Discussion

Figure 4-3a shows an electron forward scatter (FS) image for sample A. The Rolling Direction (RD) is closely aligned with specimen Y-Axis as indicated by the arrow in Figure 4-3. The variations of forward scatter electron intensities in different grains are caused by different local magnetisation polarities, which led to a different contrast in each grain, see Grain 1 (G1) and Grain 2 (G2) in Figure 4-3. The magnetic domains in Sample A have a straight, simple strip pattern in which they transferred from G1 to G2 without perturbation in the magnetic pattern. A magnified area in G1 is shown in Figure 4-3b. The in-plane angle (α) and out-of-plane angle (β) are calculated for both grains (G1 and G2) and schematically shown in 2D plane on Figure 4-3c. It appears there is a difference between the α angles in the two grains with an α value of +4.8° in G1 and +0.85° in G2. However, their deviation spread, i.e., range, is in the same direction along RD, so the total difference between them is rather small (= 3.95°) and hence reduce the effective deviation from RD. Moreover, there is a noticeable variation between β angle values for G1 and G2 with values of +2.8° and +6.1°, respectively. As in α deviation case, the β angle deviations are aligned with RD in the same direction, i.e., both have (+) values, thus the total difference is also reduced to 3.3°. It appears that this amount of deviation did not perturb the striped magnetic domain pattern during grain boundary transfer. It has recently been claimed that a grain with a β angle greater than 0.5° showed lancet magnetic domains pattern structure [10],[27]. However, in the current investigation, it appears that G1 and G2 in Sample A did not show any signs of lancet domain structure and they both have β angle values greater than 0.5°, see Figure 4-3a-c. A possible explanation is that the tensile load parallel to RD applied during electrical steel thermal flattening, as well as tension coating at the end of the

production line, caused the lancet domain to disappear and the width of the magnetic domain to be reduced. This domain width reduction has some advantages as it leads to magnetic loss minimisation, as reported in [11]. It should be emphasised here, that the grain boundary angle between G1 and G2 is 5°, which is a low angle grain boundary (LAGB). Furthermore, the Inverse Pole Figures (IPFs) in Figure 4-3c and Orientation Distribution Functions (ODFs) in Figure 4-3d showed that both G1 and G2 have a very similar orientation with a strong Goss texture component intensity. This is assisted in low deviation (α) and (β) angles and easy transfer of the strip domain.

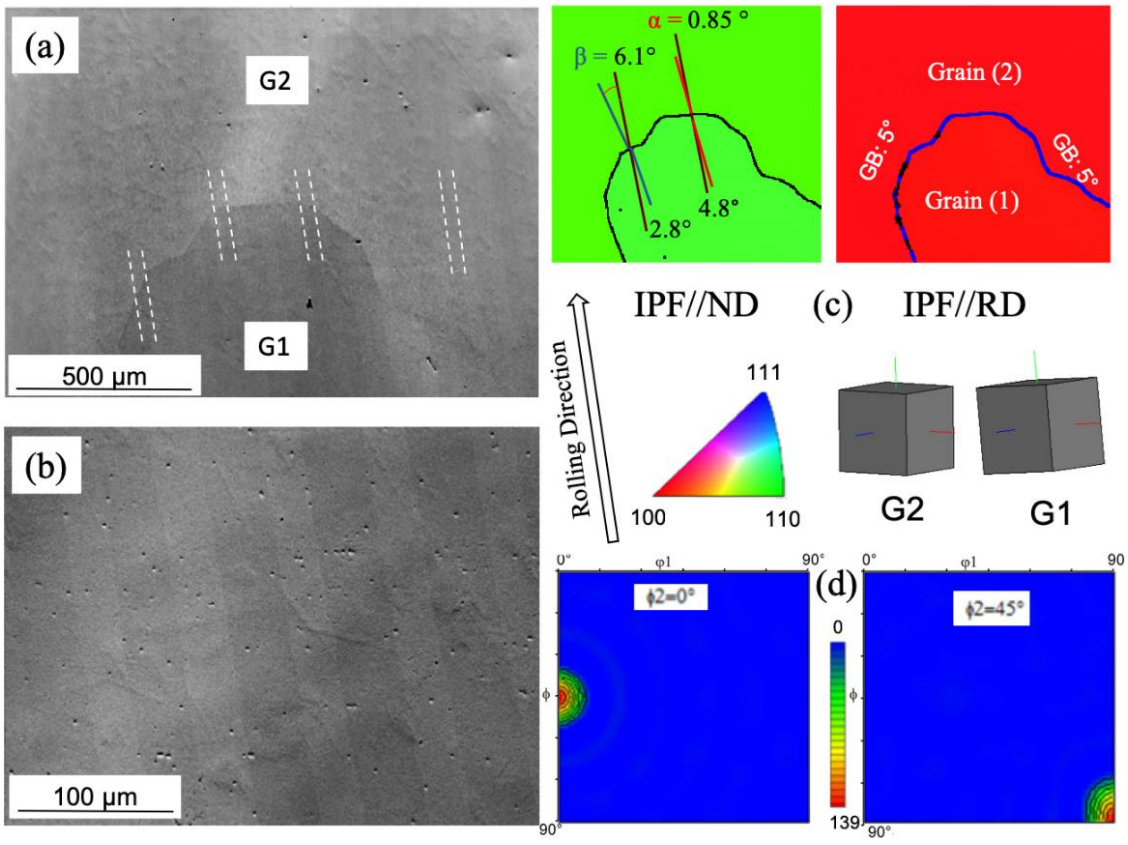

Figure 4-3 (a) FSD image of a magnetic domain in Sample A, revealing strip magnetic pattern transfer between G1 and G2, (b) high magnified area in G1, (c) IPF//RD and IPF//ND maps, grain boundary and (α and β) deviation angles are shown on the images, (d) ϕ2 = 0° and ϕ2 = 45° ODF sections for the map in (c) showing strong Goss.

Figures 4-4a and 4-4b show magnetic domain structures in three neighbouring grains and the domain transfer at a triple junction in Sample B. Figures 4-4c and 4-4d, show IPFs and ODFs of the area in Figure 4-4a, respectively. As shown in the figures, G1 with +1.6° β and +15.4° α shows a large slab pattern that aligned parallel to the G1/G2 grain boundary. The α angles in G1 and G3, are +15.4° and -6.9°, respectively. However, their deviation spread, i.e., range, is in the opposite direction from RD, so the total difference between them is very large (= 22.3°) and hence increase the effective deviation from RD significantly. Moreover, there is a slight variation between β angle values for G1 and G3 with values of +1.6° and +2.2°, respectively, but aligned with RD in the same direction, i.e., both have (+) values, thus the total difference is reduced to 0.6°. It appears that this amount of α angle deviation perturbed the magnetic domain pattern during grain boundary transfer, although the β angle range was negligible.

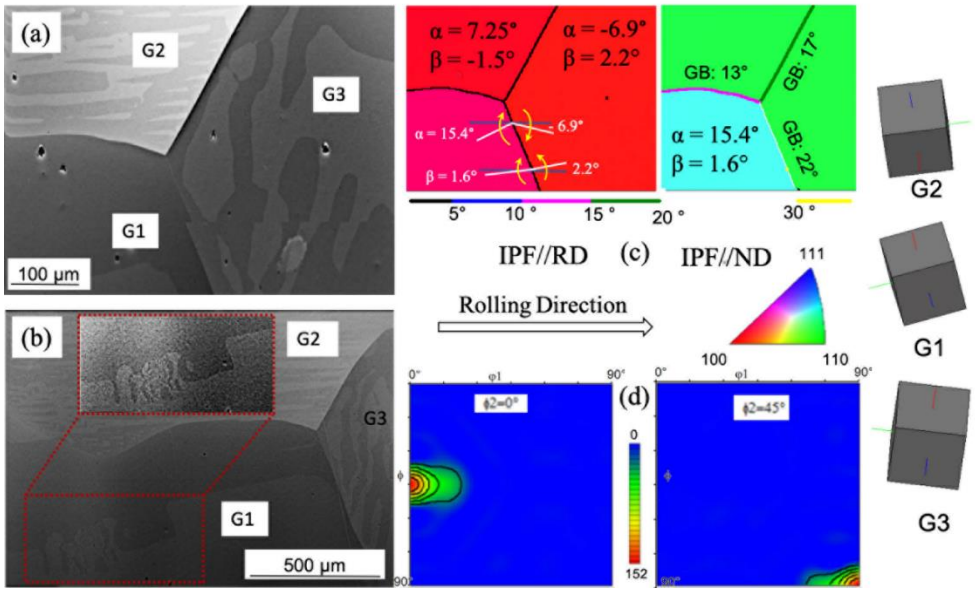

Figure 4-4 (a) Magnetic domain at triple junction in sample B: Slab magnetic pattern in G1, Lancet magnetic pattern in G2 and Complex magnetic pattern in G3, (b) A magnified magnetic image showing 90° domain wall in the same area in (A) indicated by dashed red rectangular shape, (c) IPF//RD and IPF//ND maps, grain boundary and (α and β) deviation angles are shown on the images, (d) ϕ2 = 0° and ϕ2 = 45° ODF sections for the map in (c) showing strong Goss.

As highlighted in Figure 4-4b and indicated by a dashed red rectangular shape, the magnetic domain wall has formed at a 90° angle from the main slab domain structure, which clearly indicates a strong connection to the internal transverse domain. It is widely reported that wide slab-like domains, similar to that for G1 in Figures 4-4a and 4-4b, result in large anomalous eddy-current losses [11][10][28]. Whereas, G3 in Figure 4-4a, exhibits complex domain patterns are nearly aligned parallel to G3/G1 and G3/G2 grain boundaries receiving magnetic flux from both G1 and G2 grains. Moreover, it seems that the domain structure in G3 is affected by neighbouring grains magnetic patterns and has +2.2° (β) and -6.9° (α) angles. It is evident from Figure 4-4a, that the magnetic domain structure in G3 does not follow an easy-surface magnetisation direction, i.e., <001> in RD, see the G3 3-D crystal in Figure 4-4. G2, on the other hand, has -1.5° (β) and +7.25° (α) angles and shows a complex domain structure with dagger or lancet patterns, which are also known as supplementary magnetic domains. It should be remembered that supplementary domains are the sub-domains that appear to reduce magnetostatics' energy, i.e., stray field energy, at the expense of the formation of the additional domain walls. Furthermore, the discontinuation and branching magnetic domain pattern is also observed in G2 and at the G2/G3 grain boundary, see Figure 4-4a. This resulted from the difficulty in transferring the magnetic flux of the same polarity to the nearby grains' magnetic domains due to high α and HAGBs. As shown in Figure 4-4c, the grain boundary between G1 and G2 is 13°, 22° between G1 and G3, and 17° between G2 and G3. The ODFs in Figure 4-4d, show Goss {110} <001> texture component deviation toward {110} <112>. However, this is expected as G1 has a larger orientation discrepancy with G2 and G3 as shown in the IPFs.

Figure 4-5a shows a large grain (G1) (~ 752 microns in diameter) having Cube {100} <001> orientation in Sample C, see also Figure 4-5d-e. It is well known that Cube orientation has two easy magnetisation directions [22]. This also applies to G1 due to the fact it has a small deviation from ideal Cube (100) <001> orientation with 4.8° and 2.4° β and α angles, respectively. The FS images in Figures 4-5a-c show branching magnetic domains pattern perpendicular to RD. See also the highlighted areas by dashed red rectangular shapes in Figures 4-5a and 4-5b. This is commonly found in two easy magnetisation directions crystals as stated in [29]. Two specific areas in Figure 4-5a are magnified for better domain observations; the top side of G1 in the vicinity of the G1/G4 grain boundary is shown in Figure 4-5b, and lower side of G1 on the G1/G4 boundary in Figure 4-5c. All the figures demonstrate the domain branching occurrences that is perpendicular to the RD. From Figure 4-5a, it is clear that G2 is a relatively small grain with a size of 237 microns and shows a wide strip domains pattern. G2 and G3 have low deviation of β and α angles. In G3 the magnetic domains exhibit a wide slab pattern, see Figure 4-5a. Meanwhile, G4 has a β compared to other neighbouring grains where β is equal to +6.9° and α equal to +0.5°. It is clear from Figures 4-5a-c, that G4 has a complicated magnetic domain pattern that does not follow easy-surface magnetisation direction along RD. The domains major lines in G4 are perpendicular to (⊥) RD and nearly parallel to G1 domain patterns, especially in the vicinity of G1/G4 grain boundary, see Figure 4-5b. Whereas, the magnetic domain in G4 have a complex and fragmented pattern near G1/G4 (bottom side), G4/G3 and G4/G2 grain boundaries, see Figure 4-5a-c. The magnetic structure in G4 shows signs of a transition-stage magnetic structure. This type of magnetic structure is also reported in [30],[31]. This condition leads to a transition stage where a complex fragmented domain structure and an area of complete rotated patterns toward TD can exist together within the same grain as clearly can be seen in G4. Moreover, the ODFs in Figure 4-

5d, show strong Goss in sample C, however it is not as sharp compared to sample A, see Figure 4-3d. The IPFs in Figure 4-5e reveal some orientation difference between G1 and its neighbouring grains. As shown in the figure, G1 is separated from G4 by 36°; from G2 by 32.5° and from G3 by 25.8°. Whereas, the grain boundary between G2 and G3 is 8.9° LAGB and 8.2° between G2 and G4. Moreover, the grain boundary angle between G3 and G4 is HAGB. It can be concluded here that the grain boundary has a great effect on the magnetic domain transfer. For instance, LAGBs allows magnetic pattern continuation and transfer between G2 and G3 with minimum disruption. Whereas, the HAGB could cause large magnetic domain disruption between G1 and G4, see Figure 4-5a-c.

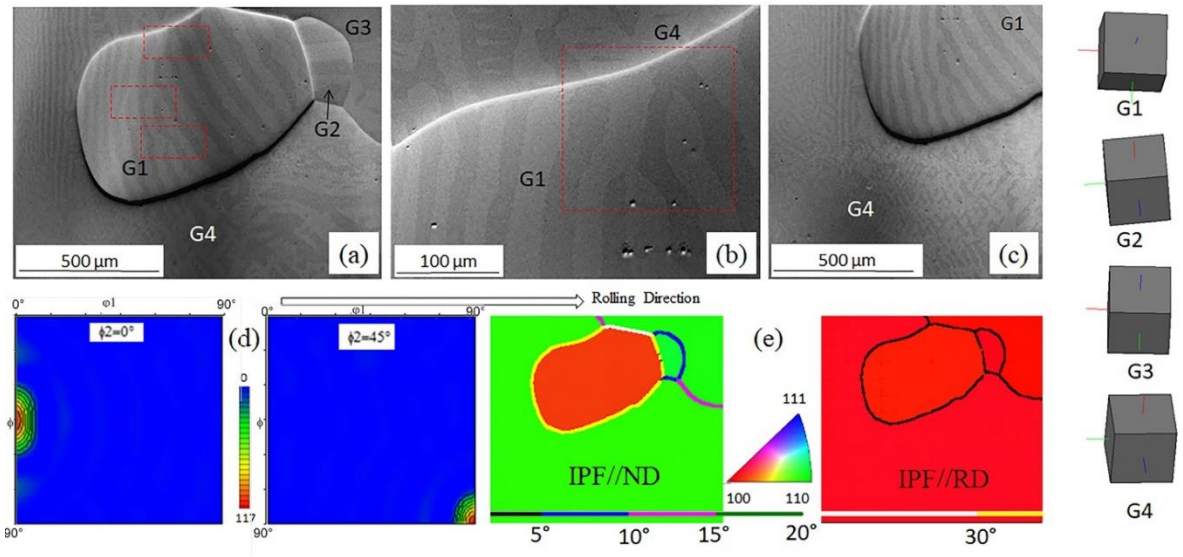

Figure 4-5 (a) FSD image of the magnetic domain in Sample C, G1 with Cubic orientation {1 0 0} ⟨0 0 1⟩ showing magnetic pattern branching perpendicular to RD indicated by red dash squares, large slab magnetic pattern in G2 and G3 and complex magnetic pattern in G4, (b) Magnified area of G1 showing magnetic stirp pattern branching, (c) Complex magnetic pattern in G4, (d) ϕ2 = 0° and ϕ2 = 45° ODF sections for the map in (e) showing strong Goss. (e) IPF//RD and IPF//ND maps, grain boundary and (α and β) deviation angles are shown on the images.

Table 4-2 summarise the grain misorientation angle between the identified grains in Samples A, B and C. As shown in Table 4-2 and Figures 4-3, 4-4 and 4-5, the grain boundary types are found to be different between Samples A, B and C. It is clear that the grains surrounded by a high angle grain boundary show supplementary magnetic domains and the continuation of these domains to neighbouring grains are disrupted by these boundaries. It was also clear that the magnetic domain is greatly affected by individual grain α and β deviation angles. Even though much of the literature has shown that the higher deviation β angles result in complex structure pattern, however, this was not observed in the current study. For instance, Sample A with a higher than 0.5º β deviation shows no sign of a supplementary domain structure.

Table 4-2 Grain boundary angles and types in Samples A, B and C.

Grains	Grain Boundary Type	Misorientation Angle (°)
Sample A		
G1-G2	LAGB	5.0°
Sample B		
G1-G2	LAGB	13.0°
G1-G3	HAGB	22.0°
G2-G3	HAGB	17.0°

Sample C		
G1-G2	HAGB	32.5°
G1-G3	HAGB	25.8°
G1-G4	HAGB	36.0°
G2-G3	LAGB	8.9°
G2-G4	LAGB	8.2°
G3-G4	LAGB	11.3°

For a better understanding of the effect of α and β deviation angles on magnetic performance, over 15 grains in each of the 7 samples with different thickness were analysed using EBSD row data. In the current study, the Gaussian Distribution Function for α and β angles is calculated for each individual grain in all the samples and shown in Figure 4-6.

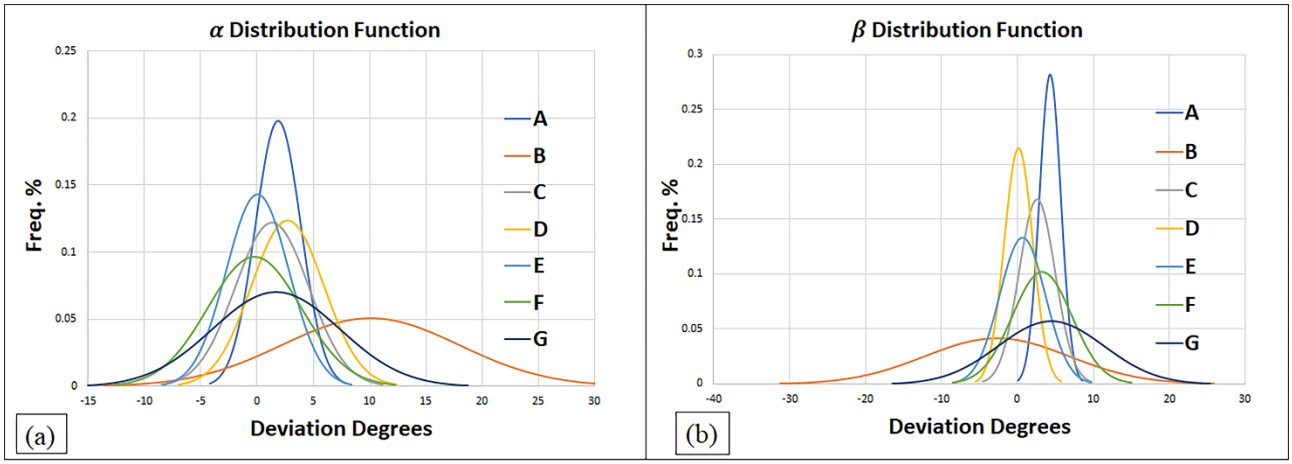

Figure 4-6 Gaussian Distribution Functions for deviation angles (a) α, (b) β, for all 7 samples A-G.

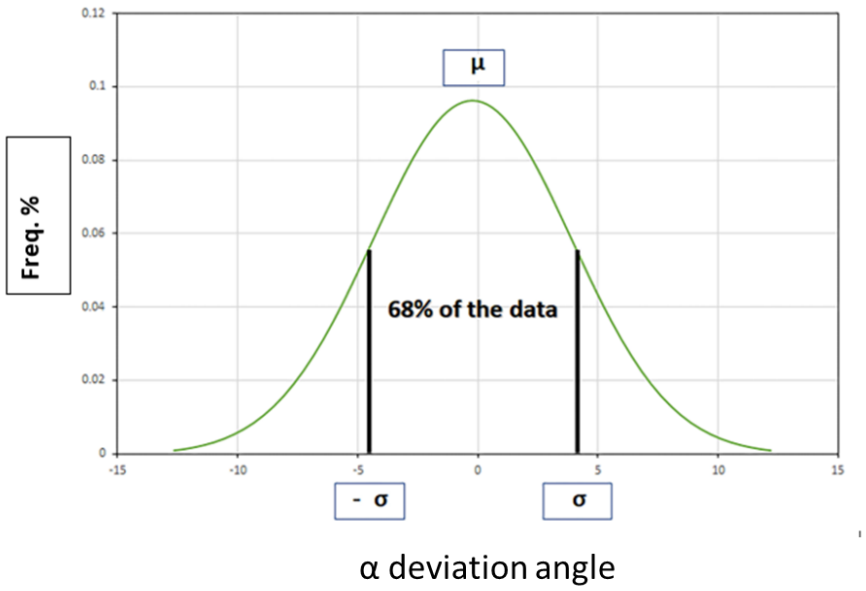

Figure 4-7 An example of Gaussian Distribution Function calculated for sample G α deviation angle; 68% of the data acquired between – σ and σ, μ is the average value.

As shown in Figures 4-6a and 4-6b, Sample A has the smallest range distribution (narrowest peak) for both α and β angles, while sample B has the largest range distribution (widest peak) for both angles. Moreover, Sample D has the smallest average deviation (~ 0) for angle β, and sample E has a small average deviation (~ 0) for angle α. Further comparison between the

samples was rather difficult using this method, thus, a new data representation method was used in this study in order to visualise the deviation angles in correlation with the magnetic performance in each sample. This new data visualisation method is clarified in Figure 4-7, where sample F used as an example. In the figure, a Gaussian distribution curve is plotted, where the average (μ) is the centre of the curve. Statistically, the majority of data have ± 1 standard deviation of the Gaussian curve, that is 68% of the data lies between ± 1 range (-σ to σ) from the average (μ). Here the standard deviation denoted by (σ). The average (σ) was calculated using Equation 6 [32]:

$$\mu = \frac{1}{n}\sum_{i=1}^{n} x_i \quad \text{..... Eq. (4-6)}$$

Where x_i are the deviation angles and (n) is the total number of the angle values. The standard deviation is calculated using Equation 7:

$$\sigma = \sqrt{\frac{\sum_{i=1}^{n}(x_i-\mu)^2}{n-1}} \quad \text{..... Eq.(4-7)}$$

The standard deviation calculation of 68% of the data is then subtracted from the average for the lower limit of the range. As for the upper limit of the range, the standard deviation is added to the average, as shown in Equations 8 and 9.

The lower limit of the range = $\mu - \sigma$ ……. Eq.(4-8)

The upper limit of the range = $\mu + \sigma$ ……. Eq.(4-9)

Plotting the range from Eq.8 to Eq. 9 (lower to the upper limit) range results in the 68% of the distribution range of the angular deviation, which is another representation of the Gaussian curve. By plotting 68% angular deviation distribution, the samples can be compared in terms of deviation angles versus magnetic losses and B800 values. Figure 4-8 shows the deviation angles of all the grains in each sample in a scatter plot, using equations 6 and 7. This data representation will assist in the range determination of the alpha and beta angles and directly correlate the angles spreads between all the samples. For instance, as shown in the figure, Sample B has a very large angle speared which reduced its magnetic performance, whereas, Sample A has the lowest range and exhibited good magnetic performance.

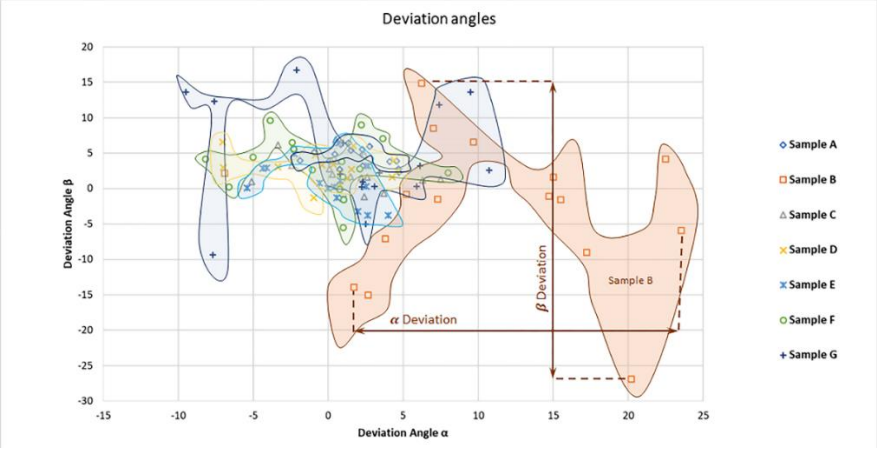

Figure 4-8 A scatter plot showing the deviation angles of all the grains in each sample plot.

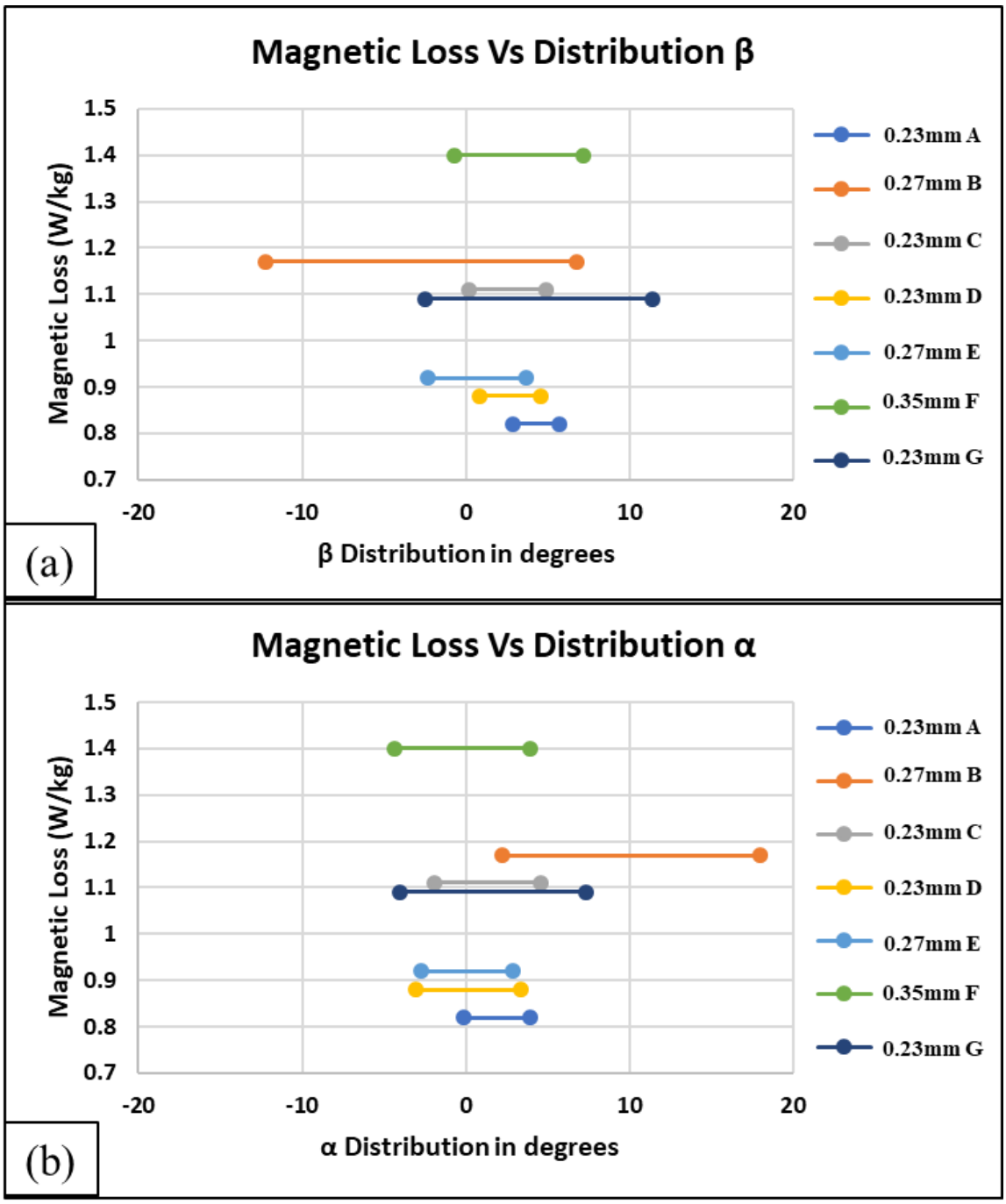

Figure 4-9 Sample magnetic losses versus (a) β deviation angle distribution, (b) α deviation angle distribution, for all the 7 samples A-G, the sample's thickness shown in the legend.

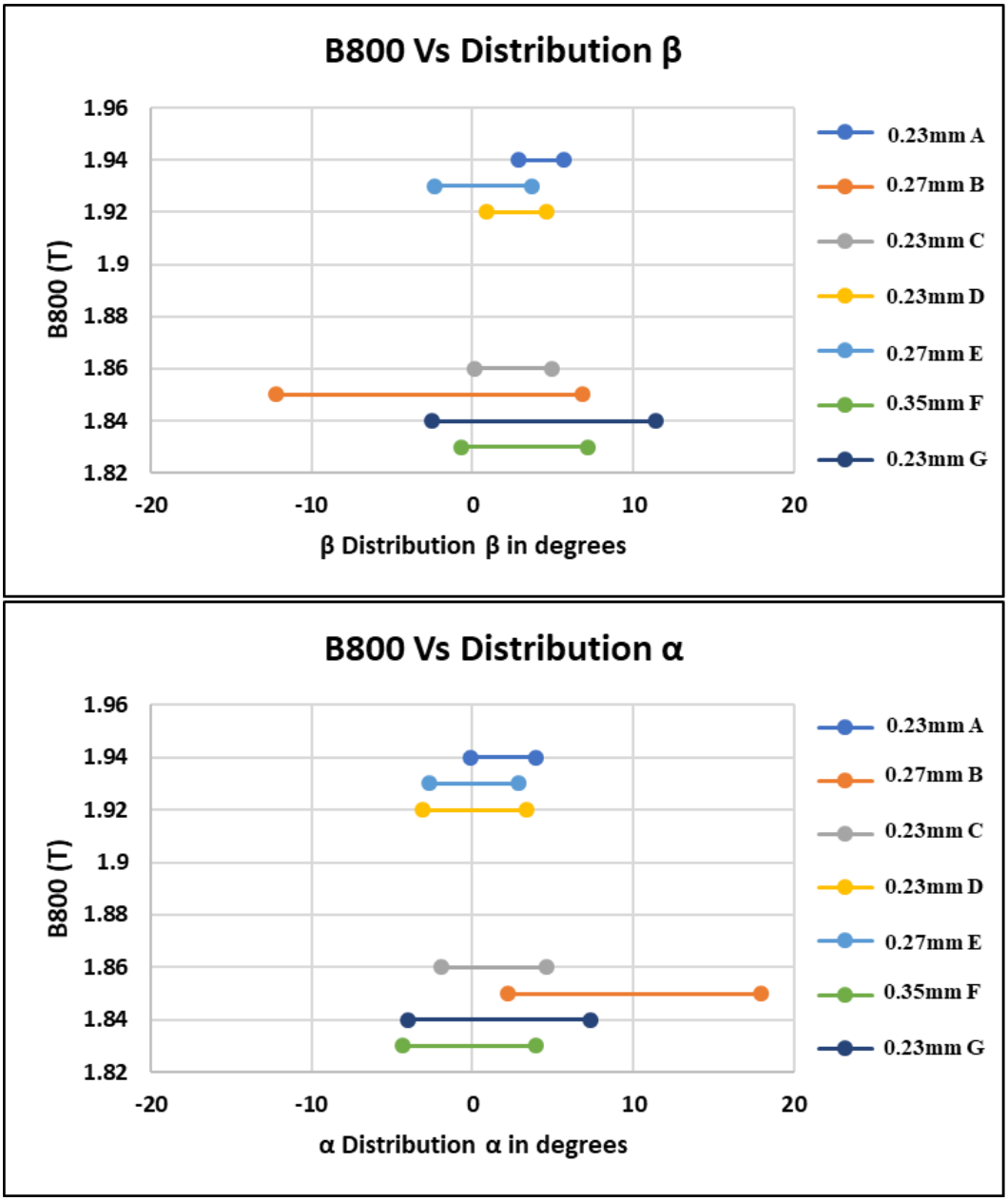

Figure 4-10 Sample B800 (T) versus (a) β deviation angle distribution (b) α deviation angle distribution, for all the 7 samples A-G, the sample's thickness shown in the legend.

The samples' β and α angular distributions versus magnetic losses and B800 values are shown in Figure 4-9 and Figure 4-10, respectively. It should be noted here that sample thickness is shown in the plot legend next to each sample. In general, Figure 4-9a shows the β angle

distribution correlation with overall magnetic loss; the smaller β distribution range results in lower magnetic losses. Figure 4-8b demonstrates similar behaviour of the effect of α deviation on magnetic losses. As shown in Figures 4-9 and 4-10, sample A has the smallest deviation spread, i.e., range, for both β and α angles, which resulted in the lowest magnetic losses and the highest B800 value. Although β value in Sample A is not as close to a zero value as the other samples, it has a very limited spread from the average value, as well as smaller distribution range in both deviation angles. Similarly, sample D has very low magnetic losses and high B800 value. Although β and α angles deviation in Sample D is close to the zero value, however, they have a wider spread compared to Sample A, which might explain the relatively higher magnetic losses and lower B800 in Sample D as shown in Figures 4-9, 4-10 and Table 4-1. Furthermore, as can be seen in Figure 4-9, Sample E has a relatively small range distribution as well as near-zero angular deviation spread. The magnetic losses in Sample E which has a 0.27 mm in thickness, is low (0.92 W/kg Value) compared to the 0.23 mm thickness sample D. From Figure 4-9, the deviation angles distribution effects on the magnetic losses can be seen, and it is evident that a small distribution in angular deviation results in lower magnetic losses. However, there is some irregularity. For instance, sample C has a relatively high magnetic loss (1.11 W/kg) although it has a low α and β deviation angle distribution ranges, see Figure 4-9. Thus, magnetic performance can be affected by other factors that have not been focused on in this investigation, such as grain size and chemical composition, for example, a relatively large grain can increase the Eddy current losses [33]. Moreover, aluminium (Al) and nitrogen (N) which forms the main primary grain growth inhibitor (AlN) are not present in sample C. This resulted in low permeability and high magnetic losses in Sample C. As for Samples B and G, the large spread of deviation angels has caused a high magnetic loss and a low permeability. Sample B has higher losses due to the fact

that it has a thicker cross-section (0.27 mm) compared to sample G (0.23 mm). It should be noted here that sample B has wider distribution ranges in both β and α angles than in Sample G, which also affects the magnetic losses, see Figure 4-9. Moreover, comparing Samples G and B to sample F, the effect of sample thickness can be clearly observed. For instance, Sample F (0.35 mm) has smaller α and β distribution ranges than in Sample G (0.23 mm) and C (0.23 mm), but it has poor magnetic performance that can be directly linked to its thickness. As reported in [13] the larger sheet thickness, the higher Eddy current losses in the sample.

Figure 4-10 shows the distribution of angular deviation from the average values of α and β angles versus the B800 value for all the 7 samples investigated in this study. In the figure, it can be seen that samples with the lowest spread in the deviation angle α have the highest B800 values. As an example, see Sample A which has B800 of 1.94 T. It is widely reported that the deviation angle α is directly correlated to permeability [34]. This is in agreement with the finding in the current study. For instance, the samples with the highest permeability, i.e., sample A, has the highest B800 value with the lowest distribution of deviation angles α and β; followed by Sample E (0.27 mm), then Sample D (0.23 mm). Although Sample D has lower β angle distribution range than in sample E, it has lower B800 1.92 T compared 1.93 T. This is directly related to the α angel distribution which is directly correlated to permeability performance since sample E has a very low α range. As for the samples with low B800 values, sample C with 1.86 T performed better than samples B, G and F (1.85 T, 1.84 T and 1.83 T, respectively). Furthermore, the sample thickness effects on the permeability are evident in Figure 4-10. For instance, although sample F (0.35 mm thickness) has much lower α and β distribution rage than that for samples G and B, but it has the lowest B800 value. This

demonstrates the high impact of sample thickness on both B800 values and magnetic losses. Moreover, sample G has a high distribution range of both deviation angles with a thickness of 0.23 mm, which is thinner than sample B (0.27 mm), yet it has a lower B800 value. Although both samples B and E have a thickness of 0.27mm, sample E magnetic performance was much higher due to the minimum deviation angles. Furthermore, the effect of thickness on magnetic performance can be magnified by reducing the deviation angles as the case of sample E, where sample E magnetic performance is higher compared to most of the other 0.23mm samples due to a smaller range of deviation angles. This trend discrepancy required further investigation in order to understand Sample G's low B800 value as well as Sample C high magnetic losses.

The effect of grain size on magnetic losses was investigated using a SOKEN tester to measure magnetic losses on two different samples with different grain size distributions. A region in Sample G was characterised for this purpose. As shown in Figure 4-11a, this region contained relatively small grain sizes. The grain orientation deviation from ideal Goss orientation is shown in Figure 4-11b. Figure 4-11d shows an overall strong Goss texture of the sample. The grain G1 in the Figure 4-11b has the highest deviation from ideal Goss orientation (> 20°) in the maps, whereas G2, G3 and G4 deviate by 15°-17° from Goss orientation and they are surrounded by grains with the smallest deviation from Goss orientation (< 5°). The inverse pole figure (IPF)s and grain boundary misorientation angles maps are shown in Figure 4-11c. From the figure, it appears that only a few grains have LAGB (< 10°) and the majority of the grain boundaries are (> 15°). It appears that the small grain size and grain boundary (> 15°) were the reasons for the increase in magnetic losses 1.13 W/kg at 1.7 T in this particular region.

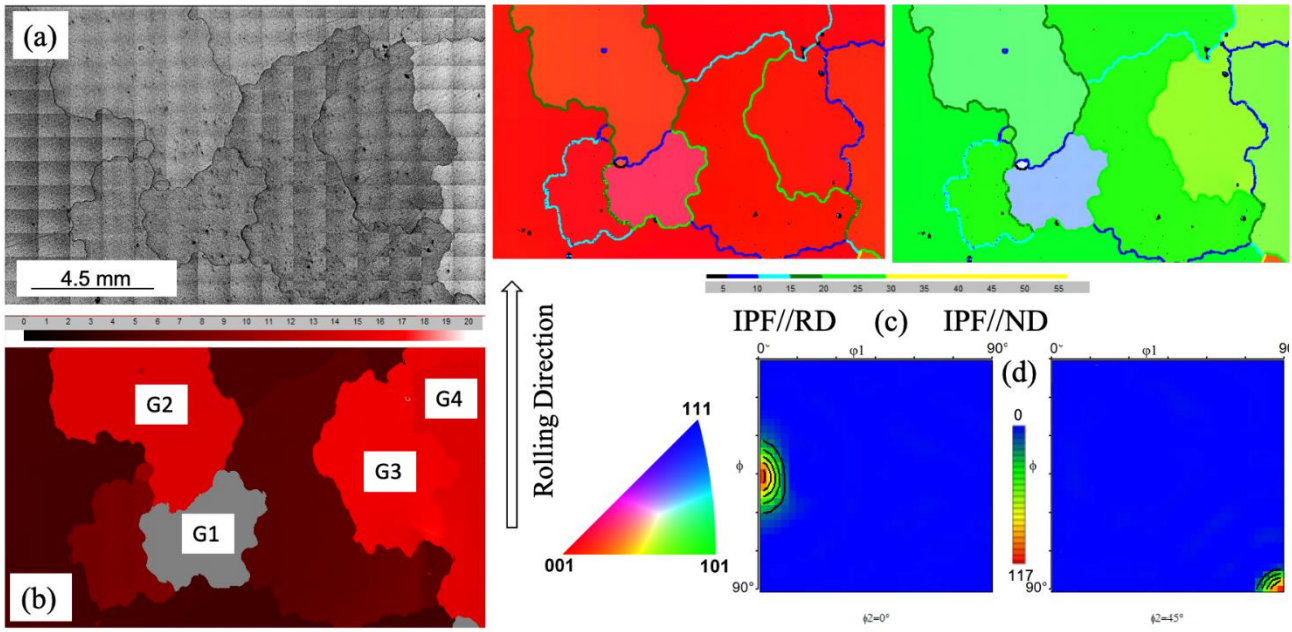

Figure 4-11 (a) A region in Sample G with a relatively small grain microstructure, (b) Goss orientation deviation map (0° to 20°) deviation from ideal Goss, (c) IPF//RD and IPF//ND maps for the area in (a), grain boundary are shown on the images, (d) $\phi 2 = 0°$ and $\phi 2 = 45°$ ODF sections for the map in (c) showing strong Goss.

Figure 4-12a shows a relatively large grain in sample D. From the magnetic measurement data it was clear that this particular area in sample D has a lower magnetic loss of 0.77 W/kg at 1.77 T compared to the area investigated in Sample G. Due to the large grain sizes, sample D was cut into a few sections to be suitable for EBSD mappings. It is clear from Figure 4-12a, that G1 is mostly surrounded by LAGBs (< 15°) and only a few segments of HAGBs > 20°. The G1 is neighbouring G2 and G3 that have Goss orientations, see Figure 4-12b. Furthermore, small grains with high deviation from ideal Goss orientation were found on G1/G2 and G1/G3 grain boundaries in this region on sample D, see Figure 4-12b. However, their very small sizes provide a little barrier to magnetic flux to encounter the neighbouring grains where the large grain boundary area fraction facilitate the flux transfer between the large grains. Therefore,

these small grains have negligible effects on overall magnetic losses. Comparing the 2 observed areas in Samples G and D, see Figures 4-11d and 4-12c, it can be seen that the region with relatively large grain in Sample D has a sharper Goss texture than the area with relatively small grain in Sample G. Hence, the grain size of the ideal Goss orientation (110) <001> have a great effect on magnetic losses and permeability.

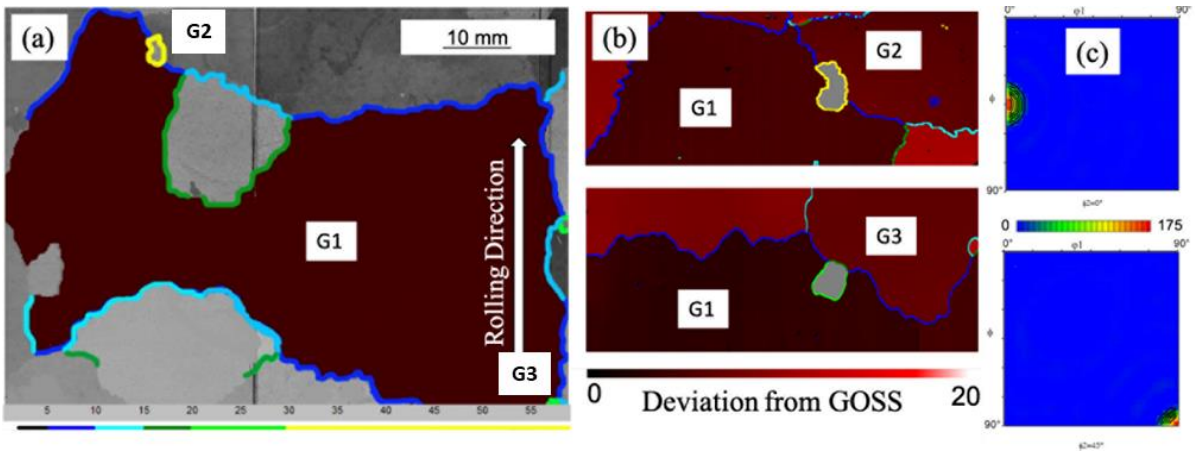

Figure 4-12 (a) A region in Sample D with large grain microstructure, a large grain with strong Goss orientation and grain boundaries are shown (b) Goss orientation deviation maps for two areas, (c) $\phi 2 = 0°$ and $\phi 2 = 45°$ ODF sections for the map in (a) showing strong Goss.

4.3 Conclusions

In the current study, magnetic domain structures and patterns were successfully captured using a FSD magnetic domain imaging technique. Also, the effects of the in-plane angle (α) and out-

of-plane angle (β) deviations from rolling direction (RD), GOES sheet thickness, grain size, crystallographic grain orientation and grain boundary misorientation on magnetic domain structure and magnetic performance were investigated. The effect of adjacent grains and GB misorientation angles was shown, where the lancet magnetic domain pattern was not present in sample A even with out-of-plane deviation angle β (>0.5°), in which contradicts earlier reports. Finally, it was shown that grains size, grain boundary and misorientation from ideal Goss have a significant impact on magnetic losses.

1. FDS method is proved to be a powerful technique to reveal magnetic domains in GOES with clearer domain visualisation than other conventional optical and Kerr microscopy tools. The advantage of this method is that no additional equipment was needed to reveal the magnetic patterns in the SEM system. However, sample preparation can be difficult. The limitation of FSD magnetic imaging is the surface finishing, as an ion beam miller can affect the magnetic structure by amorphizing the surface lattice.

2. The deviation angles; in-plane angle (α) and out-of-plane angle (β) have a great influence on the magnetic domain patterns as well as the magnetic property of GOES. The higher the α and β deviation angles, the lower permeability and higher magnetic losses. It was demonstrated that α angle deviation has more effects on the permeability than β angle deviation range, whereas β angle has more influence on magnetic losses.

3. The magnetic domain pattern continuation and transfer between the neighbouring grains are largely affected by the grain boundary misorientation angle. It was demonstrated that the magnetic domain patterns could easily be transferred across the grains through LAGB whereas the magnetic domain pattern was distorted and transformed into a complex structure when encountered grain with HAGB.

4. It was demonstrated that the thinner samples perform better despite having high α and β deviation angles from RD.

5. It was evident that the grain size of the ideal Goss orientation (110) <001> has a significant effect on magnetic losses in the Grain oriented silicon steel sheet.

6. It is concluded in the current investigation that the sample thickness and grain size are more influential factors than α and β deviation angles for magnetic property optimisation. However, the magnetic performance can be improved by reducing the deviation angles in the thick Goss sheets.

References

[1] J. W. Shilling and G. L. Houze, "Magnetic Properties and Domain Structure in Grain-Oriented 3% Si-Fe," *IEEE Trans. Magn.*, vol. 10, no. 2, pp. 195–223, 1974.

[2] A. Hubert and R. Schäfer, *Magnetic domains: the analysis of magnetic microstructures*, 3rd ed. New York: Springer Science & Business Media, 2008.

[3] A. A. Almeida, D. Rodrigues-Jr, L. Perassa, J. Leicht, and F. Landgraf, "Anomalous Loss Hysteresis Loop," *Mater. Res.*, vol. 17, no. 2, pp. 494–497, 2014.

[4] D. Dorner, S. Zaefferer, L. Lahn, and D. Raabe, "Overview of Microstructure and Microtexture Development in Grain-oriented Silicon Steel," *J. Magn. Magn. Mater.*, vol. 304, no. 2, pp. 183–186, 2006.

[5] T. Kubota, M. Fujikura, and Y. Ushigami, "Recent progress and future trend on grain-oriented silicon steel," *J. Magn. Magn. Mater.*, vol. 215, pp. 69–73, 2000.

[6] C. Gheorghies and A. Doniga, "Evolution of Texture in Grain Oriented Silicon Steels," *J. Iron Steel Res. Int.*, vol. 16, no. 4, pp. 78–83, 2009.

[7] M. Matsuo, "Review Texture Control in the Production of Grain Oriented Silicon Steels

Grain Oriented Silicon Steels Texture Control for Improved Magnetic Properties," *ISII Int.*, vol. 29, no. lO, pp. 809–827, 1989.

[8] Y. Ushigami, M. Mizokami, M. Fujikura, T. Kubota, H. Fujii, and K. Murakami, "Recent development of low-loss grain-oriented silicon steel," *J. Magn. Magn. Mater.*, vol. 254–255, pp. 307–314, 2003.

[9] N. Takahashi, Y. Suga, and H. Kobayashi, "Recent developments in grain-oriented silicon-steel," *J. Magn. Magn. Mater.*, vol. 160, pp. 98–101, 1996.

[10] T. Nozawa, M. Mizogami, H. Mogi, and Y. Matsuo, "Magnetic properties and dynamic domain behavior in grain-oriented 3 % Si-Fe," *IEEE Trans. Magn.*, vol. 32, no. 2, pp. 572–589, 1996.

[11] M. Imamura and T. Sasaki, "The status of domain theory for an investigation of magnetostriction and magnetization processes in grain-oriented si-fe sheets," *Phys. Scr.*, vol. 1988, no. T24, pp. 29–35, 1988.

[12] M. Imamura, S. Tadashi, and A. Saito, "Magnetization Process and Magnetostriction of a 4% Si-Fe single crystal close to (110)[001]," *Ieee*, vol. 17, no. 5, pp. 2479–2485, 1981.

[13] Z. Xia, Y. Kang, and Q. Wang, "Developments in the production of grain-oriented electrical steel," *J. Magn. Magn. Mater.*, vol. 320, no. 23, pp. 3229–3233, 2008.

[14] S. Chikazumi and C. D. Graham, *Physics of Ferromagnetism 2e*, vol. 94. Oxford University Press on Demand, 2009.

[15] F. Bitter, "Experiments on the nature of ferromagnetism," *Phys. Rev.*, vol. 41, no. 4, pp. 507–515, 1932.

[16] C. A. Fowler Jr and E. M. Fryer, "Magnetic domains on silicon iron by the longitudinal Kerr effect," *Physical Review*, vol. 86, no. 3. p. 426, 1952.

[17] H. J. Williams, F. G. Foster, and E. A. Wood, "Observation of magnetic domains by the Kerr effect," *Phys. Rev.*, vol. 82, no. 1, p. 119, 1951.

[18] C. D. Wright, W. W. Clegg, A. Boudjemline, and N. A. E. Heyes, "Scanning Laser Microscopy of Magneto-Optic Storage Media," *Jpn. J. Appl. Phys.*, vol. 33, no. 4R, pp. 2058–2065, 1994.

[19] H. W. Fuller and M. E. Hale, "Determination of magnetization distribution in thin films using electron microscopy," *J. Appl. Phys.*, vol. 31, no. 2, pp. 238–248, 1960.

[20] M. E. Hale, H. W. Fuller, and H. Rubinstein, "Magnetic Domain Observations by Electron Microscopy," *J. Appl. Phys.*, vol. 30, no. 5, pp. 789–791, 1959.

[21] Y. Zhao, G. C. Wang, and T. M. Lu, "Experimental methods in the physical sciences,"

Charact. Amorph. Cryst. Rough Surf. Princ. Appl., 2001.

[22] M. Gallaugher, N. Brodusch, R. Gauvin, and R. R. Chromik, "Magnetic domain structure and crystallographic orientation of electrical steels revealed by a forescatter detector and electron backscatter diffraction," *Ultramicroscopy*, vol. 142, pp. 40–49, 2014.

[23] T. Yamamoto, H. Nishizawa, and K. Tsuno, "High voltage scanning electron microscopy for observing magnetic domains," *J. Phys. D. Appl. Phys.*, vol. 8, no. 9, pp. 18–21, 1975.

[24] H.-J. BUNGE, *Texture analysis in materials science : mathematical methods*. London: Butterworth-Heinemann, 1982.

[25] V. Randle and O. Engler, *Introduction to Texture analysis: Macrotexture, Microtexture & Orientation Mapping*. Amsterdam: Gordon and Breach Science Publishers, 2000.

[26] N. Bernier, E. Leunis, C. Furtado, T. Van De Putte, and G. Ban, "EBSD study of angular deviations from the Goss component in grain-oriented electrical steels," *Micron*, vol. 54–55, pp. 43–51, 2013.

[27] W. S. Paxton and T. G. Nilan, "Domain configurations and crystallographic orientation in grain-oriented silicon steel," *J. Appl. Phys.*, vol. 26, no. 8, pp. 994–1000, 1955.

[28] S. Shin, R. Schafer, and B. C. De Cooman, “Grain boundary penetration by lancet domains in Fe-3%Si grain-oriented steel,” *IEEE Trans. Magn.*, vol. 46, no. 9, pp. 3574–3581, 2010.

[29] A. N. Bogdanov, *Magnetic Domains. The Analysis of Magnetic Microstructures*, vol. 25, no. 2. Springer Science & Business Media, 1999.

[30] L. J. Dijkstra and U. M. Martius, “Domain pattern in silicon-iron under stress,” *Rev. Mod. Phys.*, vol. 25, no. 1, pp. 146–150, 1953.

[31] O. Perevertov and R. Schäfer, “Magnetic properties and magnetic domain structure of grainoriented Fe-3%Si steel under compression,” *Mater. Res. Express*, vol. 3, no. 9, pp. 1–12, 2016.

[32] R. Peck, C. Olsen, and J. L. Devore, *Introduction to statistics and data analysis*. Boston: Cengage Learning, 2015.

[33] C. M. B. Bacaltchuk, G. A. Castello-Branco, H. Garmestani, and A. D. Rollett, “Effect of magnetic field during secondary annealing on texture and microstructure of nonoriented silicon steel,” *Mater. Manuf. Process.*, vol. 19, no. 4, pp. 611–617, 2004.

[34] M. McCarty, G. L. Houze, and F. A. Malagari, “Texture-Electrical-Property Correlations in Oriented Silicon Steel,” *J. Appl. Phys.*, vol. 38, no. 3, pp. 1096–1098, 1967.

Chapter 5: The Effect of Grain boundaries, Grain Size, Stored Energy and Coincident Site Lattice (CSL) on Goss Abnormal Grain Growth

5.1 Introduction

The unique grain growth behaviour of Goss grains attracted numerous investigations to understand Goss abnormal grain growth during GOES final annealing [1-24]. Some suggested the initial Goss grain size and orientation advantages over other orientations for abnormal grain growth (AGG) occurrence [11,13,22]. It was concluded in early investigations that while the driving force for secondary recrystallisation is the reduction of grain boundary energy, Goss grains have a large grain size compared to the primary annealed grain size [11]. Later, Coincidence site lattice (CSL) grain boundaries with the relation to the development of Goss texture were proposed [12,14–16,23]. It was assumed that Σ9 boundaries have the highest mobility and intensity around Goss grains promotes the abnormal grain growth [15],[16], while other studies included Σ7 as a possible nucleation site for abnormal grain growth where Σ7 is assumed to have higher mobility compared to Σ9 [12]. Likewise, an X-ray investigation showed the relation between abnormal grain growth and the Σ1 boundary in primary annealed samples. The results presented show that large grains have a much higher frequency of Σ1 (low mobility CSL grain boundary), which prevent these grains from undergoing abnormal

grain growth. On the other hand, Goss orientation grains have a significantly lower frequency of Σ1 and average grain size in primary annealed samples. Moreover, Goss grains were not found among the large grains in the primary annealed grains as large grains abnormal growth is inhibited by Σ1 boundaries [23].

On the contrary, the significance of coincident site lattice role on Goss abnormal grain growth was argued [21]. It was concluded that the CSL boundaries are small angle grain boundaries with low energy thus has low mobility. Thus, the high energy grain boundary is proposed, where Goss grains are surrounded by a high frequency of high angle grain boundary misorientation (20°-45°) [20,21,25,26]. These high energy boundaries have high mobility due to its structural defects. Also, the main primary orientation has less 20°-45° misorientation boundaries and more low angle grain boundaries and higher than 45° angles [21]. Besides, CSL boundaries, Σ5 and Σ7 have a low frequency around Goss. Also, Goss abnormal grain growth depends on precipitation (grain growth inhibitors), and the interaction between precipitates and low energy boundaries are stronger than high energy boundaries [21].

Moreover, it was found that general boundaries have a higher diffusion rate in comparison to CSL (coincident site lattice) boundaries, thus the grain boundary mobility is high due to atom exchange at grain boundary vacancies [27]. Even though high energy boundaries theory concentrate on the role played by 20°-45°misorientation angles in Goss abnormal grain growth, more than 50% of the misorientation boundaries are 20°-45°, and only a few grains undergo abnormal grain growth in secondary recrystallisation [28]. Furthermore, other orientation was

found to have a higher intensity of high energy boundaries than Goss that makes high energy boundary mobility to be solely responsible for Goss secondary recrystallisation texture [16]. Recent discussion on the possibility of Goss abnormal grain growth does not depend on grain boundary migration alone, as only a few sharp Goss orientation grains were observed to be abnormally growing [4,28].

With all the arguments mentioned earlier, a later simulation followed by experimental investigation proposed a new theory for Goss abnormal grain growth [7,29–32]. Rather than grain boundary mobility, it was implied that the occurrence of abnormal grain growth phenomenon is caused by solid-state wetting. A crystallographic orientation grows abnormally by solid-state wetting through anisotropic grain boundary energy. When one of the grain boundaries has higher energy than the sum of the other two grain boundaries at the triple junction, a grain grows by liquid phase (wetting) at the triple junction in the direction of the higher energy boundary which is replaced by two lower energy boundaries [31]. It is claimed that the formation of island grains and peninsula grains in the initial stages of abnormal grain growth is simple by solid-state wetting [29],[32]. These grains, island grains and peninsula grains, are the results of the unsatisfactory condition of solid state wetting [31]. Furthermore, it was mentioned that sub-boundaries with misorientation lower than 0.1° within primary annealed grains increase the probability of that grain undergoing abnormal grain growth by solid-state wetting [30,33]. Not to mention that these sub-boundaries are unique characteristics to Goss grains that undergoing abnormal grain growth [30].

Others theorised that stored energy and dislocations that accumulate during cold rolling have a substantial impact on Goss abnormal grain growth [34–38]. It was assumed that grains with low Taylor Factor values and low stored energy consume the adjacent grains with high Taylor Factor values [39]. However, it was shown later that orientations other than Goss also satisfied the solid-state wetting conditions and have low Taylor factor, but they did not grow abnormally. Here, we examined most of these theories and proposed a new mechanism for Goss oriented grain AGG during secondary annealing.

5.2 Results and Discussion

5.2.1 Goss Grain Size advantage During AGG

To validate the size and orientation advantages of Goss grains during AGG, two primary annealed samples with different nitriding conditions were analysed. Following the complete microstructure characterisations of a primary annealed specimen, the sample was then annealed interruptedly at 1030°C/10s and 1070°C/8 min with a heating rate of 0.1°C/sec. These selected temperatures were below the secondary annealing temperature in order to capture the early stage of grain growth.

Sample AA has an average grain size of ~ 20µm, and sample BB has an average grain size ~25µm. It was shown that the average grain size in primary annealed sample is ~20µm and used a threshold of 40µm for large grains. It should be noted that the data were obtained from

a very large EBSD scan area, counting over 50,000 grains. Both samples have a similar grain size average, and the volume fraction of the selected texture component within 20° misorientation analysed after each annealing stage. Figures 5-1a and 5-1b show the overall volume fraction (V.F %) of each of the selected texture component for sample AA Figure 5-1a, and for sample BB Figure 5-1b. It is evident the γ-fibre V.F was the highest during all three annealing conditions for both samples. However, Goss V.F was 3.8%-4% in both samples and was rather low in comparison with Cube 5.2%-5.8% orientation. As the sample annealed, Cube and Brass grain V.F increased whereas Goss and γ-fibre V.F decreased. At this stage, only normal grain growth is observed, and grain size is limited to ~120μm for sample AA and ~90μm for sample BB with an average grain size of ~23μm for both samples. In the early stages of grain growth, normal grain growth is not exclusive to any orientation. Besides, the V.F of Brass and Cube grains indicates the growth of these orientations, whereas the reduction of V.F of Goss grains reduction indicates that some of the Goss grains did not survive at 1070℃.

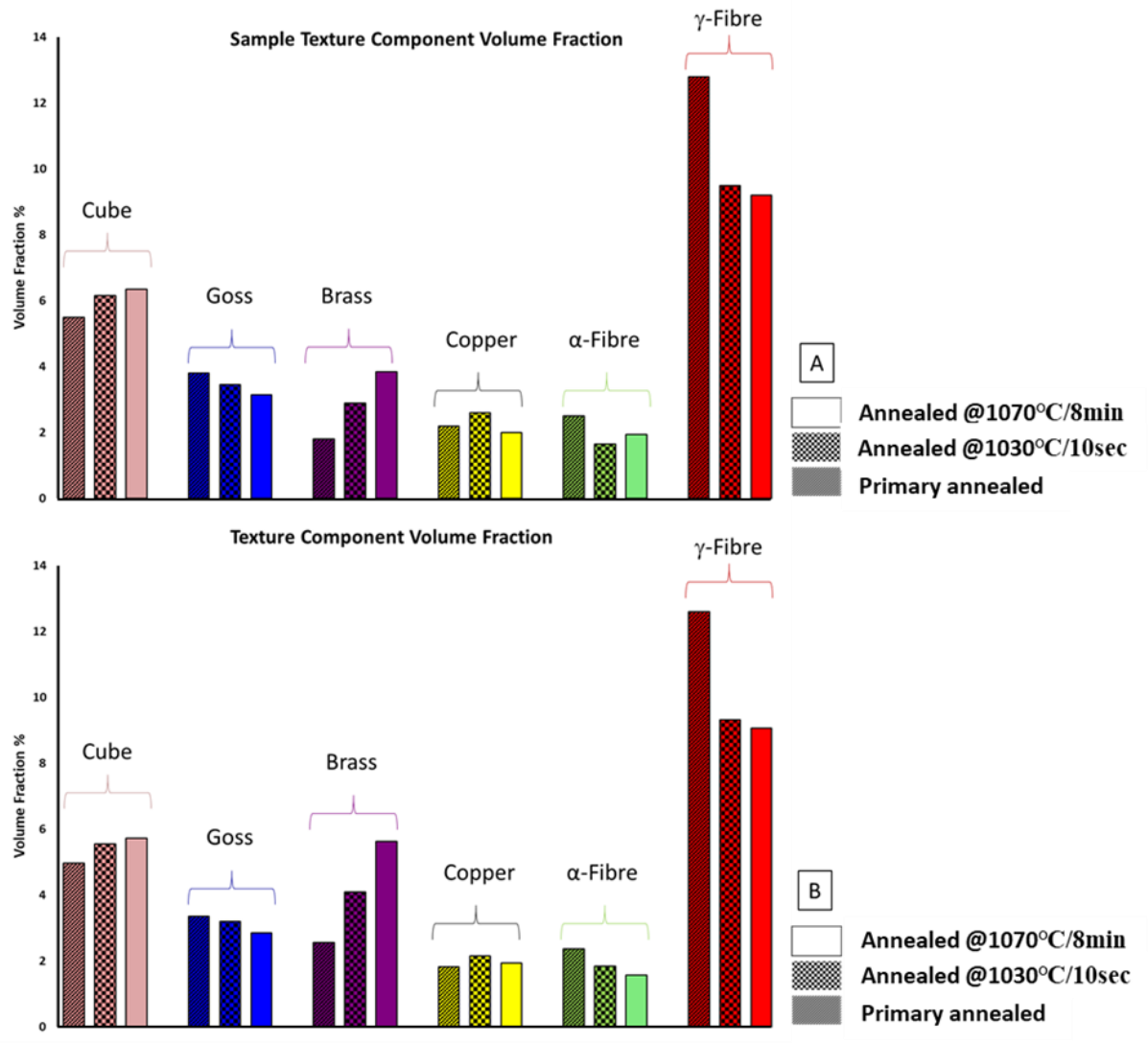

Figure 5-1 The overall volume fraction (V.F %) of selected texture components (Cube, Goss, Brass, Copper, α-fibre, γ-fibre) in primary, 1030°C/10sec and 1070°C/8min annealed specimens, sample AA (a), sample BB (b).

Figure 5-2 shows the grain size distribution of primary annealed sample and 1070℃/8min. It is clear that ~99% of the grains in primary annealed are <40µm in both samples. Also, after annealing, ~94% of the grains are <40µm, therefore a threshold of 40µm for large grains used to analyse orientation evolution.

Using a threshold of 40µm for large grains, texture component volume fraction (V.F %) of grains > 40µm were measured to analyse the effect of annealing on large grains. The volume fraction of both samples AA and BB are shown in Figures 5-3a and 5-3b. The trend changed in comparison to the overall results, the V.F at 1030℃ increased then decrease at 1070℃ with the exception of Cube and α-fibre. The results of grains > 40µm indicate that even though the overall V.F of Goss decreased, the large Goss grains V.F increased. The results clearly show the randomness of normal grain growth as some of the smaller grains consumed or reduced in size at the expense of other grains grow. Also, grain growth and survivability in the early stage of annealing is not exclusive to a specific orientation. In addition, other orientations found to have grains >40µm, and grain size advantage was not exclusive to Goss grains.

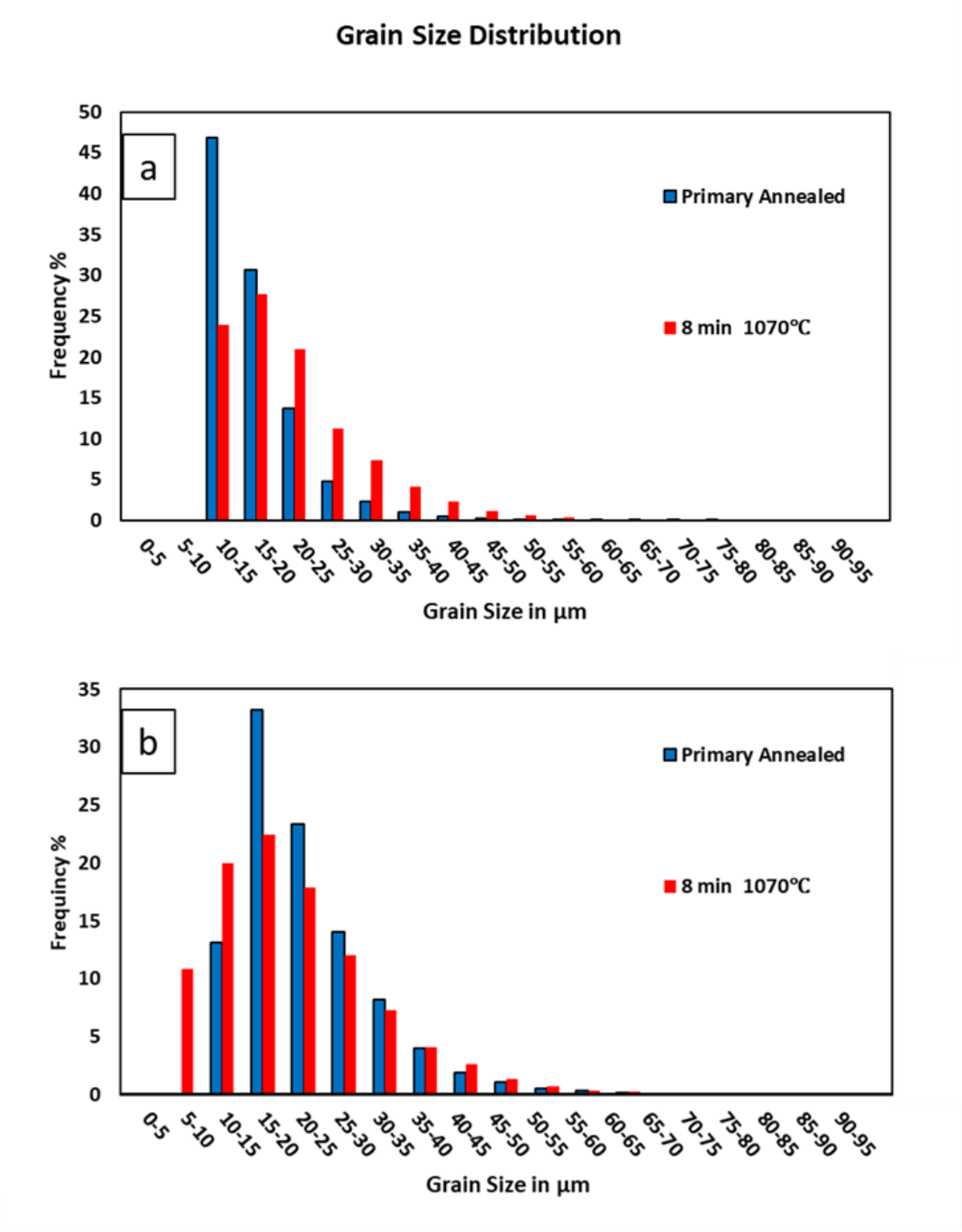

Figure 5-2 The grain size distribution of both primary and 1070℃ annealed samples (a) sample AA, (b) sample BB.

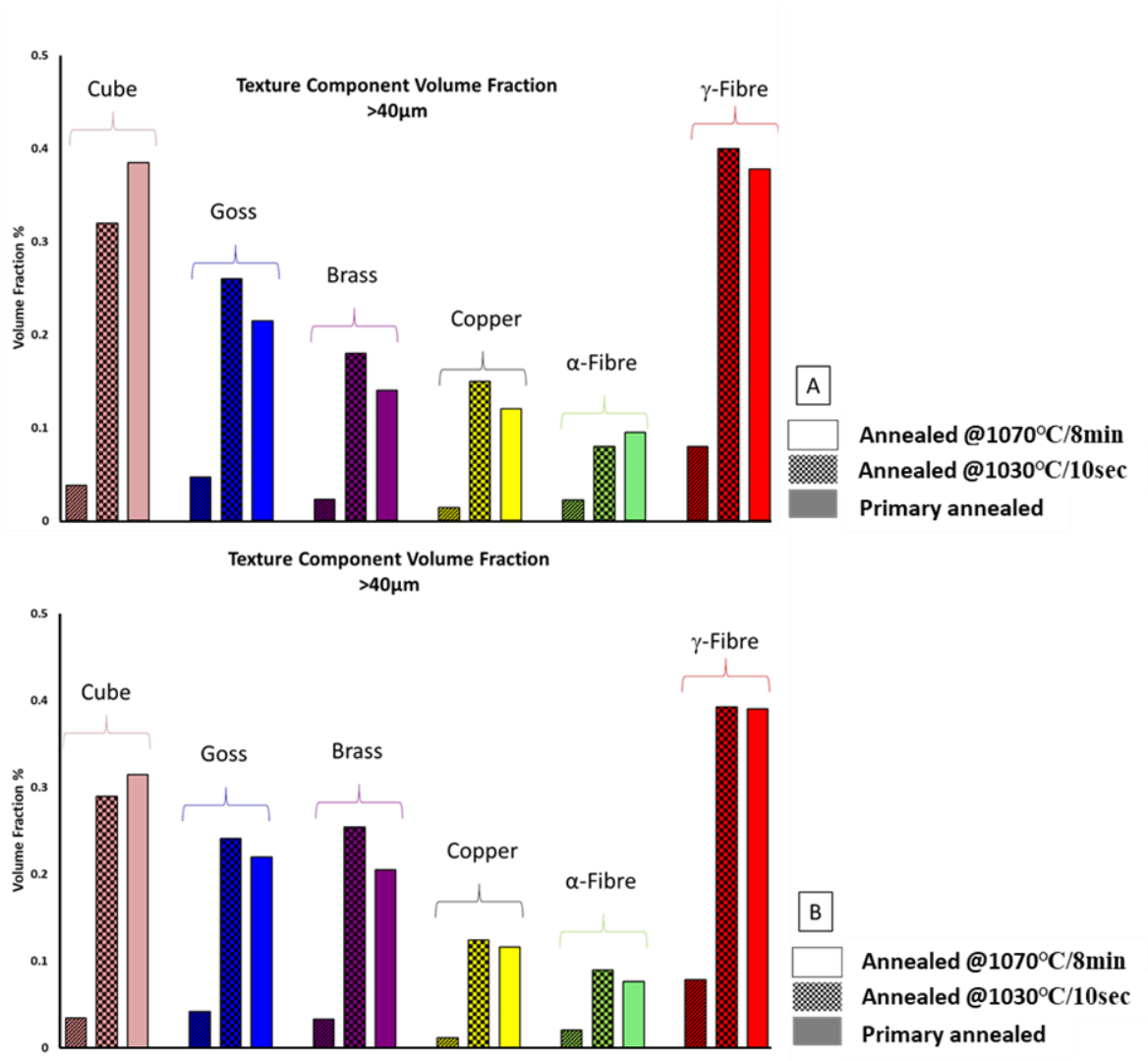

Figure 5-3 Grains >40µm volume fraction (V.F %) of selected texture components (Cube, Goss, Brass, Copper, α-fibre, γ-fibre) in primary, 1030 ℃/10sec and 1070 ℃/8min annealed specimens, sample AA (a), sample BB (b).

This is further demonstrated via microstructure observation in Figure 5-4. As shown in the figure, a selected area of a primary annealed sample AA was characterised by EBSD. The sample was then annealed at 1070°C/8 min, prepared metallographically again, and EBSD scan is performed in the same area (using the coordinate system of EBSD software). The individual grain growth was observed using such a method, and it appears there was no size preference of

Goss grains as they have similar ~ 20 µm size in the primary annealed sample. It was also evident that the Goss grains with a critical size, i.e., >40 µm, in the primary annealed sample had disappeared entirely and eliminated after the annealing at 1070°C/8min, see the dashed blue and red areas in Figure 5-4. Some Goss grains remained relatively constant in size, see Point A and some had grown dramatically from a non-Goss nucleus, see Point B. However, there is a possibility of Goss formation from a very fine Goss nucleus, but this cannot be verified due to the EBSD resolution limitation and 2D observation utilised here. Unexpectedly, the majority of the Goss grains that were larger than surrounding grains were either diminished or unchanged after annealing. Whereas, the majority of the increased grain size over 60 µm, in Figure 5-3, originated from unpredicted areas where Goss was absent, see Figure 5-4. We also examined the grain size distribution, and it was clear from Figure 5-3, no significant difference in the grain size distribution was found between primary annealed and 1070°C samples. As expected, due to the grain growth, the grain size in the range of 10-20 µm was reduced after the 1070°C annealing and an increase was observed for the grains > 20 µm. It is therefore concluded that the grain growth was not exclusive for Goss grains at the early stage of AGG as previously thought, as there was insignificant texture alteration after annealing. Moreover, the V.F and grain size for each texture components were randomly distributed following annealing trials.

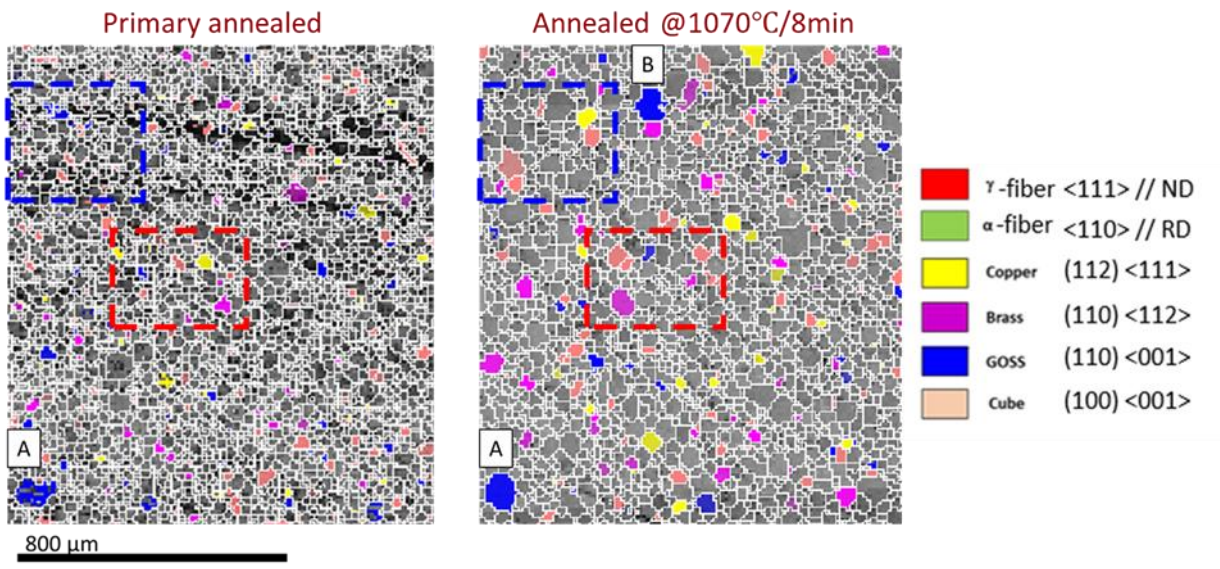

Figure 5-4 EBSD texture component maps for the same area that is marked in primary and 1070°C annealed samples observing the evolution of each oriented grains during early stages of AGG.

5.2.2 Grain Boundary and CSL

In addition to the set of experiments discussed in Section 5.2.1, two extra sets were conducted to examine GB and CSL boundary effects on AGG. To validate the findings, the primary annealed sample was further annealed at 1000 and 1100°C for 20 min to observe the evolution at the later stage of AGG. The evolution of CSL boundaries for primary, 1030°C/10sec and 1070°C/8min annealed samples shown in Figure 5-5.

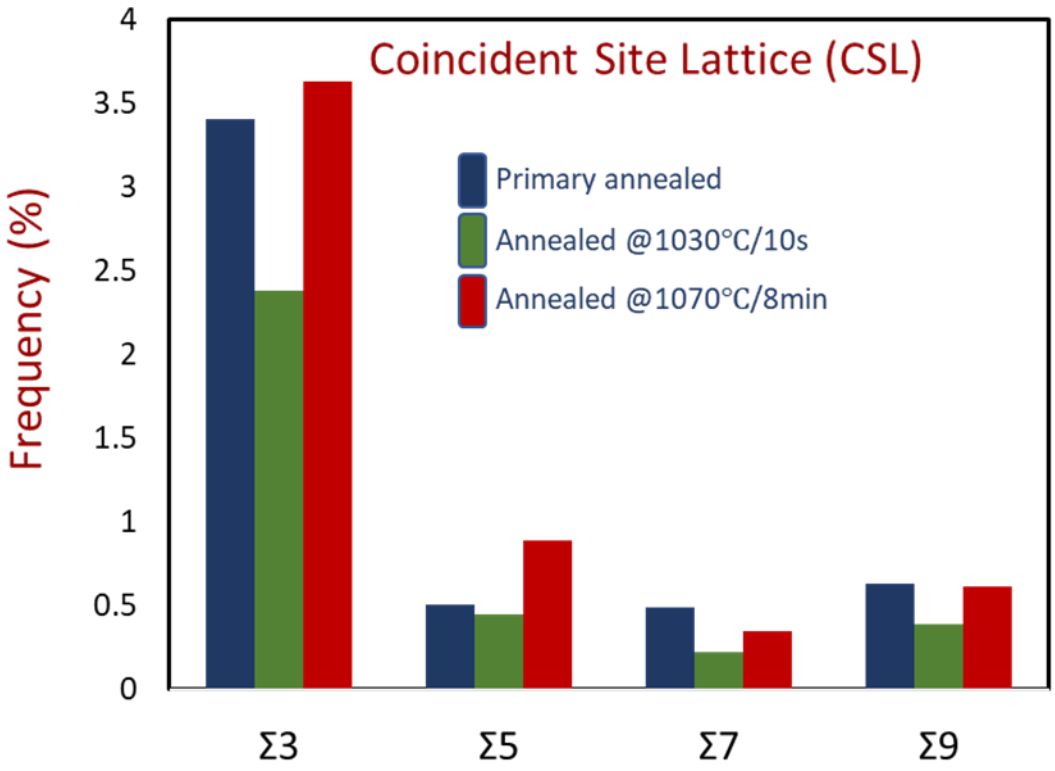

Figure 5-5 Overall volume fraction (%) of CSL boundaries of primary, 1030℃/10sec and 1070℃/8min annealed samples.

Figure 5-5 show Σ3- Σ9 boundaries, in which blue bars represent primary annealed, green bars represent 1030℃/10sec annealed, and red bars represent 1070℃/8min results. The percentage did not change significantly and to validate the findings and observe the evolution at later stages, the primary annealed sample was annealed at 1000℃ and 1100℃ for 20 min. The results were similar to Figure 5-5 as shown in Figure 5-6, and this was a clear indication that CSL boundary evolution was rather random and no specific CSL changed remarkably. The small variations between different CSL percentages were instead a dependant on the original microstructure and initial texture. The increased frequency of Σ9 in Figure 5-6 was due to its high amount in the original sample and its changes during annealing were negligible.

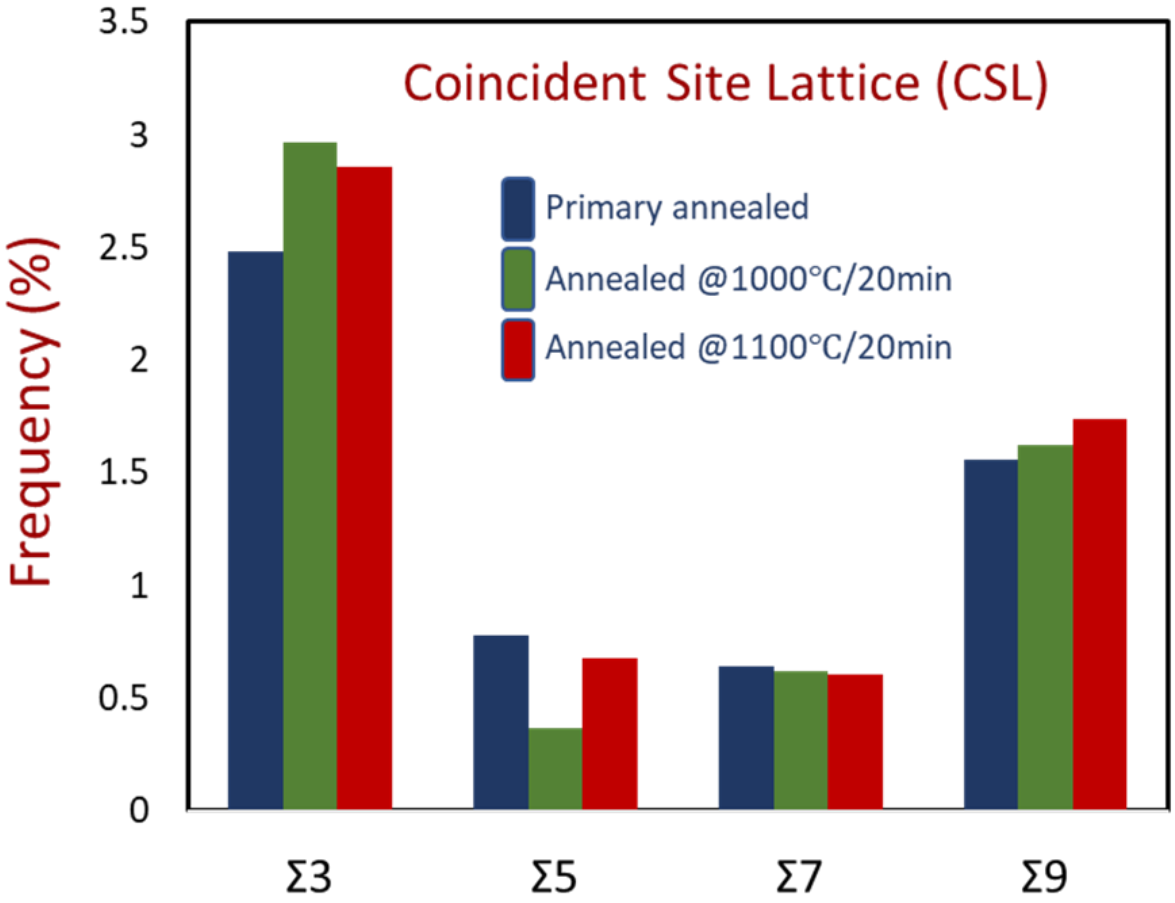

Figure 5-6 Overall volume fraction (%) of CSL boundaries of primary, 1000 ℃/20min and 1100 ℃/20min annealed samples.

The effect of grain boundary angle on grain growth was then investigated through characterising low (< 15°) and high angle (> 15°) grain boundaries, see Figure 5-7. It was clear that high angle grain boundaries (HAGB)s > 25° in primary and secondary annealed samples at 1100°C/20 min was well fitted to the Mackenzie random curve as indicated by the black line over the bar charts. These grain boundaries random distribution was not changed significantly during AGG even at 1100°C/20min. In addition, the microstructure of the primary and 1100°C/20min annealed shown in EBSD IPF//ND maps, see Figures 5-8a and 5-8b. The results

show incomplete secondary recrystallisation at 1100℃/20min, in which 520 island grains were detected inside three abnormal Goss grains. Furthermore, many of the island grains surrounded by 20°-45° grain boundaries survived and resisted abnormal grain growth. Not to mention, the reduction of high angle grain boundaries (20-°45°) was insignificant at this late stage of secondary annealing, see Figure 5-7, indicates a minimum to no contribution in Goss AGG process.

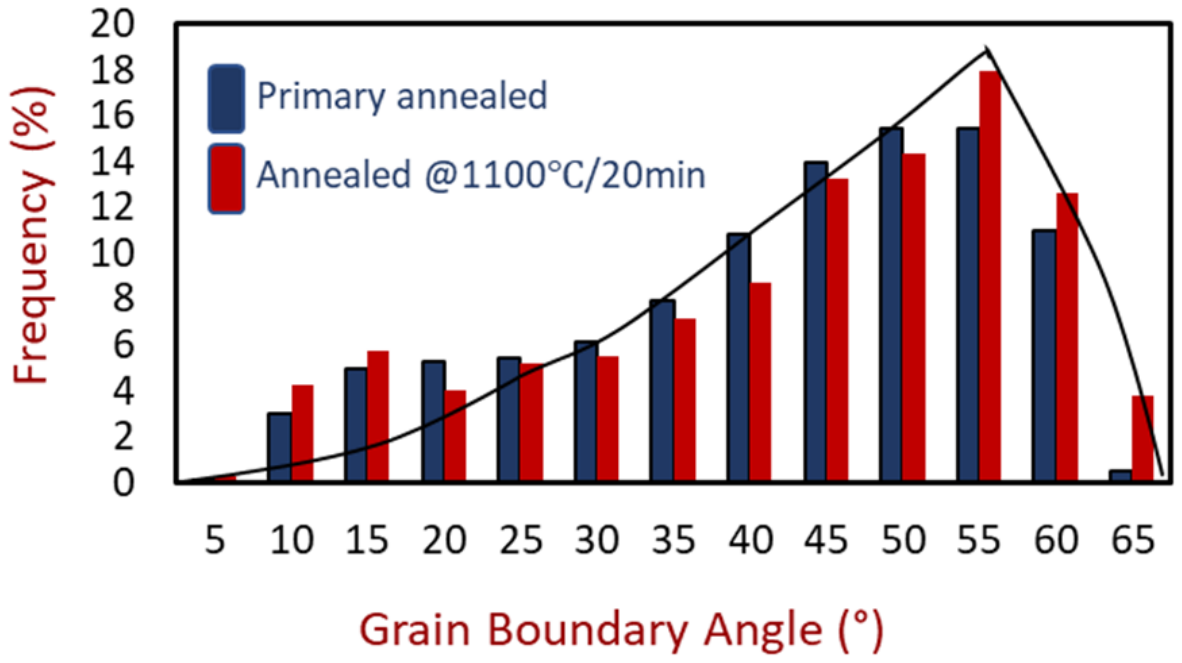

Figure 5-7 Grain boundary distribution of primary and 1100℃/20min annealed samples.

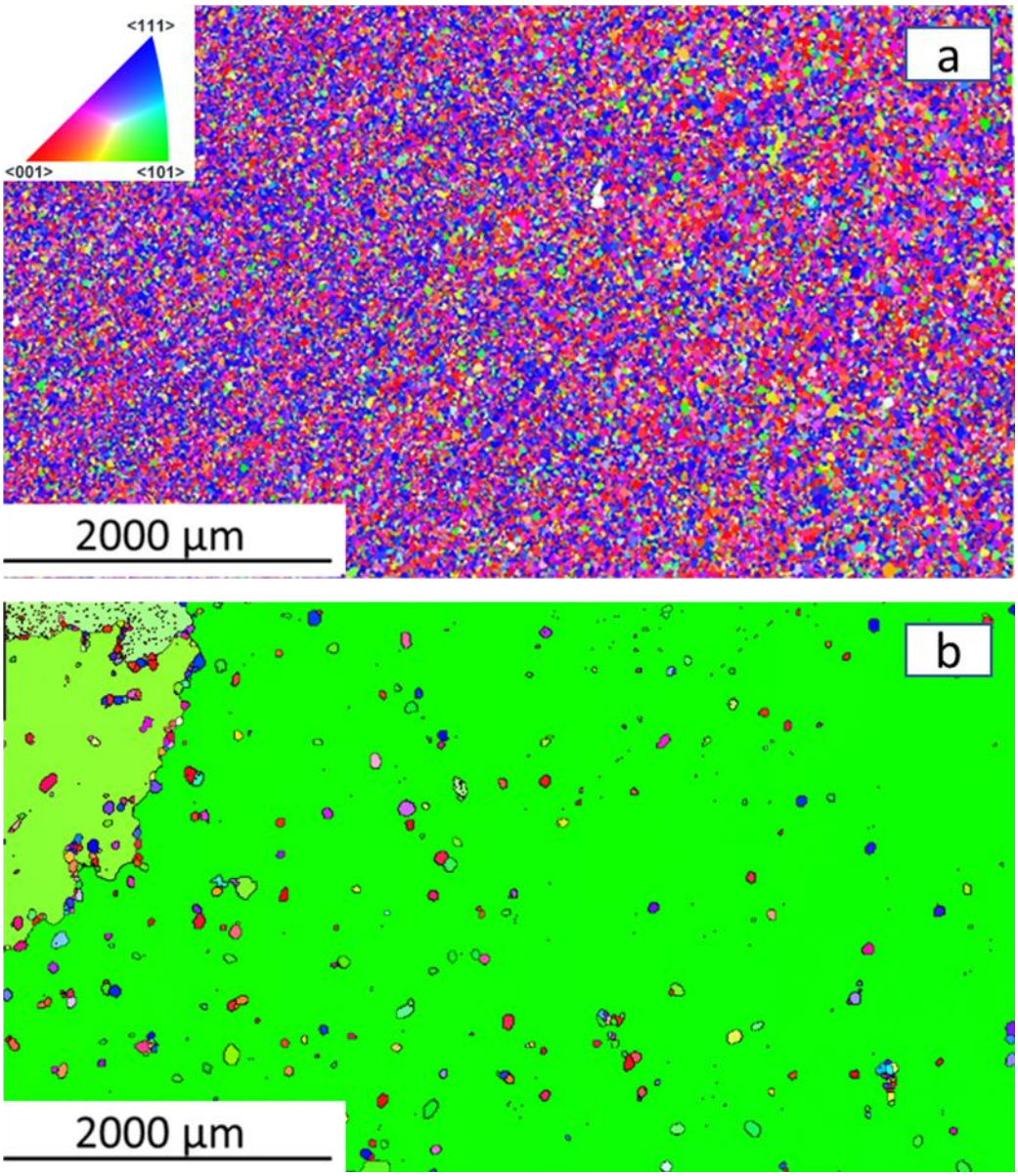

Figure 5-8 EBSD map showing the microstructure of the primary and 1100 ℃/20min samples.

Figure 5-9 shows the Goss grains in blue with general grain boundary angles in (a), and CSL (Σ3- Σ9) boundaries in (b) in the primary annealed sample. Moreover, grain boundary angles and CSL (Σ3-Σ15) volume fraction (%) plotted surrounding each texture components, see Figures 5-10a and 5-10b.

From the statistical analysis of grain boundaries, ~40% of grain boundaries surrounding Goss grains are high angle grain boundaries (20°-45°) as shown in Figure 5-10a. The high volume fraction of high angles grain boundaries was not conclusive to Goss grains as other orientation volume fraction of high angle grain boundaries range from ~38°-44° excluding Copper oriented grains. On the contrary, Goss oriented grains have the highest low angle grain boundaries <20°, ~30% whereas other orientation range from ~12%-25%. It is apparent from Figure 5-9a, microstructurally, and 5-10a, statistically, that Goss grains show no distinct behaviour at this stage. The Goss grains, similar to other orientations, were randomly surrounded by <10°, 10°-20°, 20°-45° and 45°-60° grain boundary misorientation angles. The 20°-45° GBs % V.F around Goss grains was even lower than that for Brass oriented grains in an EBSD scan area of over 10,000 grains; see Figures 5-9a and 5-10a. This observation does not support the 20°-45° HAGB effect on Goss grain AGG phenomenon as previously thought. A similar observation was found concerning CSL boundaries. As can be seen in Figures 5-9b, microstructurally, and Figure 10b, statistically, the CSLs boundaries around Goss grains were somewhat random and in fact, the Σ7 and Σ9 which thought to be responsible for Goss AGG, were lower than that for Cube, Copper and Rotated Cube oriented grains. Furthermore, the calculated energy differences between Σ5, Σ7, Σ9, and Σ11 in literature [40], are very small. It is unreasonable to suggest that this insignificant energy difference is responsible for Goss growth in a range of a few millimetres or even centimetres in some cases. With all the results shown, it can assertively be stated that grain boundary characteristics and CSL types around Goss grains have an insignificant effect on Goss grain growth at the early stage of AGG.

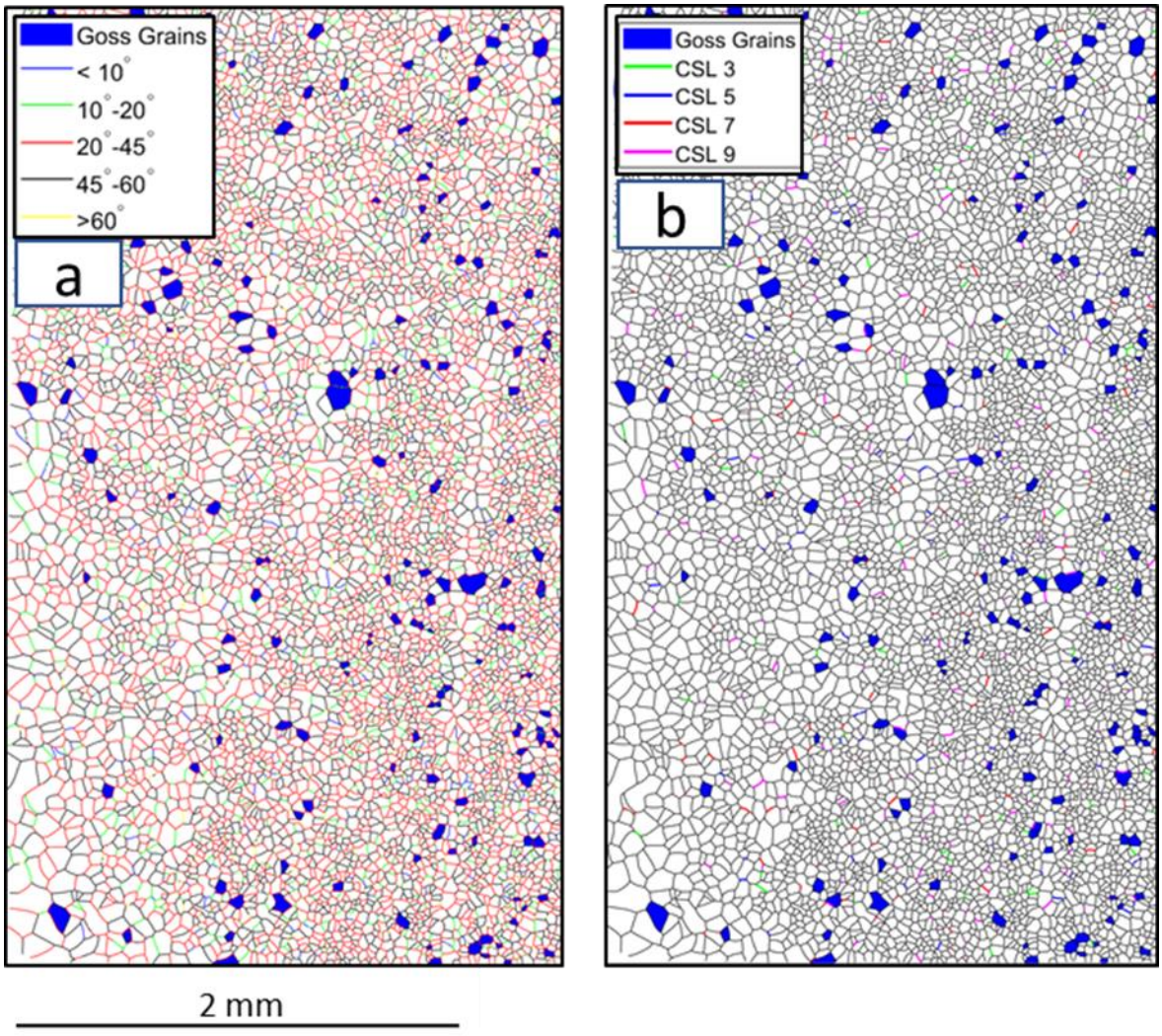

Figure 5-9 EBSD grain boundary angles maps (a), and CSL Σ3-Σ9 map (b) where Goss grains highlighted in blue.

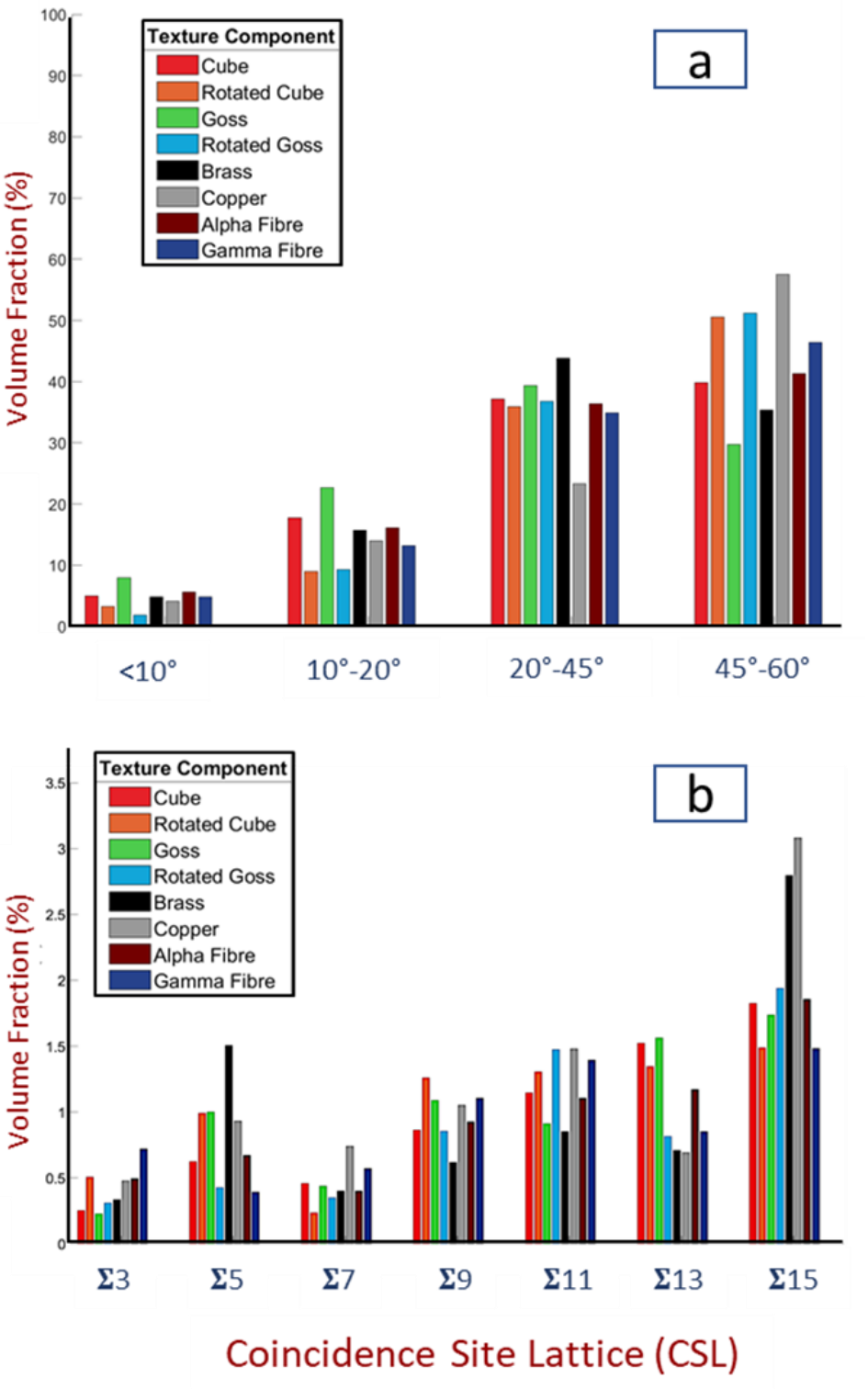

Figure 5-10 The grain boundary misorientation degree (a) and CSL type volume fraction (%) surrounding each orientation.

5.2.3 Dislocation and Taylor factor effect on Goss AGG

A set of experiment was specifically designed to study the effect of deformation degree, dislocation density and stored energy on Goss AGG. A cold rolled 3.2% Si steel (Figure 5-11a) was annealed interruptedly for 3, 4 and 5 minutes as presented at the cross-section of the sample in Figures 5-11b – 5-11d. The calculated Geometrically Necessary Dislocation (GND) maps were calculated for each stage of annealing from EBSD results using MATLAB-MTEX toolbox [41,42], and shown beneath each IPF//RD maps, and the average GND values for each texture component are presented in Figure 5-12. The GND calculation used for the selected orientation is within 15° misorientation.

As shown in Figure 5-11 and Figure 5-12, the α-fibre contains higher GND density than the γ-fibre in the cold-rolled specimen. The ODF in Figure 5-13 shows a high intensity of Rotated Cube texture and α-fibre; hence GND of Rotated Cube is calculated. The α-fibre (including Rotated Cube texture) continued to have a high GND during subsequent annealing, and the majority of GNDs were accumulated in the Rotated Cube texture component that is part of the α-fibre, see Figures 5-11 and 5-12. It appears that the γ-fibre recovered (dislocation annihilation process) and recrystallised considerably faster than the α-fibre during annealing. The GND map and GND chart values of different orientation grains are distributed and evolved rather randomly with annealing time. Also, Goss grains did not have the lowest GND, in fact, the GND values of different orientation were similar. The insignificant difference in Goss grains

average GND values with other orientation and its random changes during annealing can not be responsible for AGG or early Goss growth.

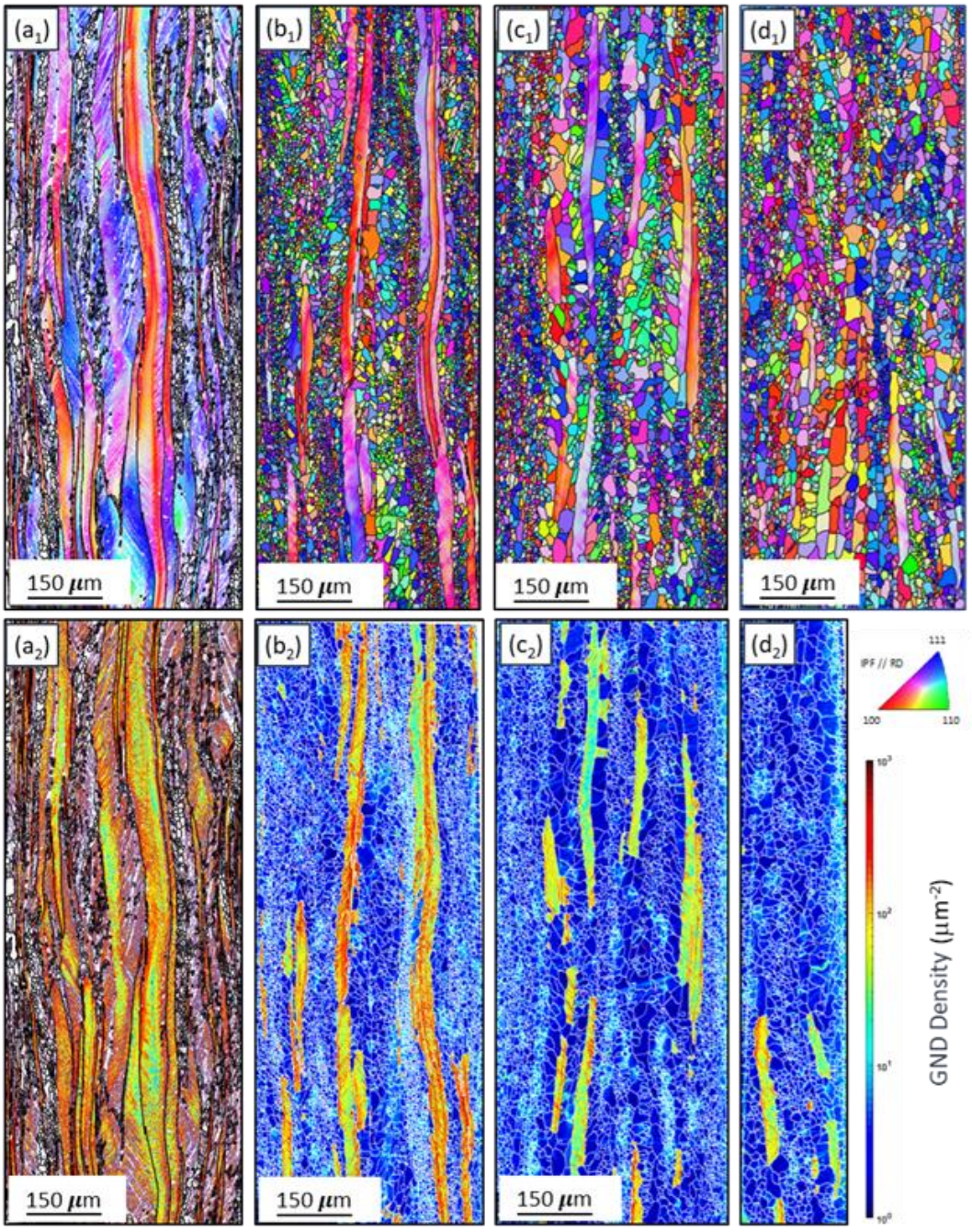

Figure 5-11 EBSD Inverse Pole Figure IPF// Rolling direction (RD) for cold rolled (a1), annealed at 850°C for 3min (b1), annealed for 4min (c1) and annealed for 5min (d1). The calculated GND maps for EBSD maps (a1, b1, c1, d1) shown in (a2, b2, c2, d2) µm/ µm^3.

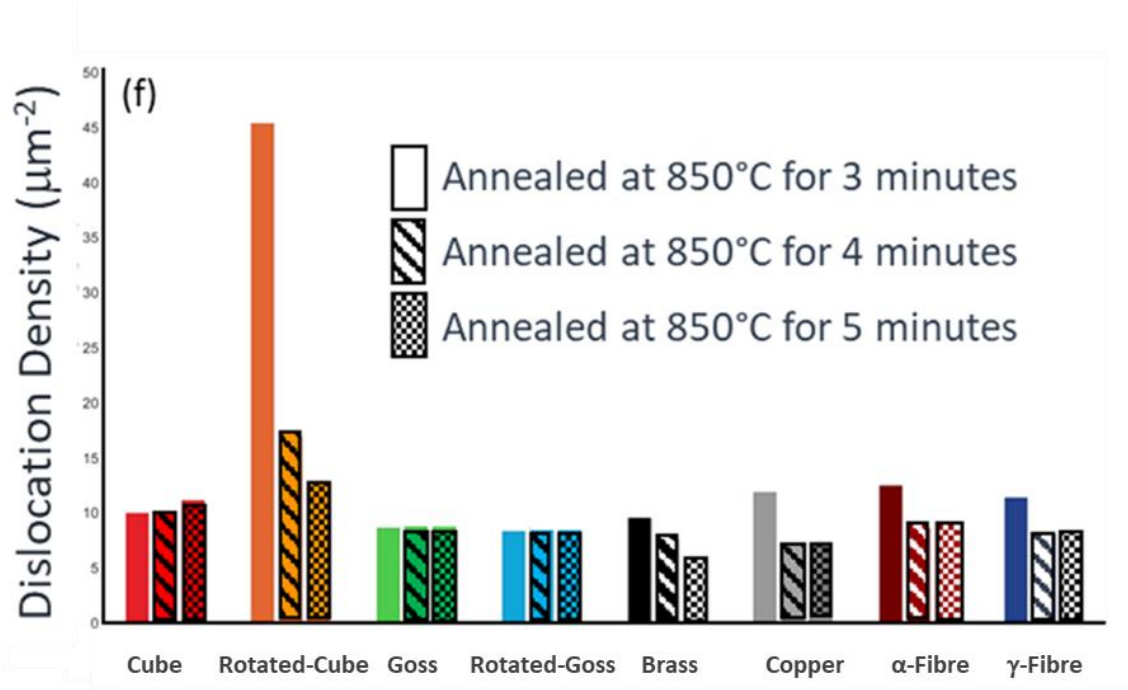

Figure 5-12 The average GND (Geometrically necessary dislocation) values for each texture component for samples annealed at 850℃ for 3min, 4min and 5min.

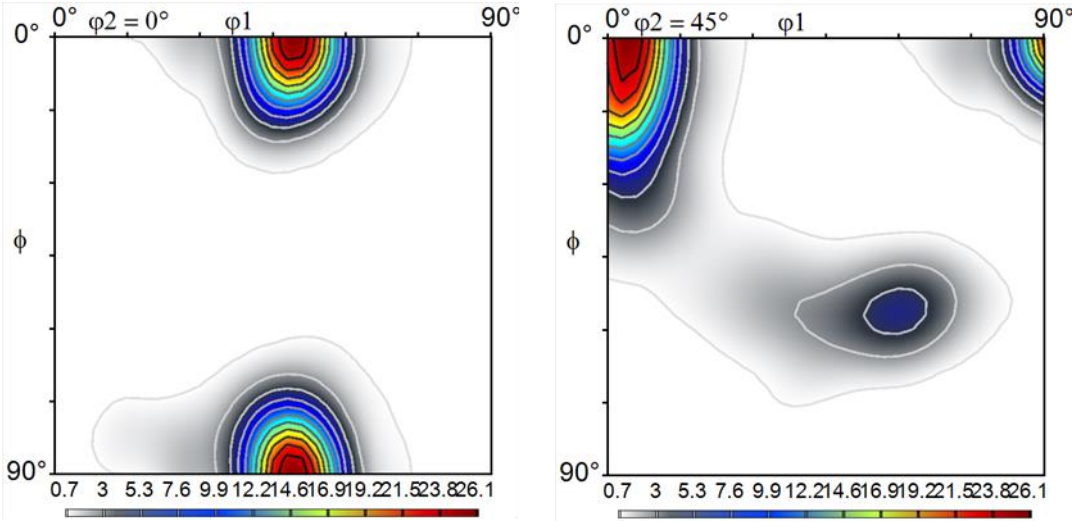

Figure 5-13 Orientation distribution function (ODF) of a cold-rolled sample.

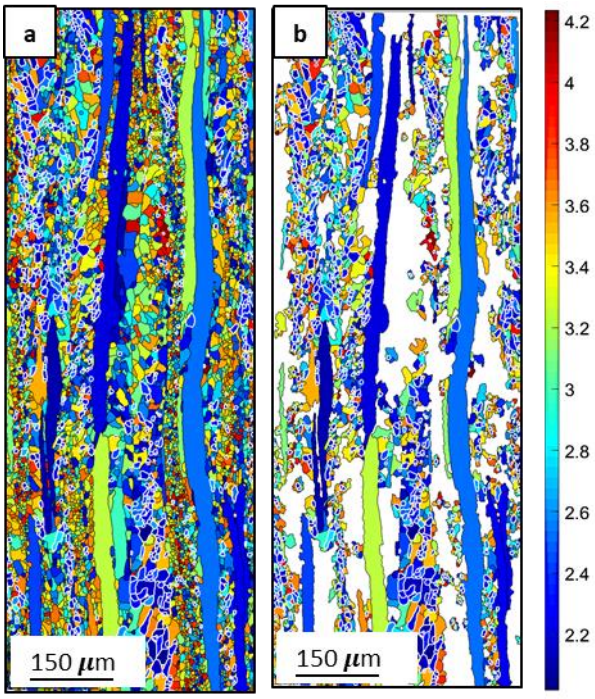

Figure 5-14 Taylor Factor map of EBSD calculated Taylor Factor (a), and Taylor Factor map of Goss neighbouring grains.

Likewise, the Taylor Factor was calculated using the same method as GND calculated (MTEX). The overall Taylor Factor map is shown in Figure 5-14a, and Taylor Factor map of Goss with the adjacent grains shown in Figure 14b are of the sample annealed at 850℃ for 3min (Figure 5-11b). The similarity of Taylor Factor values to GND can be seen in Figure 5-14, the Taylor factor values for different orientation grains are also distributed randomly.

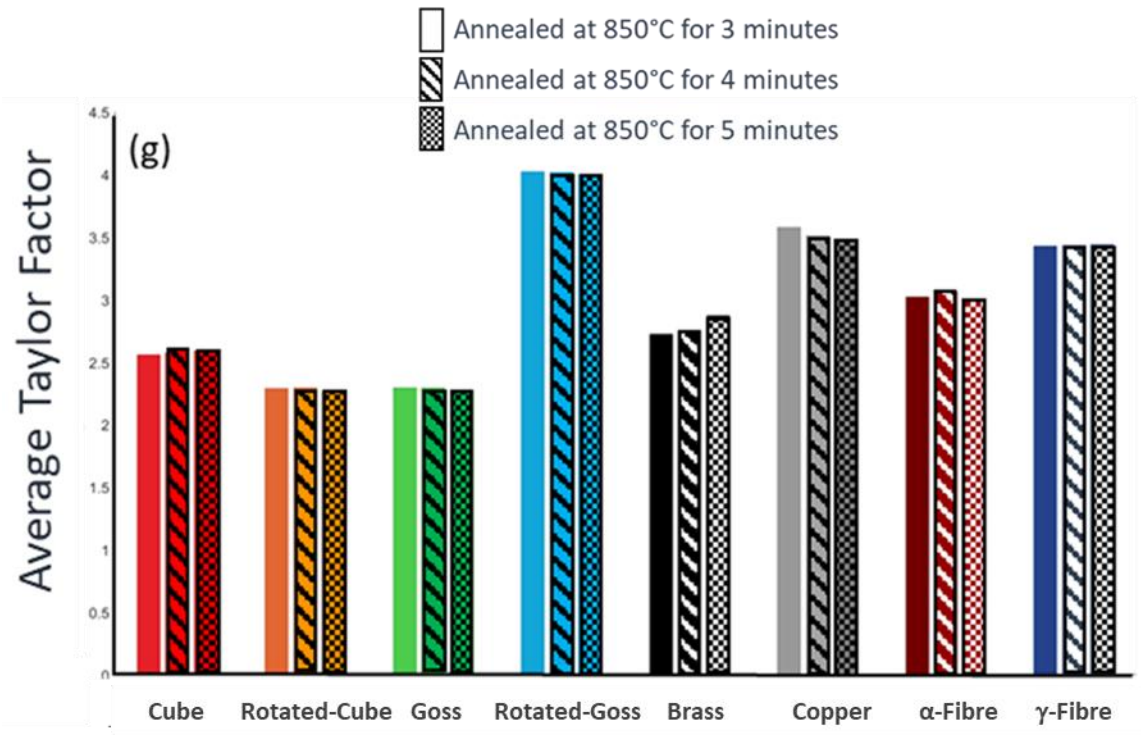

Figure 5-15 The average Taylor Factor values of each texture components for the samples of each texture component annealed at 850℃ for 3min, 4min and 5min.

To validate the assumption that nor Goss, the low Taylor Factor and low GND, surrounded by high Taylor Factor and high GND grains is responsible for AGG, the Goss neighbouring grain volume fractions plot is shown in Figure 5-16. It was evident that this assumption was not correct as reported in the literature as the Goss grains were equally neighbouring high and low Taylor Factor grains. Moreover, Goss grains seems to have larger numbers of Goss neighbours than Rotated Cube (high GND) or Rotated Goss, Cube and Copper (high Taylor Factor values). This set of experiments clearly showed that Goss's low Taylor Factor and GND could change during primary annealing and its differences with other orientations are insignificant for Goss AGG.

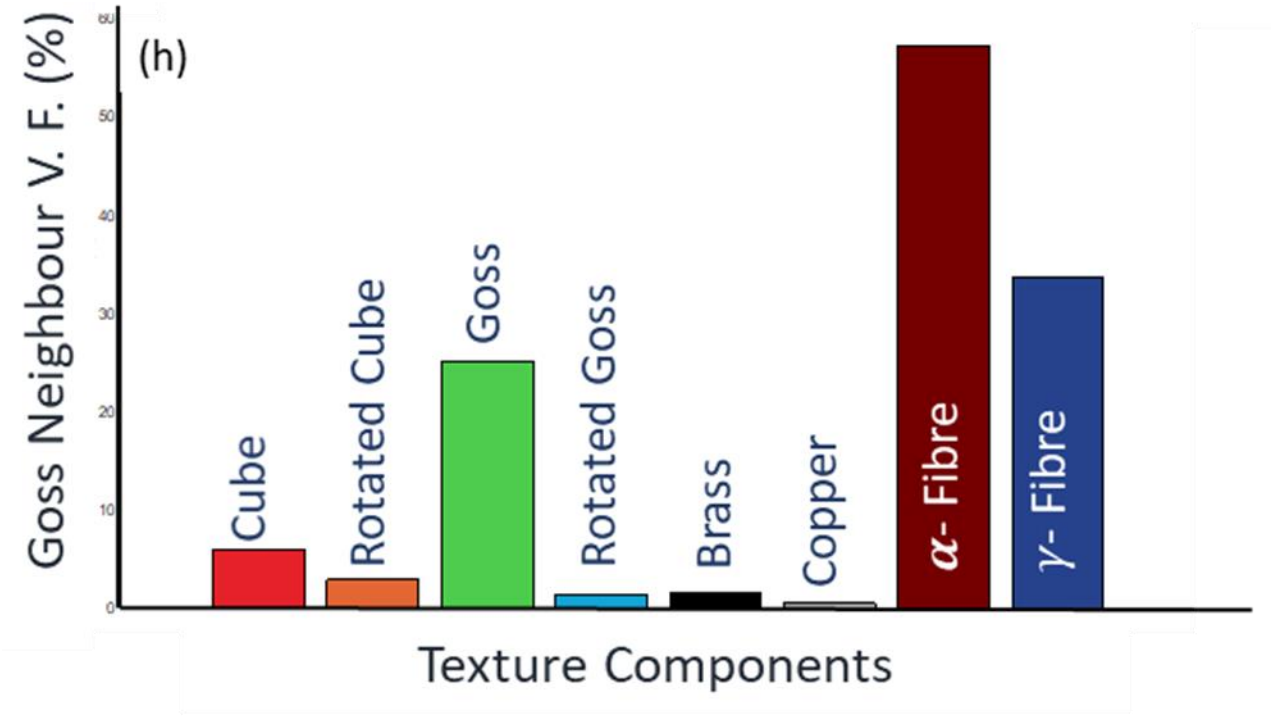

Figure 5-16 The statistical distribution of Goss neighbouring grains volume fraction (%).

5.3 Conclusion

The initial stage of Goss abnormal grain growth was investigated, where two primary annealed samples with different nitrogen (N) content. Interrupted annealing tests were carried at 1030℃/10sec and 1070℃/8min, where the volume fraction of selected orientations were extracted from EBSD data. The result show γ-fibre to have the highest volume fraction and Goss to have a rather low volume fraction. Furthermore, Goss grain volume fraction of large grains, >40μm, have similar volume fraction to other orientations in primary annealed samples. After annealing, all orientations undergo normal grain growth and Cube orientation and γ-fibre

have the highest overall volume fraction and the highest volume fraction for grains >40μm. Also, annealing at 1070℃ for 8 min show higher volume fraction of large Cube grains and large Goss grains (>40) disappeared whereas small grains show a higher growth rate.

An additional experiment was carried out to investigate the role of grain boundaries and CSL on Goss abnormal grains growth. Two samples were annealed at 1000℃ and 1100℃ for 20 min, where the grain boundaries and CSL evolution plot show random behaviour. Also, the distribution of these boundaries volume fraction surrounding selective orientations were plotted. The result shows a random distribution of grain boundaries and CSL, and also Goss grains have a similar volume fraction of high angle grain boundaries and CSL in comparison to other orientations. Moreover, the misorientation histogram shows an insignificant reduction in high angle grain boundaries after annealing at 1100℃ for 20 min, indicating an equal reduction rate of grain boundaries at the early stages of abnormal grain growth. Despite the observations reported in the literature claiming that Goss grains have a high percentages of high angle grains boundaries or Σ9 / Σ7, statistical analysis of more than 50,000 grains shows that it is not exclusive to Goss grains and other orientations have a similar or higher volume fraction of these grain boundaries.

The influence of GND and Taylor Factor was studied in an interrupted annealed test at 850℃ for 3min, 4min and 5min. It was found that the γ-fibre recovered and recrystallisation rate is faster in comparison to the α-fibre. In contrast, α-fibre continues to have high GND accumulated in Rotated Cube and low recovery and recrystallisation. In addition, Goss average

GND was similar to other orientation during different annealing stages. Beside, GND grains (high and low) and high Taylor Factor grains were found to be randomly distributed around Goss. Also, the Goss grains found to be neighbouring other Goss grains at higher volume fraction and the assumption of stored energy and low Taylor Factor Goss grains consuming high Taylor Factor grains was not satisfactory.

References

[1] D. Dorner, L. Lahn, S. Zaefferer, Investigation of the Primary Recrystallisation Microstructure of Cold Rolled and Annealed Fe 3% Si Single Crystals with Goss Orientation, in: Recryst. Grain Growth, Trans Tech Publications, 2004: pp. 129–134. doi:10.4028/www.scientific.net/MSF.467-470.129.

[2] A. Morawiec, On abnormal growth of Goss grains in grain-oriented silicon steel, Scr. Mater. 64 (2011) 466–469. doi:10.1016/j.scriptamat.2010.11.013.

[3] V. Randle, B. Ralph, Interactions of grain boundaries with coherent precipitates during grain growth, Acta Metall. 34 (1986) 891–898. doi:10.1016/0001-6160(86)90062-3.

[4] N. Chen, S. Zaefferer, L. Lahn, K. Günther, D. Raabe, Effects of topology on abnormal grain growth in silicon steel, Acta Mater. 51 (2003) 1755–1765. doi:10.1016/S1359-6454(02)00574-8.

[5] Y. Wang, Y. Xu, Y. Zhang, S. Xie, Y. Yu, G. Wang, On abnormal growth of {210}<001> grain in grain-oriented silicon steel, Mater. Res. Bull. 69 (2015) 138–141. doi:10.1016/j.materresbull.2014.12.022.

[6] N. Chen, S. Zaefferer, L. Lahn, K. Günther, D. Raabe, Abnormal Grain Growth in Silicon Steel, Mater. Sci. Forum. 408–412 (2002) 949–954. doi:10.4028/www.scientific.net/MSF.408-412.949.

[7] K.J. Ko, P.R. Cha, D. Srolovitz, N.M. Hwang, Abnormal grain growth induced by sub-

boundary-enhanced solid-state wetting: Analysis by phase-field model simulations, Acta Mater. 57 (2009) 838–845. doi:10.1016/j.actamat.2008.10.030.

[8] K.-J. Ko, J.-T. Park, J.-K. Kim, N.-M. Hwang, Morphological evidence that Goss abnormally growing grains grow by triple junction wetting during secondary recrystallization of Fe–3% Si steel, Scr. Mater. 59 (2008) 764–767. doi:https://doi.org/10.1016/j.scriptamat.2008.06.021.

[9] N.M. Hwang, Simulation of the effect of anisotropic grain boundary mobility and energy on abnormal grain growth, J. Mater. Sci. 33 (1998) 5625–5629.

[10] H.-K. Park, S.-D. Kim, S.-C. Park, J.-T. Park, N.-M. Hwang, Sub-boundaries in abnormally growing Goss grains in Fe–3% Si steel, Scr. Mater. 62 (2010) 376–378. doi:https://doi.org/10.1016/j.scriptamat.2009.11.025.

[11] C.G. Dunn, Secondary recrystallization textures and their origin in cold-rolled single crystals of silicon iron, Acta Metall. 1 (1953) 163–175. doi:10.1016/0001-6160(53)90055-8.

[12] J. Harase, R. Shimizu, Coincidence grain boundary and (100)[011] secondary recrystallization in Fe-3% Si, Acta Metall. Mater. 40 (1992) 1101–1111. doi:10.1016/0956-7151(92)90088-V.

[13] M. Hillert, On the theory of normal and abnormal grain growth, Acta Metall. 13 (1965) 227–238. doi:10.1016/0001-6160(65)90200-2.

[14] J. Harase, R. Shimizu, D.J. Dingley, Texture evolution in the presence of precipitates in Fe-3% Si alloy, Acta Metall. Mater. 39 (1991) 763–770. doi:10.1016/0956-

7151(91)90276-7.

[15] G. Britain, P. Press, O. Cedex, Evolution of local texture and grain boundary characteristics during secondary recrystallisation of Fe-3% Si sheets., 38 (1990) 1101–1107.

[16] J. Harase, R. Shimizu, J.K. Kim, J.S. Woo, The role of high energy boundaries and coincidence boundaries in the secondary recrystallization of grain-oriented silicon steel, Met. Mater. Int. 5 (1999) 429–435. doi:10.1007/BF03026155.

[17] N.C. Pease, D.W. Jones, M.H.L. Wise, W.B. Hutchinson, SEM study of origin of Goss texture in Fe-3.25Si, Met. Sci. 15 (1981) 203–209. doi:10.1179/030634581790426642.

[18] E.A. Holm, T.D. Hoffmann, A.D. Rollett, C.G. Roberts, Particle-assisted abnormal grain growth, in: IOP Conf. Ser. Mater. Sci. Eng., 2015: p. 12005.

[19] F. Citrawati, M.Z. Quadir, P.R. Munroe, Investigation on the Early Stages of Growth of Secondary Grains in a Grain Oriented Silicon Steel, Procedia Eng. 184 (2017) 750–755. doi:10.1016/j.proeng.2017.04.153.

[20] C. Su, G. Zhao, H. Xiao, Y. Lan, F. Huang, Abnormal Grain Growth of Hi--B Steel in the Secondary Recrystallization, Metallogr. Microstruct. Anal. 7 (2018) 608–617. doi:10.1007/s13632-018-0467-9.

[21] Y. Hayakawa, J.A. Szpunar, A new model of Goss texture development during secondary recrystallization of electrical steel, Acta Mater. 45 (1997) 4713–4720. doi:10.1016/S1359-6454(97)00111-0.

[22] J.E. Burke, D. Turnbull, Recrystallization and grain growth, Prog. Met. Phys. 3 (1952) 220–292. doi:https://doi.org/10.1016/0502-8205(52)90009-9.

[23] R. Shimizu, J. Harase, Coincidence grain boundary and texture evolution in Fe-3%Si, Acta Metall. 37 (1989) 1241–1249. doi:10.1016/0001-6160(89)90118-1.

[24] B. Ralph, K.B. Shim, Z. Huda, J. Furley, M.J. Edirisinghe, The effects of particles and solutes on grain boundary migration and grain growth, in: Mater. Sci. Forum, 1992: pp. 129–140.

[25] Y. Hayakawa, J.A. Szpunar, The role of grain boundary character distribution in secondary recrystallization of electrical steels, Acta Mater. 45 (1997) 1285–1295. doi:10.1016/S1359-6454(96)00251-0.

[26] A.L. Etter, T. Baudin, R. Penelle, Influence of the Goss grain environment during secondary recrystallisation of conventional grain oriented Fe-3%Si steels, Scr. Mater. 47 (2002) 725–730. doi:10.1016/S1359-6462(02)00189-6.

[27] B. Ralph, K.B. Shim, Z. Huda, J. Furley, M.J. Edirisinghe, The Effects of Particles and Solutes on Grain Boundary Migration and Grain Growth, Mater. Sci. Forum. 94–96 (1992) 129–140. doi:10.4028/www.scientific.net/MSF.94-96.129.

[28] A. Morawiec, Grain misorientations in theories of abnormal grain growth in silicon steel, Scr. Mater. 43 (2000) 275–278.

[29] K.J. Ko, J.T. Park, J.K. Kim, N.M. Hwang, Morphological evidence that Goss abnormally growing grains grow by triple junction wetting during secondary recrystallization of Fe-3% Si steel, Scr. Mater. 59 (2008) 764–767.

doi:10.1016/j.scriptamat.2008.06.021.

[30] H.K. Park, S.D. Kim, S.C. Park, J.T. Park, N.M. Hwang, Sub-boundaries in abnormally growing Goss grains in Fe-3% Si steel, Scr. Mater. 62 (2010) 376–378. doi:10.1016/j.scriptamat.2009.11.025.

[31] K.J. Ko, P.R. Cha, N.M. Hwang, Phase Field Model Simulation of Abnormal Grain Growth by Solid-State Wetting, in: THERMEC 2006, Trans Tech Publications, 2007: pp. 2557–2563. doi:10.4028/www.scientific.net/MSF.539-543.2557.

[32] K.J. Ko, P.R. Cha, J.T. Park, J.K. Kim, N.M. Hwang, Abnormal Grain Growth of Fe-3%Si Steel Approached by Solid-State Wetting Mechanism, Adv. Mater. Res. 26–28 (2007) 65–68. doi:10.4028/www.scientific.net/AMR.26-28.65.

[33] S. Suzuki, Y. Ushigami, Y. Suga, N. Takahashi, Microstructures in Secondary Recrystallized {100}<001> Grains of 3%Si-Fe, Mater. Sci. Forum. 204–206 (1996) 575–580. doi:10.4028/www.scientific.net/MSF.204-206.575.

[34] L. Kestens, J.J. Jonas, Modeling texture change during the static recrystallization of interstitial free steels, Metall. Mater. Trans. A. 27 (1996) 155–164.

[35] J.K. Kim, J.S. Woo, S.K. Chang, Influence of annealing before cold rolling on the evolution of sharp goss texture in Fe-3%Si alloy, J. Magn. Magn. Mater. 215 (2000) 162–164. doi:10.1016/S0304-8853(00)00103-7.

[36] S.H. Choi, Y.S. Jin, Evaluation of stored energy in cold-rolled steels from EBSD data, Mater. Sci. Eng. A. 371 (2004) 149–159. doi:10.1016/j.msea.2003.11.034.

[37] S.F. Castro, J. Gallego, F.J.G. Landgraf, H.-J. Kestenbach, Orientation dependence of stored energy of cold work in semi-processed electrical steels after temper rolling, Mater. Sci. Eng. A. 427 (2006) 301–305. doi:https://doi.org/10.1016/j.msea.2006.04.092.

[38] S.K. Chang, Texture change from primary to secondary recrystallization by hot-band normalizing in grain-oriented silicon steels, Mater. Sci. Eng. A. 452–453 (2007) 93–98. doi:https://doi.org/10.1016/j.msea.2006.10.118.

[39] S.M. Shin, S. Birosca, S.K. Chang, B.C. De Cooman, Texture evolution in grain-oriented electrical steel during hot band annealing and cold rolling, J. Microsc. 230 (2008) 414–423.

[40] S. Ratanaphan, D.L. Olmsted, V. V Bulatov, E.A. Holm, A.D. Rollett, G.S. Rohrer, Grain boundary energies in body-centered cubic metals, Acta Mater. 88 (2015) 346–354. doi:https://doi.org/10.1016/j.actamat.2015.01.069.

[41] F. Bachmann, R. Hielscher, P.E. Jupp, W. Pantleon, H. Schaeben, E. Wegert, Inferential statistics of electron backscatter diffraction data from within individual crystalline grains, J. Appl. Crystallogr. 43 (2010) 1338–1355. doi:10.1107/S002188981003027X.

[42] R. Hielscher, H. Schaeben, A novel pole figure inversion method: Specification of the MTEX algorithm, J. Appl. Crystallogr. 41 (2008) 1024–1037. doi:10.1107/S0021889808030112.

Chapter 6: Neutron Diffraction Investigation of Goss Abnormal Grain Growth in GOES

6.1 Introduction

In this chapter, annealing temperature and heating rate effect on secondary recrystallisation texture investigated via in-situ neutron diffraction test. Peak analysis was carried out, and the correlation between d-spacing change and Goss abnormal grain growth was investigated. Also, low and high heating rates effects on precipitates and texture evolution was studied.

During GOES primary annealing, the precipitations dispersed uniformly across the steel sheet, which inhibits the grain growth by pinning the grain boundary at the early stage of secondary recrystallisation [1]. According to Liu et al., the original texture of primary annealed steel characterisation has a significant effect on secondary recrystallisation [2]. In addition to primary texture and precipitation, the distribution and the size of AlN is crucial to achieving the desired secondary recrystallisation texture [3]. Also, the importance of γ-fibre in primary recrystallised grain oriented silicon steel has been extensively studied [2], [4], [5]. Furthermore, the γ-fibre texture component {112} <111> is easily consumed by Goss oriented grains, ensuring the success of Goss abnormal grain growth. In general, a strong γ-fibre in primary annealed samples results in strong secondary recrystallisation texture. On the other hand, the

efficiency of precipitates pinning the grain boundaries and promoting secondary recrystallisation texture is controlled by annealing conditions. Since the dissolving of precipitates depends on the annealing temperature, the heating condisions including annealing temperature and heating rate should be considered. Furthermore, with extremely high annealing temperature, the dissolution of precipitates is accelerated, and other orientations grow abnormally, thus Goss losses its advantage to grow [6], [7]. Therefore, annealing at the right temperature promotes sharp Goss grain growth and prohibits other orientations from abnormal grain growth [8].

6.2 Experimental procedure

The materials used in this experiment were commercial 3.2% Si-Fe grain oriented silicon steel, supplied by Cogen Power in Newport, UK. The specimens supplied were processed in a commercial facility to the decarburisation stage (primary annealed) with different nitriding conditions and Al content. The chemical composition is shown in Table 3.2, see Section 3.1.

The experiments were conducted using the neutron diffraction facility at Rutherford Appleton Laboratory, ISIS facility at Oxford, UK using GEM beamline. In-situ annealing was carried out at different temperatures and heating rate. The data was collected from room temperature (RT) to 1200℃ every 2 mins at a heating rate of 50℃/min (0.83℃/sec) and 10℃/min (0.17℃/sec). MAUD (Material Analysis Using Diffraction) software was used to analyse the

data acquired, diffraction peaks fitting, peak position analysis, d-spacing expansion calculation and AlN volume [9], [10]. After peak fitting and refinement, pole figures were exported, and MATLAB-MTEX toolbox was used to generate ODF (Orientation Distribution Function) [11].

6.3 Results and Discussion

6.3.1 Neutron diffraction Peak Analyses

Neutron diffraction obtained data of sample CC and sample DD in-situ annealing results of heating rate 50℃/min shown in Figure 6-1a and Figure 6-1b, respectively. Sample CC neutron diffraction peaks in-situ annealing results of heating rate 10℃/min are shown in Figure 6-2. The data was collected after annealing for 10 min at each temperature. The peak intensity is the highest for (110) followed by (211) then (200) at RT up to 1040℃, as shown in Figure 6-1 and Figure 6-2. As the temperature increase, the intensity is slightly reduced, and the diffraction peaks start to shift to higher d-spacing. The shifting in the peaks is a sign of lattice thermal expansion, as stated in [12] and [13]. As the temperature increased to 1070℃, (110) intensity decreases and the width increases compared to (211) and (200) which show no noticeable change in sample DD (50℃/min) and sample CC (10℃/min). Sample CC (50℃/min) does not show any change in peaks profile at 1070℃. The irregular peak shape and the increase of the width of the peak, not to mention the reduction in the peak intensity indicates asymmetric behaviour in the (110). The reduction in the diffraction peaks intensity, in this case, is related to AGG (abnormal grain growth) in both sample DD (50℃/min) and CC (10℃/min), while

sample CC (50℃/min) show small peak broadening at 1070℃. However, numerous report and studies conducted on diffraction peaks broadening, stating the causes of such behaviour, including phase transition, lower symmetry state and strain [14]–[17]. There can be different factors affecting peak broadening such as dislocations, lattice defects and lattice strain; these factors do not apply in this case. On the other hand, high-temperatures result in uneven d-spacing shifts and expansion as a result of transformation into a lower crystallographic symmetry state.

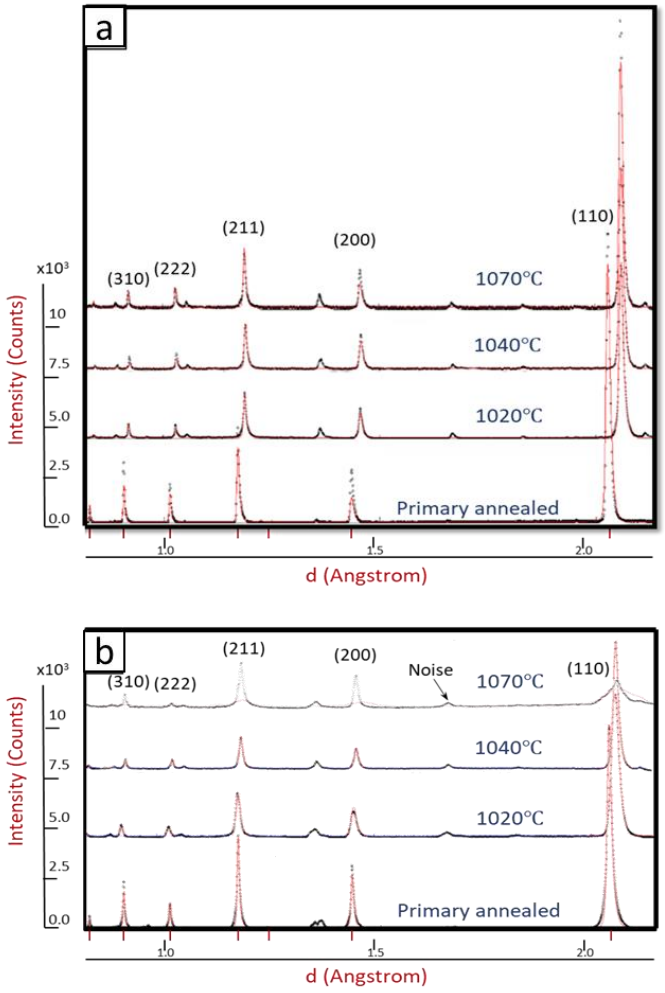

Figure 6-1 In-situ neutron diffraction result from RT to 1070 ℃ for, (a) sample CC and, (b) sample DD with a high heating rate (50 ℃/min).

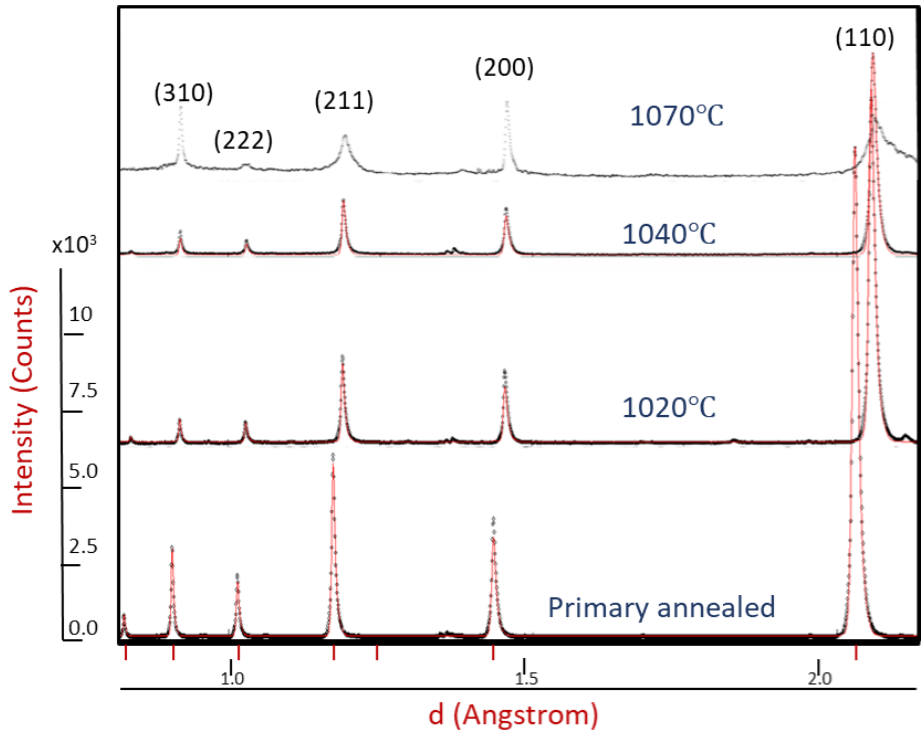

Figure 6-2 In-situ neutron diffraction result from RT to 1070℃ for sample CC with a low heating rate (10℃/min).

Similar behaviour is shown in Figure 6-3 with sample CC (50°C/min) and Figure 6-4 (10°C/min) at 1100°C, where the peaks intensity reduced and (110) peaks width increases, the red line indicates Fe-Si peak position at room temperature and the blue line indicating Nb peaks position at room temperature. After annealing for 10 min at 1100°C, the (110) show similar peak broadening as sample DD in Figure 6-1a. Also, different phases detected made the peak fitting difficult due to the furnace casing noises and Nb phase. At lower d-spacing, the Nb phase causes the results to show peaks splitting in α Fe-Si phase especially (310), higher d-spacing, peak broadening and splitting caused by asymmetric d-spacing shifts in different (110). Moreover, the peak shifting and broadening makes the fitting difficult and results from high temperature inaccurate, as shown in Figure 6-4.

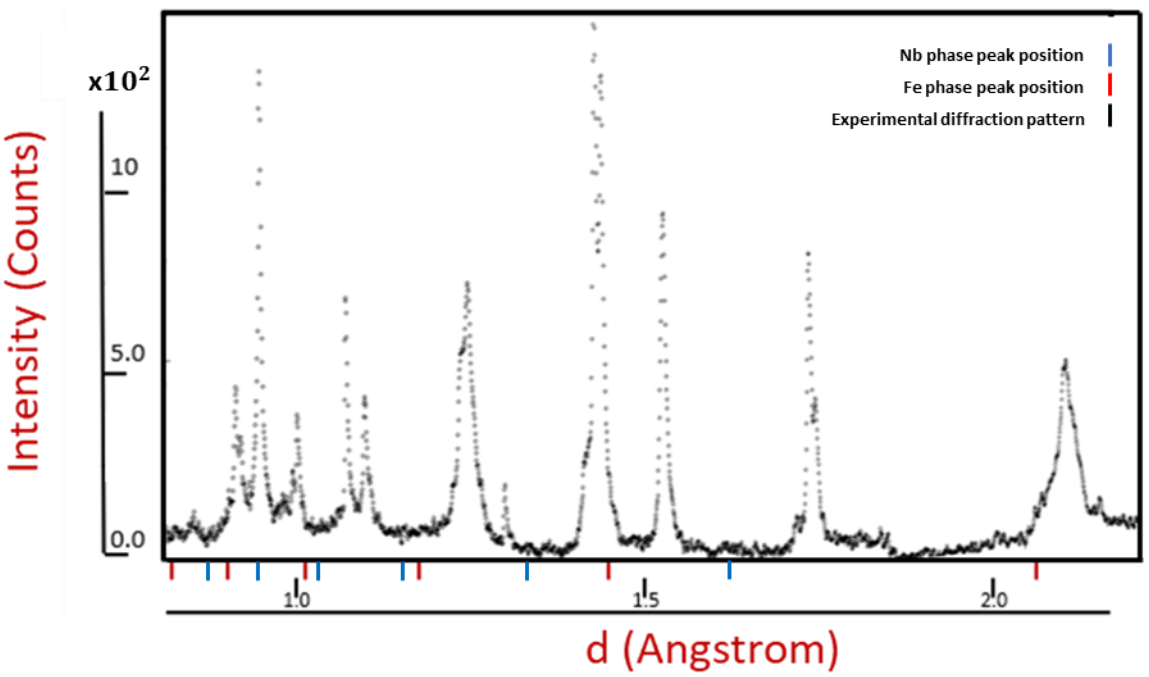

Figure 6-3 Sample CC in-situ neutron diffraction at 1100 ℃ (50 ℃/min).

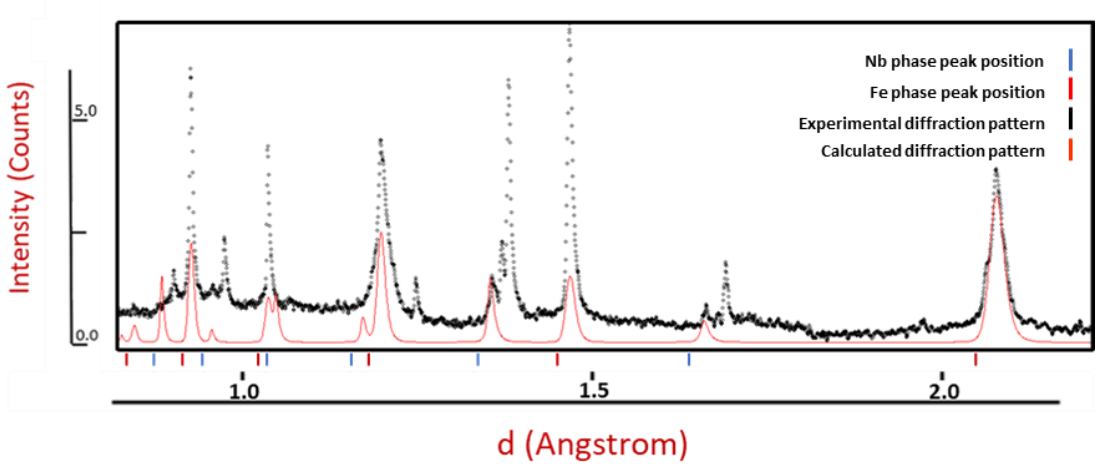

Figure 6-4 Sample CC in-situ neutron diffraction at 1100 ℃ (10 ℃/min).

The cubic cell parameter at each annealing temperature extracted using MUAD software is evident to the lattice thermal expansion, as shown in Figure 6-5 and Figure 6-6, 50℃/min and 10℃/min, respectively. Furthermore, at RT, the cell parameter is 2.8697Å and reaches saturation at 2.9143Å after annealing temperature of 1040℃ in sample DD and 2.8695Å to 2.9157 Å for sample CC for high heating rate (50℃/min). As for low heating rate (10℃/min), sample CC lattice parameter changes due to thermal expansion measured at 2.8719 Å at RT and 2.9156Å at 1070℃. Figures 6-5 and 6-6 show lattice parameter changes for both high heating rate (50℃/min) and low heating rate (10℃/min) respectively.

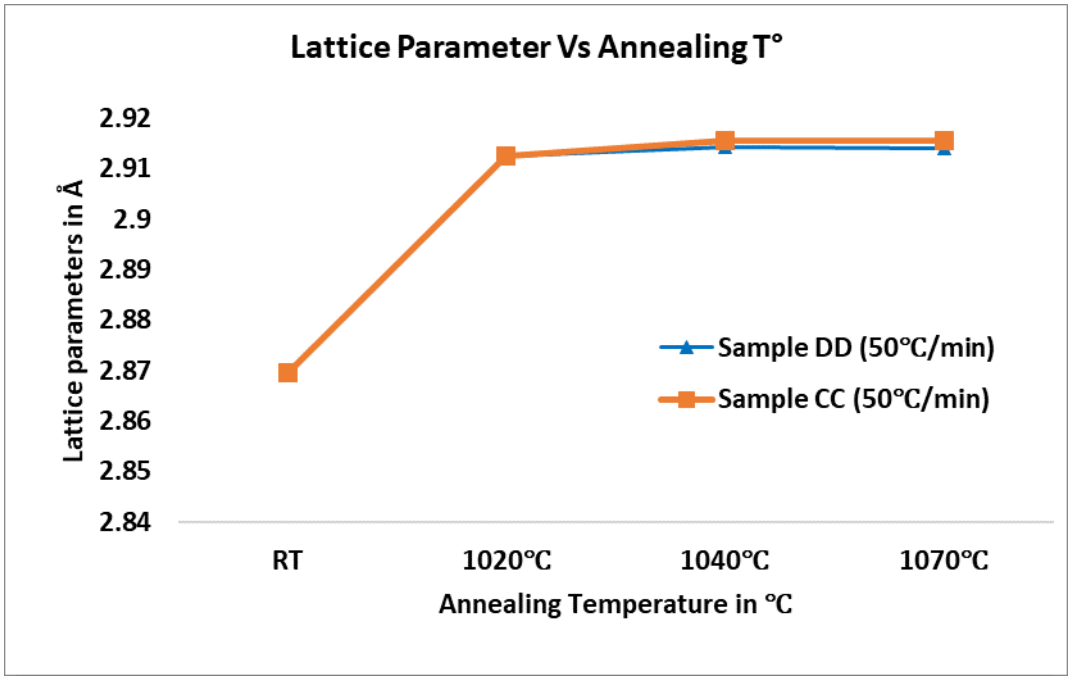

Figure 6-5 3.2% Si-Fe cell parameters obtained by neutron diffraction of sample CC and DD (50℃/min).

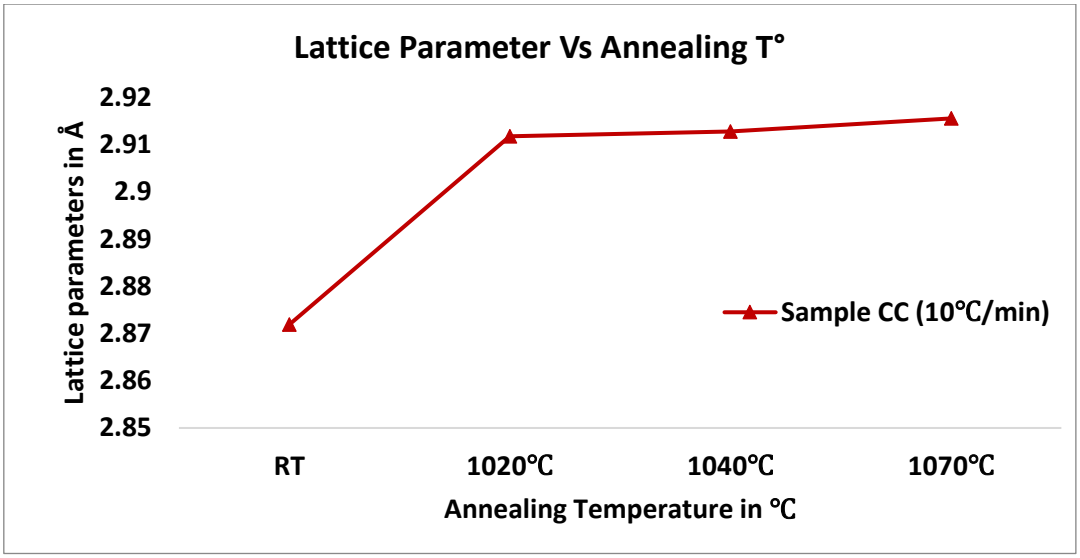

Figure 6-6 Si-Fe cell parameters obtained by neutron diffraction of sample CC (10 ℃/min).

Using Eq. 6-1, the peak shifting ration of different planes calculated from a reference point.

$$\frac{\Delta d_T}{d} = \frac{(d_T - d_{RT})}{d_{RT}} \quad \text{…….. Eq. 6-1}$$

The difference in d-spacing Δd_T at temperature T and d_{RT} is the d-spacing reference point (at room temperature). For this equation, only sample CC used for more accurate analysis and comparison of heating rate effect, as the same sample used in different heating rate.

Figure 6-7 and Figure 6-8 shows the change of $\frac{\Delta d_T}{d}$ of sample CC, at high heating (50°C/min) and low heating rate (10°C/min) respectively

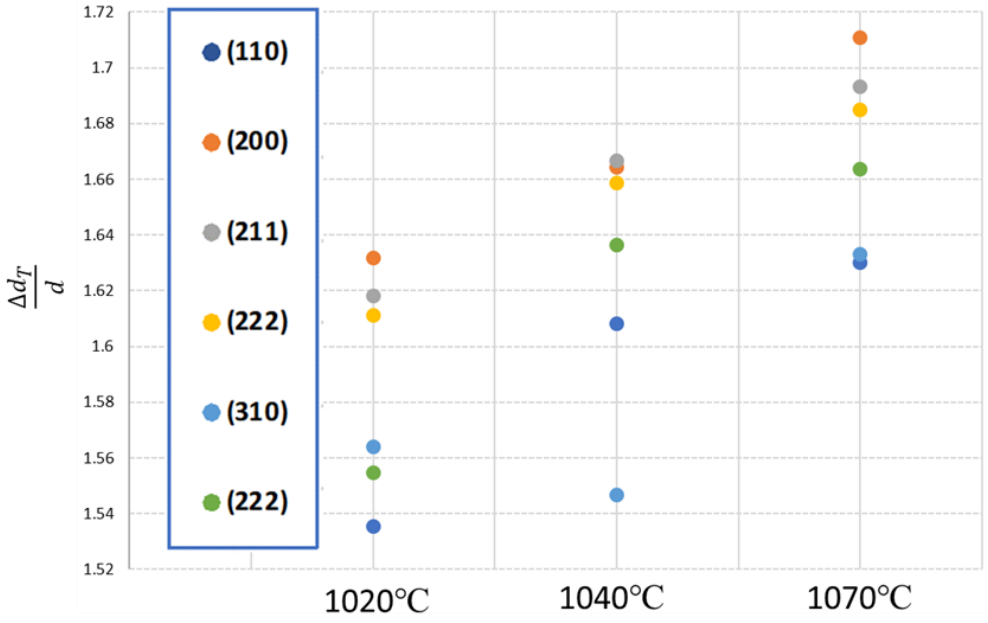

Figure 6-7 Sample CC with a heating rate of 50 ℃/min $\frac{\Delta d_T}{d}$ changes in different planes at different temperature.

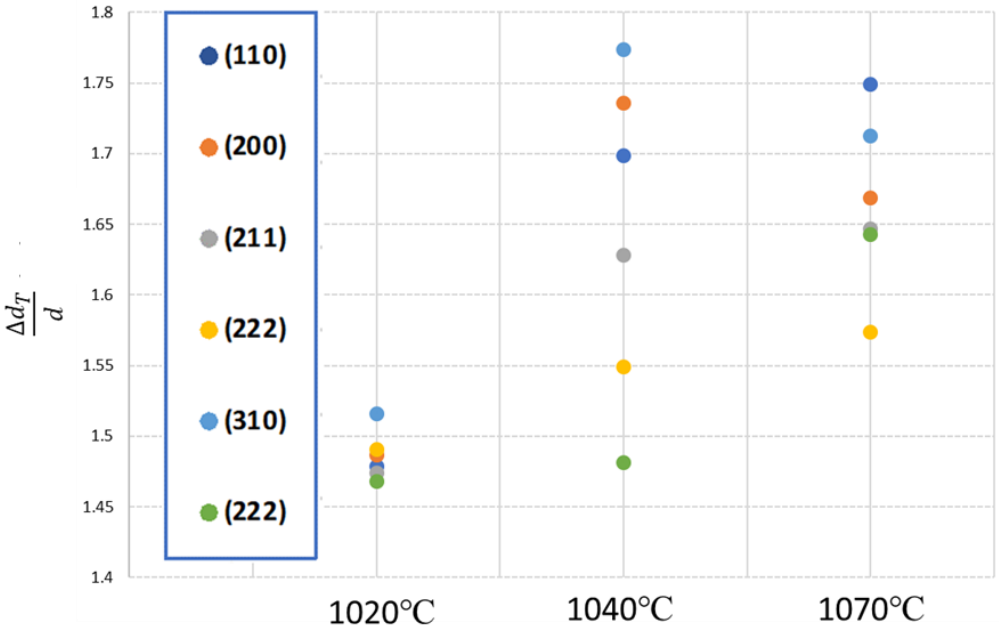

Figure 6-8 Sample CC with a heating rate of 10 ℃/min $\frac{\Delta d_T}{d}$ changes of different planes at different temperature.

Figures 6-7 and 6-8 show the d-spacing shift ratio for each plane, (110) has the highest shifting in low heating rate (10℃/min) samples CC, while high heating rate shows (200) having highest shifting rate. In Figure 6-7, the planes expand at a steady rate while Figure 6-8 shows (200) and (310) expands until 1040℃ and contract at 1070℃. In a highly symmetric system such as BCC, the peaks shift in an equal ratio/percentage in respect to the original peak position. In this experiment, the peaks are shown to have a different shifting rate as a result of the Si atom, and the lattice distortion is noticeable at high temperature.

The different change in d-spacing $\Delta \frac{d_T}{d}$ in the BCC planes is a result of the asymmetric unit cell at high temperature, wherein ideal BCC unit cell, lattice parameter expands in all direction equally, isotropic thermal expansion. Moreover, the effect of Si atom on unit cell with Si < 5 wt.% given by equation 6-2.

$$a_\alpha = 0.2861 - 0.00015\ \%Si \quad \text{…….. Eq. 6-2 [18]}$$

The lattice parameter a_α decreases with the increase of Si wt.%, and the peak shifts to lower d-spacing. On the contrary, the experimental results show the lattice parameter greater than 2.861Å. The reason for such behaviour is that with Si atom is slightly smaller, 0.2nm, substituting Fe atom, 0.248nm, the nearest eight Fe neighbours move closer to Si atom, also at least 26 nearest BCC cells are distorted and stretched resulting in an average lattice parameter greater than 2.861Å [19]. The presence of Si atom distorts the BCC lattice causing different

planes d-spacing to shift at a different rate at high temperature. Moreover, it was shown that the effect of Si distortion and impurities increases with the increase of temperature [19],[20].

Figure 6-9 shows the evolution of (110) peaks profile with the temperature at the high heating rate. The peaks shift to higher d-spacing without any visible distortion in the the BCC structure at 1040℃, whereas the distortion in BCC lattice occurs at 1070℃ as the peaks broadening initiated. In addition to peak shifting and lattice distortion at 1070℃, the (110) peak transforms into lower symmetry system and may no longer considered a BCC structure at 1100℃ as the peak broadening show signs of peak splitting. Similar behaviour is seen in (200) peak profile, where the peak shift and split at a higher temperature, as shown in Figure 6-10.

In low heating rate, the peak broadening and splitting observed in (110) is seen in Figure 6-4, the lower d-spacing peaks broadening and splitting caused by the Nb phase (neutron diffraction vacuum furnace sample holder) at high temperature. Figure 6-11 shown (110) peak profile of sample CC with a low heating rate (10℃/min) from RT to 1200℃. The peak broadening, splitting and asymmetric peak profile symmetry are reduced even further at 1200℃, which is an indication of lower symmetry lattice structure similar to the (110) results shown in Figures 6-9 and 6-10. Also, such a peak profile reported as a part of phase transition and the system transformation into a lower symmetry [21],[22]. In this state, the structure is no longer considered a BCC where different (110) and (200) shift and expand at a different rate resulting in peak broadening and splitting as shown in Figures 6-9 – 6-11.

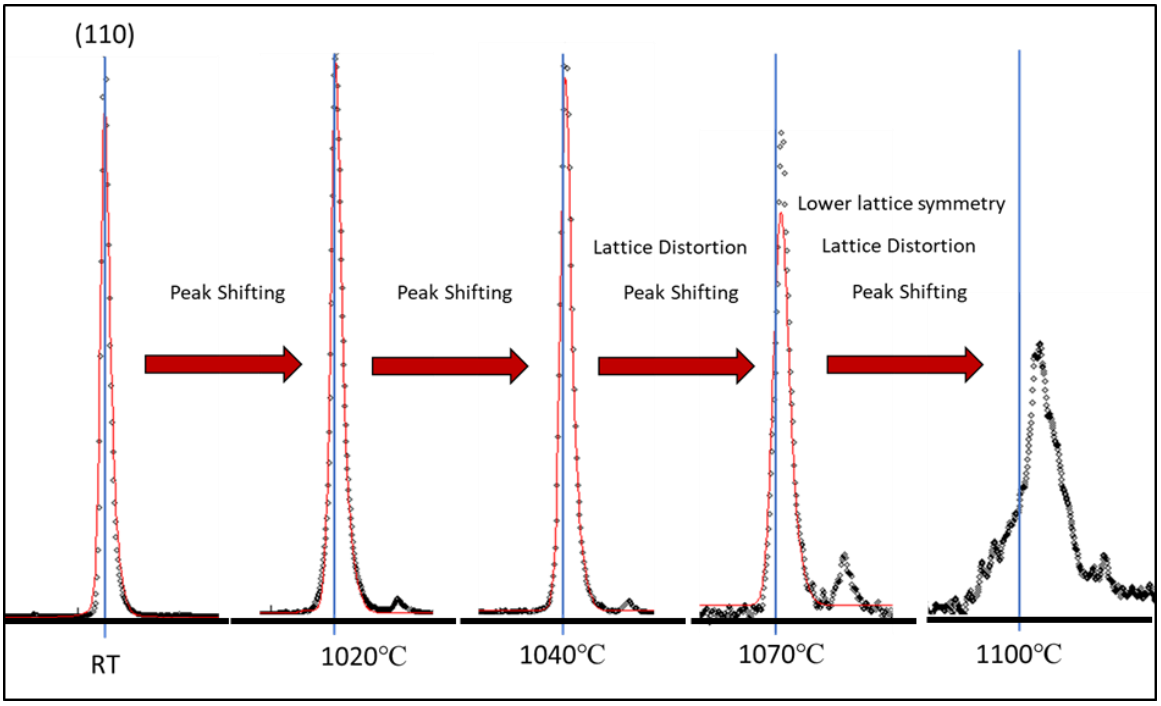

Figure 6-9 The evolution of (110) plane peak profile from RT to 1100 ℃, high heating rate (50 ℃/min).

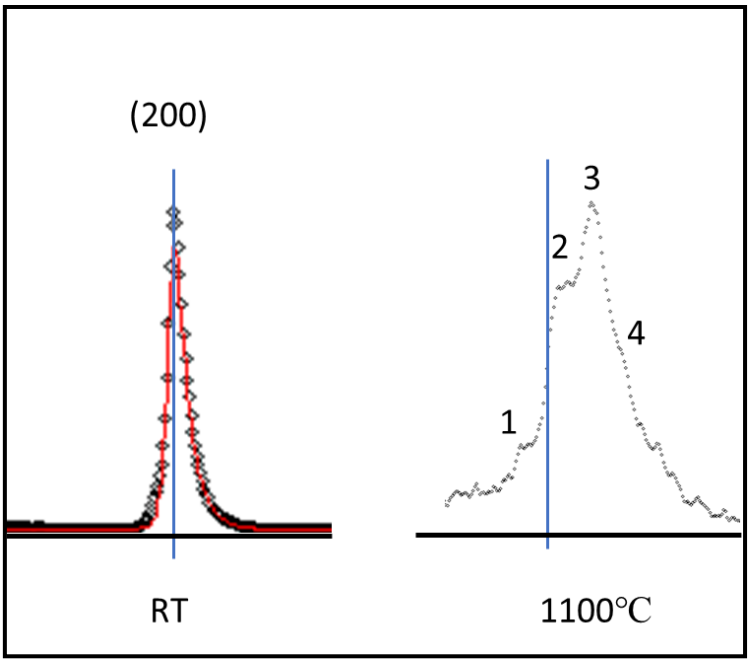

Figure 6-10 Transformation of (200) plane peak profile to lower symmetry system and shifting 1100 ℃, high heating rate (50 ℃/min).

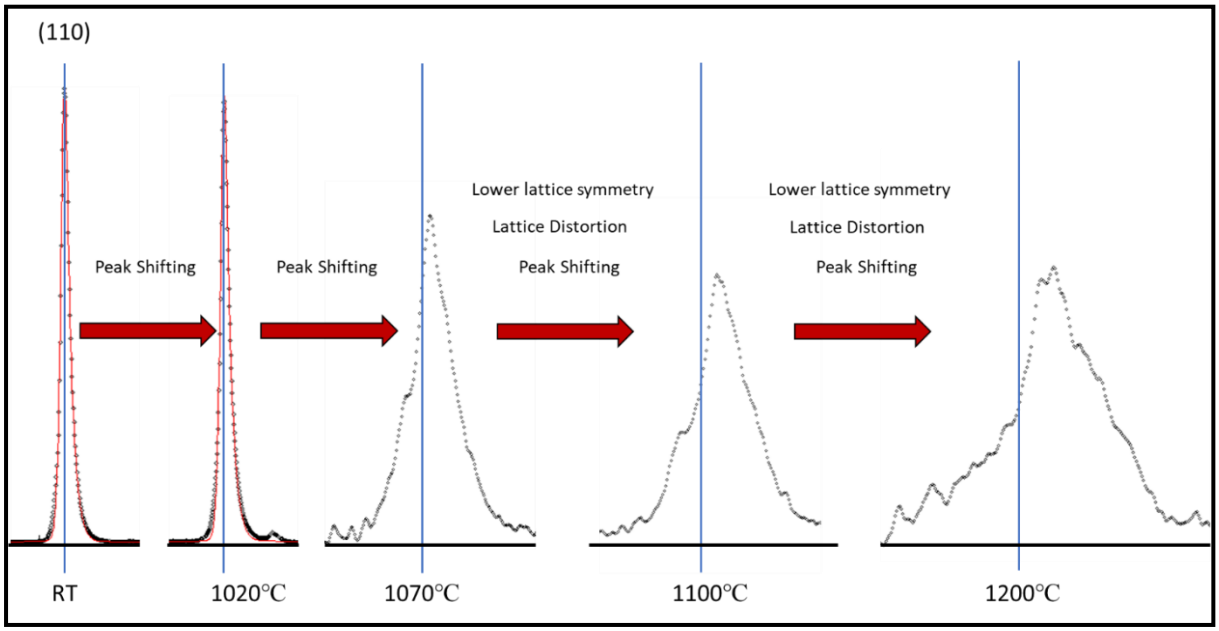

Figure 6-11 The evolution of (110) plane peak profile from RT to 1100℃, low heating rate (10℃/min).

6.3.2 Texture Evolution during in-situ Annealing

The effect of precipitation on texture evolution, the volume fraction of AlN (Aluminium Nitride), was investigated at each temperature. Table 6-1 shows the volume fraction of AlN content at different temperature in both samples, while ODF of samples CC in-situ texture evolution with high heating rate and low heating rate are shown in Figure 6-12, respectively.

Temp	AlN V. F. (wt%)	
(°C)	50°C/min	10°C/min
RT	0.0496	0.0649
1020	0.0394	0.0606
1040	0.0247	0.0499
1070	0.00178	0.0103
1100	0.00011	0.00015

Table 6-1 In-situ volume fraction dissolution of AlN of sample CC with a high heating rate and a low heating rate at different temperatures.

Both samples shown have a similar texture in the primary annealed sample, as shown in Figure 6-12. The results at 1100℃ may not be accurate due to furnace noise, irregular peak shapes, and these peaks were excluded to generate ODF. The pole figures were exported from MAUD to MTEX MATLAB to generate the ODF each sample at the stated temperatures. The minor difference in the texture shown in Figure 6-12 comes from the local orientation of each sample. At room temperature (RT), both samples have a strong γ-fibres and α`-Fibres, ~23° deviation from α-fibres, as well as orientation ~23° from rotated cube (R.C) and cube (C) orientations. The texture did not have any significant change after annealing at 1020℃-1040℃ in high heating rate, whereas the intensity of γ-fibres reduced in low heating rate. However, annealing results at 1070℃ AlN volume fraction significantly reduced, and the texture change is directly linked to the reduction of AlN contents. In Addition, low heating rate sample CC exhibit secondarily recrystallised at 1070℃, and the low heating rate sample show complete secondary recrystallised texture after annealing at 1100℃ with strong Goss. On the other hand, high heating rate sample texture annealed at 1070℃ results show a cube texture as well as Goss.

The high heating rate sample fully recrystallised at 1100℃ with cube and Goss. Both sample texture changes are where AlN volume fraction reduced significantly. Moreover, the recrystallisation texture is controlled by AlN dissolution, where sharp dissolution promotes other orientations to grow abnormally and compete with Goss abnormal growth as the case of high heating rate. On the other hand, low heating rate promotes gradual dissolution of AlN, giving the advantage for Goss abnormal grain growth, as shown in Figure 6-13.

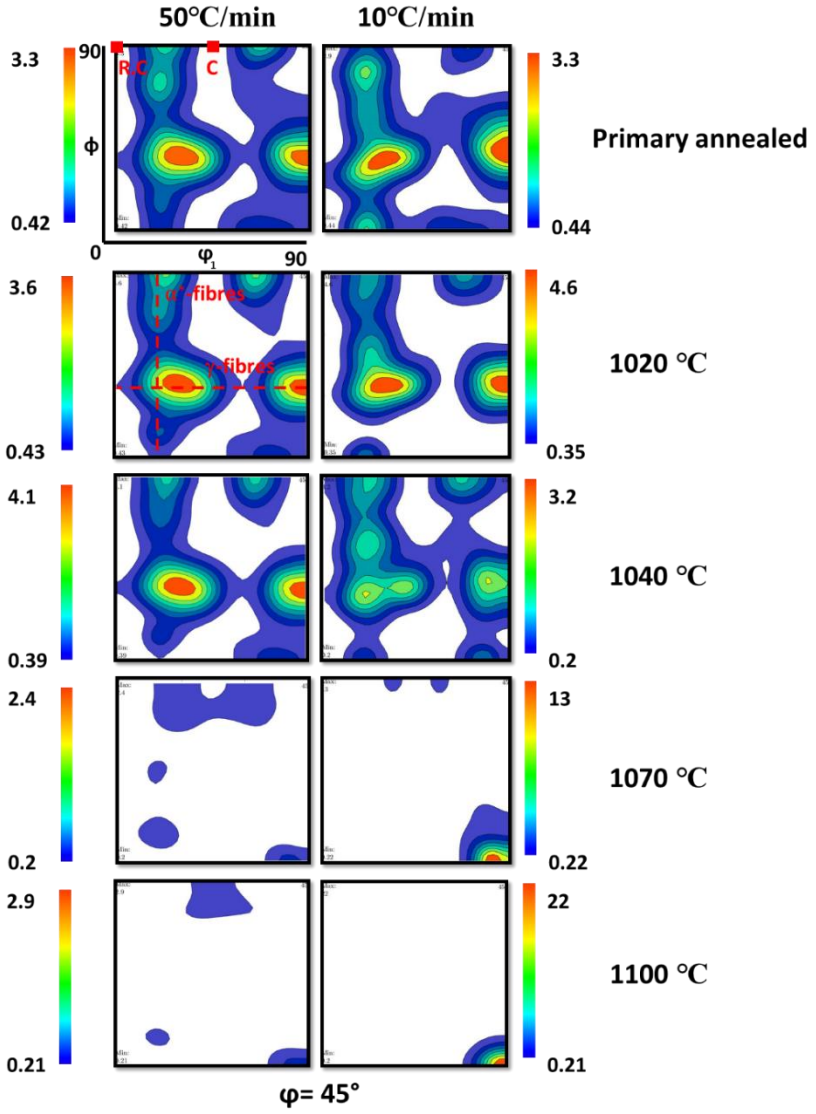

Figure 6-12 Sample CC in-situ texture evolution of high heating rate and low heating rate showing ODF ϕ2 = 45° from RT to 1100℃.

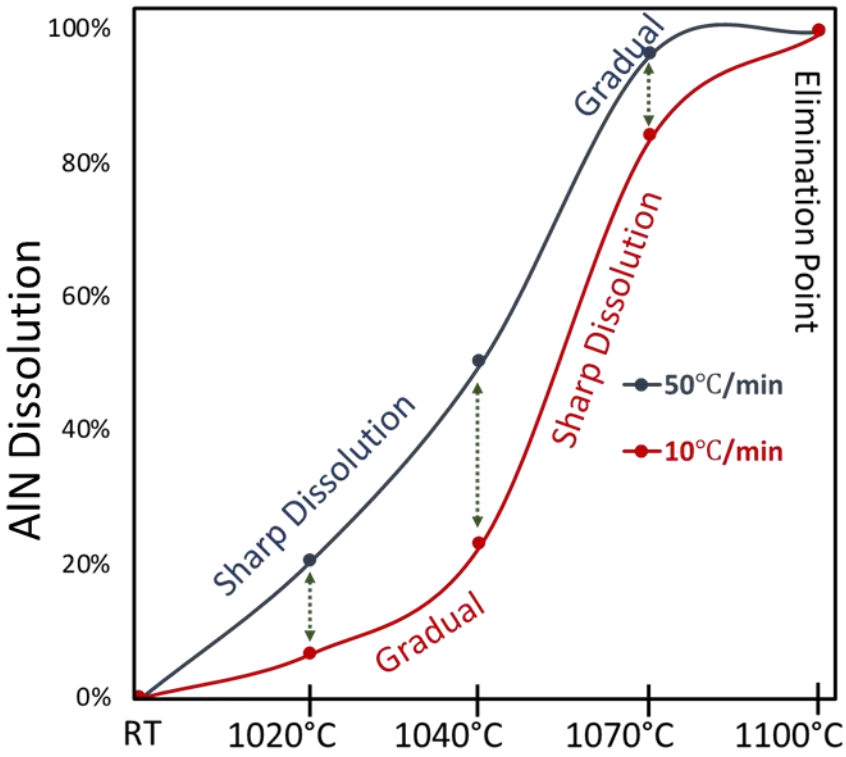

Figure 6-13 evolution of AlN (precipitation) dissolution at different two heat rate 50℃/min and 10℃/min.

6.3.3 α-Fe Distortion

In general, cubic crystalline materials, including BCC and FCC structures, have equal thermal expansion coefficient in all three principal directions. It is also well established that thermal expansion and thermal conductivity are symmetric second rank tensor and not directionally dependant. Thus, here we assume that ideal Goss grains with the perfect crystal structure, same as any other oriented grains, is elastically expanding at high temperatures equally in all X, Y and Z directions based on its BCC unit cell isotropic property. However, different lattice plane

expansions within the same unit cell as observed in Figures 6-7 and 6-8 is crystallographically possible. It is believed that the BCC lattice is slightly distorted by the addition of Si atoms to an α-Fe unit cell in Fe- 3%Si steel. The Si atoms that occupy substitutional sites in the BCC unit cell has 0.2 nm atom diameter, whereas α-Fe has 0.248 nm. This slightly smaller Si atoms make the Fe BCC lattice to be contracted according to [18], [23].

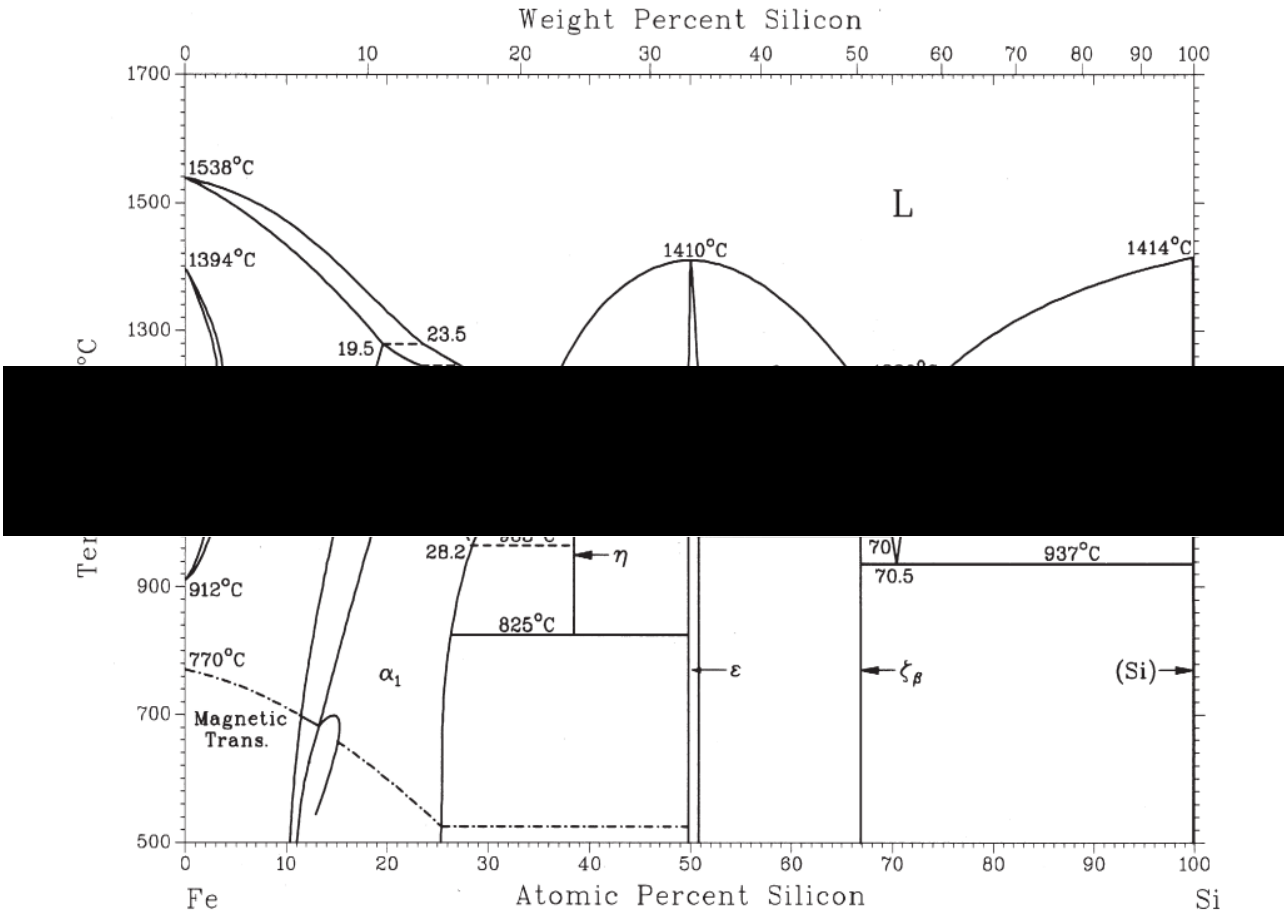

Figure 6-14 Iron Silicon Phase Diagram [24].

According to the commonly accepted phase diagram of iron–silicon alloys, as shown in Figure 6-14, there are three basic phases (α, α1, α2), where α1 and α2 seen in Si-Fe with silicon content greater than 10%. These phases are solid solution disordered, the case in this study 3.2 wt.%Si-Fe with a short-range order (α), and structures with a long-range order of the DO3 type (α1) and the B2 type (α2) [25]. Although, the addition of Si in BCC iron was investigated by many researchers to improve the magnetic property of Si steel, however, the effect of Si atoms on lattice distortion is rarely studied. Instead, most studies focused on nanostructural materials or ordered structures in order to study the magnetic properties with very high Si content [26]–[28]. Nevertheless, they established the fact that with increasing Si contents, the lattice distortion increases. Moreover, F. Lin, et al. [29] claimed that with increasing temperature up to 500°C, the (220) peak has shifted from 44.8° at RT to 45.3° at 500 °C. N. Overman. et al., [20], studied Fe-Si (3-8 wt.%) physical property, and they demonstrated that with increasing Si content, the lattice distortion increased and caused peak shifting even without altering the α-Fe BCC crystal structure. A similar finding was reported in 4.9 -5.8 % Si single crystal α-Fe in [30].

It should be emphasized here that this different plane expansion reported here and in literature is not necessarily to be observed as an overall bulk expansion in the three principal directions. The (110) lattice expansion superiority over the other lattice planes demonstrated in the current study is also observed in BCC beta titanium with the addition of hydrogen as a solid solution of the BCC structure [31]. S. Shantilal [32] also used X-ray diffraction to measure thermal lattice expansion of Fe BCC at low temperatures. He claimed that the influence of impurities on the Fe lattice parameter increases with increasing temperatures. S. Kim, et al. [33] claimed

that the thermal expansion coefficient of Fe BCC is very low. However, the volume variation may be considerable. Moreover, Z. Feng [34] applied Vegard's law [35] and concluded that the unit cell lattice parameter of an alloy, at a given temperature, changes linearly with the concentration of the substitutional elements. In general, depending on the substitutional element, the lattice expansion was observed in α-Fe at various temperature ranges. Figures 6-5 and 6-6 show the lattice parameter increased with increasing temperature, which is in agreement with the previous literature. It is recognised that the elements in the periodic table to the left of Fe, expand α-Fe lattice spacing due to their bigger sizes compared with Fe atoms. However, the elements in the periodic table to the right of Fe, that are smaller than Fe atoms (the case of Si), also displayed a lattice expansion due to the exchange repulsion between nearly filled d shells [34]–[36]. It is postulated that with decreasing atoms distance, the electron clouds approach each other further, and their electronic charge distributions overlap. This leads to a reduction of electron density between the atoms due to the Pauli exclusion principle [36]. The atoms nuclei that are positively charged will not then be shielded completely from each other and create a repulsive force between them, causing lattices expansion [34]–[36]. This is also in agreement with Figure 6-8, where Si atoms are smaller in size compared with Fe atoms.

Rationally, we think there are two major pieces of evidence of the influence of Si atoms on Goss AGG:

1. Goss grains do not grow abnormally or preferentially in other alloys including Ni, Cu, Al alloys as well as BCC steels with no Si and Al contents (Chemical Composition and Lattice Structure Factors).

2. Not all Goss grains in the same deformation band in the cold rolled as well as in the primary annealed electrical steel sheets can grow abnormally (Selective Goss AGG).

This leads us to emphasise that the Si atom position in Fe BCC is a key in Goss AGG in Si Steel, see Figure 6-15. Thus, we further considered the effect of Si content on the peak shifting observed in the current study, Figures 6-1 and 6-2. It was clear from Figures 6-5 and 6-6 that the lattice expansion, i.e., lattice parameters, increased with increasing temperature. It was also evident that the *d*-spacing of the individual crystallographic lattice planes were changed differently, see Figures 6-7 and 6-8. It should be emphasised here, this type of peak shifting along with peak broadening is also reported in other BCC structure during high temperature exposure [37], [38] and polycrystalline FCC [38]. It should also be remembered that (110) has a larger *d*-spacing (2.323 Angstrom) in an ideal α-Fe BCC structure than that for (100) at RT [40] and it appears here that its *d*-spacing increased with increasing temperatures (especially above 1070°C) at a higher rate than other planes, see Figures 6-7 and 6-8.

Further observation of Figures 6-1 and 6-2 revealed that peaks splitting, and broadening occurred after 1070°C, where dramatic AGG starts. Some areas of the diffraction peak in Figures 6-1 and 6-2 and beyond 1070°C are enlarged for further clarifications. For instance, Figure 6-16, show peak boarding of (110) peak from initial FWHM of 0.002147 at RT to 0.018126 A at 1070°C. The raw data with a simple peak fitting is shown in the same figure. Figure 6-11 shows (110) peak partial splitting that occurred at 1070°C and further progressed at 1100°C and 1200°C. The figure shows the critical breaking points on the (110) peak that are formed and increased with increasing temperature, indicating on a further split of the (110)

peak with increasing temperature. It should be emphasized here, only partial and not fully peak split observed in the current study. It is well established that peak broadening might be correlated to strain, dislocation density, grain size, as well as symmetry reduction [41], [42]. However, in our case, the material was fully annealed, thus, most of the peak broadening may be related to grain size changes during grain growth as well as BCC symmetry reduction at high temperatures. It is also well established that, peak splitting is an indication of phase transformation to a lower symmetry, for example, from cubic to tetragonal, or from tetragonal to orthorhombic [43], [44]. These observations indicate that at 1070°C, where the dramatic AGG started, the Goss grain did not grow symmetrically, and it changed to a much lower BCC symmetry when further annealed to 1100°C and 1200°C. It should be noted that peak splitting can also occur as a result of substructure and sub boundary formation, as reported in [45]. However, the data obtained in the current study was above AGG condition for 3% Si steel where the grains were fully recrystallised, and the Goss grain is grown abnormally, thus no sub-boundary could be created in such a condition.

From our basic Si atomic position calculations, we assume that in the disordered solid solution α-Fe cubic structure if Si atoms occupy 2 or more of the 8 corners, e.g., (1,1,1) and (0,0,0) (cubic atomic positions), replacing Fe atoms substitutionally, see Figure 6-15c, this atomic configuration will make 2 out of the 6 (110) plane *d*-spacings slightly even greater than that for other 4(110), (001) and other principle planes. However, if Si atom occupies only the centre position (½, ½, ½) or 1 or 2 non-opposite corners of the α-Fe cubic unit cell, the superiority of (110) *d*-spacing variation will not occur at the very high temperatures, see the atomic configurations in Figures 6-15a and 6-15b. Thus, it is reasonable to assume that not all the Goss

grains in Fe-3% Si steel can abnormally grow in the same sheet or the deformation band unless Si atoms occupy the right positions to enable only 2 of the 6 (110) planes expansion possible. In fact, we strongly believe that the lattice distortion occurrence due to Si additions in a disordered α-Fe unit cell provides a great crystallographic advantage for Goss grain AGG. However, further study and appropriate atomic simulation are needed to identify the exact Si atoms position in the α-Fe unit cell that can satisfy the preferable lattice distortion and atomic configurations for Goss AGG.

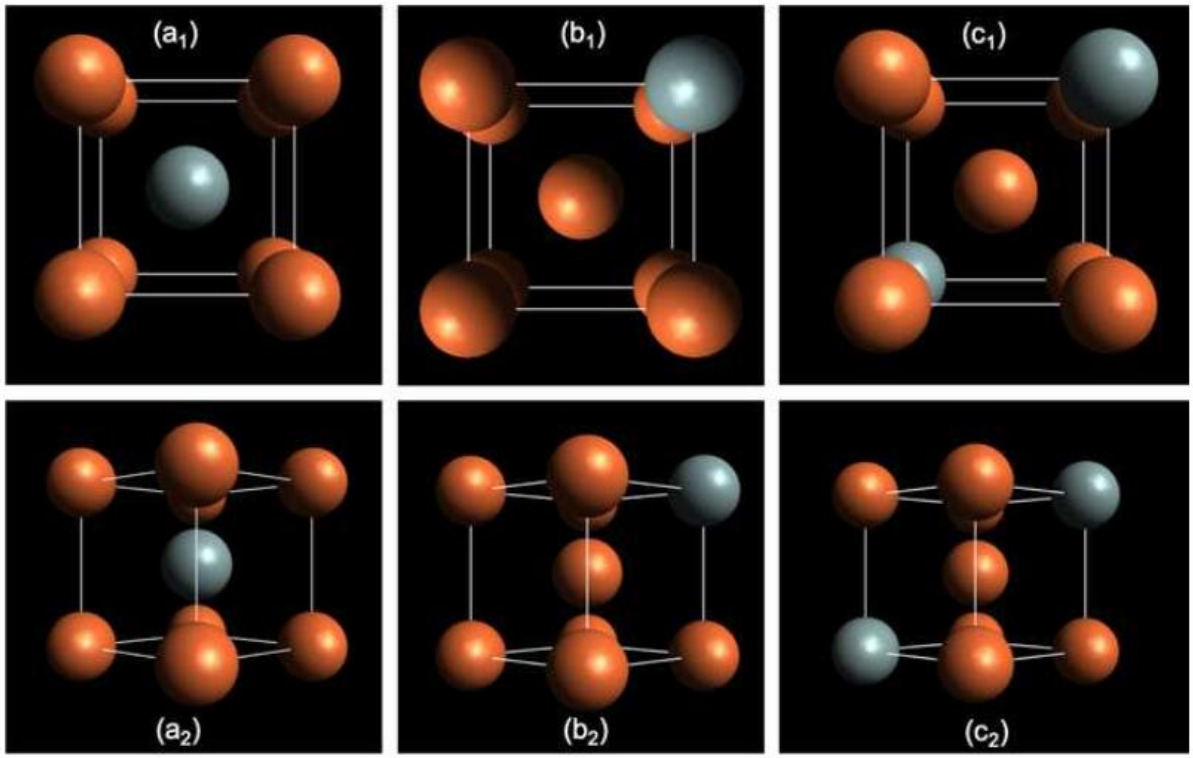

Figure 6-15 Atomic configuration of Si atom (grey) substitutional replacing Fe atom (brown) (a) Si atom in the centre position of the α-Fe cubic cell, (b) Si atom occupies one corner of the α-Fe cubic cell and (c) Si atom occupy two opposite corners of the α-Fe cubic cell.

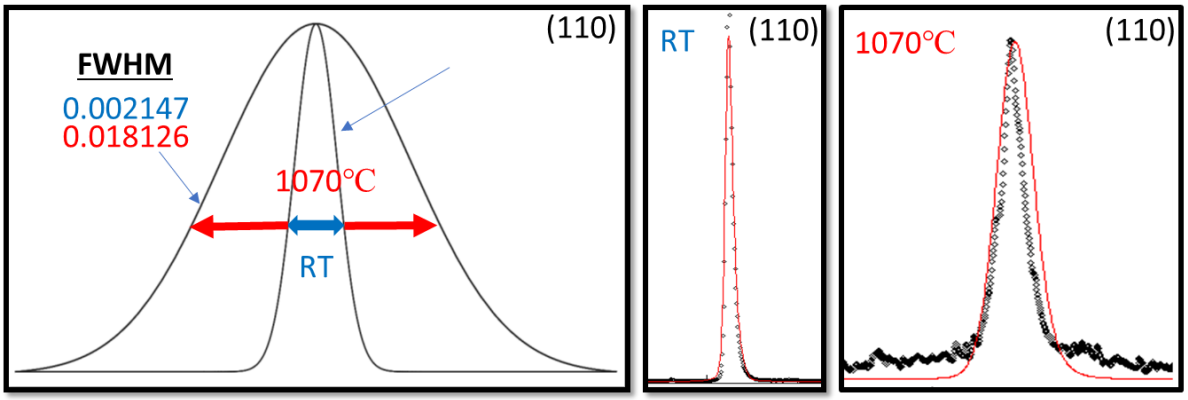

Figure 6-16 (110) peak broadening occurrence at a high temperature. The FWHM unit in Angstrom. The broadening mostly correlated to the Goss grain growth and BCC symmetry reduction.

6.4 Summary

3% Fe-Si is a slightly distorted BCC system at room temperature as seen in in-situ neutron diffraction results. The system transforms to a lower symmetry system at high temperature as a result of a slightly smaller Si atom substitute one of Fe atoms. The substitute Si atom causes BCC cell to contract and result in a smaller cell compared to pure Fe BCC cell. Whereas the average lattice parameter is greater than pure BCC iron lattice parameter as a result of a stretched crystal lattice caused by Si atom substitute Fe atom. At high temperature, 1070°C-1200°C, the system transforms into a lower symmetry state, and the system is no longer considered a BCC system as such. The signs of this lower symmetry state can be seen in the highly irregular peak profile and peak splitting as well as peak broadening indicating asymmetric expansion.

The abnormal grain growth and secondary recrystallisation are controlled by the volume fraction of AlN, where the sharp dissolution results in other orientations growing and competing with Goss abnormal grain growth. Whereas slow heating rate gradually dissolves AlN and results in the Goss abnormal grain growth advantage.

The asymmetric d-spacing shift and irregular peak profile shape give an indication of orientation growth, wherein high heating rate sample (200) has the highest average peak shift resulting in (100) <001> growth. The irregular shape and peak broadening of (200) in Figure 6-10 indicates that not all (200) planes expand in the same rate (shift to higher d-spacing), where peak broadening and splitting of (200) show that some of (200) planes have higher expansion rate than the rest of (200). It explains the high heating rate sample ODF showing cube orientation, (100) <001>, as we assume it has the highest expansion rate. On the other hand, the (110) has the lowest average in d-spacing shifting rate (d-spacing expansion). Similarly, the ODF show Goss growth as seen in high heating rate sample Figure 6-12 at 1070℃ and 1100℃ as a result of the asymmetric peak shifting and splitting (asymmetric d-spacing shift) in (110) plane. Figure 6-9 shows (110) peak split and broadening similar to (200) results, an asymmetric expansion where (110) in rolling direction has the highest expansion resulting in Goss abnormal grain growth.

6.5 Conclusion

In this chapter, in-situ neutron diffraction at ISIS Neutron and Muon Source was facility carried out to investigate 3% Fe-Si Goss abnormal grain growth during secondary recrystallisation stage.

1. The neutron diffraction method is a powerful technique to study in-situ texture evolution and the effect of heating rate on Goss abnormal grain growth.
2. The abnormal grain growth, plane expansion and AlN dissolution rate are shown to have a strong correlation. Also, the effect of heating rate on precipitation (AlN) which controls secondary recrystallisation studied.
3. Controlling precipitate dissolution rate, by controlling the heating rate, are shown to promote strong secondary recrystallisation texture, where low heating rate results in a sharp desired Goss texture.
4. 3% Si-Fe is considered a high symmetry BCC system, where neutron diffraction shows signs of slight distortion at room temperature due to Si atom substituting Fe atom, resulting in a larger lattice parameter in comparison with pure α-Fe BCC system.
5. It is evident from peak splitting and peak broadening as well as variant peak shifting ratio that 3% Fe-Si transforms to a lower symmetry system at high temperature.
6. It was shown that d-spacing expansion at a high temperature of (110) in case of low heating rate, and (200) in a high heating rate case, results in the growth of these planes in the rolling direction.

References

[1] Y. Ushigami, “Theoretical analysis and computer simulation of secondary recrystallization in grain-oriented silicon steel,” *Nippon Steel Technical Report*, no. 102, pp. 25–30, 2013.

[2] G. Liu, Z. Liu, P. Yang, and W. Mao, “Correlation between Primary and Secondary Recrystallization Texture Components in Low-temperature Reheated Grain-oriented Silicon Steel,” *Journal of Iron and Steel Research International*, vol. 23, no. 11, pp. 1234–1242, 2016.

[3] J. Y. Park, K. S. Han, J. S. Woo, S. K. Chang, N. Rajmohan, and J. A. Szpunar, “Influence of primary annealing condition on texture development in grain oriented electrical steels,” *Acta Materialia*, vol. 50, no. 7, pp. 1825–1834, 2002.

[4] Y. Wang *et al.*, “Development of microstructure and texture in strip casting grain oriented silicon steel,” *Journal of Magnetism and Magnetic Materials*, vol. 379, pp. 161–166, 2015.

[5] F. Fang *et al.*, “Inhibitor induced secondary recrystallization in thin-gauge grain oriented silicon steel with high permeability,” *Materials & Design*, vol. 105, pp. 398–403, 2016.

[6] F. Citrawati, M. Z. Quadir, and P. R. Munroe, “Investigation on the Early Stages of Growth of Secondary Grains in a Grain Oriented Silicon Steel,” *Procedia engineering*, vol. 184, pp. 750–755, 2017.

[7] A. Morawiec, “Grain misorientations in theories of abnormal grain growth in silicon steel,” *Scripta Materialia*, vol. 43, no. 3, pp. 275–278, 2000.

[8] F. Citrawati, M. Z. Quadir, and P. R. Munroe, “Effect of heating rate and annealing temperature on secondary recrystallization of Goss grains in a grain orientated silicon steel,” *ISIJ International*, vol. 57, no. 6, pp. 1112–1120, 2017.

[9] H. R. Wenk, S. Matthies, and L. Lutterotti, “Texture analysis from diffraction spectra,” in *Materials Science Forum*, 1994, vol. 157, pp. 473–480.

[10] S. Matthies, L. Lutteroti, and H. R. Wenk, “Advances in texture analysis from diffraction spectra,” *Journal of Applied Crystallography*, vol. 30, no. 1, pp. 31–42, 1997.

[11] F. Bachmann, R. Hielscher, and H. Schaeben, “Texture analysis with MTEX–free and open source software toolbox,” in *Solid State Phenomena*, 2010, vol. 160, pp. 63–68.

[12] M. Medraj, R. Hammond, M. A. Parvez, R. A. L. Drew, and W. T. Thompson, “High temperature neutron diffraction study of the Al2O3–Y2O3 system,” *Journal of the European Ceramic Society*, vol. 26, no. 16, pp. 3515–3524, 2006.

[13] W. Woo *et al.*, “In situ neutron diffraction measurements of temperature and stresses during friction stir welding of 6061-T6 aluminium alloy,” *Science and Technology of Welding and Joining*, vol. 12, no. 4, pp. 298–303, 2007.

[14] B. L. Boyce, T. A. Furnish, H. A. Padilla, D. Van Campen, and A. Mehta, “Detecting rare, abnormally large grains by x-ray diffraction,” *Journal of materials science*, vol. 50, no. 20, pp. 6719–6729, 2015.

[15] S. Brandstetter *et al.*, “Temperature-dependent residual broadening of x-ray diffraction spectra in nanocrystalline plasticity,” *Applied Physics Letters*, vol. 87, no. 23, p. 231910, 2005.

[16] D. Balzar, “X-ray diffraction line broadening: Modeling and applications to high-Tc superconductors,” *Journal of research of the National Institute of Standards and Technology*, vol. 98, no. 3, p. 321, 1993.

[17] Y. Zhao and J. Zhang, “Microstrain and grain-size analysis from diffraction peak width and graphical derivation of high-pressure thermomechanics,” *Journal of applied Crystallography*, vol. 41, no. 6, pp. 1095–1108, 2008.

[18] B. C. De Cooman, *Materials design: the key to modern steel products*. GRIPS media, 2007.

[19] Y. P. Chernenkov, V. I. Fedorov, V. A. Lukshina, B. K. Sokolov, and N. V. Ershov, “Short-range order in α-Fe–Si single crystals,” *Journal of magnetism and magnetic materials*, vol. 254, pp. 346–348, 2003.

[20] N. R. Overman *et al.*, “Physical and electrical properties of melt-spun Fe-Si (3–8 wt%) soft magnetic ribbons,” *Materials Characterization*, vol. 136, Dec. 2017, doi: 10.1016/J.MATCHAR.2017.12.019.

[21] H.-R. Wenk, I. Huensche, and L. Kestens, “In-situ observation of texture changes during phase transformations in ultra-low-carbon steel,” *Metallurgical and Materials Transactions A*, vol. 38, no. 2, pp. 261–267, 2007.

[22] Y. Tomota, P. G. Xu, T. Kamiyama, and E. C. Oliver, “In situ TOF neutron diffraction during phase transformation in an engineering steel,” *Nuclear Instruments and Methods in Physics Research Section A: Accelerators, Spectrometers, Detectors and Associated Equipment*, vol. 600, no. 1, pp. 313–315, 2009.

[23] N. I. Kulikov, D. Fristot, J. Hugel, and A. V. Postnikov, “Interrelation between structural ordering and magnetic properties in bcc Fe-Si alloys,” *Physical Review B*, vol. 66, no. 1, p. 014206, 2002.

[24] O. Kubaschewski, Iron—Binary phase diagrams, Springer Science & Business Media, 2013.

[25] N. V. Ershov, Y. P. Chernenkov, V. A. Lukshina, and V. I. Fedorov, “X-ray diffraction studies of specific features in the atomic structure of Fe-Si alloys in the α area of the phase diagram,” *Physics of the Solid State*, vol. 51, no. 3, pp. 441–447, 2009.

[26] L. Zhiqiang, L. Helie, L. Wuyan, and Z. Qingqi, “The effect on Si on the local magnetic moment and hyperfine interaction of BCC-Fe,” *Journal of Physics: Condensed Matter*, vol. 3, no. 34, p. 6649, 1991.

[27] S. M. Dubiel and W. Zinn, “Influence of Si on spin and charge density changes in bcc-iron,” *Journal of Magnetism and Magnetic Materials*, vol. 28, no. 3, pp. 261–276, 1982.

[28] M. Yousefi and S. Sharafi, “The effect of simultaneous addition of Si and Co on microstructure and magnetic properties of nanostructured iron prepared by mechanical alloying,” *Materials & Design*, vol. 37, pp. 325–333, 2012.

[29] F. Lin, D. Jiang, X. Ma, and W. Shi, “Structural order and magnetic properties of Fe3Si/Si (100) heterostructures grown by pulsed-laser deposition,” *Thin solid films*, vol. 515, no. 13, pp. 5353–5356, 2007.

[30] Y. P. Chernenkov, V. I. Fedorov, V. A. Lukshina, B. K. Sokolov, and N. V. Ershov, “Short-range order in α-Fe–Si single crystals,” *Journal of magnetism and magnetic materials*, vol. 254, pp. 346–348, 2003.

[31] O. N. Senkov, B. C. Chakoumakos, J. J. Jonas, and F. H. Froes, “Effect of temperature and hydrogen concentration on the lattice parameter of beta titanium,” *Materials research bulletin*, vol. 36, no. 7–8, pp. 1431–1440, 2001.

[32] J. S. Shah, “Thermal lattice expansion of various types of solids,” 1971.

[33] S. W. Kim, H. Tanigawa, T. Hirose, K. Shiba, and A. Kohyama, “Effects of surface morphology on fatigue behavior of reduced activation ferritic/martensitic steel,” *Journal of nuclear materials*, vol. 367, pp. 568–574, 2007.

[34] Z. Feng, “The Lattice Parameter of Gamma Iron and Iron-Chromium Alloys,” PhD Thesis, Case Western Reserve University, 2015.

[35] A. R. Denton and N. W. Ashcroft, “Vegard’s law,” *Physical review A*, vol. 43, no. 6, p. 3161, 1991.

[36] S. Brdarski and G. Karlström, “Modeling of the exchange repulsion energy,” *The Journal of Physical Chemistry A*, vol. 102, no. 42, pp. 8182–8192, 1998.

[37] H. Cao, F. Bai, J. Li, D. D. Viehland, T. A. Lograsso, and P. M. Gehring, “Structural studies of decomposition in Fe–x at.% Ga alloys,” *Journal of alloys and compounds*, vol. 465, no. 1–2, pp. 244–249, 2008.

[38] A. Goldbach, L. Yuan, and H. Xu, “Impact of the fcc/bcc phase transition on the homogeneity and behavior of PdCu membranes,” *Separation and Purification Technology*, vol. 73, no. 1, pp. 65–70, 2010.

[39] Y. Zhao and J. Zhang, “Microstrain and grain-size analysis from diffraction peak width and graphical derivation of high-pressure thermomechanics,” *Journal of applied Crystallography*, vol. 41, no. 6, pp. 1095–1108, 2008.

[40] H. D. Omar, “To investigation the structure and morphology of iron metallic by difference techniques,” *J. Nano. Adv. Mat*, vol. 3, no. 2, pp. 57–61, 2015.

[41] E. Schafler *et al.*, “A second-order phase-transformation of the dislocation structure during plastic deformation determined by in situ synchrotron X-ray diffraction,” *Acta materialia*, vol. 53, no. 2, pp. 315–322, 2005.

[42] I. S. Golovin, A. M. Balagurov, V. V. Palacheva, I. A. Bobrikov, and V. B. Zlokazov, “In situ neutron diffraction study of bulk phase transitions in Fe-27Ga alloys,” *Materials & Design*, vol. 98, pp. 113–119, 2016.

[43] H.-R. Wenk, I. Huensche, and L. Kestens, “In-situ observation of texture changes during phase transformations in ultra-low-carbon steel,” *Metallurgical and Materials Transactions A*, vol. 38, no. 2, pp. 261–267, 2007.

[44] Y. Tomota, P. G. Xu, T. Kamiyama, and E. C. Oliver, “In situ TOF neutron diffraction during phase transformation in an engineering steel,” *Nuclear Instruments and Methods in Physics Research Section A: Accelerators, Spectrometers, Detectors and Associated Equipment*, vol. 600, no. 1, pp. 313–315, 2009.

[45] T.-Y. Kim *et al.*, “Synchrotron X-ray microdiffraction analysis of abnormally growing grains induced by indentation in Fe-3% Si steel,” *Materials Characterization*, vol. 156, p. 109845, 2019.

Chapter 7: The Effect of Heating Rate, Heating Flux and Strain on Goss Abnormal Grain Growth

7.1 Introduction

In this chapter, the effects of heating rate and heating flux, i.e., heat flow direction, on Goss abnormal grain growth is investigated using electronic backscatter diffraction (EBSD). The impact of strain and heat flow on the Goss abnormal grain growth is also reported. Interrupted tests were carried out where primary annealed samples where annealed at different temperatures and at different heating rates. The change in microstructure, as well as texture evolution is reported at each incremental and processing stage. Different annealing temperatures at different dwell times using a carbolite furnace were applied to study the Goss abnormal grain growth behaviour from the initial stages of secondary recrystallisation to complete recrystallisation. The grain boundaries, as well as the initial grain size advantage influence on Goss abnormal grain growth in final stages of secondary recrystallisation, were investigated. Likewise, interrupted annealing tests were performed to investigate the microstructure evolution of grain oriented silicon steel. The strain effect on final recrystallisation and abnormal grain growth was investigated, with the samples were subjected to different strain at the edge and the centre on the samples the average numbers of grains analysed used in this study reached 60,000 grains for better analytical accuracy.

7.2 Experimental Procedure

The experimental procedure, heating schedule, heating rate, and dwell time details reported in Chapter 3. The annealing and interrupted annealing were carried out in Swansea University laboratory, and scanning electron microscopy equipped with ESBD was used to investigate the texture evolution and Goss abnormal grain growth.

7.3 Results and Discussion

7.3.1 Heating Rate Effect on Goss Abnormal Grain Growth

Figures 7-1 and 7-2 show sample AA and BB primary annealed EBSD results, respectively. The sample in inverse pole figure (IPF) in Figures 7-1a and 7-2a show equiaxed grains with an average grain size of ~19.7µm and ~21µm, respectively. The Orientation Distribution Function (ODF) are shown in Figures 7-1b and 7-2b. Major texture component volume faction considered in this study are shown in Figures 7-1d and 7-2d. The volume fraction of the texture component was calculated within 20º from ideal orientation for the primary annealed sample. The primary annealed sample has a strong α*-fibres with a maximum intensity of components away from Cube and rotated cube orientation by 22º-26º seen in Figures 7-1b and 7-2b. From Figures 7-1d and 7-2d, γ and α fibres have the highest volume fraction followed by Cube orientation. Both samples show identical results at this stage. Figures 7-1c and 7-2c show the grain boundary angles frequency where both samples are similar.

Figure 7-3 shows both samples after annealing at 1100℃ and dwell time of 20min, and a heating rate of 0.1℃/min, the edge of the sample facing the furnace heating element Figure 7-3a. In contrast, sample BB rotated at a random angle with the top side is insulated using a thermal insulator (Vermiculite treated silica cloth and Fiberfrax).

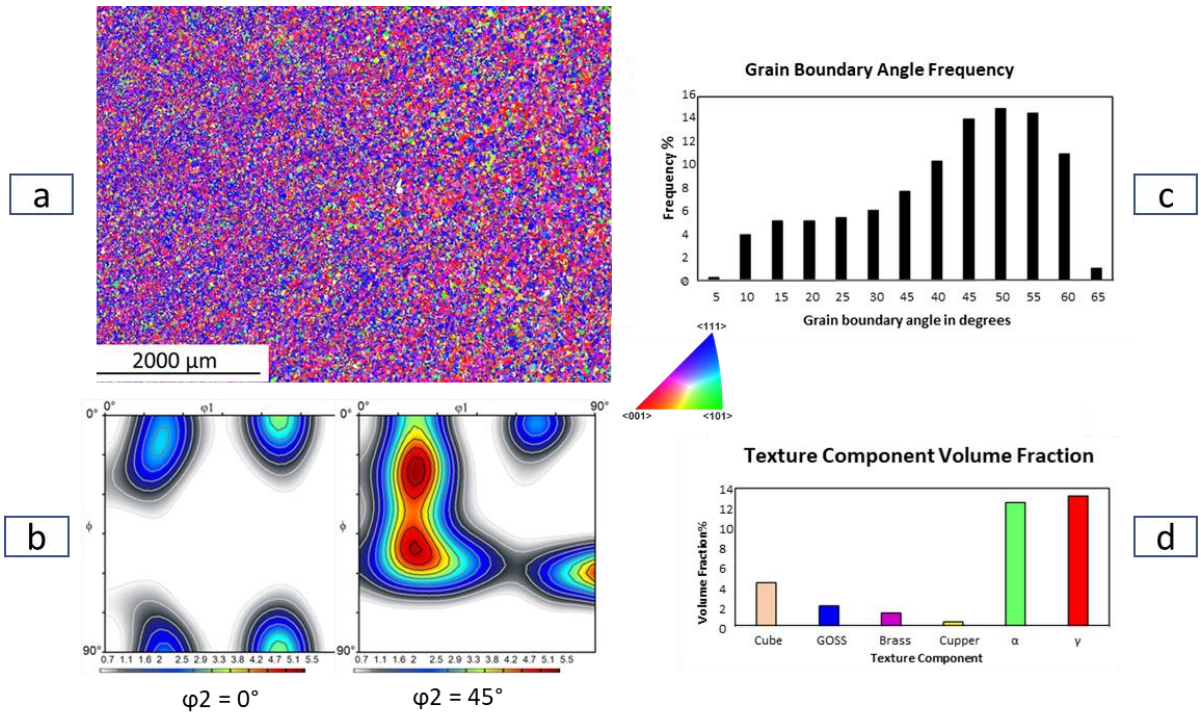

Figure 7-0-1 Sample AA primary annealed EBSD results showing microstructure in IPF map (a), ODF showing texture (b), Grain boundary angle frequency (misorientation) (c) and texture component of selected orientations (d).

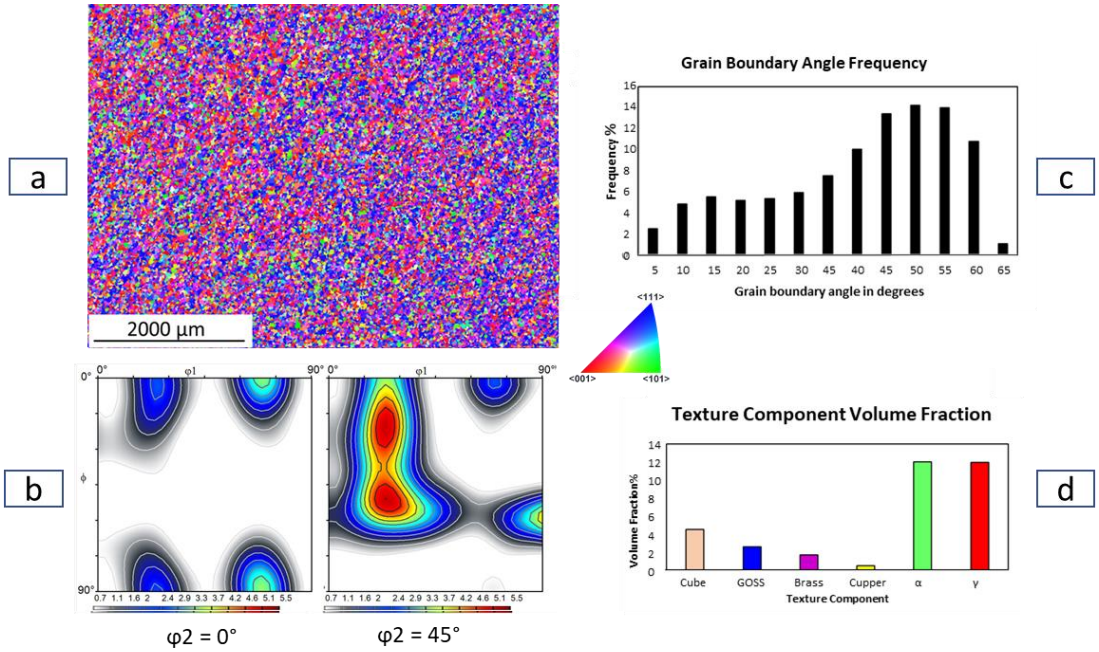

Figure 7-2 Sample BB primary annealed EBSD results showing microstructure in IPF map (a), ODF showing texture (b), Grain boundary angle frequency (misorientation) (c) and texture component of selected orientations (d).

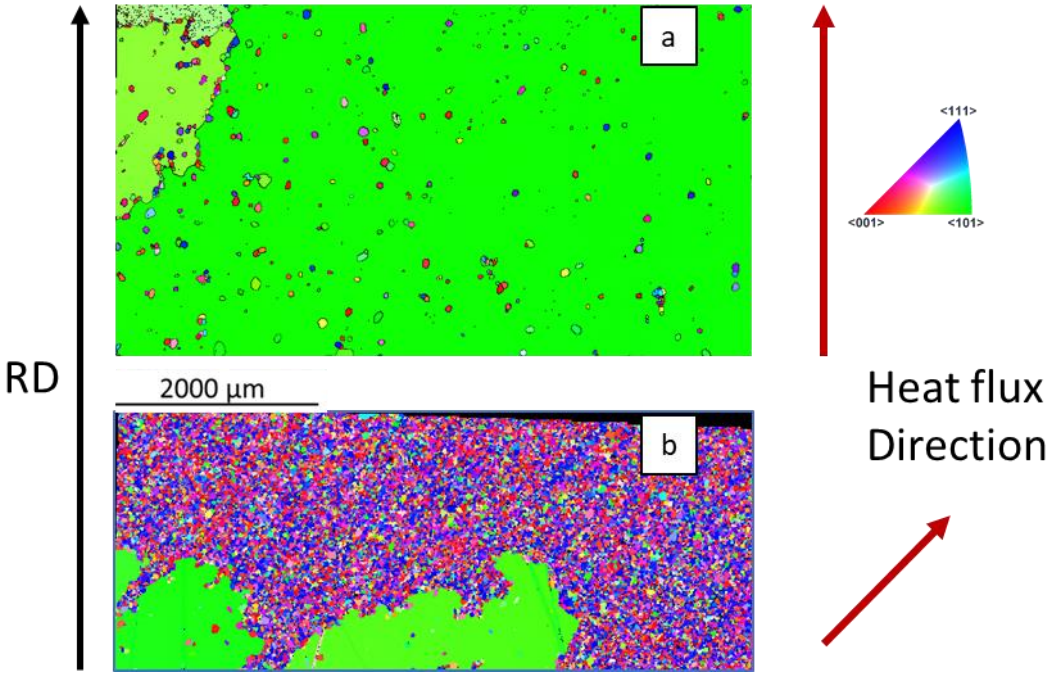

Figure 7-3 IPF map //ND showing of annealed samples at 1100°C for 20min (a) Sample AA heat flux in the rolling direction and (b) sample BB heat flux at an angle ~45°.

The growth rate of Goss grains in sample AA when heating flux parallel to the rolling direction (RD), see Figure 7-3a, was higher than the Goss growth rate in sample B, see Figure 7-3b. Besides, it was apparent that the abnormal growth of Goss grain followed a path parallel to the furnace heating direction (heat flux direction). Also, the grains with ideal or minimum deviation from (110) <001> have the advantage of abnormal growth. These findings were in agreement with [1], where the experimental results showed the relationship between the Goss deviation and growth rate. With these results, it can be confirmed that ideal and near-ideal Goss grains have the advantage of abnormal grain growth. Also, the direction of which Goss growth rate reported to be higher in RD compared to TD. Similarly, the samples heat-treated in RD have abnormal grains in the late stages of secondary recrystallisation (Figure 7-3a), whereas the rotated sample requires more heat treatment time to recrystallise completely.

Sample BB was annealed from RT in the RD to 1100℃ with a dwell time of 20mins, 60mins and 180mins, and a heating rate of 0.1℃/min. Figure 7-4, the ODF (7-4 a3, b3 and c3) show a sharp Goss texture in all of the samples with the highest intensity of Goss texture in the sample annealed for 180mins. As expected, a single abnormal Goss grain was observed in the fully annealed sample. Also, grain boundary evolutions in secondary recrystallisation seen in Figure 7-4 (a2, b2 and c2) strongly indicates the reduction of high angle grain boundary (20°-45°) to have an effect on Goss abnormal grain growth. The reduction rate of the high angle grain boundary continued until the final stages of secondary recrystallisation where abnormal grain growth consumed most of the remaining grains.

Comparing the results from Figure 7-3b and Figure 7-4a, it is evident that annealed with heat flux path is parallel to RD results in a faster growth rate. It can be assumed that the heat flux travelling in RD at a low heating rate results in a heat gradient that gives Goss grains the advantage to grow abnormally. The heat gradient in the sample creates an advantage for Goss grains to overcome grain boundary pinning.

Although the grain size is shown to have no significant role in the initiation of Goss abnormal growth, as shown in Chapter 6, it was found that it contributes to the continuation of abnormal growth. In polycrystalline materials, grain size and grain boundaies have an effect on thermal flux flow and conductivity. As the grain size increases the thermal conductivity increases [2,3]. It is reasonable to assume that grain size advantage to have an effect on the continuation of abnormal grain growth in later stages of secondary recrystallisation and provides the advantage for Goss grains to grow abnormally.

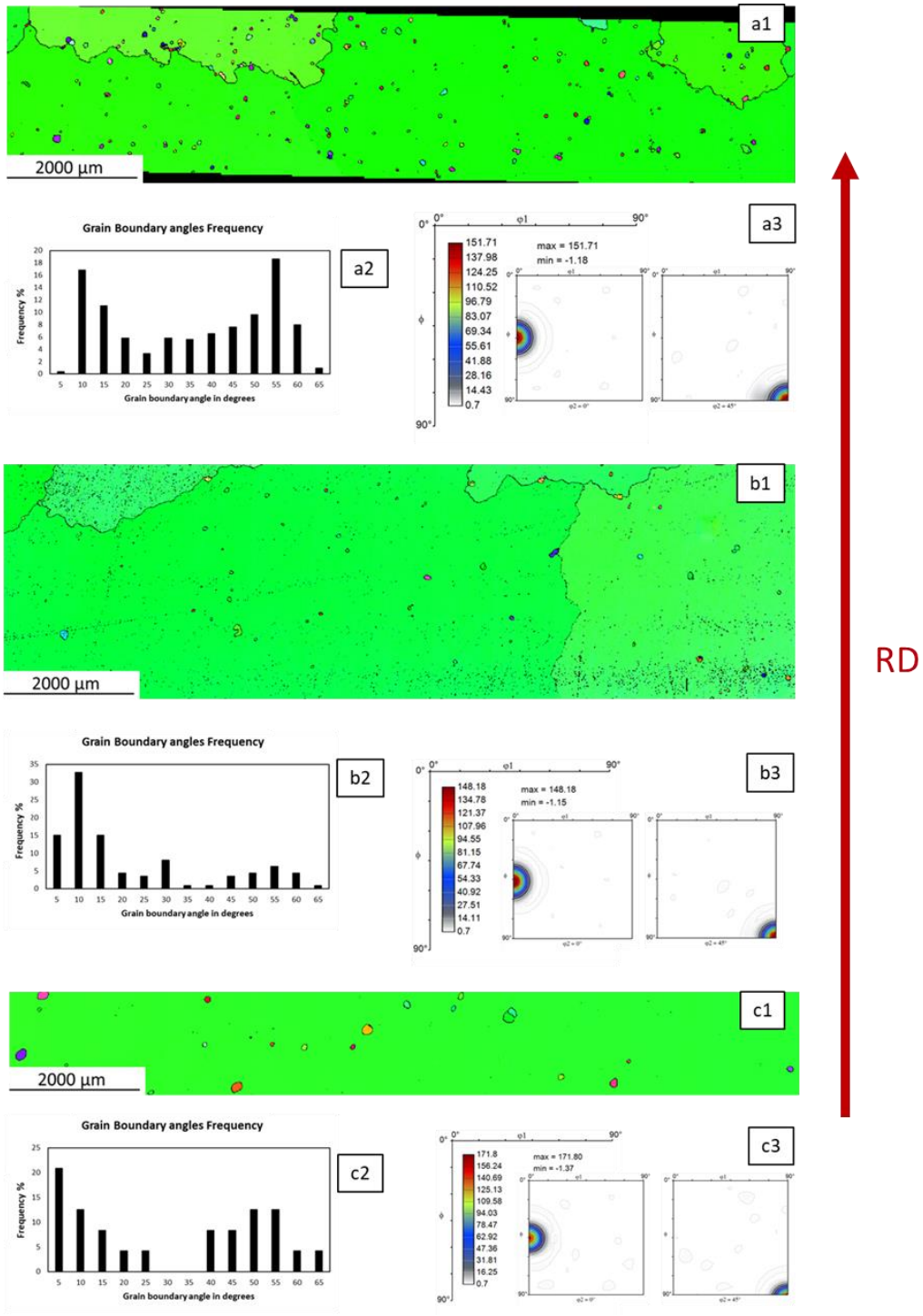

Figure 7-4 Results of annealed at 1100℃ for 20min IPF map //ND (a1), misorientation and grain boundary angle frequency (a2) and ODF (a3), results of annealed samples at 1100℃ for 60min IPF map (b1), misorientation and grain boundary angle frequency (b2) and ODF (b3), results of annealed samples at 1100℃ for 180min IPF map (c1), misorientation and grain boundary angle frequency (c2) and ODF (c3).

7.3.2 High Heating Rate Effect on Goss Abnormal Grain Growth

To investigate the effect of high heating rate on the microstructure evolution, the samples were placed in the preheated furnace of 1000℃ and annealed with a heating rate of 0.1℃/sec and maximum furnace heating rate of 0.6℃/sec to 1100℃ and dwell time of 20min and 60min. Figure 7-5 shows the results of sample AA and sample BB in a preheated furnace with a heating rate of 0.1℃/sec. The IPF maps are shown in Figure 7-5a1 and Figure 7-5b1 of sample AA and sample B, respectively and texture component map within 20° of selected orientations shown in Figure 7-5a2 and Figure 7-5b2. AA reasonable assumption to this behaviour in which random orientation grow abnormally and compete with Goss orientated grains is that the increase in the heat gradient in the sample caused by preheated furnace, allowing the precipitates (grain growth inhibitors) to dissolve randomly throughout the sample thus Goss losses the advantage to grow abnormally. Both samples in Figure 7-5a2 and Figure 7-5b2 show the competition between abnormally grown grains where Goss grains compete with Brass orientation and random orientation in both samples.

The presence of precipitates creates the advantage for Goss grains to grow abnormally by the suppression of normal grain [4],[5]. Without these precipitates, the secondary recrystallisation texture cannot develop. With the high heating rate, as shown in Figure 7-5a2 and Figure 7-5b2, the effectiveness of the precipitates reduced to a state of which other orientation also grow abnormally. Thus, the earlier assumption is made where the precipitates can dissolve abruptly so that create an environment where random orientation can grow abnormally. The results are

in disagreement with [6], where it was suggested that the effect of rapid heating and slow heating are insignificant in the development of secondary recrystallisation texture.

Furthermore, Figure 7-5a3 and Figure 7-5b3 show the misorientation and grain boundary frequency. Sample AA (Figure 7-5a3) show a slight reduction in high angles grain boundary (20°-45°), whereas sample BB (Figure 7-5b3) grain boundary frequency matches the primary annealed sample. Thus, it can be concluded that the mobility of high angle grain boundary is not a driving force for the abnormal grain growth. For instance, by changing only one parameter (e.g., heating rate), the desired secondary recrystallisation texture cannot be obtained.

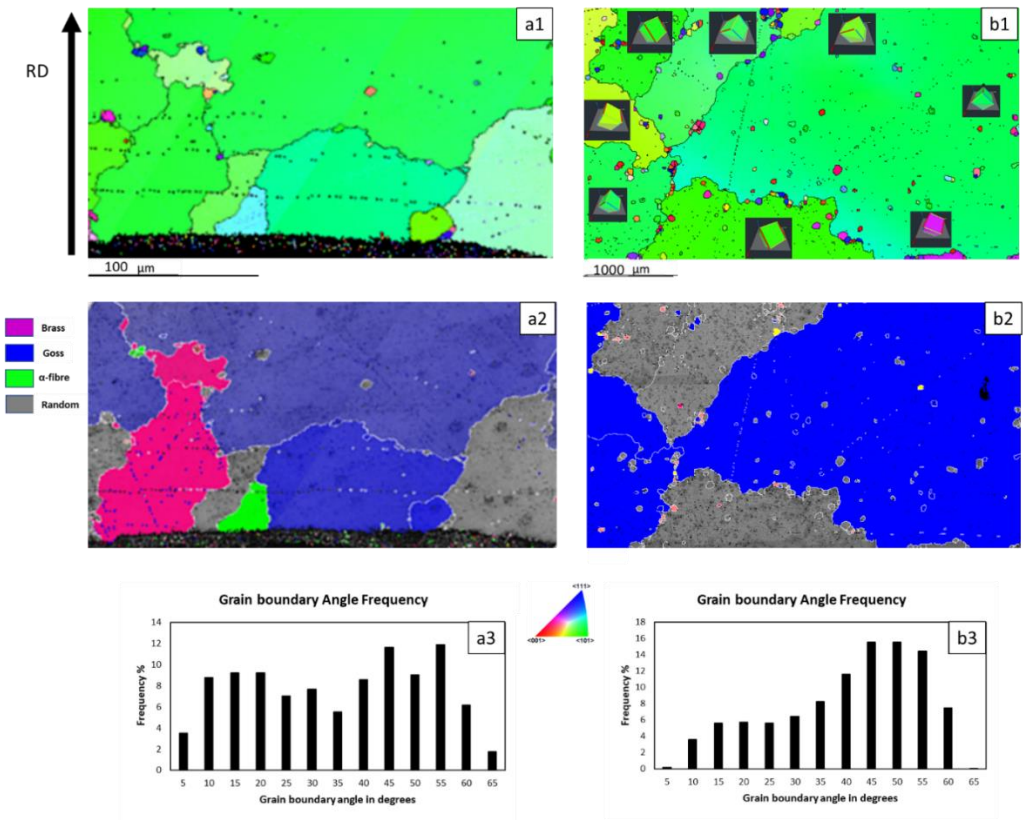

Figure 7-5 Results of the preheated furnace to 1000°C annealed at 1100°C for 20min IPF map//ND of sample AA (a1), sample BB(b1), and selected texture component of sample AA (a2), sample (b2) and grain boundary frequency of sample AA (a3) and sample BB (b3).

Figure 7-6 shows the results of annealed samples for 60 min in a preheated furnace to 1000℃ and annealed at 1100℃ at a heating rate of 0.6℃/sec.

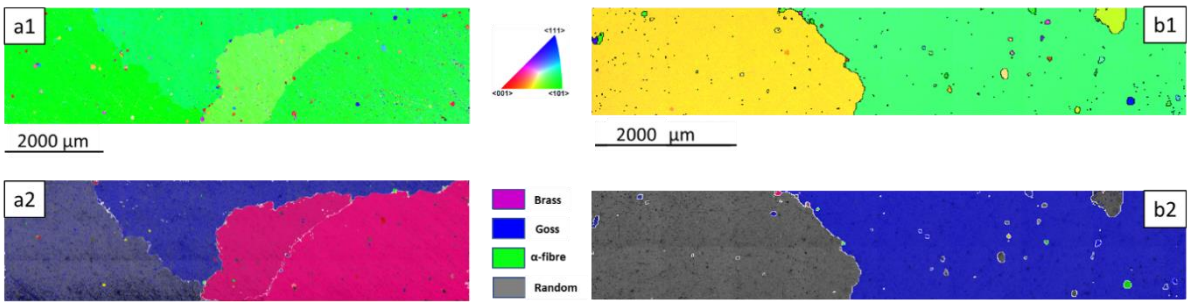

Figure 7-6 Annealed samples for 60 min in a preheated furnace to 1000℃ and annealed at 1100℃ at a heating rate of 0.6℃/sec, the IPF map//ND of sample A (a1), Sample BB (b1), and texture component map of sample A (a2), sample BB (b2).

The IPF map and texture component map of sample AA and sample BB shown in Figure 7-6a and Figure 7-6b, respectively. The growth reached saturation after heating the samples for 60 min at a higher heating rate (0.6℃/sec) in a preheated furnace. The competition of other orientations with Goss to grow abnormally with a higher heating rate similar to the results obtained in Figure 7-5. Sample AA show two abnormal Goss grains within 20° misorientation from ideal Goss and two abnormal Brass grains, whereas sample BB show a random oriented abnormal grain and abnormal Goss grain. It is evident that with a high heating rate, the Goss oriented grains loss the advantage to grow abnormally, and the desired secondary recrystallisation texture cannot be achieved. The high heating rate affects the final texture by permitting random orientation to compete with Goss orientation to grow abnormally.

7.3.3 Strain Effect on Goss Abnormal Grain Growth

A set of experiments was designed to investigate the effect of the strain on Goss abnormal grain growth. The trials were carried out by bending (folding) the samples 90° multiple times before it is straightened and cut. The affected area by bending was cut so that the edge of the sample could be examined. The samples were then annealed at different temperatures with a heating rate of 0.1℃/sec, isolating one edge and exposing the edge effected by the bending to study the effect of heat flux on the strained edges.

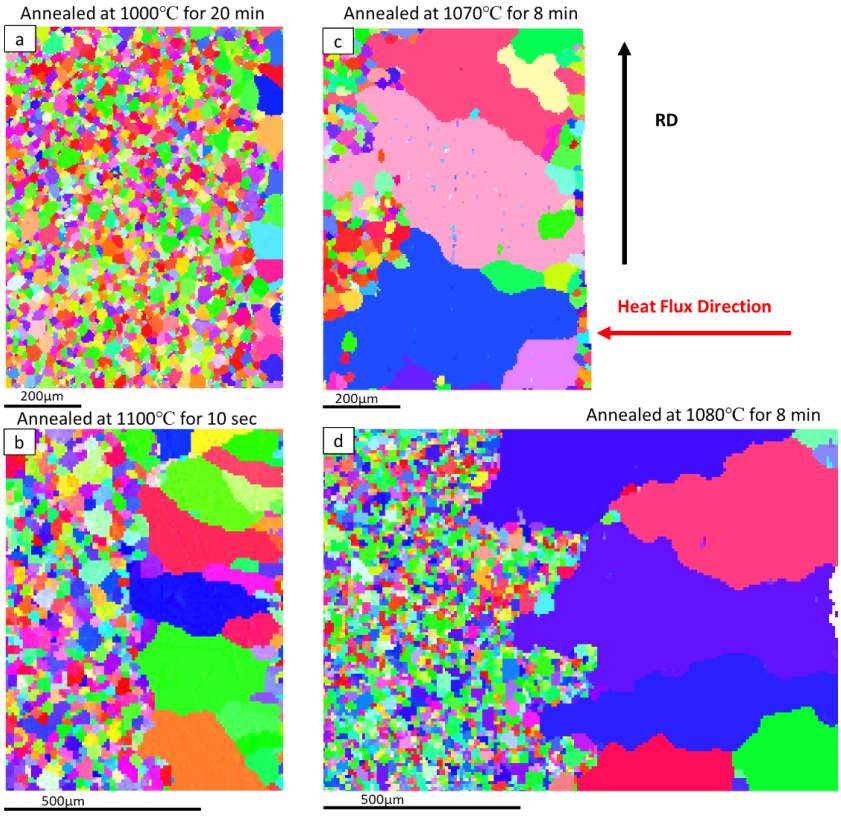

Figure 7-7 IPF map //ND edge bending results of sample AA bent for five times and annealed in TD at 1000℃ for 20min (a), annealed at 1100℃ for 10 sec (b), annealed at 1070℃ for 8 min (c) and annealed at 1080℃ for 8 min (d).

The results of sample AA, shown in Figure 7-7, where the samples were bent five times and annealed at different temperatures where the heat travels in TD (transverse direction). The affected area of the sample annealed from room temperature to 1000℃ for 20 min shows the normal grain growth at the edge of the sample where the bending was performed, as shown in Figure 7-7a. The growth of the edge grains was not exclusive to Goss oriented grains with an average of ~80µm. Figure 7-7b show the growth or random grains at the edge of the sample to ~360 µm after annealing at 1100℃. Also, the grains growing in the TD direction parallel to the heating direction. Furthermore, random grains growing abnormally in the heat flux direction up to 1mm in size. Despite the growth of the edge grains, several primary grains are seen to survive and resist grain growth at this stage.

Furthermore, annealing sample AA at 1100℃ for 20min in TD direction leads to Goss abnormal grain, as shown in Figure 7-8. Regardless of Goss growth, the affected area (edge) by bending show random large grains (>500µm) growing in heat flux direction as well as primary grains. The most affected grains (primary grains) by bending (strain) in which results in high dislocation region, thus resisted grain growth and experienced recovery and recrystallisation. Besides, the region with lower dislocation recrystallise and grow >500µm, on the other hand, abnormal Goss grains grow in heat flux direction in the region where dislocation are minimum or dislocation free region.

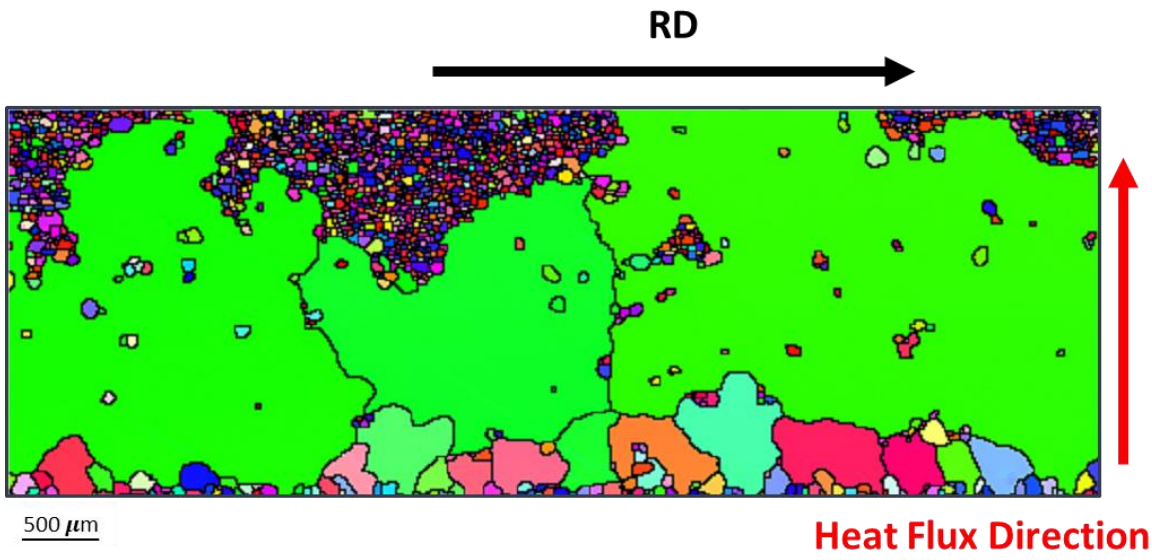

Figure 7-8 IPF map //ND of sample AA annealed in TD at 1100°C for 20min show small grains at the edge, edge abnormal grains (<800µm) and Goss abnormal grains (>2000µm).

This behaviour is further investigated by bending sample AA ten and twenty times then the sample is annealed in RD at 1100°C for 20min, as shown in Figure 7-9. The edge of the sample subjected to bending twenty times marked in blue, while the area marked in red subjected to bending five times. Similarly, the edge primary grains survived and resisted secondary recrystallisation, whereas grains in the area marked in red experience grain growth up to ~300µm.

The increase in strain (via bending) results in an increased number of survived small grains. Figure 7-9 emphasise the results obtained in Figure 7-8 and Figure 7-3; Goss abnormal grain growth has an advantage in the region free of dislocations. Also, the growth rate is higher in

samples annealed in the RD compared to TD as both Figure 7-9 and Figure 7-8 have identical annealing conditions.

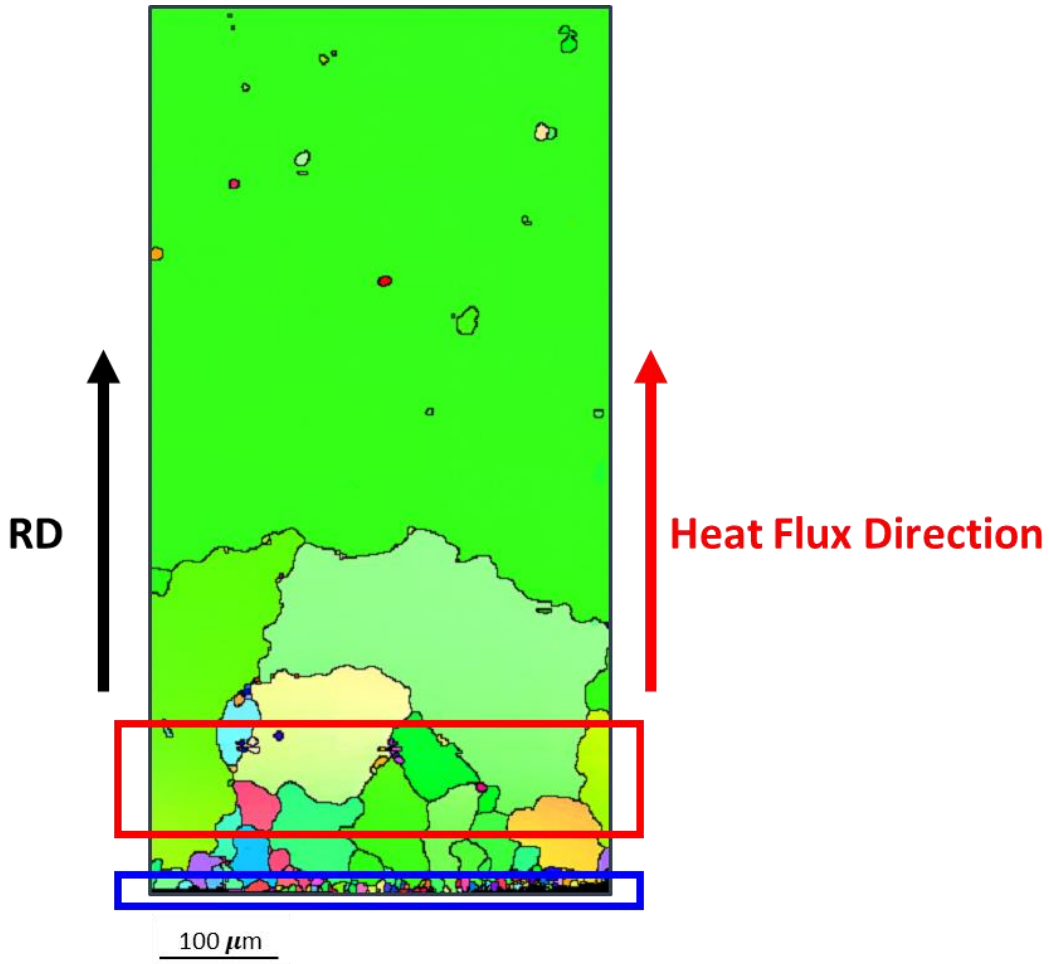

Figure 7-9 IPF map //ND showing the edge of Sample AA subjected to bending twenty times marked in blue show small grains (primary), area marked in red subjected to bending 5 times show large grains (~300µm) and Goss abnormal grain in the strain-free area.

Additionally, samples strained by bending twenty times results in more survived small grains compared to ten (Figure 7-10b) and five (Figure 7-10a) times bending. Both samples annealed to 1100℃ for 60 min show grain growth in the heat flux direction. From these results, it can

be concluded that the strain has a significant impact on secondary recrystallisation texture and grain growth evolution. The strain has a negative effect on grain size and grain growth and secondary recrystallisation texture. Furthermore, with a higher strain, more grains resist grain growth, and abnormal grains did not consume these small grains.

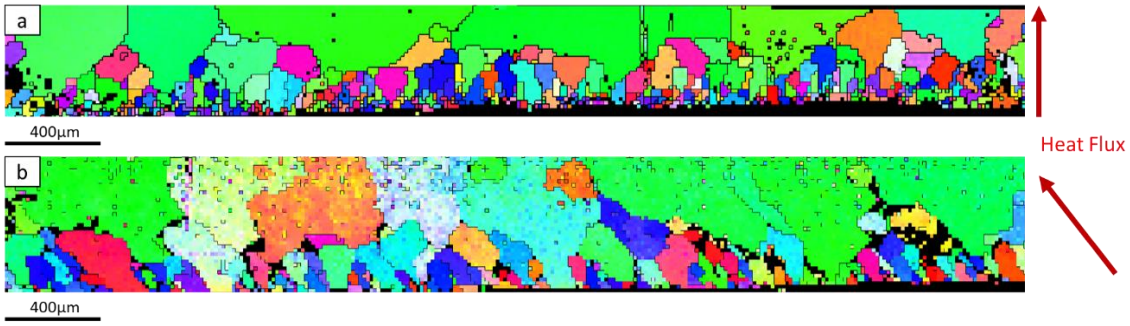

Figure 7-10 Annealed samples at 1100℃ for 60 min, (a) edge of the sample bent ten times, and (b) edge of the sample bent five times.

To further study the effect of strain and on abnormal grain growth mechanism, an additional sample AA was bent twenty times 2000µm from the edge and then straightened. The large sample (8000µm x 4000µm) was annealed at 1100℃ for 60mins in RD with a heating rate of 0.1 ℃/sec, where one edge is isolated to let the heat flow from the strain edge to the other end of the sample. Figure 7-11 shows sample AA with heat flux travelling from the right side of the sample to the left side.

From the IPF map shown in Figure 7-11, it seems that the abnormal grain growth initiated from the edge of the sample, were the grain are unaffected by the stain (flat area). However, the

centre of the bent area shows small grains and large grains <800µm at the vicinity of the small grains. The continuation of abnormal grain growth in the direction of heat flux was observed in the flat area on the left side of the bent area. It is evident that as Goss grains grow abnormally, the grains affected by the stain in the bent area were recrystallised and the grains less affected by the strain grow larger (<800µm). Also, it is evident with the higher strain, the grains recrystallise and do not grow abnormally. Besides, minimum strain promotes grain growth; nevertheless, it cannot grow abnormally. It may well be argued based on these results that grains containing sub-boundaries can grow large, but the growth is not at the scale of Goss abnormal grain growth in strain-free samples.

Although the heat flux effect on the direction of growth was clear, as discussed earlier, the disruption of Goss abnormal growth is observed in the strained area (bent area). The disruption of Goss abnormal grain growth by the strained area led to abnormal grain growth of random grains leading to abnormal growth competition between differently oriented grains. Additionally, with the evidence presented on the effect of heat flux on growth in this chapter and grain boundaries and dislocations effect on heat flow, it can be argued that strained area permits random grains to compete with Goss grains. Furthermore, an IPF map of two samples annealed under the same conditions show the advantage of Goss abnormal grain growth and achieving the desired secondary recrystallisation as in Figure 7-12.

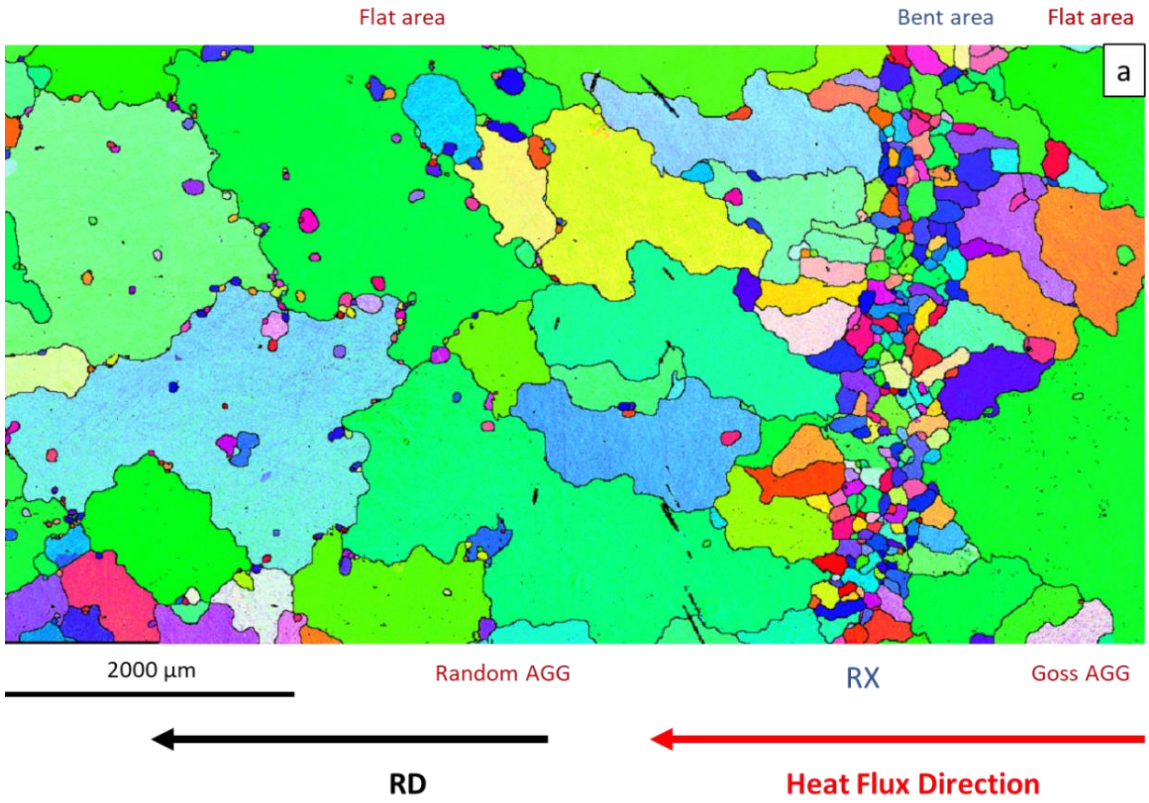

Figure 7-11 Sample AA annealed at 1100°C for 60min in RD with a heating rate of 0.1°C/sec showing the disruption of Goss abnormal grain growth in the flat area by strain-induced area (bent area).

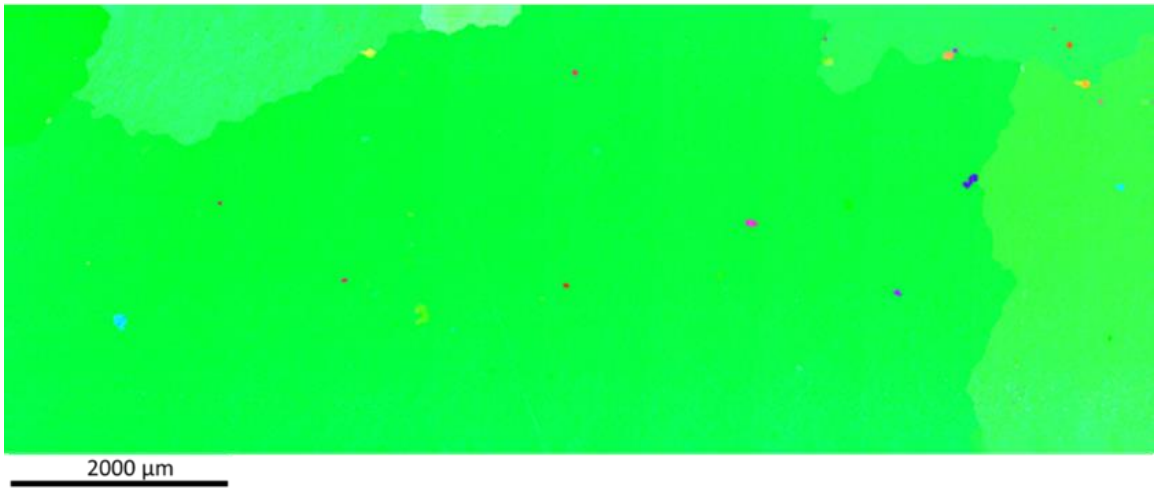

Figure 7-12 Sample AA annealed at 1100°C for 60min in RD with a heating rate of 0.1°C/sec showing Goss abnormal grains in strain-free samples

7.4 Summary

The desired secondary recrystallisation texture and Goss abnormal grain growth can be achieved by annealing primary annealed samples in a controlled environment as well as other parameters including annealing temperature, heating rate, grain size and strain. In this chapter, the heating rate and strain effect on secondary recrystallisation as well as the effect of heat flow direction (heat flux) were investigated. It was found that the heat flux direction has a significant impact on secondary recrystallisation rate (Goss abnormal grain growth rate). Annealing in the rolling direction has a higher secondary recrystallisation rate in comparison to TD or at an angle. Furthermore, the abnormal growth and normal growth of grains found to be parallel to the heat flux direction, as illustrated in Figure 7-13. As shown in Figure 7-13a, the grains grow parallel to the heating direction from both sides of the sample. Figures 7-13b and 7-13c show a sample parallel to the heating element of the furnace, and a rotated sample at a random angle respectively, where both samples are isolated from one side. In both samples, the grains grow in a direction parallel to the heating flux from the exposed side to the isolated side.

additionally, the strain was found to promote random grain growth and, disrupt Goss abnormal grain growth. The strain induces abnormal grain growth of random grains seen to have a relatively smaller grain size (<800μm) in comparison to the achieved Goss grain size in strain-free samples (>2000μm). Furthermore, the strain has a negative effect on grain size, with the higher strain the grain size decrease in secondary recrystallisation. The high strain area (bent twenty times) resist any change in secondary recrystallisation and cannot be consumed by

abnormal grains. The areas bent ten times was found to grow relatively large compared to primary grains (~400µm) whereas minimum strain grains can grow relatively large (<800µm) compared to grains affected by strain. Moreover, ideal Goss oriented grain or grains with minimum deviation from Goss were found to have an advantage in abnormal grain growth and have a considerable grain size (<2000µm) as seen in Figure 7-3, Figure 7-4 and Figure 7-12.

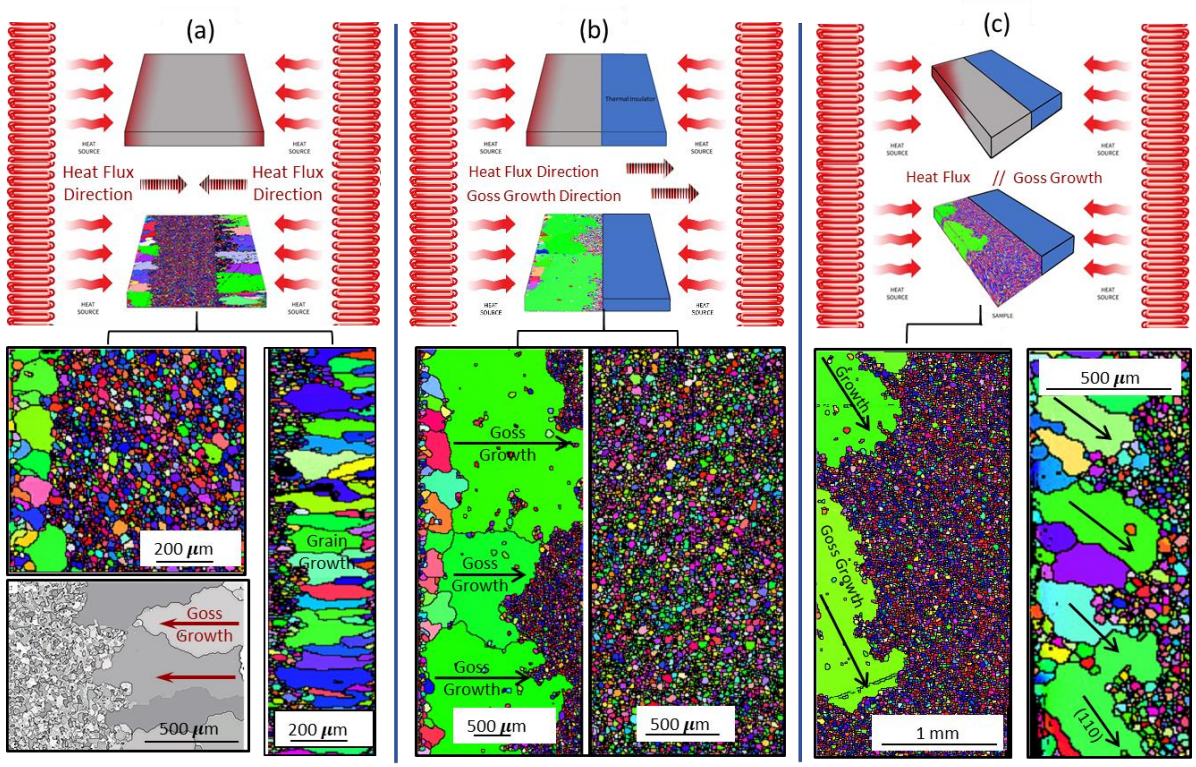

Figure 7-13 The effect of heat flux direction on grain growth (a) where grains grow parallel to heat flux on both sides of the sample, (b) grains grow parallel to heat flux on the exposed side of the sample and (c) grains growing on the exposed side and parallel to the heat flux in a rotated sample.

7.5 Conclusion

A strong secondary recrystallisation texture in 3% silicon steel was achieved by controlling the annealing parameters such as heating rate. It was found that with low heating rate Goss oriented grains have the advantage of abnormal grain growth. However, a high heating rate promotes random orientations to compete with Goss oriented grains in secondary recrystallisation. Furthermore, ideal or near-ideal Goss orientation grains are the first grains to grow abnormally at a low heating rate. While heat flux travelling on RD-TD plane, the grains grow parallel to the heat flux direction. Also, Goss orientation grains overcoming the precipitation pinning and the grow parallel to the heat flux exclusively in low heating rate scenario. Whereas in the high heating rate scenario, random grains compete with Goss grains leading to the assumption that heat flux travels through Goss grains at a higher rate causing a wider range of heat gradient. The high heating rate increases the heat gradient and causing the random orientations competing with Goss grains.

In addition, the strain has a negative correlation with grain size and growth in secondary recrystallisation. A randomly oriented grain subjected to low strain can grow abnormally to a certain degree. In contrast, a high strain leads to smaller grain growth and grains subjected to a very high strain undergo recrystallisation and cannot be consumed by abnormal grain growth. Grain boundaries and dislocations are reported in the literature to reduce the thermal conductivity in polycrystalline materials, as well as the centre, the strained sample is evidence for heat flux and heat gradient role in Goss abnormal grain growth. The grains in the centre of

the sample subjected to bending resisted and disrupted abnormal grain growth leading to random orientation competing with Goss oriented grains by disrupting the flow heat flux through the sample.

References

[1] K. Sadahiro, Y. Hayakawa, M. Kurosawa, M. Komatsubara, Investigation of secondary recrystallization kinetics in grain-oriented electrical steel using the ultrasonic interferometry, J. Appl. Phys. 85 (1999) 6019–6021.

[2] C.W. Nan, R. Birringer, Determining the Kapitza resistance and the thermal conductivity of polycrystals: A simple model, Phys. Rev. B - Condens. Matter Mater. Phys. 57 (1998) 8264–8268. doi:10.1103/PhysRevB.57.8264.

[3] B. Feng, Z. Li, X. Zhang, Prediction of size effect on thermal conductivity of nanoscale metallic films, Thin Solid Films. 517 (2009) 2803–2807. doi:https://doi.org/10.1016/j.tsf.2008.10.116.

[4] Y. Hayakawa, J.A. Szpunar, The role of grain boundary character distribution in secondary recrystallization of electrical steels, Acta Mater. 45 (1997) 1285–1295. doi:10.1016/S1359-6454(96)00251-0.

[5] A. Morawiec, On abnormal growth of Goss grains in grain-oriented silicon steel, Scr. Mater. 64 (2011) 466–469. doi:10.1016/j.scriptamat.2010.11.013.

[6] F. Citrawati, M.Z. Quadir, P. Munroe, The Effect of Final Annealing Heating Rate on Abnormal Grain Growth in a Fe-3.5% Si Steel, in: Mater. Sci. Forum, 2017: pp. 350–355.

Chapter 8: Conclusions from Overall Discussion

As reported in Chapter 4, the magnetic domain was successfully captured using FSD technique which enabled an exact correlation between magnetic domain patterns and crystallographic orientation to be observed. The orientation data, i.e., Euler angles of each individual grain was used to calculate in-plane deviation angle α and out-of-plane deviation angle β from the rolling direction. The simplicity and complexity of the magnetic domain configurations and patterns depend on both deviation angles. Also, the grain boundary angle had a significant impact on magnetic domain continuation, as shown in Figure 4-3. Furthermore, large grains with high deviation could greatly impact the magnetic patterns in the adjacent grains, as shown in Figure 4-5. In contrast, small grains had a minimum effect on the magnetic pattern passing through them, see Figure 4-2c. It appeared to be necessary to control the grain size by optimising precipitates distribution and temperature in the primary annealing process to improve the magnetic properties. The deviation angles can also have an impact on magnetic properties as shown in Figures 4-9 and 4-10. It was demonstrated that the out-of-plane deviation angle β has a higher impact on magnetic losses, while the in-plane deviation angle α has a higher impact on the magnetic permeability. In addition to the deviation angles, sheet thickness, as well as grain size, also influence the magnetic properties of 3% silicon steel (electrical steel) as shown in Figures 4-11 and 4-12. Therefore, an improvement in any of these parameters (deviation angles, sheet thickness and grain size) leads to an overall increase in magnetic performance of GOES used in transformers.

In Chapter 5, the effect of grain boundaries, CSL, grain size and stored energy on the initial stage of Goss abnormal grain growth (the initiation of Goss abnormal grain growth) was studied. Also, the results obtained in Chapter 5 clearly contradict the results reported previously in the literature [1–3] that grain size advantage of Goss grains can play a significant role in AGG during secondary annealing. In this study, it was shown that the grain size distribution was random. Additionally, in the early stages of secondary recrystallisation, randomly orientated grains could grow equally, and the growth was not exclusive to Goss grains, see Figures 5-1 – 5-4. Besides, the reduction rate of different grain boundaries and CSL was similar. The distribution of high angle grain boundaries (20°-45°), as well as CSL (Σ5, Σ7, and Σ9), were random and not exclusive to Goss oriented grains in contrast to the findings in [4–12], see Figures 5-5 – 5-7 and Figures 5-9 – 5-10. Finally, the GND and Taylor Factor were investigated, to find a correlation with Goss abnormal grain growth. The results are shown in Figures 5-11 – 5-12 and Figures 5-14 – 5-16. It is evident that GND and Taylor Factor are randomly distributed, and the grains adjacent to Goss oriented grains have random GND and Taylor Factor despite the reports in [13–18].

In Chapter 6, the neutron diffraction experiment results showed that the lattice distortion in 3% steel. It was demonstrated that the addition of Si causes the Fe crystal lattice to distort and increases with increasing temperature. This type of distortion caused the Fe crystal lattice to transform to a lower symmetry system. It was calculated that the lattice parameter of 3% Fe-Si was larger than that for pure Fe lattice[19]. Also, the importance of AlN (grain growth inhibitor/precipitates) to control the secondary recrystallisation was reported in Chapter 6. With the low heating rate, the gradual dissolving of AlN was giving the advantage for Goss grains

for AGG while Goss losses the advantage to AGG with higher heating rate due to the higher reduction rate of AlN, see Figures 6-12 and 6-13. Moreover, the asymmetric d-spacing shift of the (110) in low heating rate correlate with Goss AGG while high heating rate shows other planes to have higher asymmetric d-spacing expansion where Goss grains losses the advantage to AGG, see Figures 6-10 and 6-11. Thus, it is a valid assumption that Goss orientation grains have a different thermal property similar to magnetic permeability, with the presence of precipitates and grain growth inhibitors, Goss grains have the advantage to AGG.

In Chapter 7, heating rate, heating flux direction and strain effect on Goss abnormal grain growth were studied by EBSD, the results obtained were in agreement with neutron diffraction results reported in Chapter 6. The significant heating flux direction is shown in Figure 7-13. The abnormal grain growth direction was found to be parallel to the heating flux and the growth rate higher. It was found that ideal or near ideal Goss oriented grains have the advantage to initiate AGG, but not all Goss grain can grow equally. Furthermore, the strained areas found to resist and interfere with Goss abnormal grain growth. Also, the strain was found to allow random grain growth and disrupt abnormal grain growth, where low, strained grains can grow to 800µm while highly strained grains recrystallised and did not grow. Thus, it can be concluded that in order to achieve the desired secondary recrystallisation texture a low heating rate and heating direction (in RD) give Goss the advantage to grow, while a strain can disturb Goss AGG.

We can conclude that initially, the addition of Si into an α-Fe unit cell can distort the ideal BCC lattice parameters in favour of 1 or 2 of the 6 (110) planes expansion and superior Δ *d*-spacing during thermal exposure. Based on the Si atoms position and configuration in α-Fe BCC unit cell, not all Goss grains can grow abnormally. Thus, only a limited number of Goss grains will satisfy the (110) superior Δ *d*-spacing condition and can grow abnormally, consuming other orientations including other Goss grains with unfavourable unit cell configurations as described in Chapter 6. In the early stage of AGG 2 or less of the 6 (110) planes have the highest expansion among other crystallographic planes which results in highest Δ *d* spacing. This assists greatly in accelerating the heat flux along (110) planes to reach the Goss GB first and dissolve AlN faster than in any other orientations. This clean, i.e., precipitate free, GB increases Goss GB mobility in the heat flow and growth directions to win the growth competition with other oriented grains. At a later stage of AGG, as the thermal conductivity increases with increasing grain size, the Goss grain grows dramatically along (110) planes where the heat flows rapidly in the Goss growth direction.

References

[1] C.G. Dunn, Secondary recrystallization textures and their origin in cold-rolled single crystals of silicon iron, Acta Metall. 1 (1953) 163–175. doi:10.1016/0001-6160(53)90055-8.

[2] M. Hillert, On the theory of normal and abnormal grain growth, Acta Metall. 13 (1965) 227–238. doi:10.1016/0001-6160(65)90200-2.

[3] J.E. Burke, D. Turnbull, Recrystallization and grain growth, Prog. Met. Phys. 3 (1952) 220–292. doi:https://doi.org/10.1016/0502-8205(52)90009-9.

[4] R. Shimizu, J. Harase, Coincidence grain boundary and texture evolution in Fe-3%Si, Acta Metall. 37 (1989) 1241–1249. doi:10.1016/0001-6160(89)90118-1.

[5] J. Harase, R. Shimizu, Coincidence grain boundary and (100)[011] secondary recrystallization in Fe-3% Si, Acta Metall. Mater. 40 (1992) 1101–1111. doi:10.1016/0956-7151(92)90088-V.

[6] J. Harase, R. Shimizu, D.J. Dingley, Texture evolution in the presence of precipitates in Fe-3% Si alloy, Acta Metall. Mater. 39 (1991) 763–770. doi:10.1016/0956-7151(91)90276-7.

[7] G. Britain, P. Press, O. Cedex, Evolution of local texture and grain boundary characteristics during secondary recrystallisation of Fe-3% Si sheets., 38 (1990) 1101–1107.

[8] J. Harase, R. Shimizu, J.K. Kim, J.S. Woo, The role of high energy boundaries and coincidence boundaries in the secondary recrystallization of grain-oriented silicon steel, Met. Mater. Int. 5 (1999) 429–435. doi:10.1007/BF03026155.

[9] C. Su, G. Zhao, H. Xiao, Y. Lan, F. Huang, Abnormal Grain Growth of Hi--B Steel in the Secondary Recrystallization, Metallogr. Microstruct. Anal. 7 (2018) 608–617. doi:10.1007/s13632-018-0467-9.

[10] Y. Hayakawa, J.A. Szpunar, The role of grain boundary character distribution in secondary recrystallization of electrical steels, Acta Mater. 45 (1997) 1285–1295. doi:10.1016/S1359-6454(96)00251-0.

[11] Y. Hayakawa, J.A. Szpunar, A new model of Goss texture development during secondary recrystallization of electrical steel, Acta Mater. 45 (1997) 4713–4720.

[12] A.L. Etter, T. Baudin, R. Penelle, Influence of the Goss grain environment during secondary recrystallisation of conventional grain oriented Fe-3%Si steels, Scr. Mater. 47 (2002) 725–730. doi:10.1016/S1359-6462(02)00189-6.

[13] L. Kestens, J.J. Jonas, Modeling texture change during the static recrystallization of interstitial free steels, Metall. Mater. Trans. A. 27 (1996) 155–164.

[14] J.K. Kim, J.S. Woo, S.K. Chang, Influence of annealing before cold rolling on the evolution of sharp goss texture in Fe-3%Si alloy, J. Magn. Magn. Mater. 215 (2000) 162–164. doi:10.1016/S0304-8853(00)00103-7.

[15] S.H. Choi, Y.S. Jin, Evaluation of stored energy in cold-rolled steels from EBSD data, Mater. Sci. Eng. A. 371 (2004) 149–159. doi:10.1016/j.msea.2003.11.034.

[16] S.F. Castro, J. Gallego, F.J.G. Landgraf, H.-J. Kestenbach, Orientation dependence of stored energy of cold work in semi-processed electrical steels after temper rolling, Mater. Sci. Eng. A. 427 (2006) 301–305. doi:https://doi.org/10.1016/j.msea.2006.04.092.

[17] S.K. Chang, Texture change from primary to secondary recrystallization by hot-band normalizing in grain-oriented silicon steels, Mater. Sci. Eng. A. 452–453 (2007) 93–98. doi:https://doi.org/10.1016/j.msea.2006.10.118.

[18] S.M. Shin, S. Birosca, S.K. Chang, B.C. De Cooman, Texture evolution in grain-oriented electrical steel during hot band annealing and cold rolling, J. Microsc. 230 (2008) 414–423. doi:10.1111/j.1365-2818.2008.02001.x.

[19] Y.P. Chernenkov, V.I. Fedorov, V.A. Lukshina, B.K. Sokolov, N. V. Ershov, Short-range order in α-Fe-Si single crystals, J. Magn. Magn. Mater. 254–255 (2003) 346–348. doi:10.1016/S0304-8853(02)00845-4.

Chapter 9: Suggestions for Future Works

The microstructure characterisation and analysis were carried to investigate the driving force of Goss abnormal grain growth. Throughout this research, various theories on grain oriented silicon steel were validated and challenged. The suggested future works can be divided into two sections; (a) the study of magnetic domain dynamic behaviour in different grades of grain oriented silicon steel, and (b) further observation of the suggested Goss abnormal grain growth mechanism using an in-situ EBSD technique. Further details are shown below.

- As shown in Chapter 4, the magnetic domain structure was observed in the demagnetisation state using FSD tool. However, further understanding of the change of different magnetic domains structure can be achieved under the influence of the external magnetic field. Using magneto-optical microscopy, the correlation between grain crystallographic orientation and magnetic losses and domain structure can be further understood.
- In Chapter 5, the influence of different crystallographic variables was investigated, such as grain boundaries, grain size and stored energy, on Goss abnormal grain growth. Controlled annealing conditions, such as wet hydrogen and different temperature conditions, are highly recommended in the future works.

In Chapter 7, the correlation between Goss abnormal grain growth (AGG) and heating direction was established. In-situ EBSD can further expand our knowledge of the influence of heat flow

direction on AGG. By controlling the heat flow in RD and TD, the rate of Goss grain growth can be calculated. This type of investigation can further. can shed the light further on AGG of Goss grain during grain oriented silicon steel processing

Appendix Magnetic Domain Imaging and Complete ODF

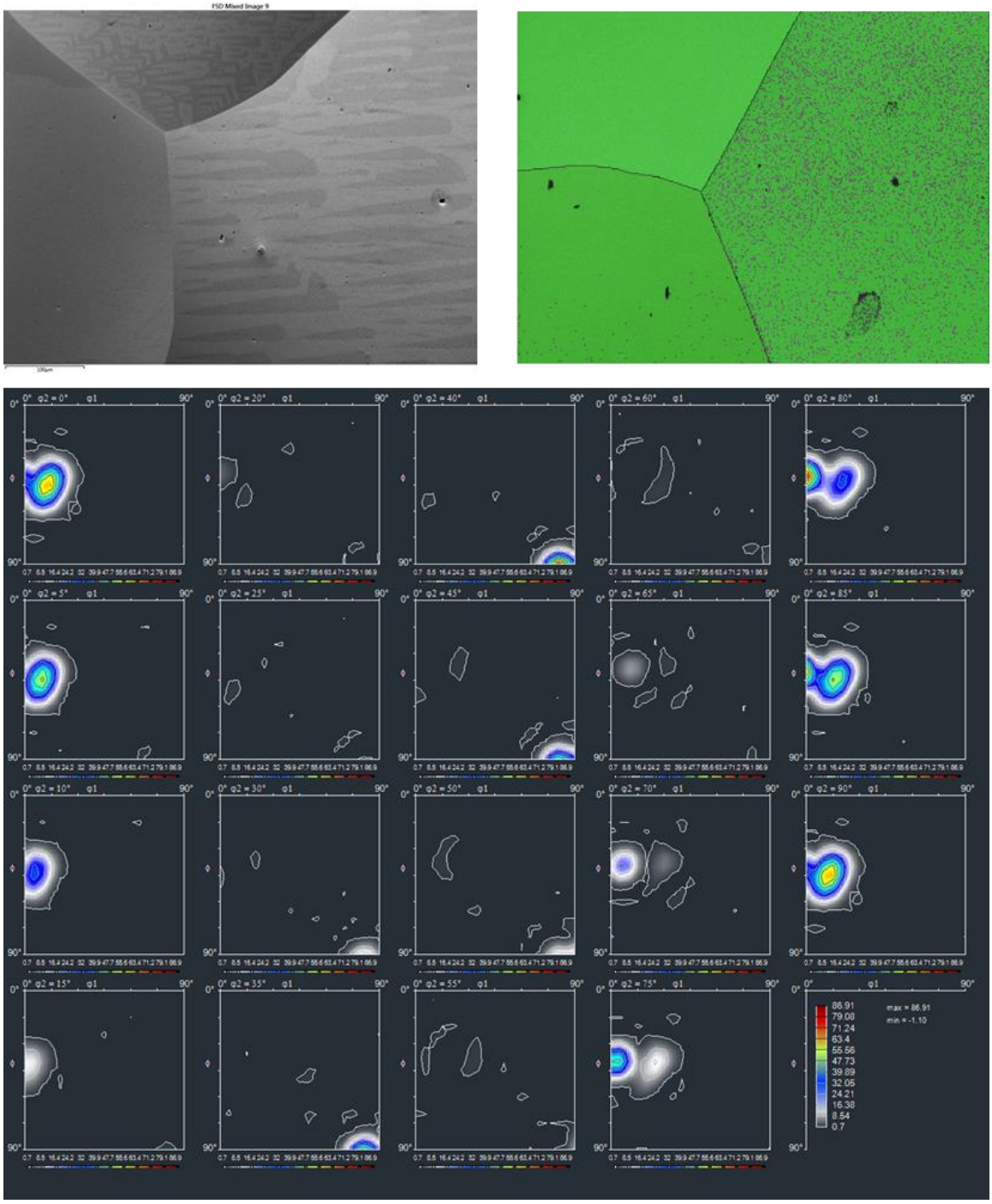

Sample B FSD magnetic pattern and complete ODF.

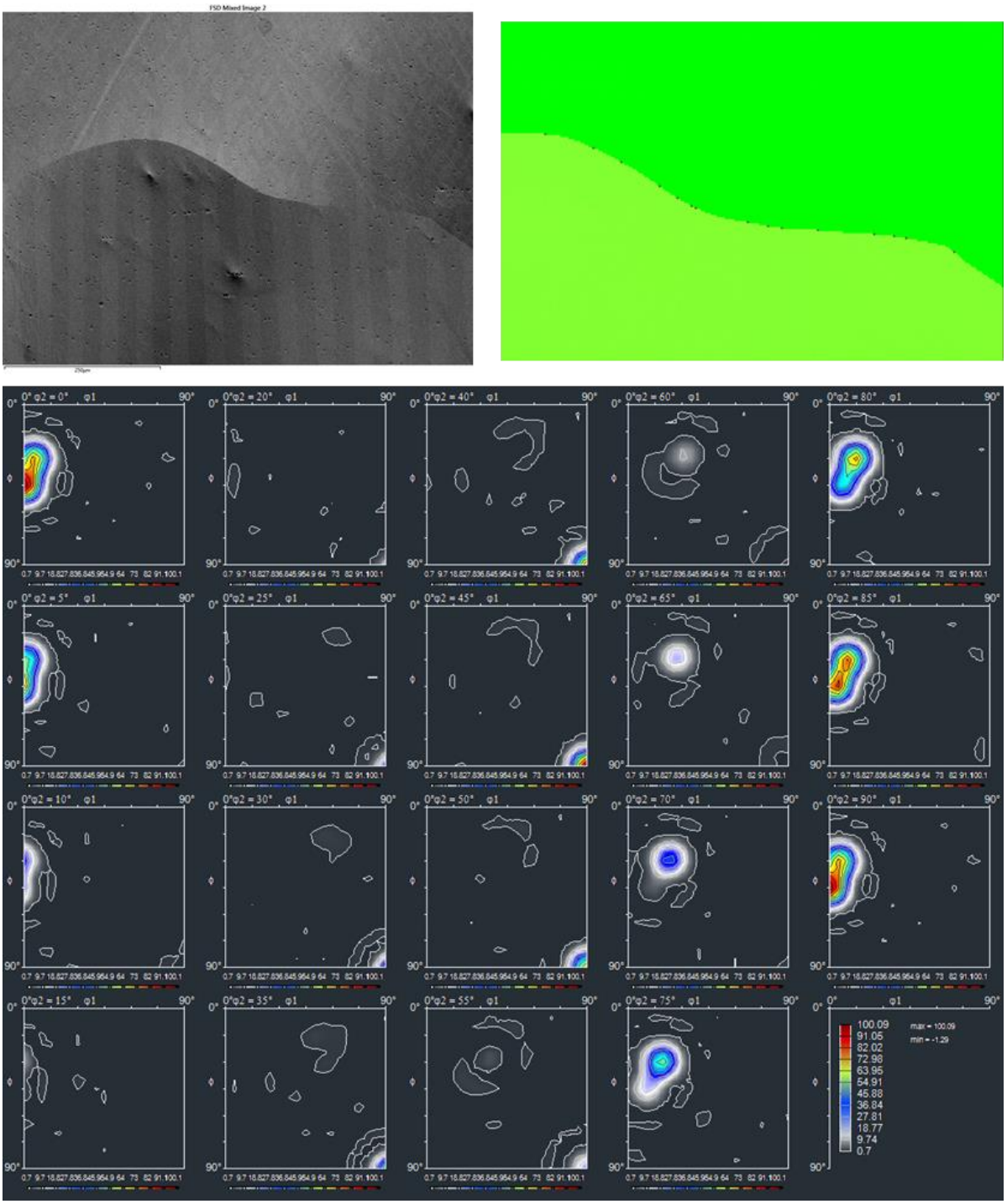

Sample C FSD magnetic pattern and complete ODF.

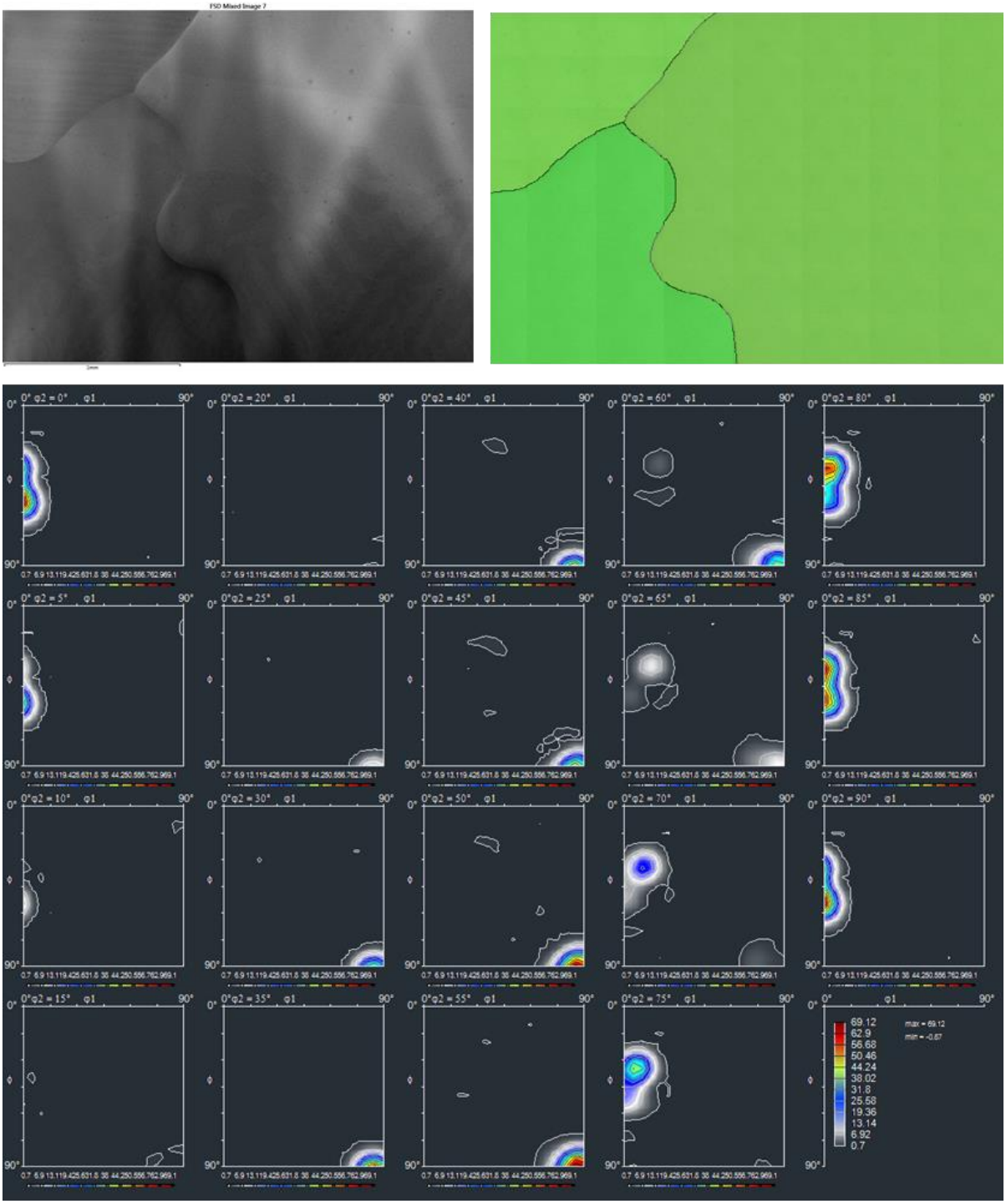

Sample C FSD magnetic pattern and complete ODF.

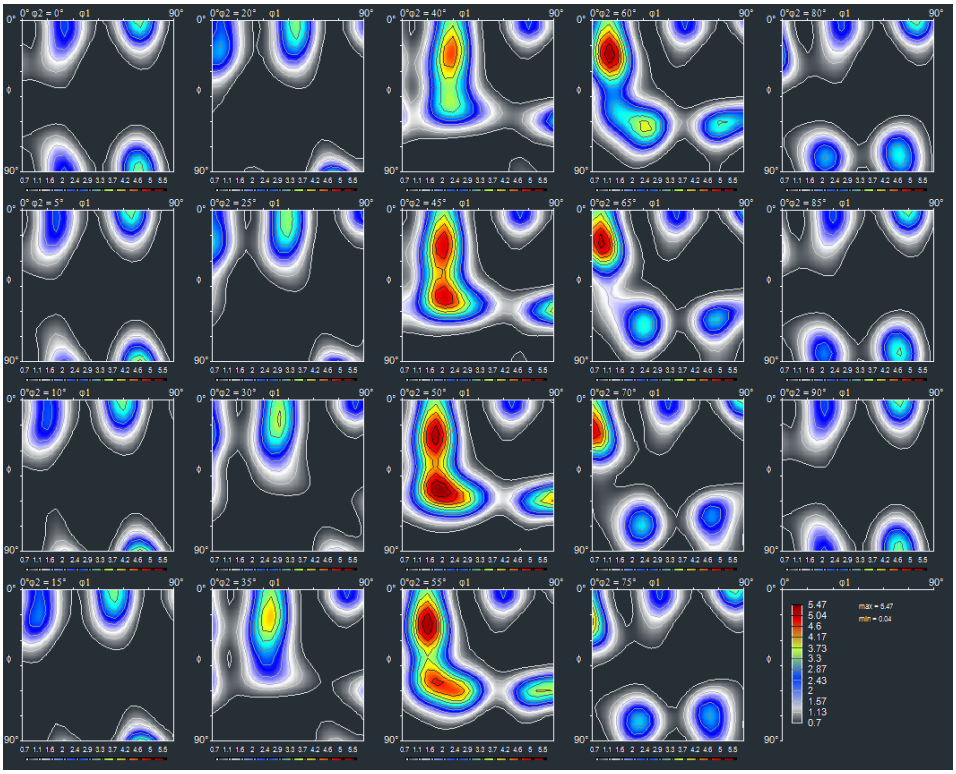

Figure 7-2 Complete ODF.

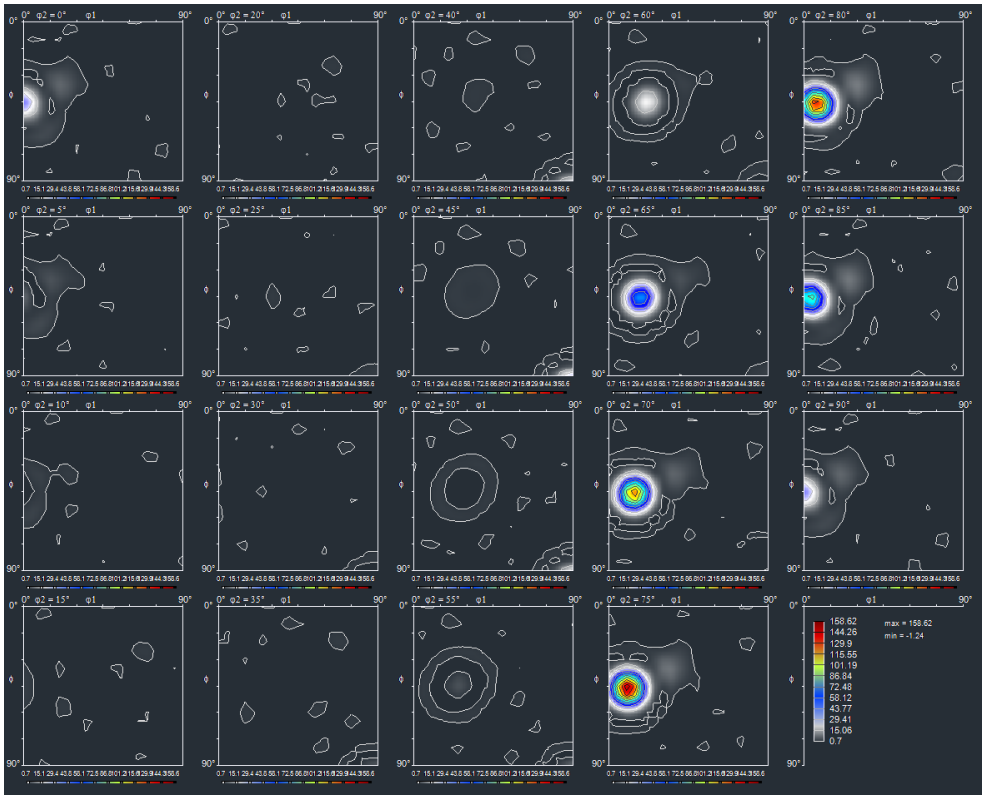

Figure 7-3a Complete ODF.

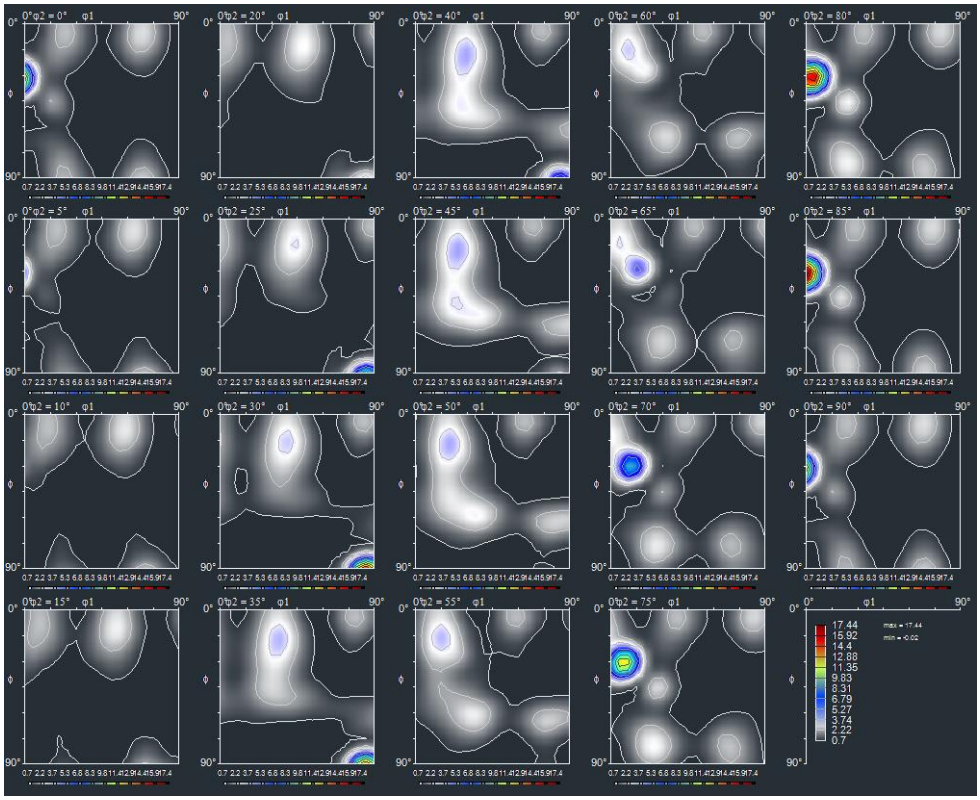

Figure 7-3b Complete ODF.

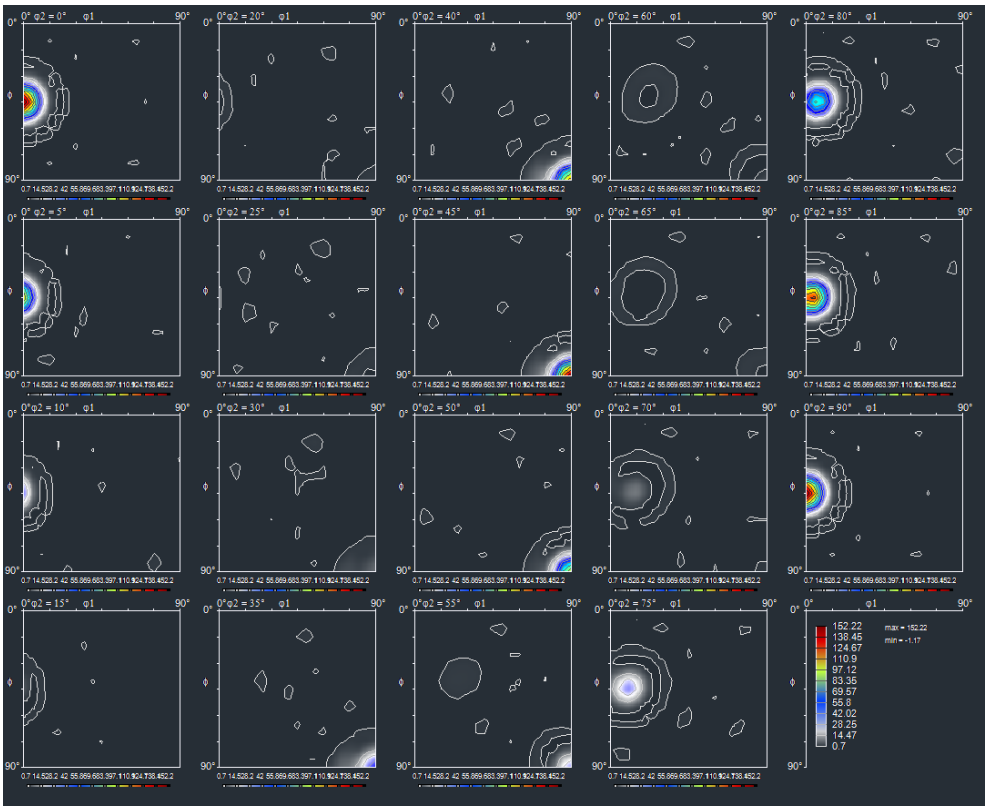

Figure 7-4a Complete ODF.

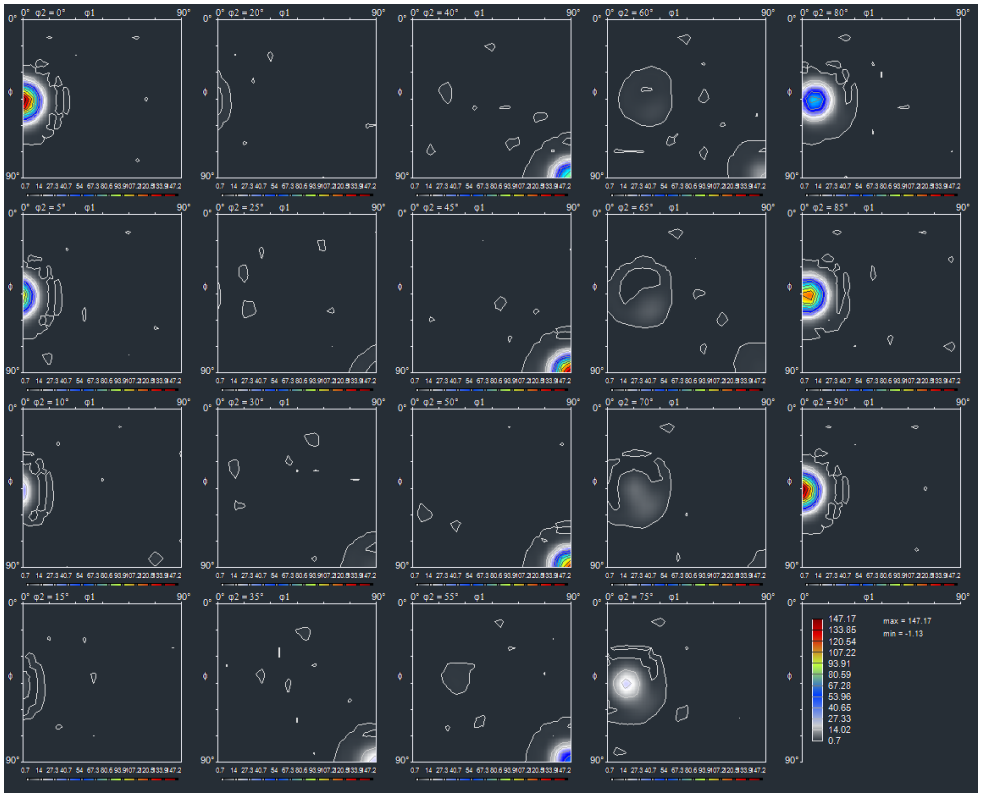

Figure 7-4b Complete ODF.

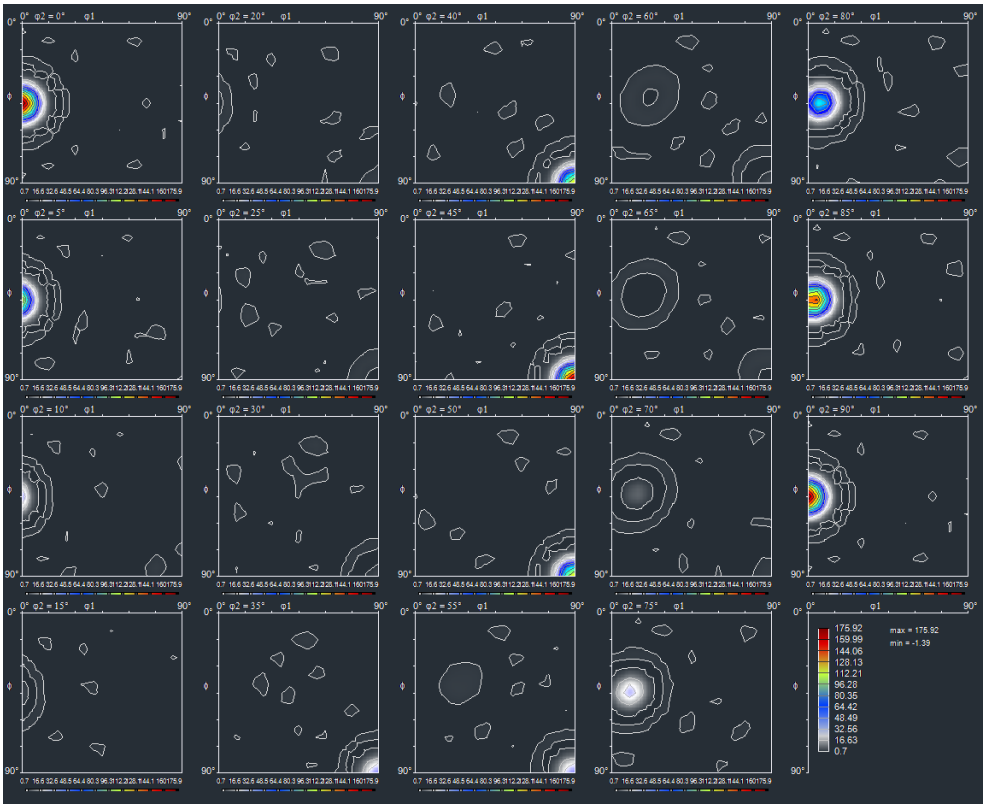

Figure 7-4c Complete ODF.

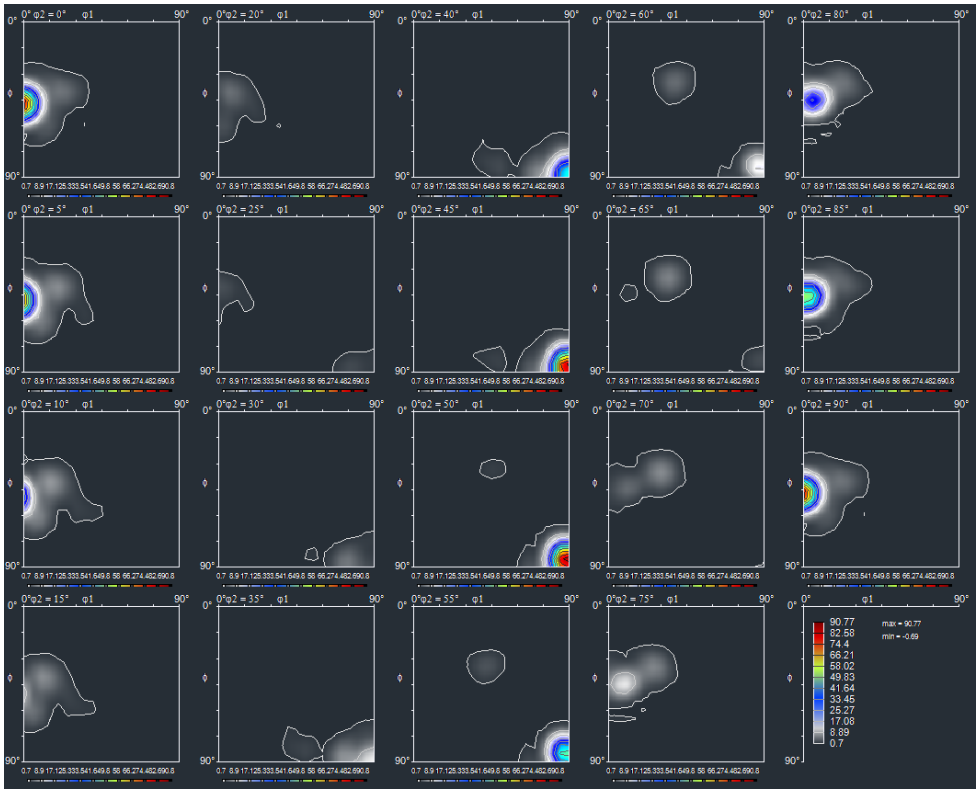

Figure 7-5a Complete ODF.

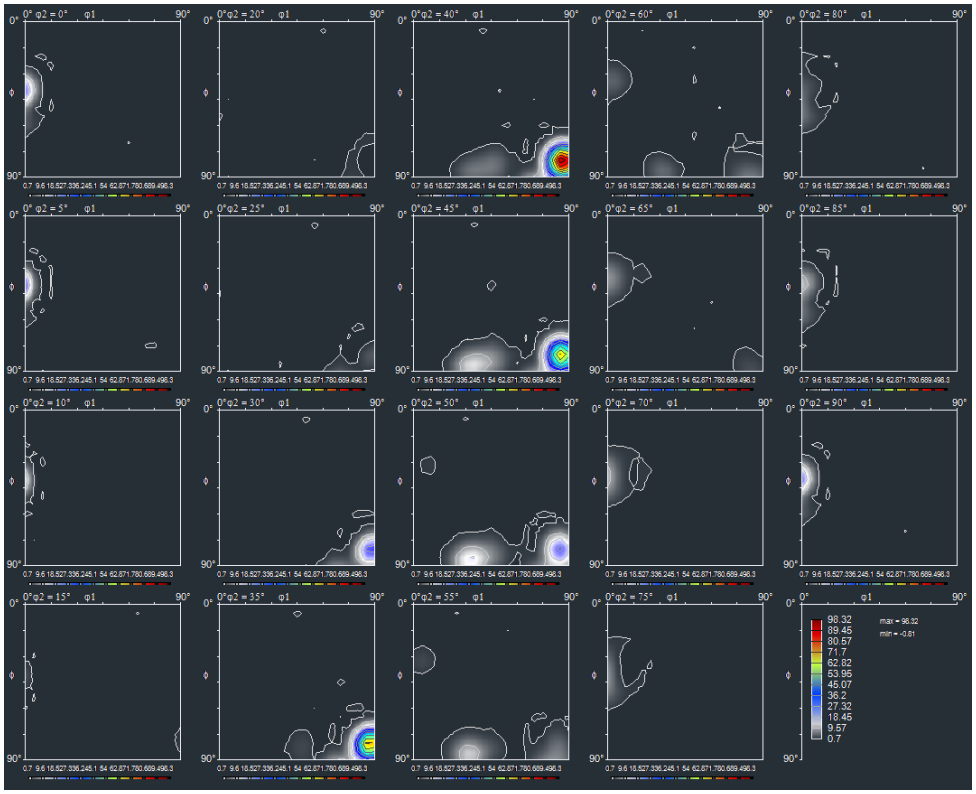

Figure 7-5b Complete ODF.

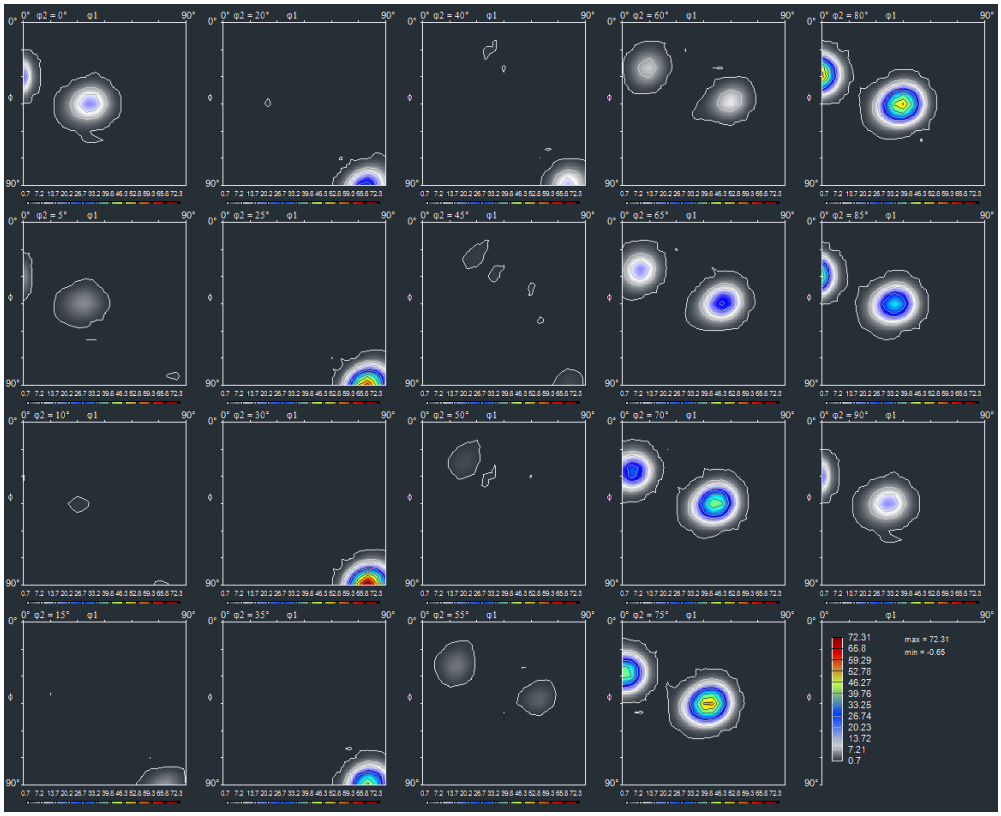

Figure 7-6a Complete ODF.

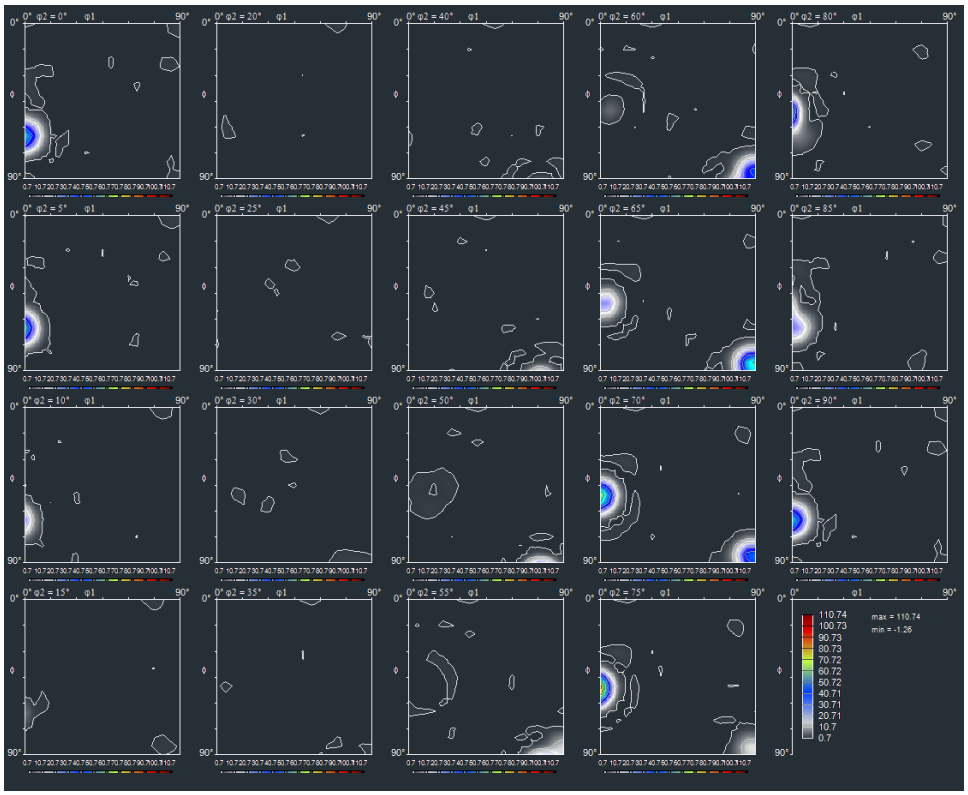

Figure 7-6b Complete ODF.

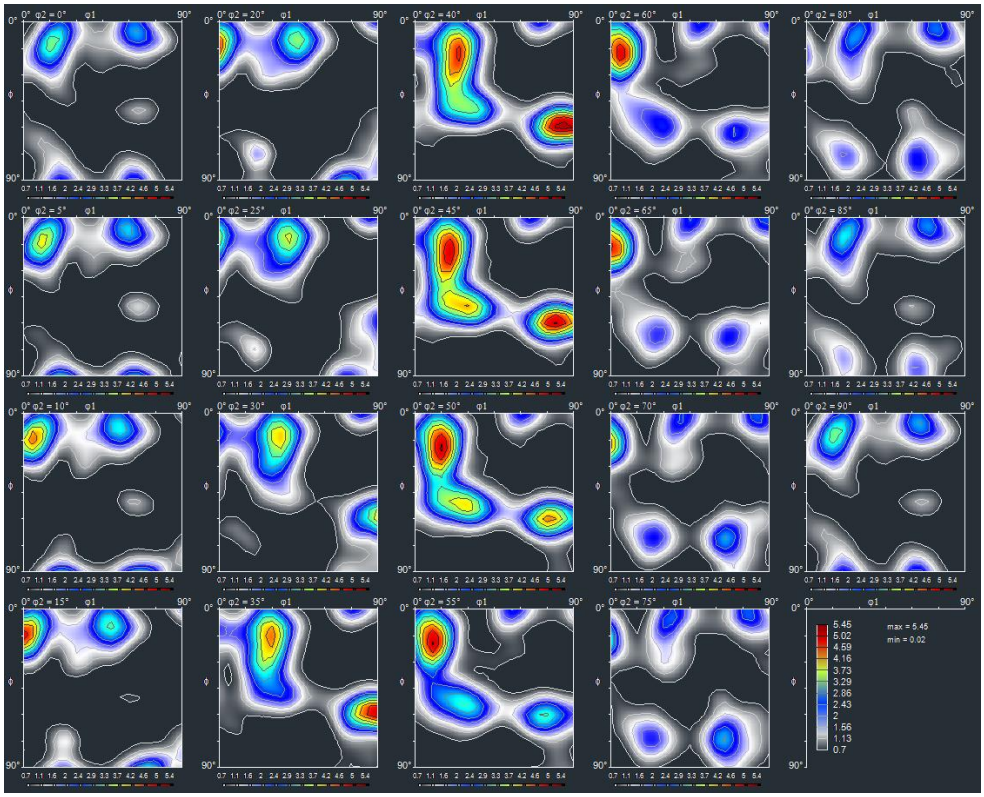

Figure 7-7a Complete ODF.

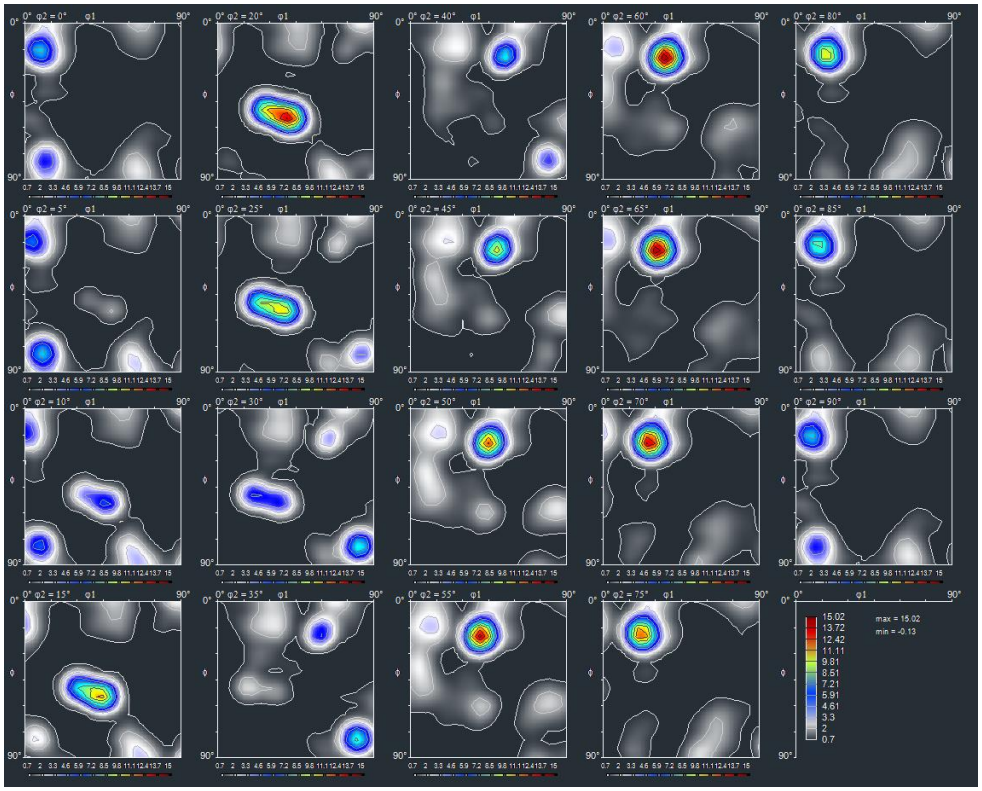

Figure 7-7b Complete ODF.

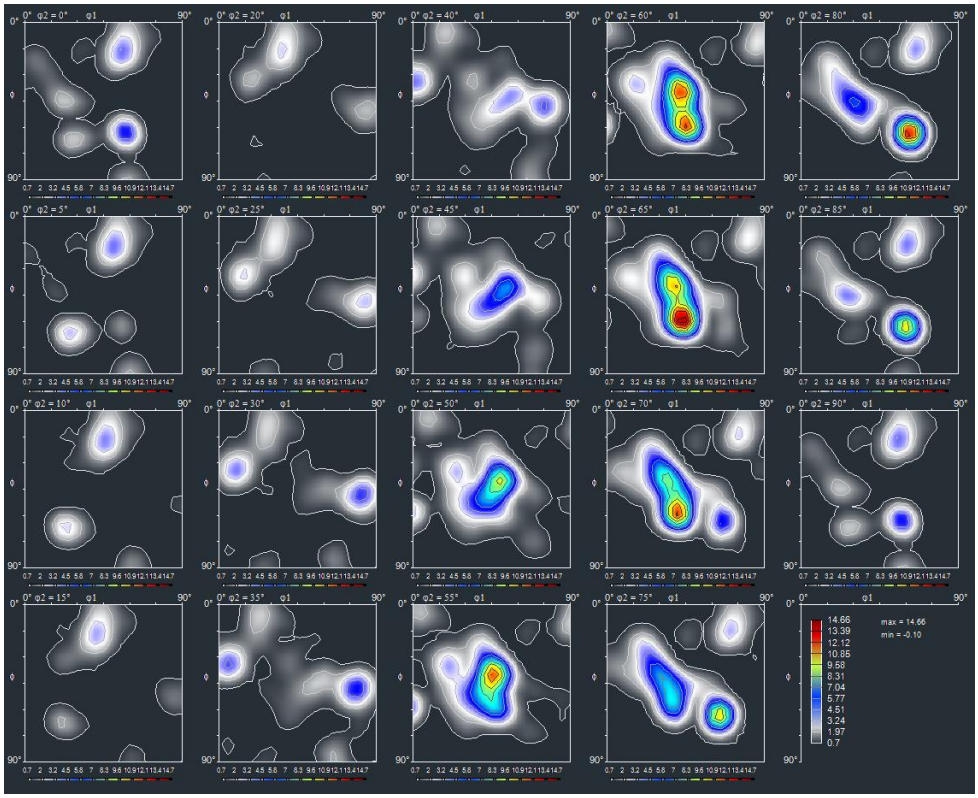

Figure 7-7c Complete ODF.

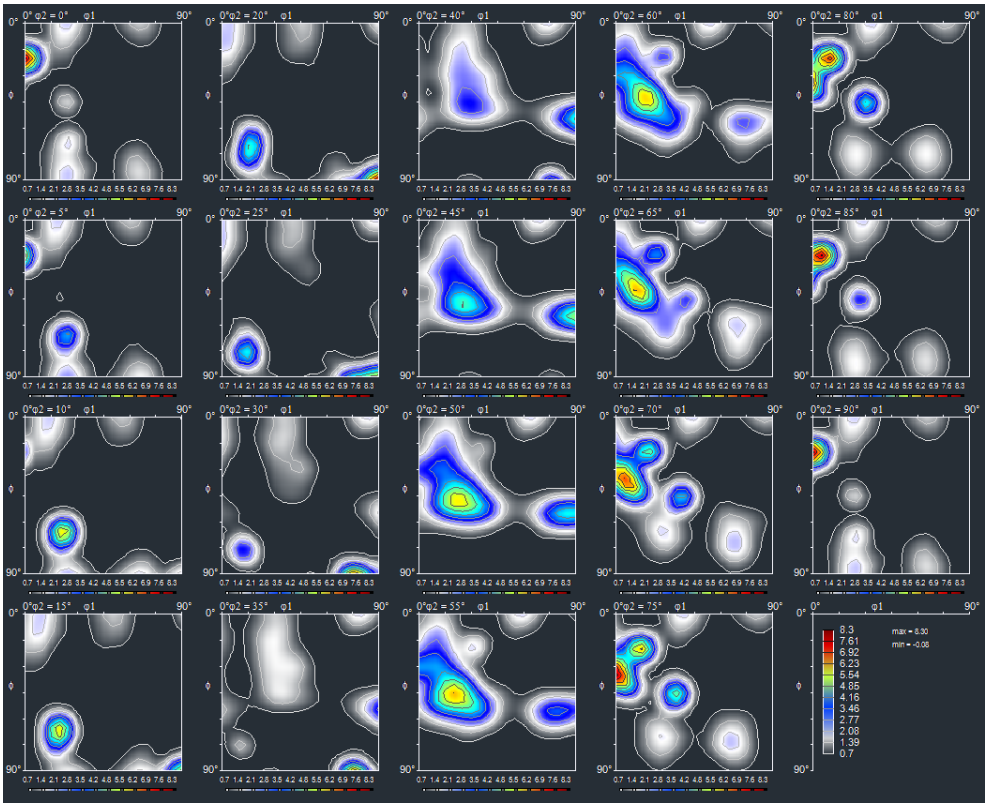

Figure 7-7d Complete ODF.

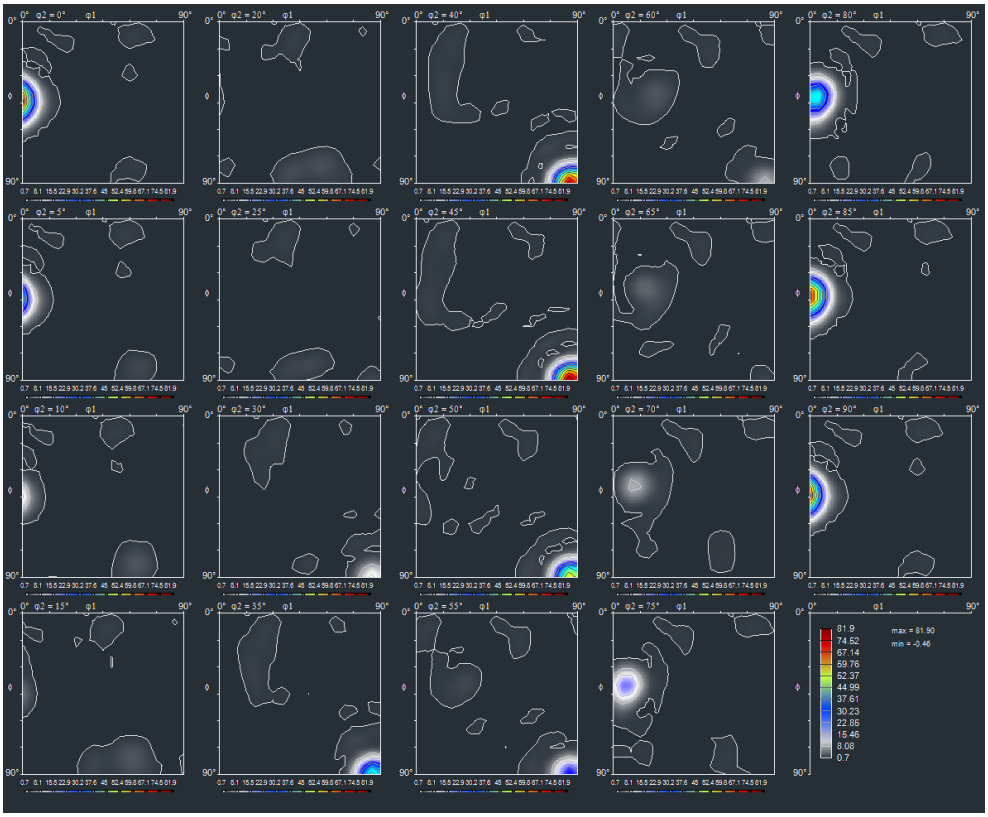

Figure 7-8 Complete ODF.

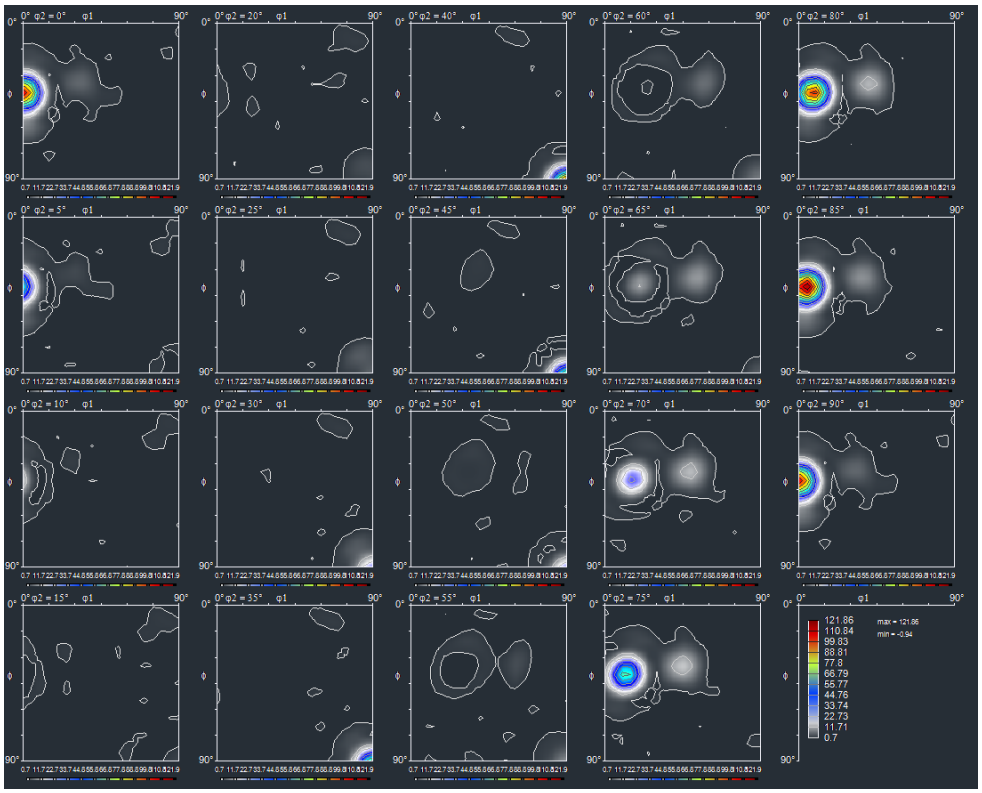

Figure 7-9 Complete ODF.

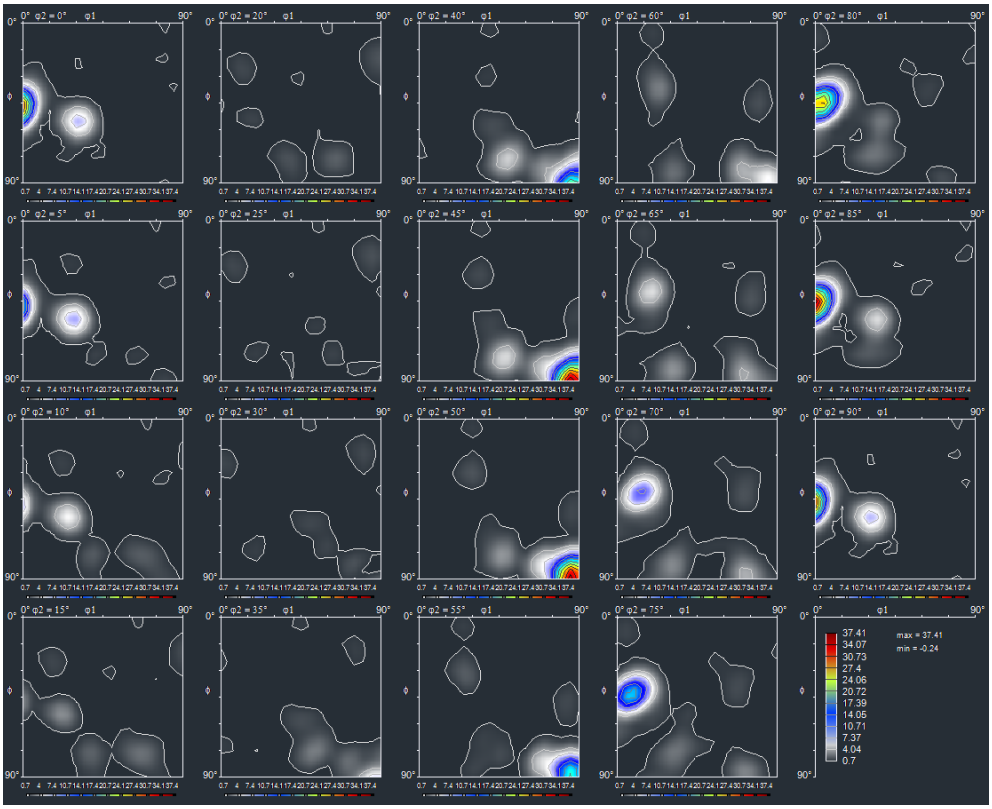

Figure 7-10a Complete ODF.

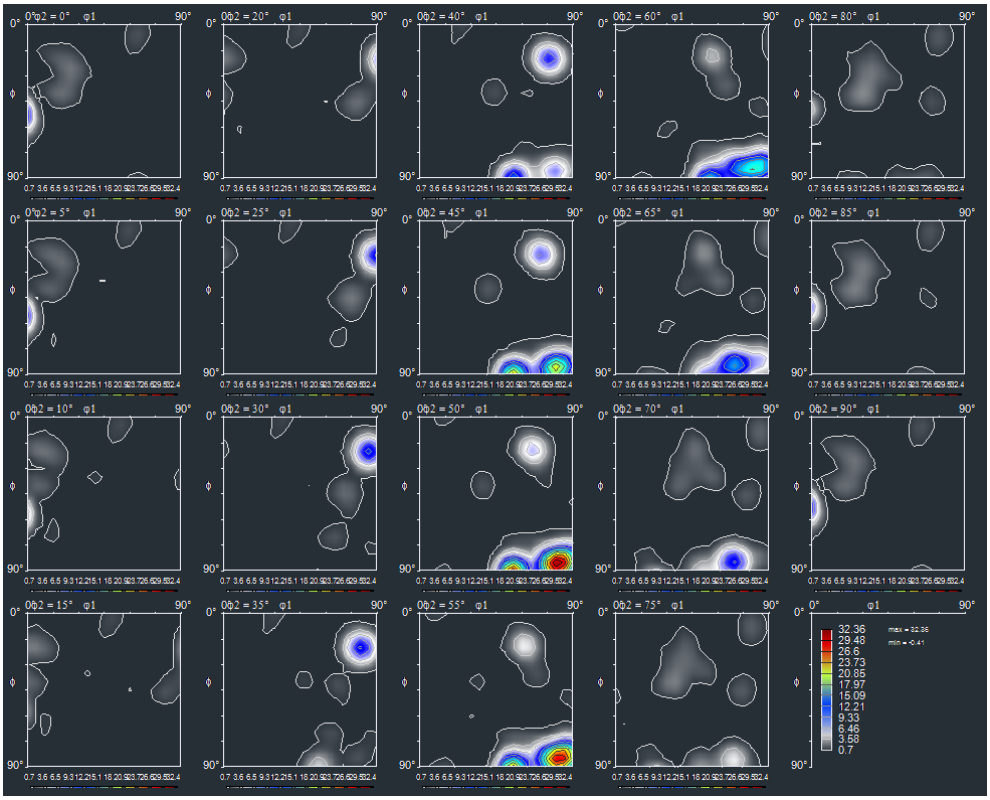

Figure 7-10b Complete ODF.

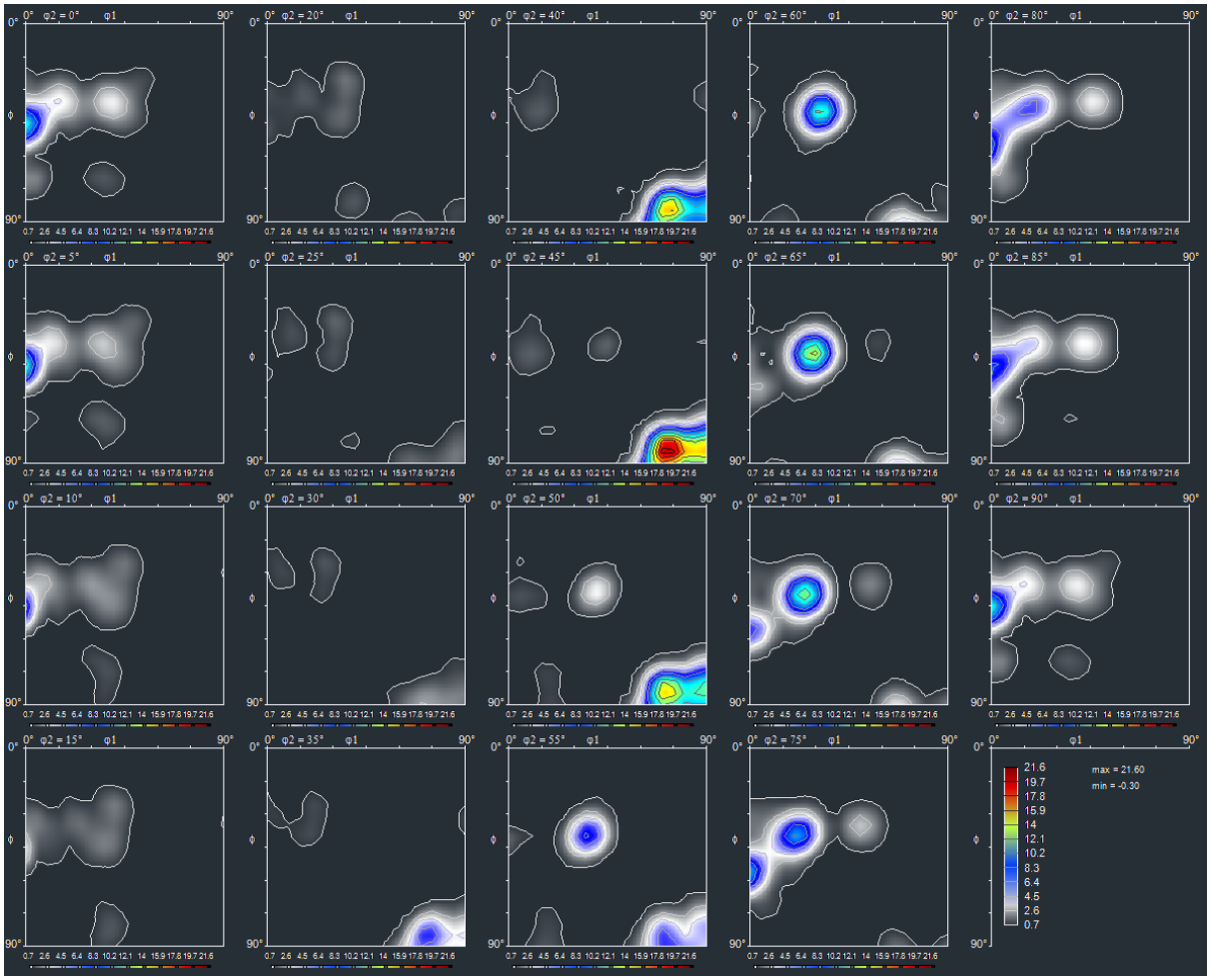

Figure 7-11 Complete ODF.

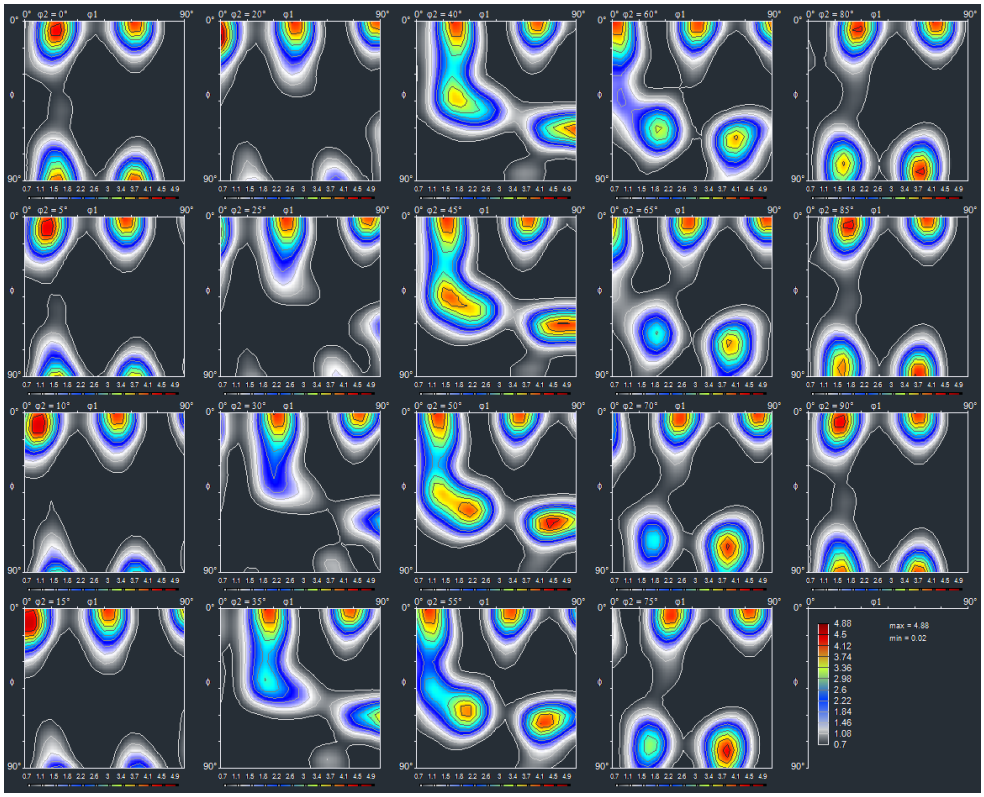

Sample complete ODF of primary annealed sample BB.

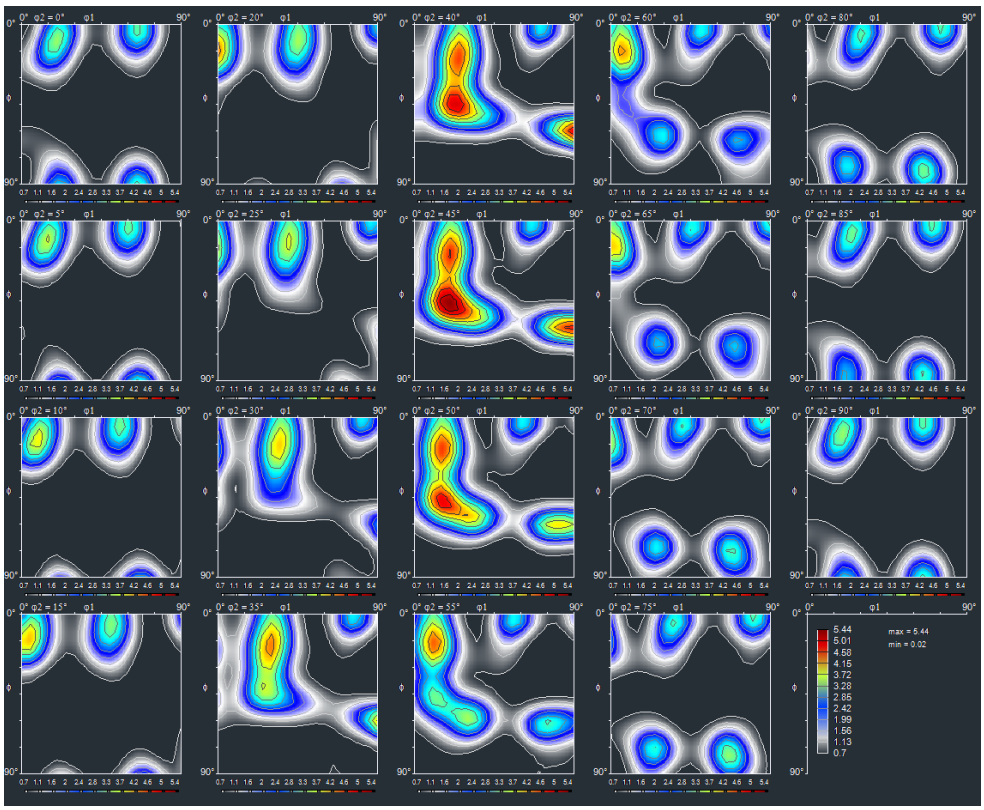

Sample complete ODF of annealed sample BB at 1000C° for 20mins.